

# Adaptive Methods in the Mechanics of Heterogeneous Materials

zur Erlangung des akademischen Grades eines  
DOKTORS DER INGENIEURWISSENSCHAFTEN (Dr.-Ing.)  
der Fakultät für Maschinenbau  
der Universität Paderborn

genehmigte  
DISSERTATION

von  
Xiaozhe Ju, M.Sc.  
aus Weihai, China

Tag des Kolloquiums: 06. Mai 2019

Referent: Prof. Dr.-Ing. habil. Rolf Mahnken, M.Sc.

Korreferenten: Univ.-Prof. Dipl.-Ing. Dr. Barbara Kaltenbacher  
Prof. Dr.-Ing. Stephan Wulfinghoff



## Abstract

A use of heterogeneous materials such as composites is very attractive in the sense of a lightweight construction, thus becoming more common in industrial practice. The growing demands on a computer simulation of such materials are not only related to a more profound theoretical treatment, but also to the associated high computational cost. This motivates the development of adaptive methods in this thesis for balancing the accuracy and the numerical efficiency of such simulations in a systematic and automated manner. Our attention is limited to a two-scale Cauchy and a micromorphic continuum, respectively in micromechanics and generalized mechanics. We handle both linear elastic and elastoplastic material behavior within a small strain theory. The adaptive procedures are mainly developed on the basis of goal-oriented error estimates, aiming at errors in a user-defined quantity of interest representing the goal of a simulation. Therewith, we control both model and discretization errors of the finite element method. For homogenization of physically nonlinear heterogeneous materials, an adaptive procedure based on an effective empirical indicator is additionally proposed.

## Zusammenfassung

Heterogene Materialien wie Verbundwerkstoffen zeigen ein hohes Potenzial in Leichtbau und finden daher in der industriellen Praxis häufig ihre Anwendung. Die wachsenden Anforderungen an eine numerische Simulation solcher Materialien beziehen sich nicht nur auf eine tiefere theoretische Behandlung, aber auch auf den damit verbundenen hohen numerischen Aufwand. Dies motiviert die Entwicklung adaptiver Methoden in dieser Dissertation, um die Genauigkeit und die numerische Effizienz solcher Simulation systematisch und automatisiert auszugleichen. Dabei wird es auf ein Zweiskalen-Cauchy und ein mikromorphes Kontinuum jeweils aus der Mikromechanik und der verallgemeinerten Mechanik zurückgegriffen. Im Rahmen einer Theorie kleiner Verformungen werden sowohl linear elastisches als auch elastoplastisches Materialverhalten behandelt. Die adaptiven Verfahren werden hauptsächlich auf der Grundlage von zielorientierten Fehlerschätzern entwickelt, die auf den Fehler in einer benutzerdefinierten Zielgröße abzielen. Damit werden sowohl Modell- als auch Diskretisierungsfehler der Finite-Elemente-Methode kontrolliert. Zur Homogenisierung von physikalisch nichtlinearen heterogenen Materialien wird zusätzlich ein adaptives Verfahren auf Basis eines wirksamen empirischen Indikators entwickelt.



# List of Pre-Publications

Parts of this thesis are already published in the following pre-publications:

- X. Ju and R. Mahnken. “An NTFA-based homogenization framework considering softening effects”. *Mechanics of Materials* 96 (2016), pp. 106–125.
- X. Ju and R. Mahnken. “Two accuracy improvements on nonuniform transformation field analysis for plasticity coupled to softening”. *PAMM* 16.1 (2016), pp. 527–528.
- X. Ju and R. Mahnken. “Error-controlled homogenization for a class of linear elastic composite problems”. *PAMM* 17.1 (2017), pp. 601–602.
- X. Ju and R. Mahnken. “Goal-oriented adaptivity for linear elastic micromorphic continua based on primal and adjoint consistency analysis”. *International Journal for Numerical Methods in Engineering* 112 (2017), pp. 1017–1039.
- X. Ju and R. Mahnken. “Model adaptivity on effective elastic properties coupled with adaptive FEM”. *Computer Methods in Applied Mechanics and Engineering* 322 (2017), pp. 208–237.
- X. Ju and R. Mahnken. “Corrigendum to: goal-oriented adaptivity for linear elastic micromorphic continua based on primal and adjoint consistency analysis”. *International Journal for Numerical Methods in Engineering* (2018). DOI: 10.1002/nme.5996.
- X. Ju and R. Mahnken. “Goal-oriented adaptivity for parameter identification in linear micromorphic elasticity”. *PAMM* (2018), e201800098. DOI: 10.1002/pamm.201800098.
- X. Ju and R. Mahnken. “Goal-oriented h-type adaptive finite elements for micromorphic elastoplasticity”. *Computer Methods in Applied Mechanics and Engineering* 351 (2019), pp. 297–329.
- R. Mahnken and X. Ju. “Goal-oriented adaptivity based on a model hierarchy of mean-field and full-field homogenization methods in linear elasticity” (2018), submitted.



# Preface

This work was carried out during my occupation as a research assistant at the Chair of Engineering Mechanics (Lehrstuhl für Technische Mechanik, LTM) at the University of Paderborn, Germany, between 2013 and 2018.

This work is based on investigations as part of the following research projects kindly funded by the German Research Foundation (Deutsche Forschungsgemeinschaft, DFG):

- CRC/Transregios “TRR 30: Process-integrated Manufacturing of Functionally Graded Structures Based on Coupled Thermo-mechanical Phenomena” – Sub-project B02 “Simulation of a hybrid-forming process considering thermal shock behaviour in the forming tool and phase transformations in the workpiece”, grant no. INST 159/11-3
- Research Grant “Goal oriented adaptive finite element method for direct and inverse problems of micromorphic continua”, grant no. MA 1979/17-1
- Research Grant “Hierarchical models for adaptive control of homogenization methods”, grant no. MA 1979/30-1

First, I am sincerely grateful to my supervisor Professor Rolf Mahnken for the provided opportunity to work on these topics as well as the given confidence and support. I would also like to express my appreciation to my co-reviewers Professor Barbara Kaltenbacher and Professor Stephan Wulfinghoff. Additionally, I would like to express my gratitude to the staff of the Chair of Engineering Mechanics for the pleasant atmosphere and the interesting discussions we have shared.

Last but not least, I would like to thank my parents, my wife Juanjuan Chen and my son Hong-Yan for everything.

Paderborn, June 2019

Xiaozhe Ju



# Contents

<b>1</b>	<b>Introduction</b>	<b>1</b>
1.1	Heterogeneous materials . . . . .	1
1.2	Classical continuum mechanics . . . . .	2
1.3	Homogenization methods . . . . .	3
1.4	Generalized continuum mechanics . . . . .	6
1.5	From a physical problem to its numerical solution . . . . .	8
1.6	Goal-oriented error estimate and adaptivity . . . . .	9
<b>2</b>	<b>Objectives</b>	<b>13</b>
<b>3</b>	<b>Summary of the papers</b>	<b>15</b>
	<b>Paper A: Model adaptivity on effective elastic properties coupled with adaptive FEM</b>	<b>19</b>
	<b>Paper B: Goal-oriented adaptivity based on a model hierarchy of mean-field and full-field homogenization methods in linear elasticity</b>	<b>61</b>
	<b>Paper C: An NTFA-based homogenization framework considering softening effects</b>	<b>105</b>
	<b>Paper D: Goal-oriented adaptivity for linear elastic micromorphic continua based on primal and adjoint consistency analysis</b>	<b>143</b>
	<b>Paper E: Goal-oriented h-type adaptive finite elements for micromorphic elastoplasticity</b>	<b>175</b>
<b>4</b>	<b>Summary</b>	<b>223</b>
<b>5</b>	<b>Outlook</b>	<b>227</b>
	<b>Bibliography</b>	<b>229</b>



# 1 Introduction

## 1.1 Heterogeneous materials

A material is heterogeneous, if individual constituents of different properties can be identified on a certain length scale. Typical examples are:

- Natural materials: polycrystals, granular materials, wood, soils etc.
- Synthetic materials: composites, foams, concrete, coating systems etc.

In some cases, several different materials are combined to design a new material of enhanced properties. For instance, fiber-reinforced polymers are attractive for a lightweight construction, by overcoming the drawbacks of their two constituents: the fibers are too brittle, while the polymer matrix is too compliant, see e.g. Fig. 1.1a for a fiber-reinforced epoxide resin. Dual-phase steel is a typical example for a material, which is made of different states (phases) of the same material. Given the fact that even microscale imperfections like microcracks or voids result into heterogeneities, see e.g. Fig. 1.1b for a porous medium, we can say that most materials are heterogeneous.

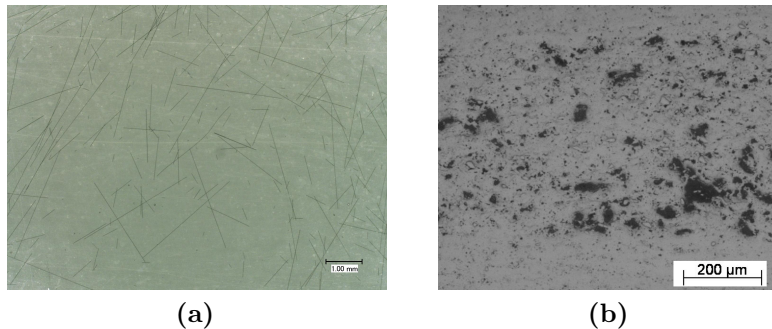


**Figure 1.1:** Several micrographs of heterogeneous materials: a) a fiber-reinforced epoxide resin (provided by Department of Chemistry – Coatings, Materials and Polymers, University of Paderborn) and b) a porous ceramic layer [56].

The study of heterogeneous materials is interdisciplinary. One important task of materials science is to characterize the microstructure of heterogeneous materials. It is of engineering interest to study the relation between the overall material properties and the underlying microstructure, for which the mathematical theory of homogenization becomes necessary. The characterization of the properties of a heterogeneous material itself is diversified, involving mechanics for mechanical

properties, thermodynamics for thermal properties, chemistry for chemical properties, electricity for electrical properties, magnetism for magnetic properties etc.

In this thesis, we focus on the mechanical behavior of heterogeneous materials. The challenges on a simulation of such behavior are, on the one hand, the need to capture subscale or microscale heterogeneities, see e.g. [49, 132, 106] for fiber-reinforced composites, [33, 139] for coating systems, [53] for polycrystalline materials and [121] for dual-phase steels. On the other hand, the mechanical behavior often shows size dependence, see e.g. [143] for metal matrix composites, [42] for multilayer materials and [113, 4, 35] for metallic and polymeric foams. Evidently, for a satisfactory description of heterogeneous materials, an in-depth theoretical treatment based on applied mechanics and mathematics is required.

## 1.2 Classical continuum mechanics

Continuum mechanics aims at the analysis of the mechanical behavior of a material, which is considered as a continuous mass rather than discrete particles in molecular dynamics, see e.g. [54, 71]. It was originated by the French mathematician Augustin-Louis Cauchy in the nineteenth century.

**A classical Cauchy continuum.** As illustrated in Fig. 1.2a, let us consider a body  $\bar{\Omega}$  bounded by  $\bar{T}$ , where no underlying microstructure is assumed. The subscripts 0 and  $t$  distinguish the reference and the current configuration, respectively. The displacement vector  $\bar{\mathbf{u}}$  is defined as

$$\bar{\mathbf{u}} = \bar{\mathbf{x}} - \bar{\mathbf{X}}, \quad (1.1)$$

where  $\bar{\mathbf{X}}$  and  $\bar{\mathbf{x}}$  are the reference and the current position vector, respectively. In a finite strain theory, one further defines

$$\bar{\mathbf{F}} = \nabla_{\bar{\mathbf{X}}} \bar{\mathbf{x}}, \quad (1.2a)$$

$$\bar{\mathbf{H}} = \nabla_{\bar{\mathbf{X}}} \bar{\mathbf{u}} = \bar{\mathbf{F}} - \mathbf{1}, \quad (1.2b)$$

$$\bar{\mathbf{C}} = \bar{\mathbf{F}}^T \cdot \bar{\mathbf{F}}, \quad (1.2c)$$

$$\bar{\mathbf{E}} = \frac{1}{2}(\bar{\mathbf{C}} - \mathbf{1}), \quad (1.2d)$$

as the deformation gradient, the displacement gradient, the right Cauchy-Green strain tensor and the Green-Lagrange strain tensor, respectively. By  $\mathbf{1}$  we denote the second-order identity tensor. In combination with the equations (1.2b) and (1.2c), Eq. (1.2d) takes an additive split as

$$\bar{\mathbf{E}} = \underbrace{\frac{1}{2}(\bar{\mathbf{H}} + \bar{\mathbf{H}}^T)}_{=: \bar{\mathbf{E}}^{\text{lin}} =: \bar{\boldsymbol{\varepsilon}}} + \underbrace{\frac{1}{2}(\bar{\mathbf{H}}^T \cdot \bar{\mathbf{H}})}_{=: \bar{\mathbf{E}}^{\text{nonlin}}}. \quad (1.3)$$

For infinitesimal deformations assumed throughout this thesis, the nonlinear part  $\bar{\mathbf{E}}^{\text{nonlin}}$  becomes sufficiently small, such that the linear part  $\bar{\boldsymbol{\varepsilon}} := \bar{\mathbf{E}}^{\text{lin}}$ , usually referred

to as a *small strain* tensor, dominates. As a result, a *geometric linearization*, i.e.  $\overline{\mathbf{E}} \approx \overline{\boldsymbol{\varepsilon}}$ , can be made by neglecting the difference between the reference and the current configuration. Furthermore, the notion of a second-order stress tensor  $\overline{\boldsymbol{\sigma}}$  is deduced from the Cauchy lemma

$$\mathbf{N} \cdot \overline{\boldsymbol{\sigma}} = \overline{\mathbf{t}}, \quad (1.4)$$

where  $\overline{\mathbf{t}}$  is the traction vector on a surface with an outward normal vector  $\mathbf{N}$ . It follows from conservation of momentum and conservation of moment of momentum, respectively, that

$$\text{Div}(\overline{\boldsymbol{\sigma}}) + \overline{\mathbf{b}} = \mathbf{0}, \quad (1.5a)$$

$$\overline{\boldsymbol{\sigma}} = \overline{\boldsymbol{\sigma}}^T, \quad \text{in } \overline{\Omega}. \quad (1.5b)$$

Here, the divergence operator  $\text{Div}(\bullet)$  is defined as  $\text{Div}(\boldsymbol{\sigma}) := \boldsymbol{\sigma} \cdot \nabla = \sigma_{ij,j} \mathbf{e}_i$  with  $\sigma_{ij,j} = \partial \sigma_{ij} / \partial X_j$ , while  $\overline{\mathbf{b}}$  denotes the body force. By neglecting an acceleration term, the equations (1.5a) and (1.5b) describe the equilibrium of the body  $\overline{\Omega}$  subjected to the following boundary conditions of Neumann and Dirichlet type

$$\mathbf{N} \cdot \overline{\boldsymbol{\sigma}} = \overline{\mathbf{t}}, \quad \text{on } \overline{\Gamma}_t, \quad (1.6a)$$

$$\overline{\mathbf{u}} = \overline{\mathbf{u}}^*, \quad \text{on } \overline{\Gamma}_u, \quad (1.6b)$$

respectively.

**Constitutive modeling.** To complete a continuum model, the relation between  $\overline{\boldsymbol{\sigma}}$  and  $\overline{\boldsymbol{\varepsilon}}$  remains to be postulated to reproduce, amongst others, isotropy, anisotropy, time dependency, isotropic hardening, Bauschinger effects, strength difference effects and/or softening effects, see e.g. [127].

There seem to be two ways to model a heterogeneous material as a classical Cauchy continuum:

1. A direct inclusion of microstructural details.
2. Phenomenological modeling.

The former way requires an extremely high resolution onto the microscale, which is not practicable for a structural analysis. The latter way heavily relies on expensive experiments and does not provide a sufficient basis for a profound understanding. Hence, a need for a more comprehensive theoretical treatment arises.

### 1.3 Homogenization methods

The mathematical theory of homogenization provides an elegant way to study partial differential equations with rapidly oscillating coefficients, see e.g. [11, 65]. When applied in continuum mechanics, a subject of mechanics of materials, namely *micromechanics*, emerges. It studies the macroscopic behavior of a material by

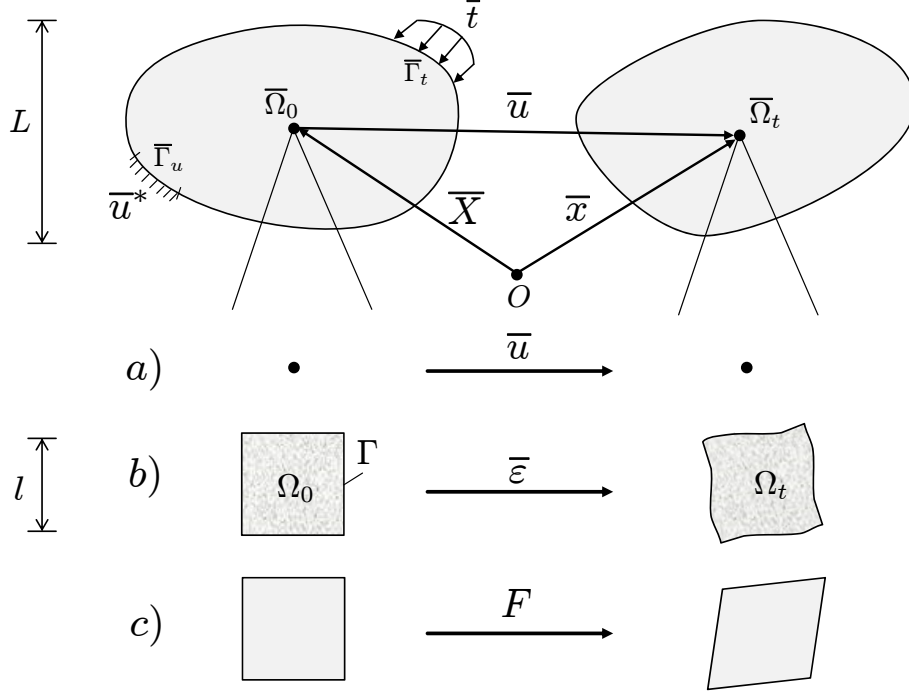


**Figure 1.2:** Illustration of the difference between a) Cauchy, b) two-scale Cauchy and c) micromorphic continuum.

considering its microstructure. Under the premise that the material properties of each micro constituent and the microstructure are known, it can predict the macroscopic material behavior without the need of physical experiments, thus providing a powerful tool for engineering design of optimum microstructures. By means of the asymptotic homogenization theory [125, 32], and assuming a clear scale separation, i.e.  $l \ll L$  in Fig. 1.2b, and local periodicity, one may arrive at a two-scale problem as follows.

**A two-scale Cauchy continuum.** As illustrated in Fig. 1.2b, the classical Cauchy continuum is equipped with a heterogeneous microstructure, which constitutes a subscale (or a microscale) continuum  $\Omega$  in addition to the macro continuum  $\bar{\Omega}$ . In addition to the macroscale equilibrium equation (1.5a), the microscale equilibrium equation

$$\text{Div}(\boldsymbol{\sigma}) = \mathbf{0}, \quad \text{in } \Omega \quad (1.7)$$

holds, where the symmetry of the micro stress tensor  $\boldsymbol{\sigma}$  ensures the conservation of moment of momentum on the microscale. By means of volume averaging theorems, the scale transition is established as

$$\bar{\boldsymbol{\varepsilon}} = \langle \boldsymbol{\varepsilon}(\mathbf{x}) \rangle, \quad (1.8a)$$

$$\bar{\boldsymbol{\sigma}} = \langle \boldsymbol{\sigma}(\mathbf{x}) \rangle, \quad (1.8b)$$

where  $\boldsymbol{\varepsilon}$  denotes the micro strain tensor and the volume averaging operator is defined as  $\langle \bullet \rangle = \frac{1}{\Omega} \int_{\Omega} \bullet \, dv$ . As a result, the two-scale Cauchy continuum does not alter the nature of a classical Cauchy continuum, i.e. the symmetry of stress tensors and local material formulations.

The well-known Hill-Mandel condition [57]

$$\langle \boldsymbol{\sigma} : \boldsymbol{\varepsilon} \rangle = \bar{\boldsymbol{\sigma}} : \bar{\boldsymbol{\varepsilon}} \quad (1.9)$$

is of utmost importance, which establishes the equivalence between the macroscopic and the microscopic energy. Accordingly, homogenization can be interpreted as a process to find a homogeneous effective material, which is energetically equivalent to the heterogeneous one under study. Moreover, Eq. (1.9) also serves as a basis to formulate different microscale boundary conditions, which are crucial to complete the micro problem (1.7). A central role is played by the concept of the so-called *representative volume element* (RVE), which is defined by [57] as a sample

- which is entirely typical of the whole microstructure on average,
- which contains a sufficient number of inclusions for the apparent effective properties to be independent of the surface values of traction and displacement.

In the past decades, many different methods for solving the micro problem, like Eq. (1.7) for small strain problems, have been developed, see e.g. [61, 118, 148, 32], leading to the following different classes of homogenization methods.

- **Mean-field methods:** This kind of methods resolves the heterogeneous micro fields merely to their means over individual material phases. Based on some assumptions and a potential use of analytical solutions, they are usually numerically efficient. In doing so, the simplest ways are the Voigt [136] and the Reuss bound [119], which fail to account for microscopic equilibrium in general. The first idea of analytical methods may be traced back to the seminal work of Eshelby [30], who considered an ellipsoidal inclusion embedded in an infinite matrix material. The solution of such a problem is often referred to as a *dilute* solution, due to the fact that it does not account for inclusion interaction. For a remedy, more sophisticated methods have subsequently been developed, see e.g. Mori-Tanaka scheme [104], self-consistent scheme [58] and generalized self-consistent scheme [62]. For a method, which possesses both an explicit structure and the ability to account for inclusion distributions, we mention the interaction direct derivative (IDD) method proposed by [142]. Nonlinear materials were also treated e.g. in [74, 78, 12].
- **Computational methods:** This class of methods employs numerical methods like the finite element method (FEM) [31, 47, 103] or the fast Fourier transform (FFT) [105, 102] to solve the RVE problem. These methods have attracted considerable attention of the international research, since they enable the possibility to consider complex microstructures, complex (nonlinear) material behaviors and further effects like imperfect interfaces. However, the main drawback is the associated high computational effort, which makes a structural analysis impracticable.
- **Model order reduction methods:** These methods aim at a numerically efficient analysis by reducing the number of degrees of freedom (DoFs) in the system, while retaining a certain level of accuracy. Concerning physical

nonlinearities, the transformation field analysis (TFA) [21, 20] enables one to precompute some localization operators under a piecewise uniform approximation, such that only a reduced set of nonlinear equations needs to be solved during an online phase of the analysis. For many cases, the inherent nonuniformity of inelastic strain fields make the piecewise uniform approximation too rough to obtain satisfactory predictions. For an accuracy improvement, more sophisticated schemes like the nonuniform transformation field analysis (NTFA) [99, 100] and the hybrid impotent-incompatible eigenstrain based homogenization [34] were developed. For large deformation problems, a model order reduction method based on the proper orthogonal decomposition (POD) was proposed in [141]. The issue of imperfect interfaces is also addressed e.g. in [88].

- **Variational methods:** They rely on variational principles and provide a powerful tool to establish higher order bounds of linear elastic properties [18, 75]. For nonlinear cases, the effective nonlinear material behavior is expressed in terms of a so-called *linear comparison material*, see e.g. [116, 15, 79, 80]. In this manner, classical bounds and estimates of linear elastic materials can be used to derive those of nonlinear ones.

The above classification is directed to first order homogenization for the case where the macroscale solution holds constant over the RVE. In the case where the macroscale solution varies rapidly over the RVE, one has to resort to certain higher order homogenization theories [72, 73, 46], which are closely related to the generalized continuum theories introduced in the subsequent Section 1.4. Additionally, for approaches considering multiple scales (more than two), we refer to [48, 92, 93].

## 1.4 Generalized continuum mechanics

The classical Cauchy continuum as well as the two-scale Cauchy continuum related to the first order homogenization theory, introduced in the previous sections 1.2 and 1.3, due to the lack of an internal length scale, are not able to capture size-dependent effects. Another issue related to an illposedness (mesh dependence) arises in the case of numerical simulation of softening behavior, see e.g. [98, 60, 19, 46]. In order to overcome these limitations, many different theories have been developed under the term of generalized continuum mechanics, which can be subdivided into the following three subclasses (see e.g. [98]):

- **Higher order theories:** They introduce additional DoFs. We will consider them in some detail below.
- **Higher grade theories:** They suggest a use of higher order gradients of the displacement field, see e.g. [115, 66].
- **Nonlocal theories:** They rely on certain integral formulations of constitutive equations, see e.g. [29, 76].

In this thesis, our attention is limited to higher order theories, which suggest a microstructural consideration. Indeed, higher order theories and homogenization methods share a common idea of introducing a microstructure, however, differ from each other in the way of considering it. Let us first consider a general case of higher order continua according to Eringen [26] as follows.

**A micromorphic continuum.** As illustrated in Fig. 1.2c, the underlying microstructure is assumed to undergo an affine micro deformation gradient  $\mathbf{F}$ , which is related to the micro displacement gradient  $\mathbf{H}$  by  $\mathbf{H} = \mathbf{F} - \mathbf{1}$ . Consequently, the microstructure can be seen as a vector triad of directors. A small strain framework following [19, 38] is considered, where the enriched kinematics requires an introduction of additional strain measures: the (second-order) relative deformation tensor

$$\mathbf{e}_r = \overline{\mathbf{H}} - \mathbf{H} \quad (1.10)$$

and the gradient of the micro displacement gradient being a third-order tensor

$$\mathbf{G} = \nabla \mathbf{H}, \quad (1.11)$$

respectively. In Eq. (1.10),  $\overline{\mathbf{H}}$  denotes the macro displacement gradient. Accordingly, the balance equations for momentum and for moment of momentum are

$$\text{Div}(\overline{\boldsymbol{\sigma}} + \mathbf{s}) + \overline{\mathbf{b}} = \mathbf{0}, \quad (1.12a)$$

$$\text{Div}(\mathbf{S}) + \mathbf{s} = \mathbf{0}, \quad \text{on } \overline{\Omega}, \quad (1.12b)$$

respectively. Here, the moment of momentum equation (1.12b) largely differs from Eq. (1.5b) for a classical Cauchy continuum, since the relative stress tensor  $\mathbf{s}$  is generally nonsymmetric. Moreover, the relative stress tensor  $\mathbf{s}$  and the relative deformation tensor  $\mathbf{e}_r$ , the third-order hyperstress tensor  $\mathbf{S}$  and the gradient of the micro displacement gradient  $\mathbf{G}$  are two further work conjugate pairs, in addition to the macro stress tensor  $\overline{\boldsymbol{\sigma}}$  and the macro strain tensor  $\overline{\boldsymbol{\varepsilon}}$ .

In a micromorphic continuum, the microstructure is endowed with full DoFs described by the micro deformation gradient  $\mathbf{F}$ , see e.g. [37, 36, 59, 50, 51, 52] for plasticity problems and [36, 51, 52] for a damage analysis. Special cases may be obtained by restricting the DoFs. The microstructure in a Cosserat continuum can only rotate, see e.g. [27, 131, 24, 23, 107] for a micropolar theory. On the contrary, microstrain theories account for the micro deformation part without rotation, see e.g. [39]. The microstretch theory [28] is a further special case of the micromorphic continua.

Furthermore, as shown in [90], higher order theories can be seen as special cases within the framework of generalized stresses [43, 44, 55, 41, 3]. The connection between higher order and higher grade theories was studied e.g. in [19]. The link between homogenization methods and generalized continua was addressed e.g. in [40, 22, 64, 13]. Most interestingly, recent studies [64, 13] show that a micromorphic continuum can be recovered by homogenization of a Cauchy continuum, such that a clear physical interpretation can be attached to the morphic variables.

## 1.5 From a physical problem to its numerical solution

Many physical problems are described by a set of partial differential equations (PDEs), see e.g. (1.5a), (1.7), (1.12a) and (1.12b) for different equilibrium problems introduced in the previous sections. This kind of PDEs is usually referred to as a *strong* form of the actual physical problem. Based on the principle of virtual work, the strong form can be transformed into a *weak* form

$$B(\mathbf{u}; \delta \mathbf{u}) = F(\delta \mathbf{u}), \quad \forall \delta \mathbf{u} \in \mathcal{V}, \quad (1.13)$$

where  $\mathbf{u}$  and  $\delta \mathbf{u}$  denote the primal solution and its variation belonging to an appropriate Sobolev space  $\mathcal{V}$ , respectively.  $B$  is a semilinear form, which is linear with respect to the argument behind the semicolon, however, may be nonlinear with respect to the argument in front of the semicolon. Moreover,  $F$  represents a linear form. Obviously, for instationary problems like plasticity, additional evolution equations are required for a complement to the weak form (1.13), see e.g. [127]. For brevity, we will not include such equations in the introductory part of this thesis. In order to establish an adaptive framework, we assume that the continuous form (1.13) is an exact model problem giving a perfect description of the actual physical problem. It serves as a datum, with which other surrogate models can be compared, see e.g. [110]. Given the fact that the exact model (1.13) is generally intractable, one has to choose a (simpler) surrogate model

$$B_0(\mathbf{u}^0; \delta \mathbf{u}^0) = F(\delta \mathbf{u}^0), \quad \forall \delta \mathbf{u}^0 \in \mathcal{V}^0, \quad (1.14)$$

which creates an essential basis for the numerical method considered below.

**The finite element method (FEM).** It was invented by first publications [17, 133] for elasticity problems and has become a widely used tool for solving many different kinds of problems, see e.g. [146, 145, 140, 63]. As illustrated in Fig. 1.3, the basic idea is the discretization of continuous space and time into a finite number of elements, which are well supported by their shape functions. Thereby, the infinite DoFs embodied in a continuous formulation are reduced to finite ones on nodes and at time points. Formally, apart from a potential temporal discretization, we have

$$B_0(\mathbf{u}_h^0; \delta \mathbf{u}_h^0) = F(\delta \mathbf{u}_h^0), \quad \forall \delta \mathbf{u}_h^0 \in \mathcal{V}_h^0, \quad (1.15)$$

for a spatially discretized version of (1.14), where  $\mathcal{V}_h^0$  is a regular FE space.

Now, it becomes clear that a numerical simulation is a process from the actual physical problem perfectly described by Eq. (1.13) to its numerical (approximate) solution  $\mathbf{u}_h^0$  of Eq. (1.15). Note that, for Eq. (1.13) to perfectly describe the actual physical problem, parameter identification [94, 95, 91, 89, 23, 137] is additionally required, however, not considered in this thesis. As a result, the following two different issues arise (cf. [122, 5, 112, 83, 84, 129]):

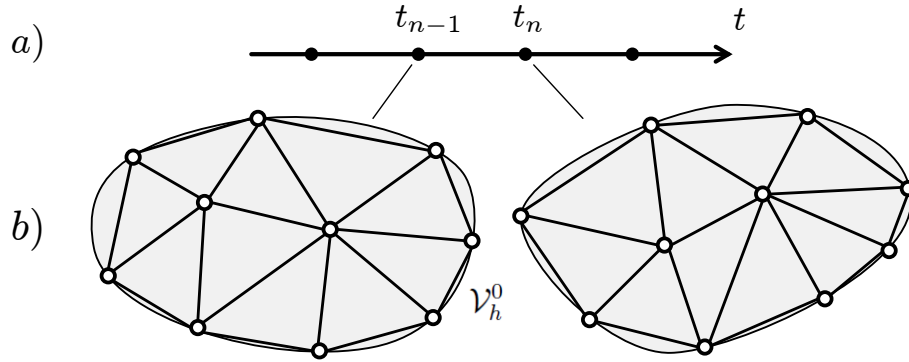


**Figure 1.3:** Basic concept of the FEM: a) temporal discretization and b) spatial discretization.

1. *Numerical validation*: It determines if a mathematical model of a physical problem represents the actual physical problem with sufficient accuracy. It remains in a numerical sense, since no experimental data are considered in this thesis.
2. *Numerical verification*: It determines if a computational model obtained by discretizing a mathematical model of a physical problem represents the mathematical model with sufficient accuracy.

To address these issues, certain error assessment becomes necessary as shown in the subsequent Section 1.6. Note that there are other definitions of *experimental verification* and *experimental validation* related to parameter identification based on experimental data, see e.g. [89].

## 1.6 Goal-oriented error estimate and adaptivity

A *posteriori* error estimate is a class of error estimate, where the primal solution  $\mathbf{u}$  itself is used to assess the error, see e.g. [25, 135, 2, 77, 6, 128]. As an error estimate directed to a global energy norm [7] does not necessarily meet the real engineering interest, the power of *goal-oriented* error estimate [25, 9] is its ability to account for a *quantity of interest*  $Q$ , which is a user-defined function depending on the primal solution  $\mathbf{u}$ . For instance,  $Q$  could represent a real engineering interest by being local displacements or stresses on a certain domain. Within a goal-oriented framework, one may introduce different error sources by an additive split as

$$E(\mathbf{u}, \mathbf{u}_h^0) = \underbrace{Q(\mathbf{u}) - Q(\mathbf{u}_h^0)}_{\text{total error}} = \underbrace{Q(\mathbf{u}) - Q(\mathbf{u}^0)}_{\text{model error}} + \underbrace{Q(\mathbf{u}^0) - Q(\mathbf{u}_h^0)}_{\text{discretization error}}, \quad (1.16)$$

whereby both issues of model validation and numerical verification in Section 1.5 are separated, see [109, 108, 83, 110]. Indeed, model validation requires an access to the model error, while the discretization error has to be handled for a numerical verification. An important task of mathematics is to find exact error representations, for which the following concept of duality arguments plays a key role.

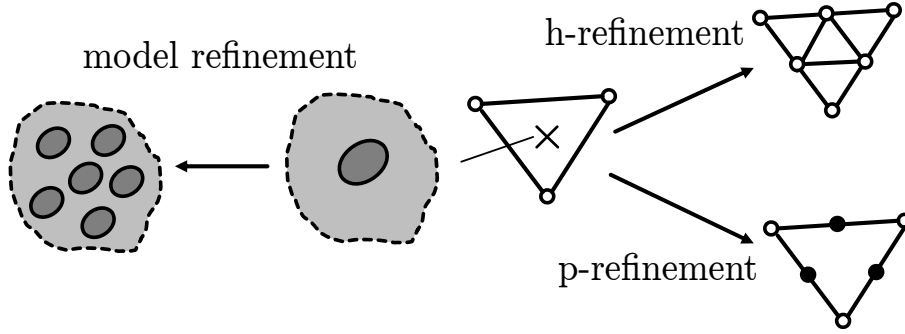


**Figure 1.4:** A finite element with a hierarchical improvement potential (◦: existing nodes in a lower order element, ●: additional nodes in a higher order element and ×: integration point).

**Duality techniques.** By means of a *dual* solution  $\mathbf{z}$  of a dual (auxiliary) problem

$$B_S^*(\mathbf{u}, \mathbf{u}_h^0; \mathbf{z}, \delta \mathbf{u}) = Q_S(\mathbf{u}, \mathbf{u}_h^0; \delta \mathbf{u}), \quad \forall \delta \mathbf{u} \in \mathcal{V}, \quad \text{where} \quad (1.17a)$$

$$B_S(\mathbf{u}, \mathbf{u}_h^0; \mathbf{e}, \delta \mathbf{u}) := \int_0^1 B'(\mathbf{u}_h^0 + s\mathbf{e}; \mathbf{e}, \delta \mathbf{u}) ds, \quad (1.17b)$$

$$Q_S(\mathbf{u}, \mathbf{u}_h^0; \mathbf{e}) := \int_0^1 Q'(\mathbf{u}_h^0 + s\mathbf{e}; \mathbf{e}) ds, \quad (1.17c)$$

the total error becomes

$$E(\mathbf{u}, \mathbf{u}_h^0) = \varrho(\mathbf{u}_h^0; \mathbf{z}) := F(\mathbf{z}) - B(\mathbf{u}_h^0; \mathbf{z}), \quad (1.18)$$

see e.g. [124, 84]. Here, the relation  $\mathbf{e} = \mathbf{u} - \mathbf{u}_h^0$  holds. In the dual problem (1.17a), the argument replacements  $\delta \mathbf{u} \rightarrow \mathbf{z}$  and  $\mathbf{e} \rightarrow \delta \mathbf{u}$  are performed, while  $B^*$  denotes the adjoint form of  $B$ . In the equations (1.17b) and (1.17c),  $B'$  and  $Q'$  are the Gâteaux differentials of  $B$  and  $Q$ , respectively. Note that the definition of a dual problem is not unique. For instance, in [9, 110], a dual problem in a tangent form is obtained from a Lagrange method. It is obvious from Eq. (1.18) that the total error  $E$  is represented as a residual  $\varrho$  weighted by the dual solution  $\mathbf{z}$ . Thereby,  $\mathbf{z}$  can be interpreted as an influence vector or a generalized Green's function. Hence, such kind of approach is often called the *dual weighted residual* (DWR) method, see e.g. [10]. A direct connection to the Betti's (reciprocal) theorem applied in structural mechanics was found in [16].

With this mathematical foundation at hand, one may establish an adaptive strategy for an error control. The premise for that is the hierarchical structure for both the surrogate models and the FEM. The additive error split in Eq. (1.16) enables a separate treatment of model and discretization errors with respective concerns of model validation and numerical verification, thus leading to the following two well-established research fields:

- **Adaptive FEM:** It deals with the issue of numerical verification, where the discretization error is estimated and adaptively controlled. For a treatment

of the temporal discretization error of time-dependent problems, which is not considered in this thesis, the interested reader is referred to [87, 126, 138] for time step adaptivities. In this thesis, we merely focus on the spatial discretization error with respect to the quantity of interest  $Q$  in Eq. (1.16), see also [9, 114, 16, 117]. An obstacle is the fact that the exact solution required for an exact error representation is generally intractable. For an error estimate, the exact solution is approximately replaced by an enhanced solution based on the working one. This requires the finite elements to have a hierarchical improvement potential, as illustrated in Fig. 1.4. Indeed, the quality of a finite element may be generally improved by reducing the element size (h-refinement) or increasing the polynomial order of the shape functions (p-refinement). Considerable effort has been also paid towards an efficient construction of the fine solution, see e.g. [82, 138] for several recovery techniques. For a practical evaluation of the dual problem (1.17a), a linearization towards a tangent problem is additionally required, see e.g. [82, 124, 84]. This tangent problem usually preserves a similar structure as that of the primal (actual physical) problem. An essential step for an adaptive control is to localize the global error to its local (element-wise or point-wise) contributions, which serve as local error indicators, see e.g. [8, 120] for several localization techniques. On this basis, one of the common refinement strategies like fixed element quota or fixed error reduction can be chosen for an error control, where the hierarchical finite element structure is used again. The adaptive control loop is repeated until a user-defined error tolerance is reached. In this manner, an economic mesh meeting the preset accuracy level becomes accessible.

- **Model adaptivity:** It handles the issue of model validation, where the model error is estimated and adaptively controlled. Earlier works on this topic can be found e.g. in [147, 111, 134, 129, 108, 109, 110, 14, 83] for both linear and nonlinear problems. In analogy to the adaptive FEM, a hierarchical model structure is of crucial importance. It is common to establish a model hierarchy, consisting of a series of mathematical models, from the simplest to the most complex (state-of-the-art) model with an ascending hierarchical order. Within the model hierarchy, a *fine* model, with a higher hierarchical order than the working model, is then used to estimate and adaptively control the model error. As illustrated in Fig. 1.4, a model refinement is referred to as a switch from the working to the fine model, at an integration point in the context of the FEM. Similar localization concepts and refinement strategies as for the adaptive FEM can be adopted, such that an economic model distribution becomes accessible, see e.g. [84, 110]. In the context of multiscale modeling, the so-called *Goals* algorithm was proposed in several different versions [111, 134, 110] for linear elastic heterogeneous materials. A domain of influence is determined by the goal-oriented error estimate, where a fine-scale model has to be chosen, whereas in other domains an efficient homogenization scheme is adopted. In [96], this procedure was referred to as a binary model switch. Additionally, the work [96] shed some new light on model adaptivity by considering it as an optimization problem. Finite deformation problems were considered by [84] in a fully coupled two-scale manner, where the macro model error is considered as a consequence

of discretization errors on the micro scale. In [85], different micro boundary conditions for computational homogenization were used to establish a model hierarchy, where the so-called *power of duality* was shown: the dual solution can be used to compute both errors and algorithmic tangents for the primal problem.

For balancing both model and discretization error, model adaptivity and adaptive FEM are frequently applied in a coupled manner, see e.g. [84, 130, 14, 83]. Furthermore, the work [86] extended two-scale adaptive FE analysis to account for a seamless scale-bridging. The so-called adaptive reduced basis finite element heterogeneous multiscale method [1] incorporates the adaptive FEM with reduced basis.

## 2 Objectives

This thesis intends to cover the following two cases in the mechanics of heterogeneous materials:

1. The characteristic length of heterogeneities is much smaller than the wavelength of strain and stress field variations in the structure, where classical (first order) homogenization methods apply.
  - For linear elasticity, a general adaptive framework will be established, which couples both model adaptivity and adaptive FEM on the basis of goal-oriented error estimate, as depicted in Fig. 2.1. Particular attention will be paid to establish hierarchical models for model adaptivity. To this end, an investigation of various homogenization methods is required.

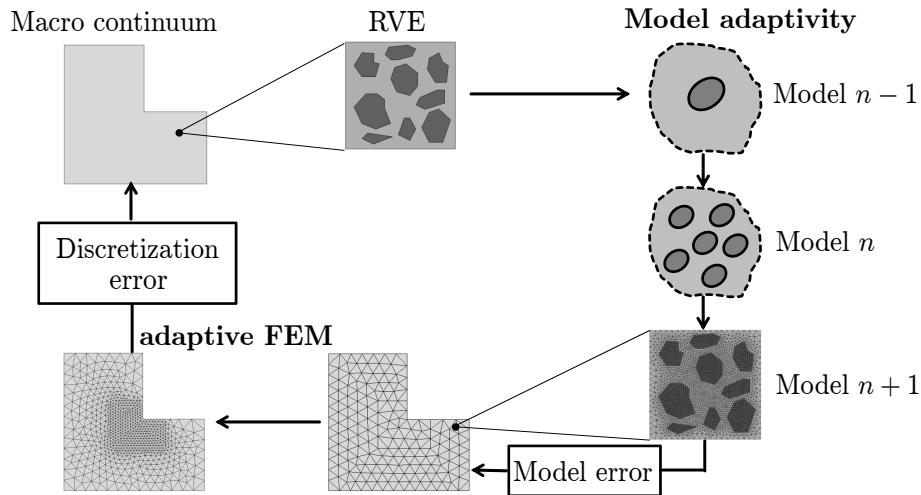


**Figure 2.1:** A coupled adaptive computational strategy.

- For nonlinear cases, a reduced order homogenization scheme considering softening effects will be developed towards an efficient two-scale damage analysis. The strong nonlinearities caused by the softening behavior might give rise to a less accurate prediction of such reduced order scheme. Hence, strategies for an accuracy improvement will be additionally considered, where an adaptive strategy for a selective model reduction is particularly relevant.
2. If a clear scale separation is not given, a need for generalized continuum mechanics arises. Here, our attention is limited to micromorphic continua for two reasons: 1. an analogy to the homogenization methods can be seen in view of a microstructural consideration, and 2. the micromorphic continuum is a

general case of higher order continua. However, we will not deal with the way to obtain such a continuum as an effective continuum, which is related to higher order homogenization theories. In other words, we consider a conventional micromorphic continuum on a phenomenological basis. While the concept of the adaptive FEM has been well developed and widely applied in classical mechanical problems in the literature, an application to micromorphic problems seems to be a completely open research area. In this context, by means of goal-oriented error estimate, adaptive finite elements will be developed for both linear elasticity and elastoplasticity in a micromorphic continuum. Due to the time-dependent feature of the later case (micromorphic elastoplasticity), errors accumulate over time. Apparently, this makes a goal-oriented error estimate much more complex than that of the elastic case. For simplicity, we merely deal with spatial discretization errors of the FEM.

For the topic to be limited, small strains are assumed throughout this thesis.

### 3 Summary of the papers

**Paper A** aims at a development of a coupled adaptive strategy for homogenization of linear elastic heterogeneous materials. Model adaptivity and adaptive FEM are simultaneously applied on the macro scale. In this manner, a balance of macroscale model and macroscale discretization error is achieved. In the framework of goal-oriented adaptivity aiming at a quantity of interest, exact error representations are derived by means of duality techniques. A crucial step towards a computable error estimate is to approximate the unknown exact solutions, for which a novel patch recovery technique is proposed. This recovery technique is inspired by the well-known superconvergent patch recovery [144], where the main idea is to extrapolate the working solution onto an enhanced FE space, such that the issue of the Galerkin orthogonality with a direct use of the working solution can be avoided. Compared with other existing techniques like local type recovery techniques [137], the proposed technique is shown to be more effective for both error estimate and error control. For model adaptivity, a variational method [18, 75] for higher order bounds of effective properties is used, where a hierarchical model structure is established by a truncation of the related Neumann series. Most importantly, this eliminates the need of combining different methods based on a priori knowledge. For a practical evaluation of these bounds, a singular approximation is made. As a new finding, this may, under certain circumstances, give rise to an overlap effect. For a remedy, a correction is additionally proposed. The effectiveness of the proposed adaptive procedure is illustrated by three different classes of materials: macroscopically homogeneous composites, functionally graded composites and random composites.

**Paper B** presents a continuation of Paper A by considering two major concerns arising in homogenization of linear elastic heterogeneous materials:

- The need for a computational (full-field) method where a mean-field method does not suffice for the pursued accuracy level.
- An adaptive selection of the unit cell size for the case where the working unit cell does not represent the micro heterogeneities with a sufficient accuracy. Here, we refer to a *unit cell* as an arbitrary sample of microstructure, which does not necessarily meet the requirements of an RVE.

It is shown that these two concerns can be simultaneously addressed by one single model hierarchy within the framework of goal-oriented adaptivity. This model hierarchy is established on the basis of mean-field and full-field homogenization methods. For the former we consider several well-established schemes like Mori-Tanaka or self-consistent as basic models, and for the latter, as superior models, unit cell problems are solved via the FEM under an a priori chosen boundary condition. To limit the use of computational methods for error estimate, hierarchical models, as

an intermediate stage of the model hierarchy, are additionally established within the frame of mean-field methods using a priori knowledge. For a final stage of the model hierarchy, we consider hierarchical unit cells within the frame of the FEM towards an adaptive selection of the unit cell size. The generality of the proposed model hierarchy is discussed in some detail. On this basis, the coupled adaptive strategy developed in Paper A is used for balancing both model and discretization errors of the finite element method (FEM) on a macroscale. By means of several numerical examples, the effectiveness of the resulting adaptive procedure is illustrated.

**Paper C** develops a reduced order homogenization framework for physically nonlinear materials. Particular attention is paid to a softening material behavior after a certain hardening stage within the frame of elastoplasticity. For a model reduction, the nonuniform transformation field analysis (NTFA) [99, 100] is tailored for the present case, where a new macroscopic evolution law with an even model structure is proposed to account for the softening behavior. Hence, we refer to it as *even NTFA*. The thermodynamic consistency is guaranteed on both scales (micro and macro). Like many other model reduction techniques, the even NTFA consists of two phases of analysis: an offline phase allows to precompute some relevant information including the so-called *plastic modes* as reduced basis functions for heterogeneous microscopic plastic strains and some related reduced variables, such that only a reduced set of equations have to be solved during an online phase. Since the number of plastic modes is much less than that of the primal DoFs in the system, a striking numerical efficiency of the even NTFA is ensured. However, it is found that the even NTFA is not able to give a good prediction on the softening initiation and the softening rates for some reasons. For an accuracy improvement, a new method named as *uneven NTFA* is proposed, where additional correction parameters are introduced, thus leading to an uneven model structure. Alternatively, a so-called *adaptive NTFA* is developed by incorporating the concept of adaptive modeling. Based on an empirical indicator, a model reduction is only adopted on the region, where an accurate prediction is expected.

**Paper D** incorporates the well-established concept of goal-oriented adaptivity with linear micromorphic elasticity, where the discretization error of the FEM is controlled. Using a notion of the generalized solution, the abstract setting preserves the classical format. Goal-oriented error estimator is derived in terms of duality techniques, where a novel patch recovery technique is proposed to efficiently approximate the exact dual solution and compared to a *full computation* technique. Additionally, the FE discretizations are shown to be consistent for the primal problem and adjoint-consistent for the dual problem. This theoretically ensures an optimal convergence order of the proposed adaptive procedure. Several numerical examples illustrate the effectiveness of the adaptive procedure.

**Paper E** extends the topic of Paper D to consider micromorphic elastoplasticity, where both a spatial and a temporal discretization have to be performed for an FE solution. For simplicity, we merely focus on the spatial discretization errors. Due to the time-dependent character of the underlying problem, discretization errors accumulate over time. As pointed out in [83], there are two different sources for error accumulation:

- *Error generation*: discretization errors are newly generated on each single time

step.

- *Error transport*: discretization errors generated on the current time step are transported into the next time step.

For ease of the derivation of a goal-oriented error estimate, a *double multifield* formulation of micromorphic plasticity problems is proposed. The first multifield formulation stems from the nature of micromorphic continua, where the notion of generalized solution is introduced for an abstract setting. The second multifield formulation accounts for local evolution of internal variables, where a general matrix representation is adopted. Accordingly, weak forms in a time integration sense are established for both formulations, respectively. For a goal-oriented error estimate, a backwards-in-time dual problem is deduced from a Lagrange method. It is shown to be able to account for both error generation and error transport, where terms for error transport, called *transport terms*, are additionally identified. As a merit, the dual problem preserves a similar structure as for the primal one such that many terms and structures of the primal problem can be reused, see also [138]. Additionally, a forwards-in-time dual problem is obtained by omitting the transport terms. This approximate dual problem is quite attractive from a computational point of view, since it eliminates the need of additional memory to store the primal solutions computed over all time steps. By means of duality techniques, exact error representations are derived. For practice, four computable error estimators are proposed, where both dual problems are considered in combination with two different methods for enhanced solutions. By means of certain localization techniques, these estimators are used to drive an adaptive mesh refinement algorithm. Their effectiveness is confirmed by several numerical examples based on a prototype model.



---

## Paper A

Xiaozhe Ju and Rolf Mahnken

*Model adaptivity on effective elastic properties coupled with adaptive FEM*  
Computer Methods in Applied Mechanics and Engineering 322 (2017), 208-237

---



# Model adaptivity on effective elastic properties coupled with adaptive FEM

Xiaozhe Ju and Rolf Mahnken

Chair of Engineering Mechanics, University of Paderborn,  
Warburger Str. 100, 33098 Paderborn, Germany

## Abstract

The research field of model adaptivity is well established, aiming at adaptive selection of mathematical models from a well defined class of models (model hierarchy) to achieve a preset level of accuracy. The present work addresses its application to a class of linear elastic composite problems. We will show that the classical bounding theories can provide a model hierarchy in a natural and theoretically consistent manner, without combination of different methods using a priori knowledge. To arrive at computable higher order bounds, the classical singular approximation is made. As a new finding, this may, under certain circumstances, give rise to an overlap effect. To overcome this, a correction is proposed. Additionally, the model adaptivity is coupled to the well established adaptive finite element method (FEM), such that both macro model and macro discretization errors are controlled. The proposed adaptive procedure is driven by a goal-oriented a posteriori error estimator based on duality techniques. For efficient computation of the dual solution, a patch-based recovery technique is proposed and compared to existing methods. For illustration, numerical examples are presented.

**Keywords:** effective properties, higher order bounds, model adaptivity, adaptive finite element method, goal-oriented error estimate, recovery techniques

## 1 Introduction

For the development of innovative industrial products, increasing demands are posed on simulation methods, which have to meet two major requirements: enhancement of prediction qualities and reduction of computational costs. To fulfill the first requirement, subscale effects have to be taken into account, e.g. typically for simulation of composites, however, giving rise to an increased computational complexity. Hence, it becomes important to develop a systematic method for keeping the two above mentioned requirements balanced. This can be achieved by an interdisciplinary interaction between multiscale and adaptive methods, including the following three well established research fields: multiscale methods, adaptive finite element method (FEM) and model adaptivity.

Multiscale methods have been an active area of research for several decades. They are particularly helpful to understand the overall (effective) behavior of a material by taking certain subscale effects into account. A comprehensive overview on this field can be found e.g. in [14, 65, 52, 20]. We restrict ourselves to two-scale problems, where the following main groups of homogenization methods can be distinguished:

- Mean-field methods: They are usually based on certain approximations on the micro level. As a main merit, they are computationally efficient. Well established methods of this kind are, just to mention a few of them, the Eshelby solution [13], Mori-Tanaka [41] and interaction direct derivative [10] etc. Nonlinear materials are also treated e.g. in [26, 30, 5].
- Variational methods: This kind of methods derives bounds for potentials, such as free energy function or dissipation potential (see e.g. [50]). For linear elastic properties, the formal theory for higher order bounds is proposed in [9] and subsequently extended by [28]. For nonlinear cases, we refer to [49, 31, 32].
- Computational methods: These allow consideration of any substructures and any material behaviors on the subscale, whereas the extremely high computational cost is its main drawback, see e.g. [17, 40, 65] for the FE<sup>2</sup> method.
- Model reduction: This kind of methods focuses on reduction of the degrees of freedom in the equation system, while retaining certain accuracy. For instance, the transformation field analysis (TFA) [11] and its nonuniform extension (NTFA) [39] are concerned with approximation of inelastic fields on the micro level. A standard proper orthogonal decomposition is applied e.g. in [62].

Adaptive refinement is a systematic methodology to find a proper mesh for the simulations and thus save computational costs compared to uniform refinement. The basis for adaptive refinement is error estimate, for which there are different possibilities. In this work, goal-oriented a posteriori error estimate is considered. On the one hand, this procedure can be employed to calculate an estimate of a quantity of the solution. In this step, no mesh refinement is involved. On the other hand, one can use the local residuals calculated from the goal-oriented error estimate procedures to steer optimal mesh refinement with respect to that quantity. Both procedures can be effectively combined. For the general framework of a posteriori error estimate, we refer to [12, 58, 1, 29, 2, 55]. The term “goal-oriented” means that the refinement is governed w.r.t. a quantity of interest. Usually, the aim of a simulation is to find solutions for a certain quantity. Adaptive mesh refinement is then governed by error indicators which are localizations of the global error to elements. It is then advantageous to refine the mesh with the goal of minimizing the error in this quantity of interest. Contributions to this topic can be found in [3, 48, 8, 51]. An application on phase field problems can be found in [37]. In our recent work [24], goal-oriented adaptivity has also been applied to micromorphic continua.

The notion of model adaptivity was established much later than the adaptive FEM, where the error due to modeling can be defined, estimated and adaptively

controlled. Earlier works on this topic can be found e.g. in [66, 45, 57, 56, 44, 46, 47, 7, 33, 34] for both linear and nonlinear problems. The key idea is to establish a model hierarchy, consisting of a series of mathematical models, from the simplest to the most complex (state-of-the-art) model with an ascending hierarchical order. Within the model hierarchy, a better model, with a higher hierarchical order than the working model, is then used to estimate and adaptively control the model errors (the errors due to modeling). Similarly to the adaptive FEM, the goal-oriented error estimate can be used to estimate the error w.r.t. a quantity of interest, such that an optimal model distribution becomes accessible. Concerning multiscale problems, the so-called *Goals* algorithm was proposed in several different versions [45, 57, 47] for linear elastic heterogeneous materials. A domain of influence is determined by the goal-oriented error estimate, where the heterogeneous material is simulated in a full resolution, whereas in other domains an analytical homogenization scheme is adopted. In [38], this procedure is referred to as a binary model switch. However, the manner, solving composite problems in a full resolution, is not practicable for real three-dimensional problems. Large deformation problems were considered by [34] in a fully coupled two-scale manner, where the macro model error is considered as a consequence of discretization errors on the micro scale. In [35], different micro boundary conditions for computational homogenization were used to establish a model hierarchy.

In our preparatory works [22, 23] concerning nonlinear homogenization, a reduced order homogenization method (NTFA) and the FE<sup>2</sup> method are adaptively coupled to arrive at an acceptable accuracy for simulation of softening effects, where an empirical indicator for a model switch is proposed. In this work, we restrict ourselves to linear elastic composite problems. In order to determine the effective properties, the classical bounding theory according to Dederichs and Zeller [9] and Kröner [28], belonging to the category of variational methods, is adopted. As a main advantage, the bounding theory provides a model hierarchy with convergence properties, required for model adaptivity. The model hierarchy is established in a theoretically consistent manner, where the hierarchical order is well defined. To arrive at a computable solution, the singular approximation is made (see e.g. [15, 16, 21]). As a new result, this may lead to an overlap effect. Consequently, a corrected version is proposed. Two different adaptive strategies (model adaptivity and adaptive FEM) are applied in a coupled manner. Based on a goal-oriented a posteriori error estimator, we consider both macro discretization and macro model errors. For efficient computation of the enhanced dual solution, which is essential for error estimate, a patch-based recovery technique proposed in our recent work [24] is tailored for the present case. A comparison with other existing methods is also given.

This paper is structured as follows: In Section 2, the general framework of a two-scale modeling is introduced; some relevant basics in micromechanics and the bounding theory are briefly revisited, then, a singular approximation is introduced and a corrected version is proposed. Section 3 is concerned with goal-oriented adaptivity, for which a dual problem is introduced and computable error representations for both discretization and model errors are derived; additionally, different methods for computation of the enhanced dual solution are compared. For illustration purposes, numerical examples are presented in Section 4. A conclusion and an outlook

on further research are given in Section 5.

Notation: The scalar products of two vectors  $\mathbf{a}$  and  $\mathbf{b}$ , and two second-order tensors  $\mathbf{A}$  and  $\mathbf{B}$  are

$$\mathbf{a} \cdot \mathbf{b} = a_i b_i, \quad \mathbf{A} : \mathbf{B} = A_{ij} B_{ij}, \quad (1)$$

respectively, using the Einstein summation convention for repeated indices. The gradient operator  $\nabla$  is introduced as

$$\nabla \mathbf{c} := \mathbf{c} \otimes \nabla = c_{i,j} \mathbf{e}_i \otimes \mathbf{e}_j, \quad \text{with } c_{i,j} = \frac{\partial c_i}{\partial X_j}, \quad (2)$$

where  $\mathbf{e}_i$ ,  $i = 1, 2, 3$  is a Cartesian orthonormal basis and  $X_i$  are coordinates of the reference position  $\mathbf{X}$ . The divergence operator  $\text{Div}(\bullet)$  is defined as

$$\text{Div}(\boldsymbol{\sigma}) := \nabla \cdot \boldsymbol{\sigma} = \sigma_{ij,i} \mathbf{e}_j, \quad \text{with } \sigma_{ij,i} = \frac{\partial \sigma_{ij}}{\partial X_i}. \quad (3)$$

Additionally, the volume averaging operator on a domain  $\Omega$  is defined as

$$\langle \bullet \rangle = \frac{1}{\Omega} \int_{\Omega} \bullet dv. \quad (4)$$

Let  $\phi = \phi(\omega)$ ,  $\forall \omega \in \Omega$  be a variable statistically depending on a realization  $\omega$  out of the *ensemble*  $\Xi$ , then the ensemble average is defined as

$$\langle \phi \rangle_{\Xi} = \lim_{M \rightarrow \infty} \frac{1}{M} \sum_{i=1}^M \phi(\omega_i). \quad (5)$$

Gâteaux differentiation of a linear form  $F$  and a semilinear form  $B$  w.r.t. the argument  $\mathbf{u}$  is denoted as

$$D_{\mathbf{u}} F(\mathbf{u}; \mathbf{v}) = \lim_{\theta \rightarrow 0} \frac{1}{\theta} [F(\mathbf{u} + \theta \mathbf{v}) - F(\mathbf{u})], \quad (6a)$$

$$D_{\mathbf{u}} B(\mathbf{u}; \mathbf{w}, \mathbf{v}) = \lim_{\theta \rightarrow 0} \frac{1}{\theta} [B(\mathbf{u} + \theta \mathbf{v}; \mathbf{w}) - B(\mathbf{u}; \mathbf{w})], \quad (6b)$$

respectively.

## 2 A linear elastic composite problem

### 2.1 Two-scale problem

We consider a two-scale problem of solids, where each material point at the macro level is associated with an additional microscopic problem. These relations are shown in Fig. 1, where  $\overline{\Omega}_0$  and  $\overline{\Omega}_t$  represent the macroscopic domains with respect to the initial and the current configuration, respectively. An analogous notation is used for the microscopic problems with the underlying domains  $\Omega_0$  and  $\Omega_t$ , denoted as the representative volume elements (RVE).

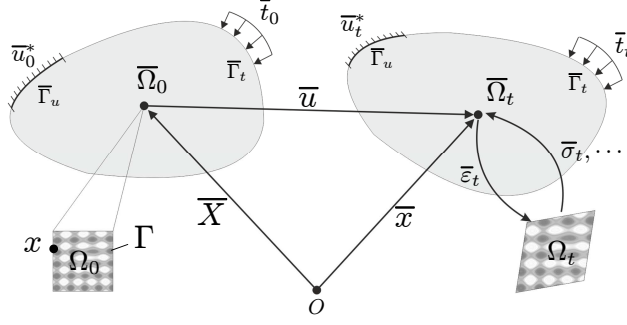


Figure 1: Illustration of a two-scale problem

The displacement of a material point and the small strain tensor are defined as

$$\bar{\mathbf{u}} = \bar{\mathbf{x}} - \bar{\mathbf{X}}, \quad (7a)$$

$$\bar{\boldsymbol{\varepsilon}} = \text{sym}(\nabla_{\bar{\mathbf{x}}}\bar{\mathbf{u}}), \quad (7b)$$

respectively. In Eq. (7a),  $\bar{\mathbf{X}}$  and  $\bar{\mathbf{x}}$  are the location vectors with respect to a reference point  $O$ , respectively in the initial and the current state. Moreover, the macroscopic equilibrium problem  $\bar{P}$  and the underlying microscopic equilibrium problem  $P$  read

$$\bar{P}: \begin{cases} \text{Div}(\bar{\boldsymbol{\sigma}}) + \mathbf{b} = \mathbf{0}, & \text{in } \bar{\Omega} \\ \bar{\boldsymbol{\sigma}}\bar{\mathbf{n}} = \bar{\mathbf{t}}, & \text{on } \bar{\Gamma}_t \\ \bar{\mathbf{u}} = \bar{\mathbf{u}}^*, & \text{on } \bar{\Gamma}_u \end{cases}, \quad (8a)$$

$$P: \begin{cases} \text{Div}(\boldsymbol{\sigma}) = \mathbf{0}, & \text{in } \Omega \\ + \text{boundary conditions} \end{cases}, \quad (8b)$$

respectively. In problem  $\bar{P}$ ,  $\bar{\boldsymbol{\sigma}}$  denotes the macroscopic stress tensor and  $\bar{\mathbf{t}}$  represents the tractions imposed on  $\bar{\Gamma}_t$  satisfying the Neumann boundary condition. The body force is symbolized by  $\mathbf{b}$ , while  $\bar{\mathbf{u}}^*$  indicates the prescribed displacements on the Dirichlet boundary  $\bar{\Gamma}_u$  with the properties  $\bar{\Gamma}_u \cup \bar{\Gamma}_t = \bar{\Gamma}$  and  $\bar{\Gamma}_u \cap \bar{\Gamma}_t = \emptyset$ , where  $\bar{\Gamma}$  symbolizes the total boundary for the macroscopic problem. To solve the macro problem  $\bar{P}$  with the FEM, let us establish its weak form:

$$\underbrace{\int_{\bar{\Omega}} \bar{\boldsymbol{\varepsilon}}[\delta\bar{\mathbf{u}}] : \bar{\boldsymbol{\sigma}}(\bar{\boldsymbol{\varepsilon}}[\bar{\mathbf{u}}]) dv}_{:=\bar{B}(\bar{\mathbf{u}}; \delta\bar{\mathbf{u}})} = \underbrace{\int_{\bar{\Omega}} \delta\bar{\mathbf{u}} \cdot \bar{\mathbf{b}} dv + \int_{\bar{\Gamma}_t} \delta\bar{\mathbf{u}} \cdot \bar{\mathbf{t}} da}_{:=\bar{F}(\delta\bar{\mathbf{u}})}, \quad \forall \delta\bar{\mathbf{u}} \in \mathcal{V}^0, \quad (9)$$

where  $\bar{\mathbf{u}}$  and  $\delta\bar{\mathbf{u}}$  are the macro displacement vector and its variation, respectively.  $\mathcal{V}^0$  is an appropriate Sobolev space. By definition  $\bar{B}(\cdot; \cdot)$  is a semilinear form, which is linear w.r.t. the arguments behind the semicolon and may be nonlinear w.r.t. the arguments in front of the semicolon, while  $\bar{F}(\cdot)$  is a linear form. We shall rewrite Eq. (9) in a residuum form as

$$\bar{\varrho}(\bar{\mathbf{u}}; \delta\bar{\mathbf{u}}) := \bar{F}(\delta\bar{\mathbf{u}}) - \bar{B}(\bar{\mathbf{u}}; \delta\bar{\mathbf{u}}) = 0. \quad (10)$$

The micro problem  $P$  is completed with some proper boundary conditions, depending on the chosen homogenization method. Here  $\boldsymbol{\sigma}$  and  $\boldsymbol{\varepsilon}$  are, respectively, the

microscopic stress and the microscopic strain tensor, which are generally heterogeneously distributed within the RVE, while  $\bar{\boldsymbol{\varepsilon}}$  denotes the macroscopic strain tensor. In this work,  $P$  is solved by an analytical method, for which a weak form is not required.

Additionally, the scale transition, which couples both problems  $\bar{P}$  and  $P$ , is established by

$$\bar{\boldsymbol{\varepsilon}} = \langle \boldsymbol{\varepsilon}(\mathbf{x}) \rangle, \quad (11a)$$

$$\bar{\boldsymbol{\sigma}} = \langle \boldsymbol{\sigma}(\mathbf{x}) \rangle, \quad (11b)$$

$$\langle \boldsymbol{\sigma} : \boldsymbol{\varepsilon} \rangle = \langle \boldsymbol{\sigma} \rangle : \langle \boldsymbol{\varepsilon} \rangle = \bar{\boldsymbol{\sigma}} : \bar{\boldsymbol{\varepsilon}}. \quad (11c)$$

For any microscopic statically admissible stress fields  $\boldsymbol{\sigma}(\mathbf{x})$  and any microscopic compatible strain fields  $\boldsymbol{\varepsilon}(\mathbf{x})$ , the well established Hill-Mandel condition (11c) is valid (see [19]).

## 2.2 Lippmann-Schwinger equation for the micro problem

We restrict ourselves to linear elastic problems, for which Hooke's law applies for each micro coordinate  $\mathbf{x}$  as

$$\boldsymbol{\sigma}(\mathbf{x}) = \mathbb{C}(\mathbf{x})\boldsymbol{\varepsilon}(\mathbf{x}) = (\mathbb{C}^0 + \underbrace{\mathbb{C}(\mathbf{x}) - \mathbb{C}^0}_{:=\Delta\mathbb{C}(\mathbf{x})})\boldsymbol{\varepsilon}(\mathbf{x}) = \mathbb{C}^0\boldsymbol{\varepsilon}(\mathbf{x}) + \underbrace{\Delta\mathbb{C}(\mathbf{x})\boldsymbol{\varepsilon}(\mathbf{x})}_{:=\mathbf{p}(\mathbf{x})}, \quad (12)$$

with the micro elasticity tensor  $\mathbb{C}$ . Here we adopt the classical concept of stress polarization, where a homogeneous *comparison material* with the elastic property  $\mathbb{C}^0$  is introduced. Furthermore,  $\mathbf{p}$  is the *polarization* stress, while  $\Delta\mathbb{C}$  denotes the difference of elastic properties between the current and the comparison material. Inserting Eq. (12) into the micro equilibrium condition in Eq. (8b) renders the reformulated problem

$$\text{Div}(\boldsymbol{\sigma}(\mathbf{x})) = \text{Div}(\mathbb{C}^0\boldsymbol{\varepsilon}(\mathbf{x}) + \mathbf{p}(\mathbf{x})) = \mathbf{0}, \quad (13)$$

which has a general formal solution (see e.g. [43, 52])

$$\boldsymbol{\varepsilon}(\mathbf{x}) = \boldsymbol{\varepsilon}^0 - \mathbb{G}[\mathbf{p}(\mathbf{x})], \quad \text{where} \quad (14a)$$

$$\mathbb{G}[\mathbf{p}(\mathbf{x})] := \int_{V'} \boldsymbol{\Gamma}(\mathbf{x}, \mathbf{x}')\mathbf{p}(\mathbf{x}')dV'. \quad (14b)$$

Here  $\boldsymbol{\varepsilon}^0$  denotes the strain in the comparison material,  $\mathbb{G}$  is an integral operator and the nonlocal strain Green operator  $\boldsymbol{\Gamma}(\mathbf{x}, \mathbf{x}')$  depends on the second spatial derivatives of the Green function  $\mathbf{g}(\mathbf{x}, \mathbf{x}')$  for the comparison material and formally reads

$$\boldsymbol{\Gamma}(\mathbf{x}, \mathbf{x}') = \frac{1}{2} \left( \frac{\partial^2 g_{ik}}{\partial x_j \partial x'_l} + \frac{\partial^2 g_{jk}}{\partial x_i \partial x'_l} \right) \mathbf{e}_i \otimes \mathbf{e}_j \otimes \mathbf{e}_k \otimes \mathbf{e}_l, \quad (15)$$

see e.g. [63, 28]. Inserting the definition of  $\mathbf{p}$  in Eq. (12) into Eq. (14a) renders an equivalent form of (14a) as

$$\boldsymbol{\varepsilon}(\mathbf{x}) + \mathbb{G}[\Delta\mathbb{C}(\mathbf{x})\boldsymbol{\varepsilon}(\mathbf{x})] = \boldsymbol{\varepsilon}^0, \quad (16)$$

which is nothing else but the strain-based Lippmann-Schwinger equation (see e.g. [42]). As shown in [27], the stress-based Lippmann-Schwinger equation, which is equivalent to (16), takes the form

$$\boldsymbol{\sigma}(\boldsymbol{x}) + \mathbb{H}[\Delta\mathbb{S}(\boldsymbol{x})\boldsymbol{\sigma}(\boldsymbol{x})] = \boldsymbol{\sigma}^0, \quad (17)$$

where  $\boldsymbol{\sigma} = \mathbb{C}\boldsymbol{\varepsilon}$ ,  $\boldsymbol{\sigma}^0 = \mathbb{C}^0\boldsymbol{\varepsilon}^0$ ,  $\Delta\mathbb{S} = \mathbb{S} - \mathbb{S}^0$  and  $\mathbb{H} = \mathbb{C}^0 - \mathbb{C}^0\mathbb{G}\mathbb{C}^0$ , and where  $\mathbb{S} = \mathbb{C}^{-1}$  and  $\mathbb{S}^0 = (\mathbb{C}^0)^{-1}$  are the elastic compliance tensors for the current and the comparison material, respectively.

## 2.3 Variational principles

Starting from the two definitions

$$\bar{\mathbb{C}}\langle\boldsymbol{\varepsilon}\rangle := \langle\mathbb{C}\boldsymbol{\varepsilon}\rangle, \quad (18a)$$

$$\bar{\mathbb{S}}\langle\boldsymbol{\sigma}\rangle := \langle\mathbb{S}\boldsymbol{\sigma}\rangle \quad (18b)$$

for the effective elasticity tensor  $\bar{\mathbb{C}}$  and the effective elastic compliance tensor  $\bar{\mathbb{S}}$ , respectively, we obtain from (11c) the equivalent forms of the Hill condition (11c) as

$$\langle\boldsymbol{\varepsilon}\rangle : \bar{\mathbb{C}}\langle\boldsymbol{\varepsilon}\rangle = \langle\boldsymbol{\varepsilon} : \mathbb{C}\boldsymbol{\varepsilon}\rangle, \quad (19a)$$

$$\langle\boldsymbol{\sigma}\rangle : \bar{\mathbb{S}}\langle\boldsymbol{\sigma}\rangle = \langle\boldsymbol{\sigma} : \mathbb{S}\boldsymbol{\sigma}\rangle. \quad (19b)$$

In order to establish a bounding theory, which will be introduced in Section 2.5, we recall the well-known result of [18], i.e. the minimum energy and the complementary energy principle as

$$\langle\boldsymbol{\varepsilon}\rangle : \bar{\mathbb{C}}\langle\boldsymbol{\varepsilon}\rangle = \langle\boldsymbol{\varepsilon} : \mathbb{C}\boldsymbol{\varepsilon}\rangle \leq \langle\delta\boldsymbol{\varepsilon} : \mathbb{C}\delta\boldsymbol{\varepsilon}\rangle, \quad \forall\delta\boldsymbol{\varepsilon}, \quad (20a)$$

$$\langle\boldsymbol{\sigma}\rangle : \bar{\mathbb{S}}\langle\boldsymbol{\sigma}\rangle = \langle\boldsymbol{\sigma} : \mathbb{S}\boldsymbol{\sigma}\rangle \leq \langle\delta\boldsymbol{\sigma} : \mathbb{S}\delta\boldsymbol{\sigma}\rangle, \quad \forall\delta\boldsymbol{\sigma}, \quad (20b)$$

respectively. Here  $\delta\boldsymbol{\varepsilon}$  represents an arbitrary strain field compatible with the given surface displacements, while  $\delta\boldsymbol{\sigma}$  denotes an arbitrary stress field compatible with the given surface forces.

## 2.4 Exact representations of the effective elastic properties

It is shown, e.g. in [9, 28, 61, 21], that there are several different ways to express the exact effective elastic properties on the basis of the Lippmann-Schwinger equations (16) and (17). In order to have a point of departure for the bounding theory in the subsequent section, we choose, in the following, a statistical method according to [28].

As common in scattering theories [4], we introduce a deviation operator  $\mathbb{P}$ , which extracts the deviation part of an arbitrary quantity  $\boldsymbol{\phi}(\boldsymbol{x})$  as

$$\mathbb{P}\boldsymbol{\phi}(\boldsymbol{x}) := \boldsymbol{\phi}(\boldsymbol{x}) - \langle\boldsymbol{\phi}(\boldsymbol{x})\rangle \quad (21a)$$

$$\implies \langle\mathbb{P}\boldsymbol{\phi}(\boldsymbol{x})\rangle = \mathbf{0}, \quad (21b)$$

$$\mathbb{P}\boldsymbol{\phi}^0 = \mathbf{0}. \quad (21c)$$

Eq. (21b) follows from the idempotence property  $\langle\langle\boldsymbol{\phi}(\mathbf{x})\rangle\rangle = \langle\boldsymbol{\phi}(\mathbf{x})\rangle$  and Eq. (21c) is valid for a homogeneous field  $\boldsymbol{\phi}^0(\mathbf{x}) = \text{const}$ . Applying  $\mathbb{P}$  to the Lippmann-Schwinger equation (16) with  $\boldsymbol{\varepsilon} = \mathbb{P}\boldsymbol{\varepsilon} + \langle\boldsymbol{\varepsilon}\rangle$  yields

$$\mathbb{P}\boldsymbol{\varepsilon}(\mathbf{x}) + \mathbb{P}\mathbb{G}\Delta\mathbb{C}(\mathbf{x})\boldsymbol{\varepsilon}(\mathbf{x}) = \mathbb{P}\boldsymbol{\varepsilon}(\mathbf{x}) + \mathbb{P}\mathbb{G}\Delta\mathbb{C}(\mathbf{x})[\mathbb{P}\boldsymbol{\varepsilon}(\mathbf{x})] + \mathbb{P}\mathbb{G}\Delta\mathbb{C}(\mathbf{x})\langle\boldsymbol{\varepsilon}(\mathbf{x})\rangle = \mathbf{0}, \quad (22)$$

where (21c) is used for the right hand side of (16). Multiplication of (22) by  $\Delta\mathbb{C}$  from the left and a simple transformation yield the identity

$$\Delta\mathbb{C}\mathbb{P}\boldsymbol{\varepsilon} = -(\mathbb{I}^S + \Delta\mathbb{C}\mathbb{P}\mathbb{G})^{-1}\Delta\mathbb{C}\mathbb{P}\mathbb{G}\Delta\mathbb{C}\langle\boldsymbol{\varepsilon}\rangle, \quad (23)$$

where  $\mathbb{I}^S$  is the fourth-order identity tensor on symmetric second-order tensors. Based on the definition (18a), we may further write

$$\begin{aligned} \bar{\mathbb{C}}\langle\boldsymbol{\varepsilon}\rangle &= \langle\mathbb{C}\boldsymbol{\varepsilon}\rangle = \langle\mathbb{C}(\langle\boldsymbol{\varepsilon}\rangle + \mathbb{P}\boldsymbol{\varepsilon})\rangle = \langle\mathbb{C}\rangle\langle\boldsymbol{\varepsilon}\rangle + \langle\mathbb{C}\mathbb{P}\boldsymbol{\varepsilon}\rangle \\ &= \langle\mathbb{C}\rangle\langle\boldsymbol{\varepsilon}\rangle + \langle\Delta\mathbb{C}\mathbb{P}\boldsymbol{\varepsilon}\rangle + \underbrace{\langle\mathbb{C}^0\mathbb{P}\boldsymbol{\varepsilon}\rangle}_{=\mathbb{C}^0\langle\mathbb{P}\boldsymbol{\varepsilon}\rangle=\mathbf{0}}, \end{aligned} \quad (24)$$

because of Eq. (21b). Inserting (23) into (24) and eliminating  $\langle\boldsymbol{\varepsilon}\rangle$ , we finally obtain a formal result for the effective elasticity tensor  $\bar{\mathbb{C}}$  as

$$\bar{\mathbb{C}} = \langle\mathbb{C}\rangle - \langle(\mathbb{I}^S + \Delta\mathbb{C}\mathbb{P}\mathbb{G})^{-1}\Delta\mathbb{C}\mathbb{P}\mathbb{G}\Delta\mathbb{C}\rangle. \quad (25)$$

Expanding the expression  $(\mathbb{I}^S + \Delta\mathbb{C}\mathbb{P}\mathbb{G})^{-1}$  into a Neumann series as

$$(\mathbb{I}^S + \Delta\mathbb{C}\mathbb{P}\mathbb{G})^{-1} = \sum_{k=0}^{\infty} (-\Delta\mathbb{C}\mathbb{P}\mathbb{G})^k, \quad (26)$$

Eq. (25) becomes

$$\bar{\mathbb{C}} = \langle\mathbb{C}\rangle - \langle\Delta\mathbb{C}\mathbb{P}\mathbb{G}\Delta\mathbb{C}\rangle + \langle\Delta\mathbb{C}\mathbb{P}\mathbb{G}\Delta\mathbb{C}\mathbb{P}\mathbb{G}\Delta\mathbb{C}\rangle + \dots. \quad (27)$$

For the special choice of the comparison material  $\mathbb{C}^0 = \langle\mathbb{C}\rangle$ , the identity

$$\mathbb{P}\Delta\mathbb{C} = \mathbb{P}[\mathbb{C} - \langle\mathbb{C}\rangle] = \mathbb{C} - \langle\mathbb{C}\rangle - \underbrace{\langle\mathbb{C} - \langle\mathbb{C}\rangle\rangle}_{=0} = \Delta\mathbb{C} \quad (28)$$

holds, thus leading to a simplified version of (27) as

$$\bar{\mathbb{C}} = \langle\mathbb{C}\rangle - \langle\Delta\mathbb{C}\mathbb{G}\Delta\mathbb{C}\rangle + \langle\Delta\mathbb{C}\mathbb{G}\Delta\mathbb{C}\mathbb{G}\Delta\mathbb{C}\rangle + \dots. \quad (29)$$

In exactly the same way, proceeding with the stress-based Lippmann-Schwinger equation (17), we may write the effective compliance tensor as

$$\bar{\mathbb{S}} = \langle\mathbb{S}\rangle - \langle\Delta\mathbb{S}\mathbb{H}\Delta\mathbb{S}\rangle + \langle\Delta\mathbb{S}\mathbb{H}\Delta\mathbb{S}\mathbb{H}\Delta\mathbb{S}\rangle + \dots, \quad (30)$$

where we make the choice  $\mathbb{C}^0 = (\mathbb{S}^0)^{-1} = (\langle\mathbb{S}\rangle)^{-1}$ .

**Remark 1.** The results represented in the series (29) and (30) are exact. Specific micromorphologies are considered by the integral operator  $\mathbb{G}$  based on the corresponding Green functions  $\mathbf{g}(\mathbf{x}, \mathbf{x}')$ .

**Remark 2.** For the sake of a better comprehension, we have not introduced the notion of a *random composite* as done in the works [9, 28], where the statistical distribution of the micro elastic moduli is given in terms of  $n$ -point correlation functions. Instead, the heterogeneity of the material remains in its natural sense, i.e. spatial dependencies are used throughout this work. The equivalence to [9, 28] is given by the hypothesis of ergodicity (see e.g. [15, 21]), which states that the ensemble average in Eq. (5) of a certain quantity  $\phi(\mathbf{x}, \omega)$  is equivalent to its volume average in Eq. (4), i.e.  $\langle \phi(\omega) \rangle_{\Xi} = \langle \phi(\mathbf{x}) \rangle$ . Given the difficulty to have an infinite number of realizations, it is more practicable to use volume averages instead of ensemble averages.

## 2.5 A bounding theory for effective elastic properties

To establish a model hierarchy, which is essential for model adaptivity, in this section the bounding theory following [9, 28] for a class of disordered materials is briefly revisited.

In order to show an upper bound for a truncated series of  $\bar{\mathbb{C}}$ , by use of  $\mathbb{C} = \mathbb{C}^0 + \Delta\mathbb{C}$ , Eq. (27) is rewritten as

$$\bar{\mathbb{C}} = \mathbb{C}^0 + \langle \Delta\mathbb{C}\mathbb{A} \rangle = \langle \mathbb{C}\mathbb{A} \rangle, \quad \text{where} \quad (31a)$$

$$\mathbb{A} = \mathbb{I}^S - \mathbb{P}\mathbb{G}\Delta\mathbb{C} + \mathbb{P}\mathbb{G}\Delta\mathbb{C}\mathbb{P}\mathbb{G}\Delta\mathbb{C} + \dots = \sum_{k=0}^{\infty} (-\mathbb{P}\mathbb{G}\Delta\mathbb{C})^k. \quad (31b)$$

Note that the fourth-order tensor  $\mathbb{A}$  is nothing else but the strain localization tensor with the definition  $\boldsymbol{\varepsilon}(\mathbf{x}) = \mathbb{A}(\mathbf{x})\bar{\boldsymbol{\varepsilon}}$ . Also note that the latter equality in Eq. (31a) is obtained by using the property  $\langle \mathbb{A}(\mathbf{x}) \rangle = \mathbb{I}^S$ . Using the definition  $\delta\boldsymbol{\varepsilon} := \mathbb{B}\bar{\boldsymbol{\varepsilon}}$  with a trial strain localization tensor  $\mathbb{B}$ , the minimum energy principle (20a) becomes

$$\bar{\mathbb{C}} \leq \langle \mathbb{B}^T \mathbb{C} \mathbb{B} \rangle. \quad (32)$$

Then, we adopt

$$\mathbb{A}_{(m)} = \sum_{k=0}^m (-\mathbb{P}\mathbb{G}\Delta\mathbb{C})^k = \mathbb{B} \quad (33)$$

as a trial field, being the series (31b) truncated after the  $(m+1)$ -th term with  $m = 0, 1, 2, \dots$ , and obtain from (32)

$$\bar{\mathbb{C}} \leq \langle (\mathbb{A}_{(m)})^T \mathbb{C} \mathbb{A}_{(m)} \rangle = \langle \mathbb{C} \mathbb{A}_{(n_0-1)} \rangle =: \bar{\mathbb{C}}^{n_0}, \quad \text{where } n_0 = 2m + 1 = 1, 3, 5, \dots \quad (34)$$

For a detailed proof of the first equality in (34), we refer to [28]. Here, the upper bounds  $\bar{\mathbb{C}}^{n_0}$  of an odd order  $n_0$  correspond to the series (27) truncated after the  $n_0$ -th term.

In exactly the same way, based on the complementary energy principle (20b), we may obtain

$$\bar{\mathbb{S}}^{n_0} := \langle (\mathbb{A}_{(m)})^T \mathbb{S} \mathbb{A}_{(m)} \rangle = \langle \mathbb{S} \mathbb{A}_{(n_0-1)} \rangle \geq \bar{\mathbb{S}}, \quad \text{where } \mathbb{A}_{(m)} = \sum_{k=0}^m (-\mathbb{P}\mathbb{H}\Delta\mathbb{S})^k \quad (35)$$

as an upper bound of  $\bar{\mathbb{S}}$  being the series (30) truncated after the  $n_0$ -th term with the choice  $\mathbb{S}^0 = \langle \mathbb{S} \rangle$ , thus leading to a lower bound of  $\bar{\mathbb{C}}$  as

$$\bar{\mathbb{C}}_{n_0} := (\bar{\mathbb{S}}^{n_0})^{-1} \leq \bar{\mathbb{C}}, \quad (36)$$

see [9, 28] for further details.

The results (34) and (36) for the bounds  $\bar{\mathbb{C}}^{n_0}$  and  $\bar{\mathbb{C}}_{n_0}$  were firstly derived in [9, 28]. They fulfill the requirement of model adaptivity in such a manner that, with a higher approximation order  $n_0$ , the bounds are closer to the exact solution (as will be shown in Fig. 4), however, more computationally expensive. These bounds will be used to establish a model hierarchy (see the sections 3.4 and 4.2 for details).

**Remark 3.** The bounds (34) and (36) contain some well-known bounds as special cases. For instance, the first order bounds  $\bar{\mathbb{C}}^1$  and  $\bar{\mathbb{C}}_1$ , with  $m = 0$  and  $n_0 = 1$ , correspond to the classical Voigt and Reuss bound, respectively.

**Remark 4.** For simplicity, only odd order bounds suggested in [9] are considered in this work. Even bounds extended by [28] involve additional optimization problems.

**Remark 5.** As already stated in the original works [9, 28], the results (34) and (36) are formal, since the multiple integrals involved are generally too complicated to lead to analytical results. Hence, to arrive at easily computable results, especially for higher order bounds, we resort to the singular approximation, which will be introduced in the subsequent section.

**Remark 6.** If required, the micro scale solution of a corresponding approximation order  $n_0$  can be recovered by the localization tensors  $\mathbb{A}_{(n_0-1)}$  and  $\mathbb{A}^{(n_0-1)}$  in the equations (34) and (35), see e.g. [52, 21]. The microscopic strain field  $\boldsymbol{\varepsilon}(\mathbf{x})$  and the microscopic stress field  $\boldsymbol{\sigma}(\mathbf{x})$  associated to the approximation order  $n_0$  are formally obtained w.r.t. upper bounds by

$$\boldsymbol{\varepsilon}^{n_0}(\mathbf{x}) = \mathbb{A}_{(n_0-1)}(\mathbf{x}) \bar{\boldsymbol{\varepsilon}}, \quad (37a)$$

$$\boldsymbol{\sigma}^{n_0}(\mathbf{x}) = \mathbb{C}(\mathbf{x}) \mathbb{A}_{(n_0-1)}(\mathbf{x}) \bar{\boldsymbol{\varepsilon}}, \quad (37b)$$

and w.r.t. lower bounds by

$$\boldsymbol{\varepsilon}_{n_0}(\mathbf{x}) = \mathbb{S}(\mathbf{x}) \mathbb{A}^{(n_0-1)}(\mathbf{x}) \bar{\boldsymbol{\sigma}}, \quad (38a)$$

$$\boldsymbol{\sigma}_{n_0}(\mathbf{x}) = \mathbb{A}^{(n_0-1)}(\mathbf{x}) \bar{\boldsymbol{\sigma}}, \quad (38b)$$

respectively.

## 2.6 Singular approximation

To arrive at easily computable results, a singular approximation according to [15, 16] is introduced. Within this concept, only the local part of the Green operator in Eq. (14b) is considered, i.e.

$$\mathbb{\Gamma}(\mathbf{x}, \mathbf{x}') = \underbrace{\mathbb{\Gamma}_0 \delta(\mathbf{x}, \mathbf{x}')}_{\text{local}} + \underbrace{\mathbb{\Gamma}_1(\mathbf{x}, \mathbf{x}')}_{\text{nonlocal}} \approx \underbrace{\mathbb{\Gamma}_0 \delta(\mathbf{x}, \mathbf{x}')}_{\text{local}}, \quad (39)$$

where  $\delta(\mathbf{x}, \mathbf{x}')$  denotes the Dirac delta function. As shown in [6], if the comparison material is chosen as an isotropic medium with two eigenvalues  $c_1$  and  $c_2$

$$\mathbb{C}^0 = c_1 \mathbb{P}_1 + c_2 \mathbb{P}_2, \quad \mathbb{P}_1 = \frac{1}{3} \mathbf{1} \otimes \mathbf{1}, \quad \mathbb{P}_2 = \mathbb{I}^S - \mathbb{P}_1, \quad (40)$$

the integral operator  $\mathbb{G}$  can be replaced by

$$\mathbb{G}[\bullet] = \mathbb{G}^0 = g_1 \mathbb{P}_1 + g_2 \mathbb{P}_2, \quad g_1 = \frac{1}{c_1 + 2c_2}, \quad g_2 = \frac{2(c_1 + 3c_2)}{5c_2(c_1 + 2c_2)}. \quad (41)$$

Here  $\mathbf{1}$  denotes the second-order identity tensor. Obviously, the localized operator  $\mathbb{G}^0$  makes the evaluation of the terms in the series (29) and (30) much simpler.

**Remark 7.** The singular approximation (39) neglects the nonlocal part of the Green operator  $\mathbb{T}(\mathbf{x}, \mathbf{x}')$ , and hence, does not account for fine micromorphology effects such as phase distributions in a composite. Therefore,  $\mathbb{G}^0$  in Eq. (41) corresponds to the Hill polarization tensor for isotropic two-point statistics, see e.g. [61, 21]. As a result, the two-scale scheme reduces to a mean-field one, meaning that the micro scale fields in the equations (37a), (37b), (38a) and (38b) become phase-wise uniform. Despite of this restriction, the singular approximation seems to be suitable for certain kinds of materials, e.g. silicon nitride in [6].

**Remark 8.** For a convergence investigation of the bounds (34) and (36) obtained by the singular approximation, we adopt the *singular approximation estimate* following e.g. [61, 21] as a reference solution. In doing so, we solve the Lippmann-Schwinger equation (16) for  $\boldsymbol{\varepsilon}(\mathbf{x})$  and find

$$\boldsymbol{\varepsilon}(\mathbf{x}) = (\mathbb{I}^S + \mathbb{G}\Delta\mathbb{C})^{-1} \boldsymbol{\varepsilon}^0 := \mathbb{A}(\mathbf{x}) \bar{\boldsymbol{\varepsilon}}, \quad (42)$$

where the last equality corresponds to the standard definition of the strain localization tensor  $\mathbb{A}(\mathbf{x})$ . Applying the volume average on both sides of the latter equality in (42) yields

$$\langle (\mathbb{I}^S + \mathbb{G}\Delta\mathbb{C})^{-1} \rangle \boldsymbol{\varepsilon}^0 = \langle \mathbb{A}(\mathbf{x}) \rangle \bar{\boldsymbol{\varepsilon}} \implies \boldsymbol{\varepsilon}^0 = (\langle (\mathbb{I}^S + \mathbb{G}\Delta\mathbb{C})^{-1} \rangle)^{-1} \bar{\boldsymbol{\varepsilon}}, \quad (43)$$

which, together with (42), indicates

$$\mathbb{A} = (\mathbb{I}^S + \mathbb{G}\Delta\mathbb{C})^{-1} (\langle (\mathbb{I}^S + \mathbb{G}\Delta\mathbb{C})^{-1} \rangle)^{-1}. \quad (44)$$

Inserting Eq. (44) and the approximation (41) into Eq. (31a), we finally obtain a singular approximation estimate for the effective elasticity tensor

$$\bar{\mathbb{C}} = \langle \mathbb{C}\mathbb{A} \rangle \approx \langle \mathbb{C}(\mathbb{I}^S + \mathbb{G}^0\Delta\mathbb{C})^{-1} \rangle (\langle (\mathbb{I}^S + \mathbb{G}^0\Delta\mathbb{C})^{-1} \rangle)^{-1}. \quad (45)$$

It should be pointed out that the maximum accuracy level of the bounds (34) and (36) in combination with the singular approximation is that of the singular approximation estimate (45). For a higher level of accuracy one has to resort to numerical methods, which will not be considered in this work. For instance, Kabel and Andrä [25] developed a numerical solver to compute bounds of effective elastic properties for multi-phase composites.

## 2.7 A corrected version

As will be shown in Section 4.2, an overlap effect, as a deficiency of the singular approximation (39), might occur for higher order bounds. As the work [6] considered only bounds up to the approximation order  $n_0 = 5$ , no reference on this point exists. Hence, we may consider this overlap effect as a new result. The reason is that, due to the strong simplification (41), the micro strain fields become phase-wise uniform, and this may make the strain fields incompatible. In other words, as stated in [28], in contrast to  $\mathbb{G}\boldsymbol{\tau}$  with an arbitrary function  $\boldsymbol{\tau}$ , the approximate expression  $\mathbb{G}^0\boldsymbol{\tau}$  is not generally a compatible strain field, thus violating the compatibility condition for the variational principle (20a) or (32).

As these issues may not be known a priori, we propose here a simple correction as

$$\overline{\mathbb{C}}^{n_0^c} = \overline{\mathbb{C}}_{n_0^c} = \frac{1}{2}(\overline{\mathbb{C}}^{n_0} + \overline{\mathbb{C}}_{n_0}), \quad \text{if } \overline{E}^{n_0} < \overline{E}_{n_0}, \quad (46)$$

where we adopt the effective elasticity modulus  $\overline{E}$  as an indicator, and where  $\overline{\mathbb{C}}^{n_0^c}$  and  $\overline{\mathbb{C}}_{n_0^c}$  represent the corrected upper and the corrected lower bound of the effective elasticity tensor  $\overline{\mathbb{C}}$ , respectively. Moreover, the effective elasticity moduli  $\overline{E}^{n_0}$  and  $\overline{E}_{n_0}$  are calculated from the original bounds  $\overline{\mathbb{C}}^{n_0}$  and  $\overline{\mathbb{C}}_{n_0}$ , respectively.

**Remark 9.** Although the singular approximation loses its mathematical rigor, it is the most efficient method to solve the series (29) and (30) for any odd approximation order  $n_0$ . The convergence of the corresponding bounds will be numerically investigated in Section 4.2.

**Remark 10.** For simplicity, we consider, in this work, only macroscopically isotropic materials, whose elastic properties can be described by two elasticity constants.

## 3 Goal-oriented adaptivity

In this section, we focus on fitting a model hierarchy based on the bounding theory in the sections 2.5-2.7 into the common framework of the well established goal-oriented adaptivity. In the following, we keep in mind that  $Q(\overline{\mathbf{u}})$  is a *quantity of interest* depending on macroscale solution  $\overline{\mathbf{u}}$ , which is our goal for solving problem  $\overline{P}$ . The error w.r.t.  $Q$  is intended to be estimated and controlled in a systematic and automated manner.

### 3.1 Exact error representations

The exact model (10) is, in general, highly complex, even intractable. It serves as a datum, with which other (simpler) models can be compared. To further establish model adaptivity and adaptive FEM, additionally to Eq. (10) we introduce the working (surrogate) model

$$\overline{\varrho}^{(n)}(\overline{\mathbf{u}}^{(n)}; \delta\overline{\mathbf{u}}) = \overline{F}(\delta\overline{\mathbf{u}}) - \overline{B}^{(n)}(\overline{\mathbf{u}}^{(n)}; \delta\overline{\mathbf{u}}) = 0, \quad \forall \delta\overline{\mathbf{u}} \in \mathcal{V}^0 \quad (47)$$

with a hierarchical order  $n \geq 0$  and the computable model

$$\bar{\varrho}^{(n)}(\bar{\mathbf{u}}_h^{(n)}; \delta \bar{\mathbf{u}}) = \bar{F}(\delta \bar{\mathbf{u}}) - \bar{B}^{(n)}(\bar{\mathbf{u}}_h^{(n)}; \delta \bar{\mathbf{u}}) = 0, \quad \forall \delta \bar{\mathbf{u}} \in \mathcal{V}_h^0. \quad (48)$$

Here  $\mathcal{V}_h^0 \in \mathcal{V}^0$  represents the approximate FE-space.

Following the lines of [34, 35], with the computable solution  $\bar{\mathbf{u}}_h^{(n)}$ , we formulate a residuum as

$$\begin{aligned} \bar{\varrho}(\bar{\mathbf{u}}_h^{(n)}; \delta \bar{\mathbf{u}}) &= \bar{F}(\delta \bar{\mathbf{u}}) - \bar{B}(\bar{\mathbf{u}}_h^{(n)}; \delta \bar{\mathbf{u}}) \\ &= \underbrace{\bar{F}(\delta \bar{\mathbf{u}}) - \bar{B}^{(n)}(\bar{\mathbf{u}}_h^{(n)}; \delta \bar{\mathbf{u}})}_{:=\bar{\varrho}_h} + \underbrace{\bar{B}^{(n)}(\bar{\mathbf{u}}_h^{(n)}; \delta \bar{\mathbf{u}}) - \bar{B}(\bar{\mathbf{u}}_h^{(n)}; \delta \bar{\mathbf{u}})}_{:=\bar{\varrho}_m}, \end{aligned} \quad (49)$$

which defines the discretization error  $\bar{\varrho}_h$  and the model error  $\bar{\varrho}_m$ . Note that the special cases  $\bar{\varrho} = \bar{\varrho}_m$  and  $\bar{\varrho} = \bar{\varrho}_h$  are obtained for  $h \rightarrow 0$  and  $n \rightarrow \infty$ , respectively. To arrive at the exact error representation, we rewrite the total residuum  $\bar{\varrho}$  in Eq. (49) as

$$\bar{\varrho}(\bar{\mathbf{u}}_h^{(n)}; \delta \bar{\mathbf{u}}) = \bar{B}(\bar{\mathbf{u}}; \delta \bar{\mathbf{u}}) - \bar{B}(\bar{\mathbf{u}}_h^{(n)}; \delta \bar{\mathbf{u}}) = \bar{B}_S(\bar{\mathbf{u}}, \bar{\mathbf{u}}_h^{(n)}; \delta \bar{\mathbf{u}}, \bar{\mathbf{e}}), \quad (50)$$

with the error w.r.t. primal solution  $\bar{\mathbf{e}} = \bar{\mathbf{u}} - \bar{\mathbf{u}}_h^{(n)}$ . Here we introduce the secant form of  $\bar{B}$  as

$$\bar{B}_S(\bar{\mathbf{u}}, \bar{\mathbf{u}}_h^{(n)}; \delta \bar{\mathbf{u}}, \bar{\mathbf{e}}) := \int_0^1 D_{\bar{\mathbf{u}}} \bar{B}(\bar{\mathbf{u}}_h^{(n)} + s\bar{\mathbf{e}}; \delta \bar{\mathbf{u}}, \bar{\mathbf{e}}) ds, \quad (51)$$

with  $0 \leq s \leq 1$ , see e.g. [53]. In the same way, the total error  $E$  w.r.t. the quantity of interest  $Q$  is formally formulated as

$$E(\bar{\mathbf{u}}, \bar{\mathbf{u}}_h^{(n)}) := Q(\bar{\mathbf{u}}) - Q(\bar{\mathbf{u}}_h^{(n)}) = Q_S(\bar{\mathbf{u}}, \bar{\mathbf{u}}_h^{(n)}; \bar{\mathbf{e}}), \quad (52)$$

with the secant form of  $Q$

$$Q_S(\bar{\mathbf{u}}, \bar{\mathbf{u}}_h^{(n)}; \bar{\mathbf{e}}) = \int_0^1 D_{\bar{\mathbf{u}}} Q(\bar{\mathbf{u}}_h^{(n)} + s\bar{\mathbf{e}}; \bar{\mathbf{e}}) ds. \quad (53)$$

To set a link between the two secant forms (51) and (53), we introduce a *dual Lagrangian functional*  $\mathcal{L}$  as

$$\mathcal{L}(\bar{\mathbf{u}}, \bar{\mathbf{u}}_h^{(n)}; \delta \bar{\mathbf{z}}, \bar{\mathbf{z}}) := Q_S(\bar{\mathbf{u}}, \bar{\mathbf{u}}_h^{(n)}; \delta \bar{\mathbf{z}}) - \bar{B}_S^*(\bar{\mathbf{u}}, \bar{\mathbf{u}}_h^{(n)}; \bar{\mathbf{z}}, \delta \bar{\mathbf{z}}), \quad (54)$$

where  $\bar{B}_S^*$  is the adjoint form of  $\bar{B}_S$ , satisfying  $\bar{B}_S^*(\bar{\mathbf{u}}, \bar{\mathbf{u}}_h^{(n)}; \bar{\mathbf{z}}, \delta \bar{\mathbf{z}}) = \bar{B}_S(\bar{\mathbf{u}}, \bar{\mathbf{u}}_h^{(n)}; \delta \bar{\mathbf{z}}, \bar{\mathbf{z}})$ . Furthermore,  $\delta \bar{\mathbf{z}} \in \mathcal{V}^0$  and  $\bar{\mathbf{z}} \in \mathcal{V}^0$  are test functions. The dual problem is then established by

$$\text{stat}_{\delta \bar{\mathbf{z}}} \{ \mathcal{L}(\bar{\mathbf{u}}, \bar{\mathbf{u}}_h^{(n)}; \delta \bar{\mathbf{z}}, \bar{\mathbf{z}}) \} \implies Q_S(\bar{\mathbf{u}}, \bar{\mathbf{u}}_h^{(n)}; \delta \bar{\mathbf{u}}) - \bar{B}_S^*(\bar{\mathbf{u}}, \bar{\mathbf{u}}_h^{(n)}; \bar{\mathbf{z}}, \delta \bar{\mathbf{u}}) = 0, \quad (55)$$

with the dual solution  $\bar{\mathbf{z}}$ . For self-adjoint problems (true for the present case), we have

$$\bar{B}_S(\bar{\mathbf{u}}, \bar{\mathbf{u}}_h^{(n)}; \bar{\mathbf{z}}, \delta \bar{\mathbf{u}}) = Q_S(\bar{\mathbf{u}}, \bar{\mathbf{u}}_h^{(n)}; \delta \bar{\mathbf{u}}). \quad (56)$$

Combining equations (52), (56), (49) and (50) renders

$$E(\bar{\mathbf{u}}, \bar{\mathbf{u}}_h^{(n)}) = \bar{\varrho}(\bar{\mathbf{u}}_h^{(n)}, \bar{\mathbf{z}}) = \bar{\varrho}_h(\bar{\mathbf{u}}_h^{(n)}, \bar{\mathbf{z}}) + \bar{\varrho}_m(\bar{\mathbf{u}}_h^{(n)}, \bar{\mathbf{z}}) \quad (57)$$

as an exact error representation, requiring the knowledge of the exact model  $\bar{B}$  and depending on the exact dual solution  $\bar{\mathbf{z}}$ . In combination with the Galerkin orthogonality, we finally obtain

$$E(\bar{\mathbf{u}}, \bar{\mathbf{u}}_h^{(n)}) = \underbrace{\bar{\varrho}_h(\bar{\mathbf{u}}_h^{(n)}, \bar{\mathbf{z}} - \pi\bar{\mathbf{z}})}_{:=E_h(\bar{\mathbf{u}}, \bar{\mathbf{u}}_h^{(n)})} + \underbrace{\bar{\varrho}_m(\bar{\mathbf{u}}_h^{(n)}, \bar{\mathbf{z}})}_{:=E_m(\bar{\mathbf{u}}, \bar{\mathbf{u}}_h^{(n)})}, \quad (58)$$

where  $\pi\bar{\mathbf{z}} \in \mathcal{V}_h^0$  is the projection of  $\bar{\mathbf{z}}$  onto the FE-space  $\mathcal{V}_h^0$ .

### 3.2 Approximations for a computable error representation

To arrive at a computable error representation, the following three approximations have to be made:

1. The exact model of hierarchical order  $n \rightarrow \infty$  is replaced by a *fine* model of a hierarchical order  $n^+ > n$ . Hence, we obtain from (49)

$$\bar{\varrho}_m(\bar{\mathbf{u}}_h^{(n)}, \bar{\mathbf{z}}) \approx \bar{\varrho}_m^+(\bar{\mathbf{u}}_h^{(n)}, \bar{\mathbf{z}}) := \bar{B}^{(n)}(\bar{\mathbf{u}}_h^{(n)}; \bar{\mathbf{z}}) - \bar{B}^{(n^+)}(\bar{\mathbf{u}}_h^{(n)}; \bar{\mathbf{z}}). \quad (59)$$

2. The exact dual problem (56) also depends on the exact primal solution  $\bar{\mathbf{u}}$  and requires knowledge of the exact model. Hence, we introduce an approximate dual problem

$$\bar{B}_S^{(n)}(\bar{\mathbf{u}}_h^{(n)}, \bar{\mathbf{u}}_h^{(n)}; \bar{\mathbf{z}}, \delta\bar{\mathbf{u}}) = Q_S^{(n)}(\bar{\mathbf{u}}_h^{(n)}, \bar{\mathbf{u}}_h^{(n)}; \delta\bar{\mathbf{u}}) \quad (60)$$

by the replacements  $\bar{B}_S \approx \bar{B}_S^{(n)}$ ,  $Q_S \approx Q_S^{(n)}$  and  $\bar{\mathbf{u}} \approx \bar{\mathbf{u}}_h^{(n)}$ , leading to a linearization of (56).

3. In practice, the approximate dual problem (60) is not solved exactly. Instead a spatially discretized version of (60), i.e.

$$\bar{B}_S^{(n)}(\bar{\mathbf{u}}_h^{(n)}, \bar{\mathbf{u}}_h^{(n)}; \bar{\mathbf{z}}_h, \delta\bar{\mathbf{u}}) = Q_S^{(n)}(\bar{\mathbf{u}}_h^{(n)}, \bar{\mathbf{u}}_h^{(n)}; \delta\bar{\mathbf{u}}), \quad (61)$$

is solved via FEM, using the same mesh as for the primal problem and thus preserving an analogous structure of the primal problem (see e.g. [60]). Here  $\bar{\mathbf{z}}_h$  is the FE solution of the approximate dual problem (60), which is not directly useful for the error formula (58). Methods to compute an approximation of the exact dual solution  $\bar{\mathbf{z}}$  will be described in Section 3.3.

**Remark 11.** An alternative way to approximate (56) is to apply the trapezoidal rule on both sides of (56) as

$$\bar{B}_S(\bar{\mathbf{u}}, \bar{\mathbf{u}}_h^{(n)}; \delta\bar{\mathbf{u}}, \bar{\mathbf{e}}) \approx \frac{1}{2} \left( D_{\bar{\mathbf{u}}} \bar{B}(\bar{\mathbf{u}}_h^{(n)}; \delta\bar{\mathbf{u}}, \bar{\mathbf{e}}) + D_{\bar{\mathbf{u}}} \bar{B}(\bar{\mathbf{u}}; \delta\bar{\mathbf{u}}, \bar{\mathbf{e}}) \right), \quad (62a)$$

$$Q_S(\bar{\mathbf{u}}, \bar{\mathbf{u}}_h^{(n)}; \bar{\mathbf{e}}) \approx \frac{1}{2} \left( D_{\bar{\mathbf{u}}} Q(\bar{\mathbf{u}}_h^{(n)}; \bar{\mathbf{e}}) + D_{\bar{\mathbf{u}}} Q(\bar{\mathbf{u}}; \bar{\mathbf{e}}) \right), \quad (62b)$$

leading to a linearized version of (56) as

$$D_{\bar{\mathbf{u}}}\bar{B}(\bar{\mathbf{u}}_h^{(n)}; \bar{\mathbf{z}}, \delta\bar{\mathbf{u}}) + D_{\bar{\mathbf{u}}}\bar{B}(\bar{\mathbf{u}}; \bar{\mathbf{z}}, \delta\bar{\mathbf{u}}) = D_{\bar{\mathbf{u}}}Q(\bar{\mathbf{u}}_h^{(n)}; \delta\bar{\mathbf{u}}) + D_{\bar{\mathbf{u}}}Q(\bar{\mathbf{u}}; \delta\bar{\mathbf{u}}), \quad (63)$$

see also [54]. Using the approximations  $\bar{B} \approx \bar{B}^{(n)}$ ,  $Q \approx Q^{(n)}$  and  $\bar{\mathbf{u}} \approx \bar{\mathbf{u}}_h^{(n)}$ , we arrive at

$$D_{\bar{\mathbf{u}}}\bar{B}^{(n)}(\bar{\mathbf{u}}_h^{(n)}; \bar{\mathbf{z}}, \delta\bar{\mathbf{u}}) = D_{\bar{\mathbf{u}}}Q^{(n)}(\bar{\mathbf{u}}_h^{(n)}; \delta\bar{\mathbf{u}}), \quad (64)$$

which is the same result as obtained from (60).

### 3.3 Different methods for computation of the enhanced dual solution

For a practical evaluation of the exact error representation (58), we need a better approximation of the dual solution  $\bar{\mathbf{z}}_{h+}$  than  $\bar{\mathbf{z}}_h$ , which replaces the exact one  $\bar{\mathbf{z}}$ . To this end, several ways shown in literature, e.g. [36, 59] and references therein, can be adopted. They usually share a common idea that  $\bar{\mathbf{z}}_{h+}$  belongs to an enhanced FE-space  $\mathcal{V}_{h+}^0$  satisfying  $\mathcal{V}_h^0 \subset \mathcal{V}_{h+}^0 \subset \mathcal{V}^0$ , using the hierarchical FE structure by increasing the polynomial interpolation order. In this work, we adopt linear triangular elements for  $\mathcal{V}_h^0$ , whose enhanced space  $\mathcal{V}_{h+}^0$  consists of quadratic triangular elements. We additionally introduce two indices 1 and 2, which represent the degrees of freedom associated with  $\mathcal{V}_h^0$  and the additional degrees of freedom in  $\mathcal{V}_{h+}^0$ , respectively. In this manner, we may write the enhanced dual solution as  $\bar{\mathbf{z}}_{h+} = [\hat{\bar{\mathbf{z}}}_1 \ \hat{\bar{\mathbf{z}}}_2]$ .

(a) *Full computation*: The most straightforward way to obtain  $\bar{\mathbf{z}}_{h+}$  is to compute

$$D_{\bar{\mathbf{u}}}\bar{B}^{(n)}(\hat{\bar{\mathbf{u}}}_1^{(n)} + \hat{\bar{\mathbf{u}}}_2^{(n)}; \hat{\bar{\mathbf{z}}}_1 + \hat{\bar{\mathbf{z}}}_2, \delta\hat{\bar{\mathbf{u}}}_1 + \delta\hat{\bar{\mathbf{u}}}_2) = D_{\bar{\mathbf{u}}}Q^{(n)}(\hat{\bar{\mathbf{u}}}_1^{(n)} + \hat{\bar{\mathbf{u}}}_2^{(n)}; \delta\hat{\bar{\mathbf{u}}}_1 + \delta\hat{\bar{\mathbf{u}}}_2) \quad (65)$$

directly on the enhanced FE-space  $\mathcal{V}_{h+}^0$ , where  $\hat{\bar{\mathbf{z}}}_1 = \pi\bar{\mathbf{z}}_{h+}$ . Consequently, the computational cost is much higher than for (61).

(b) *Decoupled computation*: To reduce the computational cost of (65), the approximation  $\hat{\bar{\mathbf{z}}}_1 \approx \bar{\mathbf{z}}_h$  is made. Consequently, only a reduced version of (65)

$$D_{\bar{\mathbf{u}}}\bar{B}^{(n)}(\hat{\bar{\mathbf{u}}}_1^{(n)} + \hat{\bar{\mathbf{u}}}_2^{(n)}; \bar{\mathbf{z}}_h + \hat{\bar{\mathbf{z}}}_2, \delta\hat{\bar{\mathbf{u}}}_1 + \delta\hat{\bar{\mathbf{u}}}_2) = D_{\bar{\mathbf{u}}}Q^{(n)}(\hat{\bar{\mathbf{u}}}_1^{(n)} + \hat{\bar{\mathbf{u}}}_2^{(n)}; \delta\hat{\bar{\mathbf{u}}}_1 + \delta\hat{\bar{\mathbf{u}}}_2) \quad (66)$$

has to be solved for  $\hat{\bar{\mathbf{z}}}_2$ , whose computational cost is of the order as for (61).

(c) *Local recovery - variant 1*: Alternatively,  $\bar{\mathbf{z}}_{h+}$  can be obtained by certain recovery techniques without computations of the type (65) or (66), leading to a further reduction of computational cost. Two local variants of recovery methods are suggested in our preparatory work [59]. Taking gradients into account, these approaches require merely information from one single element after a smoothing procedure. We consider here the first variant, where all nodal values on the enhanced FE-space are fully recovered.

(d) *Local recovery - variant 2*: The second variant in [59] has the difference from the first variant that only the additional nodal values on the enhanced FE-space are recovered. For further details, we refer to the original paper [59].

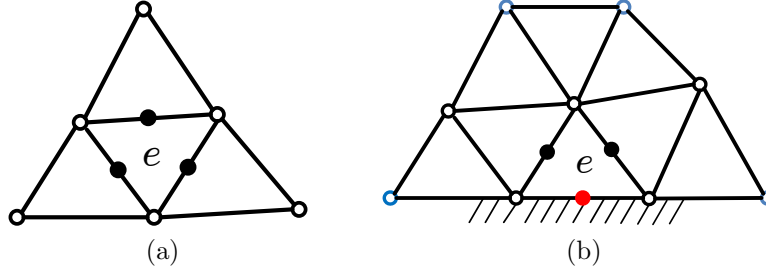


Figure 2: Illustration of patch-based recovery approach: (a) Regular case for interior elements (○: existing nodes and ●: additional nodes in the locally enhanced FE-space) and (b) Special case for boundary elements (○: extended nodes and ●: boundary nodes in the locally enhanced FE-space)

- (e) *Patch recovery*: A patch-based recovery technique, based on the idea of a locally enhanced FE-space in [36], is proposed in our recent work [24] for micromorphic continuum problems. With the approximation  $\hat{\bar{z}}_1 \approx \bar{z}_h$ , we focus on determining  $\hat{\bar{z}}_2$ . As shown in Fig. 2a, we define a locally enhanced FE-space  ${}^e\mathcal{V}_{h+}^0$  for each element  $e$ , which is referred to as *patch*. Similarly to the so-called superconvergent patch recovery [64], in  ${}^e\mathcal{V}_{h+}^0$ , each component  ${}^e\bar{z}_{h+}^i$  of  ${}^e\bar{z}_{h+}$  is assumed to be expressed as a higher order polynomial representation

$${}^e\bar{z}_{h+}^i = \underline{P} \cdot \underline{a}^i, \quad (67)$$

where the index  $i$  is related to nodal degrees of freedom. For two-dimensional cases, we have  $i = 1, 2$ . For an enhanced quadratic representation, we define  $\underline{P} := [1 \ x_1 \ x_2 \ x_1^2 \ x_1x_2 \ x_2^2]$ , while  $\underline{a}^i := [a_1^i \cdots a_k^i \cdots a_6^i]^T$  contains six unknown coefficients. Here  $x_i$ , with  $i = 1, 2$ , correspond to single components of the coordinate  $\mathbf{x}$ . To determine the unknown coefficients in  $\underline{a}$ , minimization problems are formulated as

$$f(\bar{z}_h^i, {}^e\bar{z}_{h+}^i) := \sum_{j=1}^{N^h} (\bar{z}_h^i(x_1^j, x_2^j) - {}^e\bar{z}_{h+}^i(x_1^j, x_2^j))^2 \rightarrow \min, \quad \text{for } i = 1, 2, \quad (68)$$

where  $\bar{z}_h^i$  is the corresponding component of the dual solution obtained from (61). Furthermore,  $N^h$  is the number of existing nodes in the current FE-space  ${}^e\mathcal{V}_h^0$ . Combining (67) and (68) renders

$$f(\bar{z}_h^i, {}^e\bar{z}_{h+}^i) = \sum_{j=1}^{N^h} (\bar{z}_h^i(x_1^j, x_2^j) - \underline{P}(x_1^j, x_2^j) \cdot \underline{a}^i)^2 \rightarrow \min, \quad \text{for } i = 1, 2, \quad (69)$$

which has a simple formal solution

$$\underline{a}^i = \underline{A}^{-1} \underline{b}^i, \quad \text{where} \quad (70a)$$

$$\underline{A} := \sum_{j=1}^{N^h} \underline{P}^T(x_1^j, x_2^j) \underline{P}(x_1^j, x_2^j), \quad (70b)$$

$$\underline{b}^i := \sum_{j=1}^{N^h} \bar{z}_h^i(x_1^j, x_2^j) \underline{P}^T(x_1^j, x_2^j). \quad (70c)$$

Note that the matrix  $\underline{A}$  is independent on the index  $i$ . With the result  $\underline{a}^i$ , the additional nodal values  ${}^e\hat{\underline{z}}_2$  can be simply obtained from (67). Obviously, to obtain the global vector  $\hat{\underline{z}}_2$ , the equations (70) have to be solved for all elements  $e = 1, \dots, N_{el}$  and all nodal degrees of freedom  $i = 1, 2$ . Given that different nodal values on the same node can be obtained by different computations of (70), the global vector  $\hat{\underline{z}}_2$  is calculated by weighted averaging of  ${}^e\hat{\underline{z}}_2$  from adjacent elements. As shown in Fig. 2b, special care must be paid for boundary elements, which do not have sufficient number of surrounding elements in the same manner as shown in Fig. 2a. Consequently, additional nodes have to be included to arrive at a sufficient number of surrounding elements. Additionally, the boundary values must be corrected correspondingly.

### 3.4 The linear elastic composite problem

We are now in the position to specify the abstract setting described in the sections 3.1-3.3 for the case of linear elasticity. For this purpose, we define the exact, the working and the fine model as

$$\bar{B}(\bar{\mathbf{u}}; \delta\bar{\mathbf{u}}) = \int_{\bar{\Omega}} \bar{\boldsymbol{\varepsilon}}[\delta\bar{\mathbf{u}}] : (\bar{\mathbb{C}}\bar{\boldsymbol{\varepsilon}}[\bar{\mathbf{u}}]) dv, \quad (71a)$$

$$\bar{B}^{(n)}(\bar{\mathbf{u}}; \delta\bar{\mathbf{u}}) = \int_{\bar{\Omega}} \bar{\boldsymbol{\varepsilon}}[\delta\bar{\mathbf{u}}] : (\bar{\mathbb{C}}^{(n)}\bar{\boldsymbol{\varepsilon}}[\bar{\mathbf{u}}]) dv, \quad (71b)$$

$$\bar{B}^{(n^+)}(\bar{\mathbf{u}}; \delta\bar{\mathbf{u}}) = \int_{\bar{\Omega}} \bar{\boldsymbol{\varepsilon}}[\delta\bar{\mathbf{u}}] : (\bar{\mathbb{C}}^{(n^+)}\bar{\boldsymbol{\varepsilon}}[\bar{\mathbf{u}}]) dv, \quad (71c)$$

respectively. To complete the definitions (71b) and (71c), we make a choice based on the bounding theory described in Section 2.5 as

$$\bar{\mathbb{C}}^{(n)} = \frac{1}{2}(\bar{\mathbb{C}}^{n_0} + \bar{\mathbb{C}}_{n_0}), \quad \bar{\mathbb{C}}^{(n^+)} = \frac{1}{2}(\bar{\mathbb{C}}^{n_0+2} + \bar{\mathbb{C}}_{n_0+2}), \quad (72)$$

where  $n_0 = 2n + 1$  holds. Note that one could also make a different choice like  $\bar{\mathbb{C}}^{(n)} = \bar{\mathbb{C}}^{n_0}$  and  $\bar{\mathbb{C}}^{(n^+)} = \bar{\mathbb{C}}_{n_0+2}$  for the purpose of a safe design.

Using the enhanced dual solution  $\bar{\mathbf{z}}_{h^+}$  obtained by one of the methods described in Section 3.3 and combining equations (49), (58), (59) and (71), we finally obtain the computable error representations for the model error

$$E_m(\bar{\mathbf{u}}, \bar{\mathbf{u}}_h^{(n)}) = \bar{\varrho}_m(\bar{\mathbf{u}}_h^{(n)}, \bar{\mathbf{z}}) \approx \int_{\bar{\Omega}} \bar{\boldsymbol{\varepsilon}}[\bar{\mathbf{z}}_{h^+}] : \left( (\bar{\mathbb{C}}^{(n)} - \bar{\mathbb{C}}^{(n^+)})\bar{\boldsymbol{\varepsilon}}[\bar{\mathbf{u}}_h^{(n)}] \right) dv = \tilde{E}_m \quad (73)$$

and for the discretization error

$$\begin{aligned} E_h(\bar{\mathbf{u}}, \bar{\mathbf{u}}_h^{(n)}) &= \bar{\varrho}_h(\bar{\mathbf{u}}_h^{(n)}, \bar{\mathbf{z}} - \pi\bar{\mathbf{z}}) \\ &\approx \bar{F}(\bar{\mathbf{z}}_{h^+} - \pi\bar{\mathbf{z}}_{h^+}) - \int_{\bar{\Omega}} \bar{\boldsymbol{\varepsilon}}[\bar{\mathbf{z}}_{h^+} - \pi\bar{\mathbf{z}}_{h^+}] : (\bar{\mathbb{C}}^{(n)}\bar{\boldsymbol{\varepsilon}}[\bar{\mathbf{u}}_h^{(n)}]) dv = \tilde{E}_h, \end{aligned} \quad (74)$$

respectively. The local errors  $\eta_m^e$  and  $\eta_h^e$  for each single element  $e$  are then obtained

from the corresponding elemental contributions of (73) and (74), respectively, i.e.

$$\tilde{E}_m = \sum_{e=1}^{N_{el}} \eta_m^e, \quad (75a)$$

$$\tilde{E}_h = \sum_{e=1}^{N_{el}} \eta_h^e, \quad (75b)$$

$$\tilde{E} = \tilde{E}_m + \tilde{E}_h. \quad (75c)$$

Note that the sign of  $\eta_m^e$  and  $\eta_h^e$  indicates the direction of the deviation w.r.t. the quantity of interest  $Q$ , hence, only their absolute values are considered as local indicators in the adaptive algorithm, which will be described in the subsequent section.

### 3.5 Adaptive algorithm

Up to now, both the model and the discretization error can be estimated. In order to control both errors adaptively, we propose the algorithm in Algorithm 1.

Initialization: set the initial mesh  $\mathcal{V}_{h^0}^0$  with the initial (uniform) elastic property  $\bar{\mathbb{C}}^{(n=0)}$ ;

Define a the stopping criterion  $\tilde{E} = \tilde{E}_h + \tilde{E}_m \leq TOL$  for the adaptive refinement loop, where  $TOL$  is a user-defined threshold value related to the desired accuracy;

**while**  $\tilde{E} = \tilde{E}_h + \tilde{E}_m > TOL$  **do**

    Solve the computable working model problem (48);

    Solve the approximate dual problem (61) on the current mesh and compute the enhanced dual solution following one of the methods in Section 3.3;

    Compute the local fine models  $\bar{\mathbb{C}}^{(n_e^+)}$ ;

    Compute the error representations (local and global) according to the equations (73), (74) and (75);

    Adaptive refinement: a fixed refinement ratio, such as  $\alpha = 10\%$ , of the elements with the largest  $|\eta_h^e|$  and  $|\eta_m^e|$  is spatially refined and enhanced by  $\bar{\mathbb{C}}^{(n_e)} \rightarrow \bar{\mathbb{C}}^{(n_e^+)}$ , respectively; update the local hierarchical order  $n_e \rightarrow n_e^+$  for enhanced elements.

**end**

**Algorithm 1:** Adaptive algorithm

**Remark 12.** For linear elasticity, the effective properties need to be computed only once for a certain microstructure. For macroscopically homogeneous materials, in each adaptive step  $i = 0, 1, 2, \dots$ , the (maximal reachable) fine model  $\bar{\mathbb{C}}^{(n^+=i+1)}$  is computed only once for all and stored for a possible call by subsequent steps. Obviously, computational cost can not be saved in this manner, when the considered material is macroscopically heterogeneous, or when the mechanics problem is coupled to an additional problem such as phase transformation.

## 4 Numerical examples

### 4.1 Preliminaries

In this section, a perforated sheet is investigated. As shown in Fig. 3a, we consider a quarter model, which is stretched by a displacement  $u = 0.01$  mm in the horizontal direction. We restrict ourselves to a two-dimensional case, where the thickness of the sheet is  $t = 1$  mm. The indices 1 and 2 represent the horizontal and the vertical direction, respectively. A plane strain state is assumed, where the third strain component  $\epsilon_{33}$  implying the strain in the thickness direction is always zero.

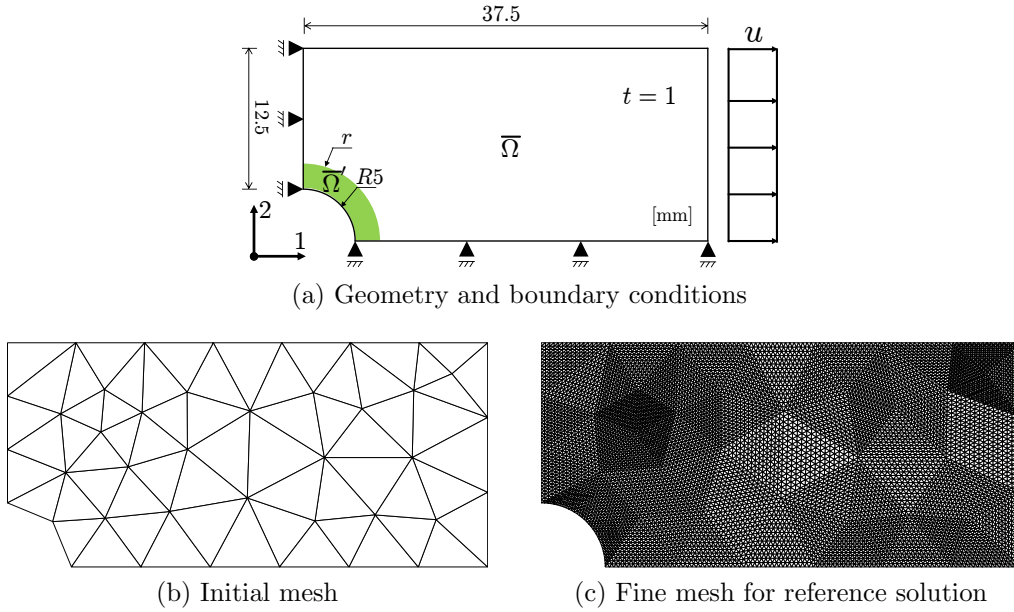


Figure 3: Perforated sheet in linear elasticity

The sheet is made of a composite material, consisting of a matrix material ( $E_0 = 70000$  MPa and  $\nu_0 = 0.2$ ) and unoriented short fibers ( $E_1 = 147000$  MPa and  $\nu_1 = 0.285$ ). In the subsequent examples, we will consider three different types of materials as follows:

- macroscopically homogeneous composite with a constant volume fraction of the fibers  $c_f = \text{const.}$
- functionally graded composite with a given function  $c_f = c_f(\mathbf{x})$
- macroscopically random composite with  $c_f(\mathbf{x})$  according to certain statical properties.

Obviously, for the latter two cases, the material is macroscopically heterogeneous, such that an individual computation of effective properties for each macro material point is required.

The adaptive procedure starts with the initial mesh  $\mathcal{V}_{h_0}^0$  shown in Fig. 3b, consisting of linear triangular elements. To illustrate the power of goal-oriented adaptivity,

we define the quantity of interest  $Q$  as a local type quantity

$$Q := \int_{\bar{\Omega}'} \bar{\sigma}_{ij} dv, \quad (76)$$

where  $\bar{\sigma}_{ij}$  represents coefficients of the macro stress tensor  $\bar{\sigma}$ . For this work, we choose  $i = j = 1$ . Furthermore,  $\bar{\Omega}'$  is a local domain out of the whole domain  $\bar{\Omega}$ , i.e. the green area marked in Fig. 3a, with  $r = 8$  mm.

## 4.2 Model hierarchy

Before getting started with goal-oriented adaptivity, we first investigate the bounding theory in the sections 2.5-2.7 and show how a model hierarchy is established. We choose for computation of the upper bounds the comparison material as the Voigt bound, i.e.  $\mathbb{C}^0 = \langle \mathbb{C} \rangle$ , and for computation of the lower bounds the comparison material  $\mathbb{C}^0 = (\mathbb{S}^0)^{-1} = (\langle \mathbb{S} \rangle)^{-1}$  as the Reuss bound. The volume fraction of the fibers is assumed to be  $c_f = 5\%$ . As described in the sections 2.5 and 2.6, the upper bounds  $\bar{\mathbb{C}}^{n_0}$  and the lower bounds  $\bar{\mathbb{C}}_{n_0}$  are computed via the series (29) and (30) for odd order  $n_0$ , respectively. By means of the effective elasticity modulus  $\bar{E}$ , the numerical results without and with correction according to Eq. (46) are illustrated in the figures 4a and 4b, respectively. Fig. 4a shows that a slight overlap effect occurs for  $n_0 > 27$ . The reason has already been discussed in Section 2.7. Despite of this deficiency, a comparison with the reference solution obtained by the estimate (45) shows a satisfactory convergence behavior of the bounds (see figures 4a and 4b). Additionally, according to the results shown in Fig. 4a, the original bounds with  $n_0 \leq 27$ , which do not require a correction, are still sufficient for our purpose, since the bounds of higher order  $n_0 \geq 19$  are fairly narrow. To further establish a model hierarchy, we make use of Eq. (72), where the arithmetic means of the bounds are adopted. Based on the results shown in Fig. 4b, the obtained model hierarchy is illustrated in Fig. 4c, where the effective elasticity modulus  $\bar{E}$  with increasing hierarchical order  $n$  tends to a constant. Note that the hierarchical order  $n$  has to be distinguished from the approximation order  $n_0$ , i.e. there holds  $n = (n_0 - 1)/2$ . Obviously, the bounds without correction in Fig. 4a would render the same result as shown in Fig. 4c.

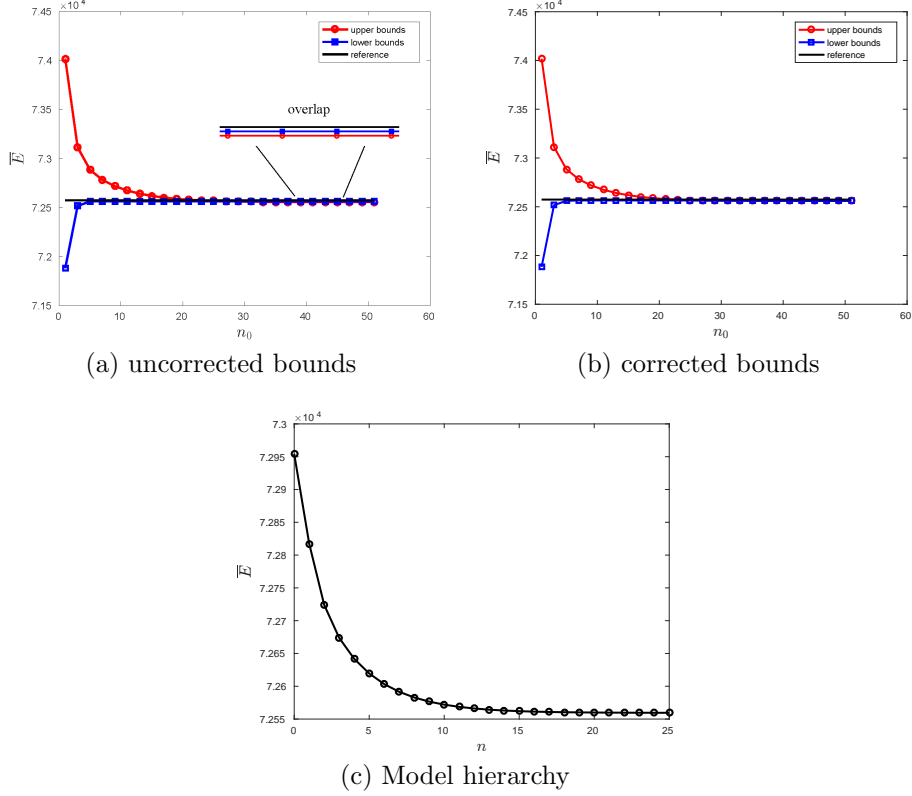


Figure 4: Results of the bounding theory

### 4.3 Goal-oriented adaptivity for a macroscopically homogeneous composite

In this section, we consider a macroscopically homogeneous composite, where the volume fraction of the fibers is assumed to be  $c_f = \text{const.} = 5\%$ . In the following, a detailed comparison of adaptive results based on different enhanced dual solutions will be given. We consider the five methods (a)-(e) described in Section 3.3. For an efficiency investigation, we set the refinement ratio  $\alpha$  in Algorithm 1 to be sufficiently small, i.e.  $\alpha = 5\%$ .

In Fig. 5, different distributions of the local discretization error indicator  $|\eta_h^e|$ , obtained from all five different methods, are shown for different adaptive steps. For the initial step, the distributions are rather different for different methods, indicating that the enhanced dual solution  $\bar{z}_{h+}$  has a large influence on the error computation. The full computation by (65) serves as a reference solution for the remaining four methods. For further adaptive steps, the differences between the distributions obtained from the remaining four methods and the reference one become larger, since the resulted adaptive refinements (meshes and model distributions) are also different. The local discretization error  $|\eta_h^e|$  is strongly reduced by the adaptive algorithm for all methods. In the final step, a strongly heterogeneous distribution of  $|\eta_h^e|$ , computed by the first variant of local recovery, is still observable, whereas the local error  $|\eta_h^e|$  is balanced by the other four methods.

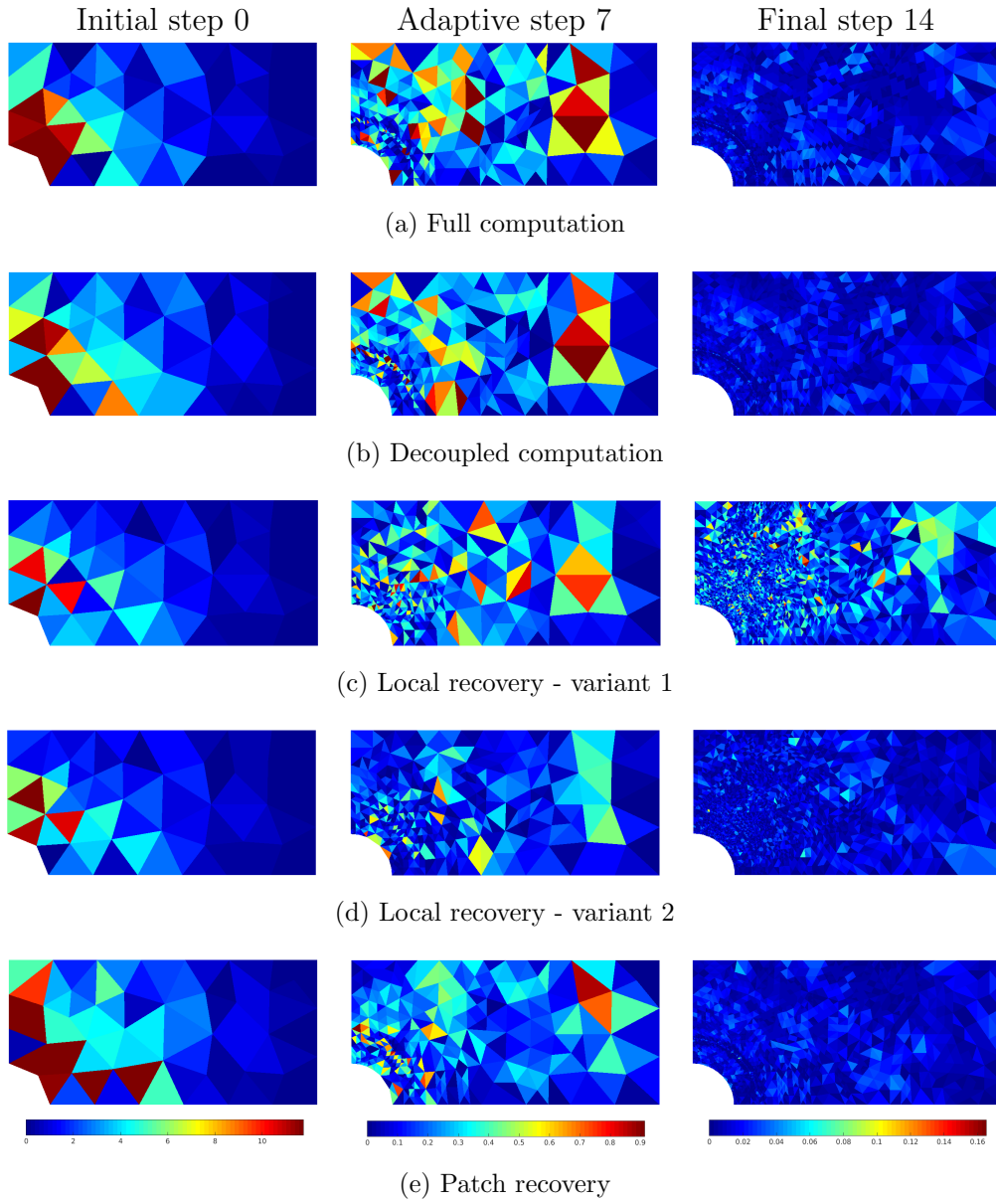


Figure 5: Macroscopically homogeneous composite - Comparison of local discretization error indicator  $|\eta_h^e|$

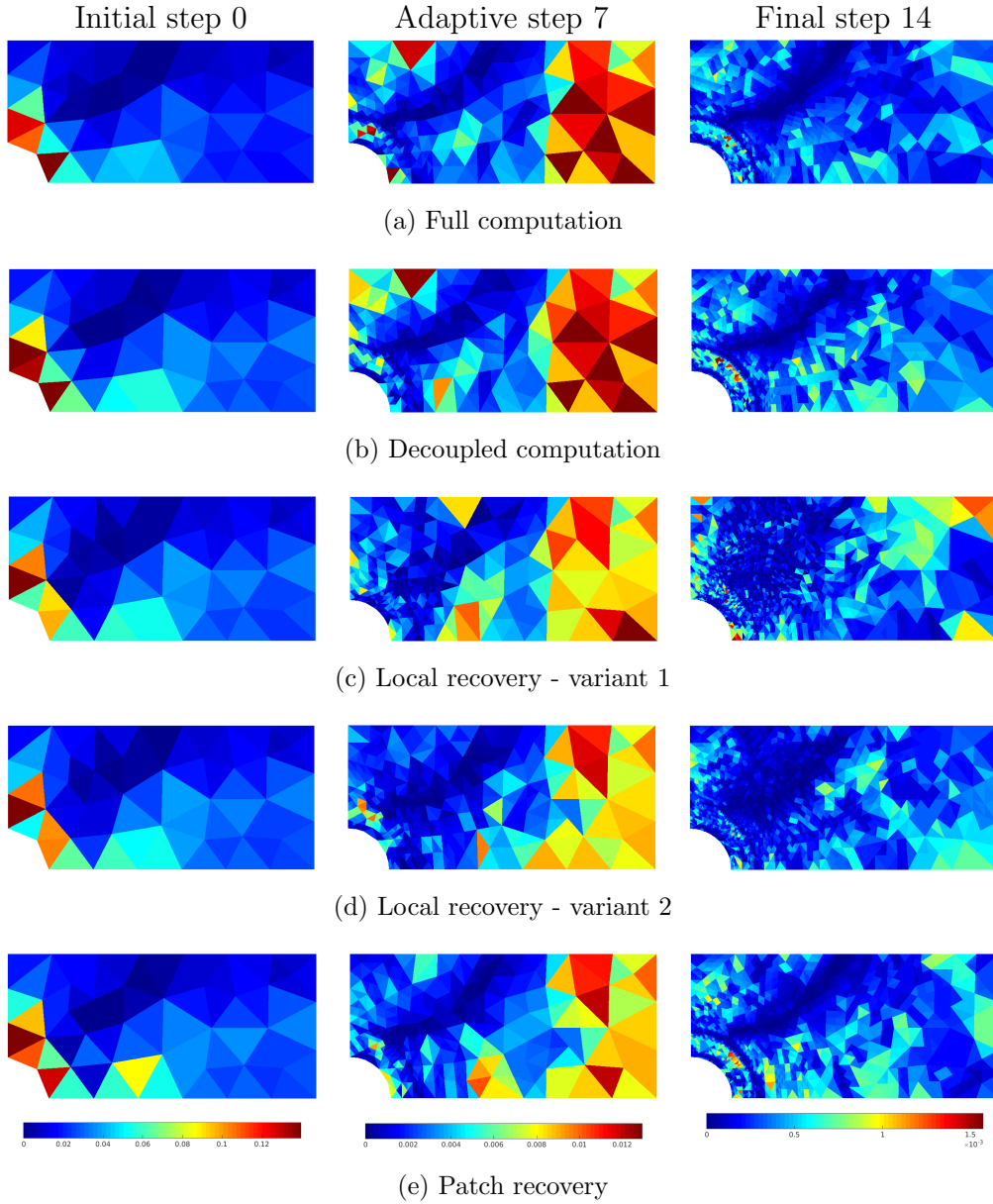


Figure 6: Macroscopically homogeneous composite - Comparison of local model error indicator  $|\eta_m^e|$

In Fig. 6, different distributions of the local model error indicator  $|\eta_m^e|$  are illustrated in the same manner, supporting the same statements as in Fig. 5. The main difference is that, in the final step, a heterogeneous distribution of the local model error  $|\eta_m^e|$  is still clearly observable for all methods.

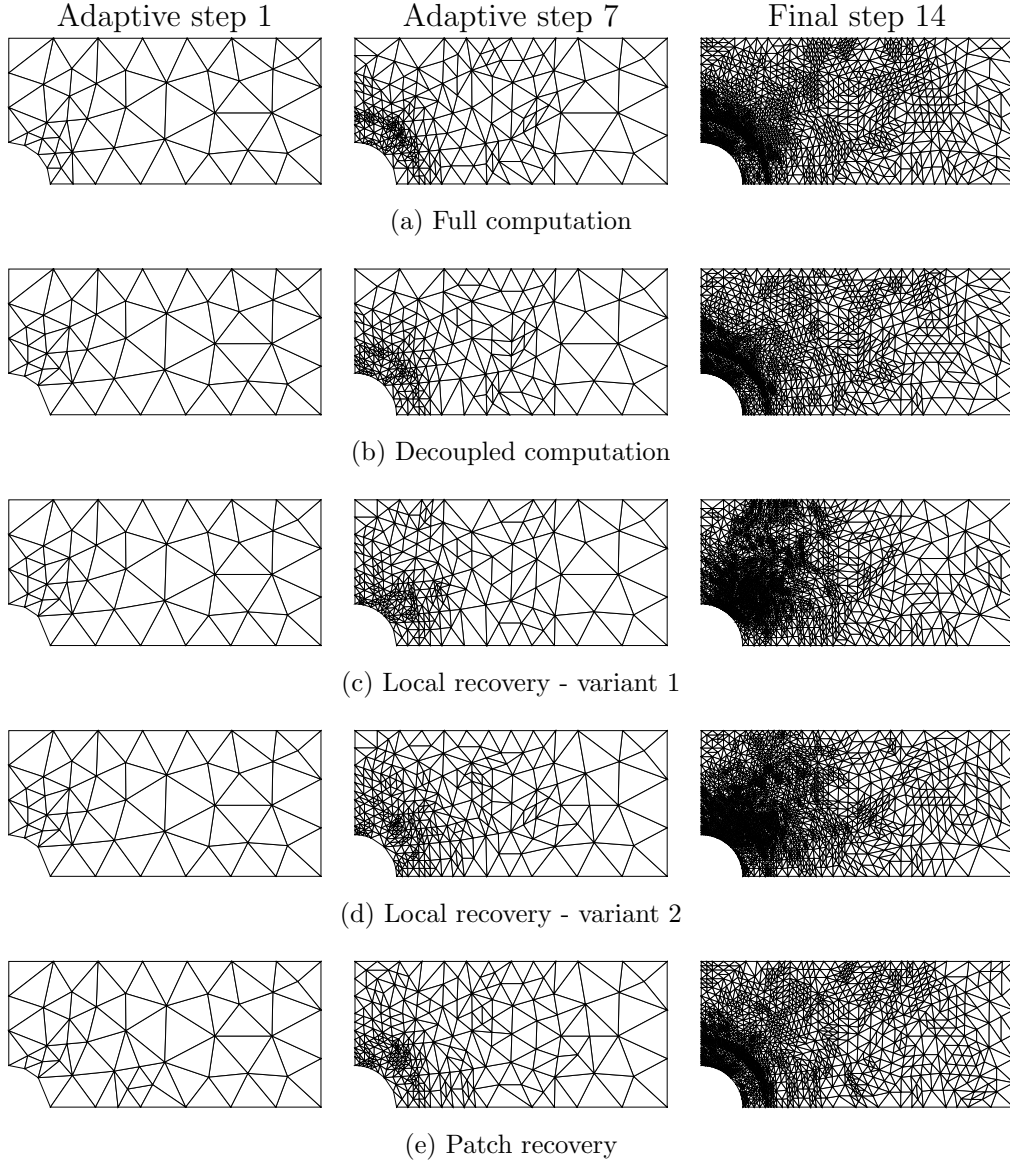


Figure 7: Macroscopically homogeneous composite - Comparison of adaptively refined meshes

A comparison of adaptively refined meshes is given in Fig. 7, while Fig. 8 makes a comparison of model distributions. The final meshes of both local recovery methods (c) and (d) are quite similar, however, strongly differ from the reference mesh obtained from full computation. The final meshes of decoupled computation and patch recovery are fairly close to the reference mesh, where adaptive refinements are mainly concentrated in the local domain  $\bar{\Omega}'$ , especially in its boundary regions. Concerning model distributions, the maximal possible hierarchical order, here  $n_{\max} = 14$ , is not reached for all methods, since the distributions of the local model error  $|\eta_m^e|$  always change for different meshes and different model distributions, such that the peak values of  $|\eta_m^e|$  are not always located in a certain region. Furthermore, both local recovery methods (c) and (d) achieve the highest hierarchical order (9). For all methods, the highest hierarchical orders are located on the right side of the sheet,

where coarsest discretizations are adopted.

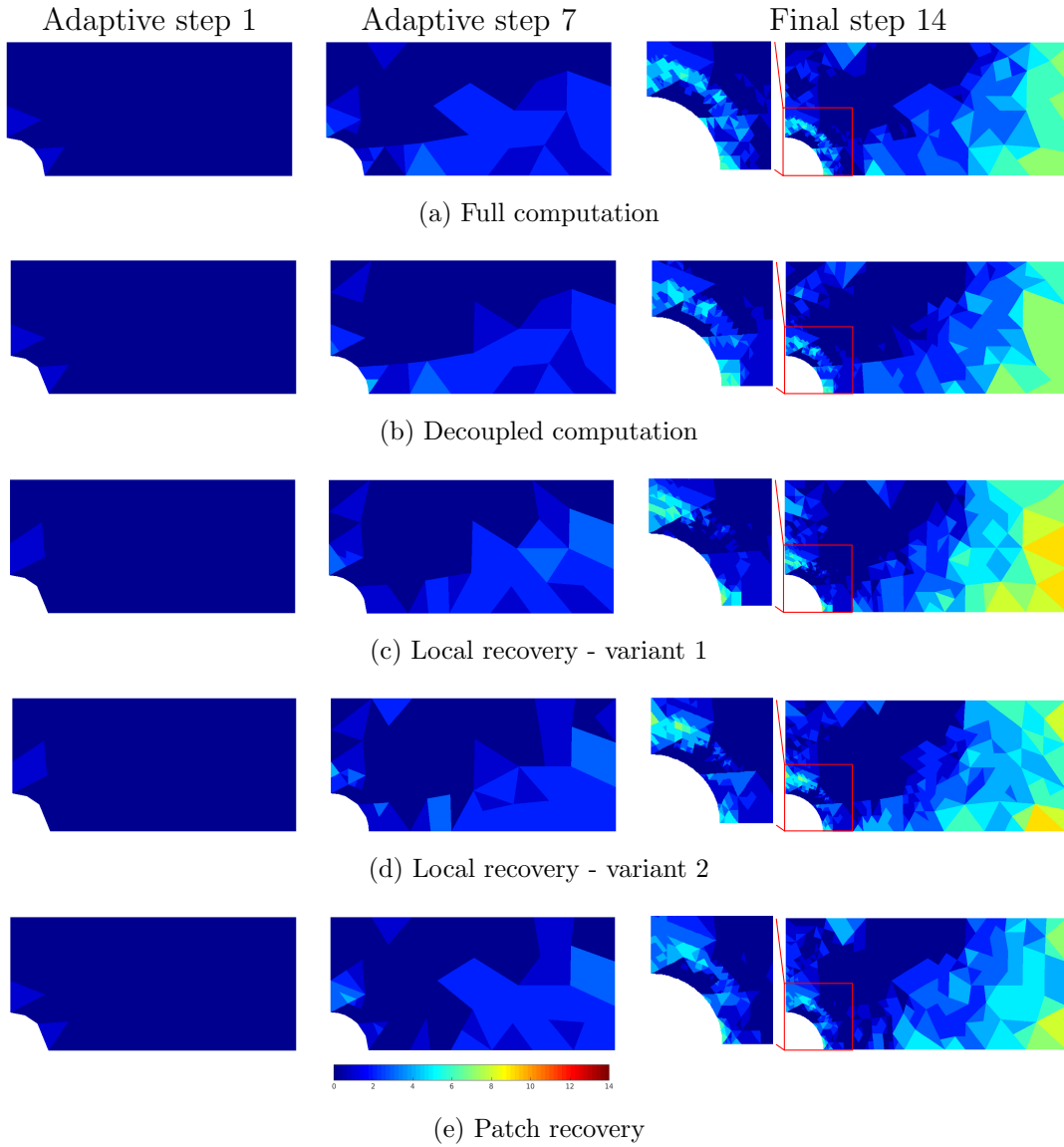
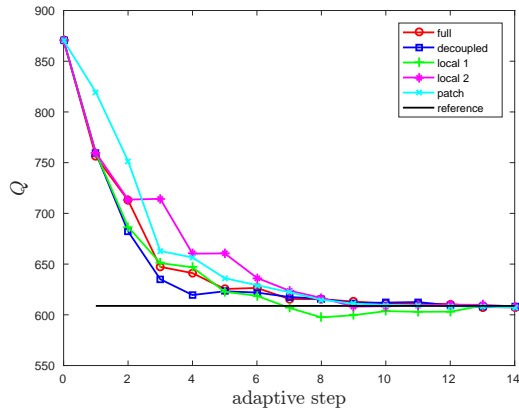
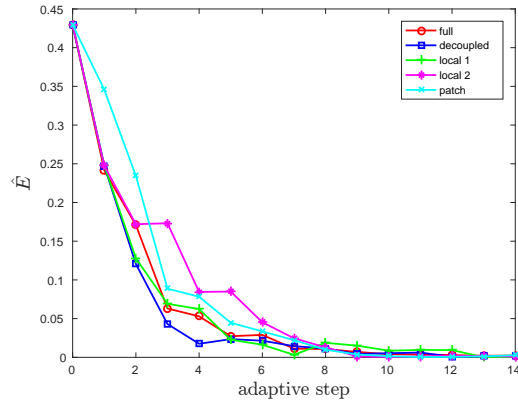


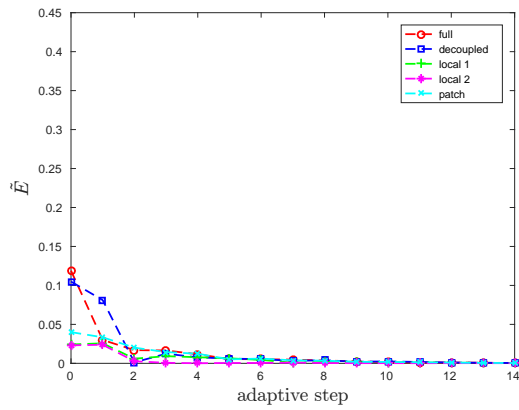
Figure 8: Macroscopically homogeneous composite - Comparison of model distributions



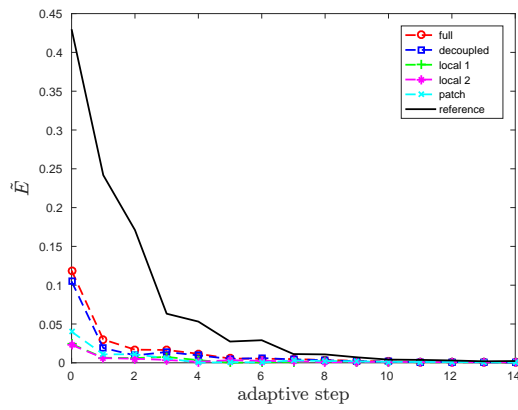
(a) Quantity of interest  $Q$



(b) Error measure  $\hat{E}$  of  $Q$



(c) Estimated error  $\tilde{E}$  of  $Q$  (normalized)



(d) Estimated error  $\tilde{E}$  of  $Q$  on the same sequence of refinements obtained from full computation

Figure 9: Macroscopically homogeneous composite - Comparison of the quantity of interest  $Q$

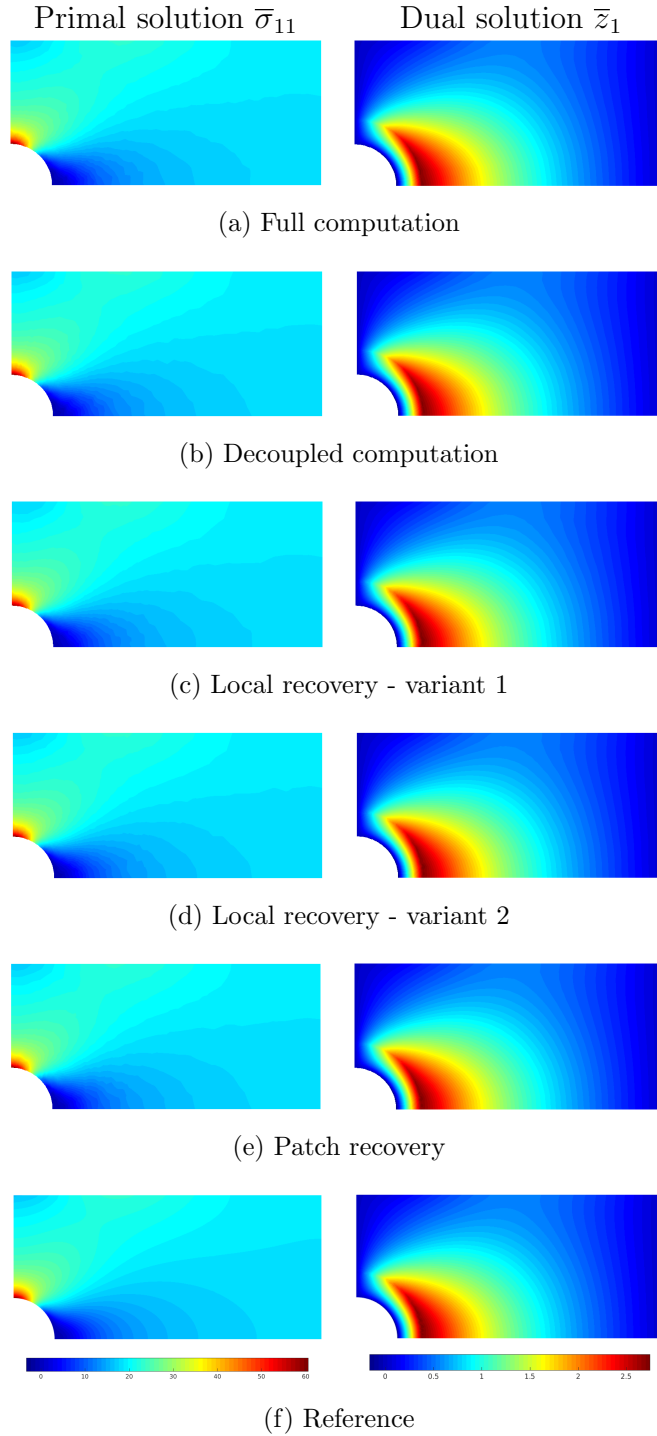


Figure 10: Macroscopically homogeneous composite - Comparison of primal and dual solutions for the final step 14

In Fig. 9, we consider the quantity of interest  $Q$  and the estimated global errors, in order to investigate the effectivity of the proposed adaptive procedure. Fig. 9a shows the quantity of interest  $Q$  versus the adaptive step for different methods, giving a comparison with the reference solution, which is computed with the fine mesh shown in Fig. 3c and the maximal reached hierarchical order  $n_e = \text{const.} = 9$ .

In Fig. 9b, a normalized measure representing the global error  $E$  is defined as

$$\hat{E} := \left| \frac{Q_{ref} - Q_{FEM}}{Q_{ref}} \right|, \quad (77)$$

where  $Q_{ref}$  represents the reference value shown in Fig. 9a. Note that  $\hat{E}$  is still an estimate, since  $Q_{ref}$  is not exact. Although differences between different methods are visible in the intermediate steps in Fig. 9b, the global error represented by  $\hat{E}$  is strongly reduced by all methods, showing a satisfactory convergence behavior of the adaptive procedure. For a comparison with the reference error measure  $\hat{E}$ , the estimated global error  $\tilde{E}$  defined in Eq. (75c) is plotted in a normalized manner in Fig. 9c. For all methods, the global error  $E$  in Eq. (58) is significantly underestimated, especially for the previous steps. However, this underestimate effect is quite reasonable, and we will list the possible reasons in the final section. In Fig. 9c, a full comparability is only given for the initial step, where both the same mesh and the same model distribution are adopted for all methods. In order to obtain a full comparability throughout the adaptive steps, we have done an additional computation, where the total errors are estimated by different methods on the same sequence of refined meshes obtained from the full computation approach. In Fig. 9d, the estimated errors  $\tilde{E}$  are compared with the reference error  $\hat{E}$ . Taking the deviations from the reference as a criterion, we may make a descending order according to the accuracy as follows: 1. full computation (a) (reference), 2. decoupled computation (b), 3. patch recovery (e) and 4. local recoveries (c) and (d).

Finally, Fig. 10 gives a comparison of the primal solution  $\bar{\sigma}_{11}$  and the dual solution  $\bar{z}_1$  for the final step, where  $\bar{z}_1$  represents the first component of  $\bar{\mathbf{z}}_h$  computed from (61). The reference solution is computed with the fine mesh shown in Fig. 3c and the uniform model distribution  $n_e = const. = 9$ . All methods render a satisfactory result, which is fairly close to the reference one, especially for the local domain  $\bar{\Omega}$  involved in the quantity of interest  $Q$ .

#### 4.4 Goal-oriented adaptivity for a functionally graded composite

In this section, we consider a functionally graded composite, whose volume fraction of fibers  $c_f$  depends on macro coordinates  $\mathbf{x} = [x_1 \ x_2]$  and is known as

$$c_f = c_f(\mathbf{x}) = 0.5 - 3 \cdot 10^{-4} \text{mm}^{-2} \cdot x_1^2 - 2 \cdot 10^{-4} \text{mm}^{-2} \cdot x_2^2, \quad (78)$$

resulting into a macroscopically heterogeneous distribution shown in Fig. 11. Here,  $c_f$  varies spatially from 1.7% to 49.5%. The same material parameters given in Section 4.1 are used. Since  $c_f$  varies within each single element, a three integration point version of quadrature is adopted to evaluate the element integrals in our FE implementation. At each integration point, the effective elasticity tensor is individually computed according to the actual fiber volume fraction given by (78).

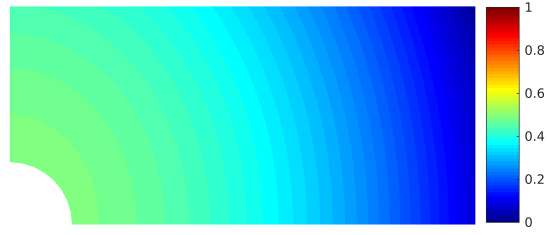


Figure 11: Functionally graded composite - Illustration of the heterogeneous distribution of the fiber volume fraction  $c_f$

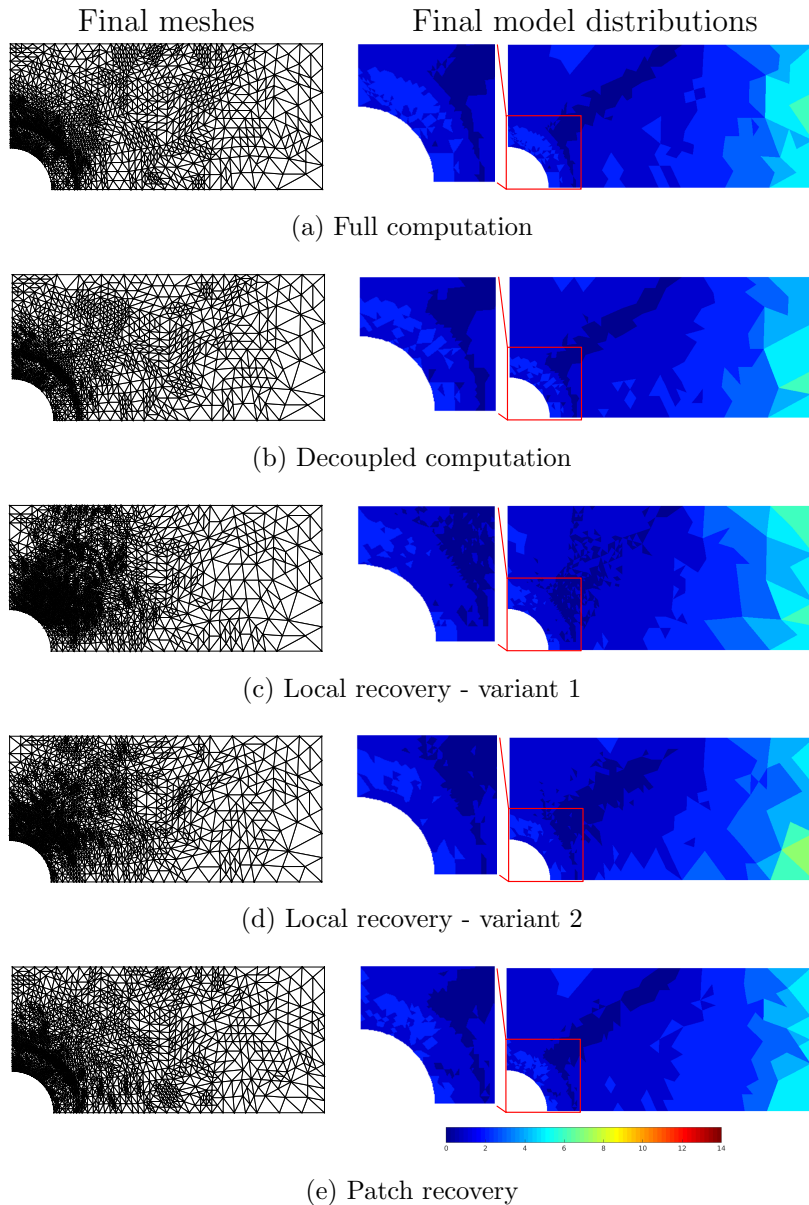
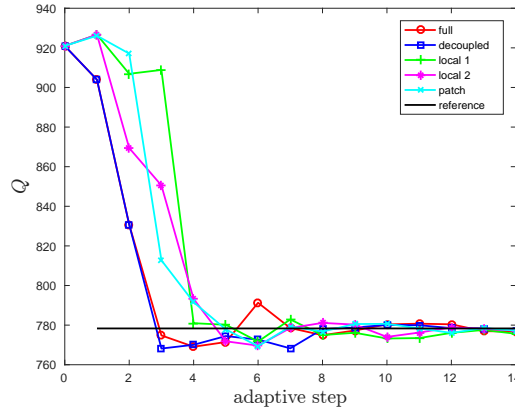


Figure 12: Functionally graded composite - Comparison of final adaptive results

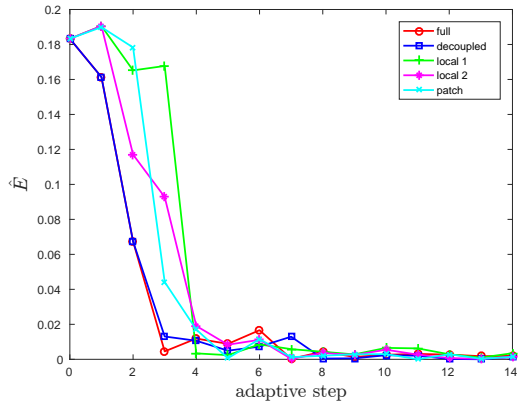
The adaptive computations with the same parameterization as Section 4.3 are done. Fig. 12 shows the final adaptive results by different methods after 14 adaptive

steps, supporting the same statements as Section 4.3. Amongst the three recovery methods (c), (d) and (e), patch recovery provides an adaptive mesh that is closest to the reference mesh obtained from full computation, where adaptive refinements are mainly concentrated in the local domain  $\bar{\Omega}'$ , especially in its boundary regions. The decoupled computation approach performs also well. Concerning model distributions, the local recovery method (d) achieves the highest hierarchical order (8). As a coupling effect with the adaptive mesh refinement, for all methods, the highest hierarchical orders are located on the right side of the sheet, where coarsest discretizations are adopted.

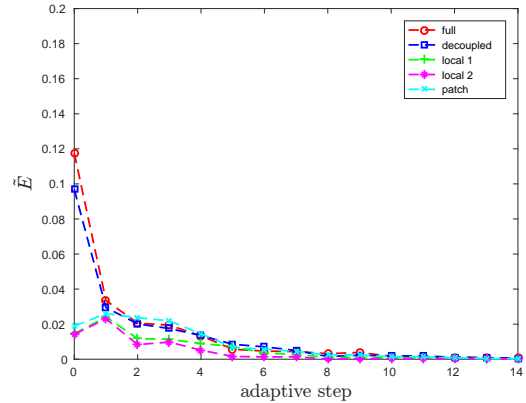
In Fig. 13, we consider the quantity of interest  $Q$ , the actual and the estimated global errors ( $\hat{E}$  and  $\tilde{E}$ ), where we make use of a reference solution computed with the fine mesh shown in Fig. 3c and the uniform model distribution  $n_e = \text{const.} = 9$ . A satisfactory convergence behavior for all methods can be observed in Fig. 13b, although the three recovery methods converge somewhat slower than the full and decoupled computation. By a comparison of the estimated error  $\tilde{E}$  in Fig. 13c with  $\hat{E}$  in Fig. 13b, the performance of the full and decoupled computation is striking. Amongst recovery methods (c), (d) and (e), patch recovery (e) shows an improved accuracy on error estimate.



(a) Quantity of interest  $Q$



(b) Error measure  $\hat{E}$  of  $Q$



(c) Estimated error  $\tilde{E}$  of  $Q$  (normalized)

Figure 13: Functionally graded composite - Comparison of the quantity of interest  $Q$

## 4.5 Goal-oriented adaptivity for a macroscopically random composite

In this section, we handle a macroscopically random composite, which may result from inaccuracies and uncertainties of the production process. While the same material parameters given in Section 4.1 are used, the fiber volume fraction  $c_f$  is randomly distributed on the macro domain  $\bar{\Omega}$ . The distribution of the fiber volume fraction is assumed to satisfy some statistical properties like the statistical mean  $\langle c_f \rangle_{\Xi} = 25\%$  and the standard deviation  $\text{dev}(c_f) = 5 \cdot 10^{-3}$ . For simplicity, we consider here only one of the possible realizations. In doing so, we choose 1124 sampling points, which are, as illustrated in Fig. 14, uniformly located on the macro domain  $\bar{\Omega}$ . Then, by means of a random number generator we generate 1124 different values of  $c_f$  satisfying the given statistical information, where each value is assigned to a corresponding sampling point, see Fig. 14 for a result. Moreover,  $c_f$  varies randomly from 23.4% to 26.8%. Note that this sampling procedure is done once for all the following FE computations and serves as a basis for determining  $c_f(e)$  for each element  $e$ . In our numerical implementation, if the element  $e$  contains at least one of those sampling points, the element volume fraction  $c_f(e)$  is set to be the arithmetic mean of all the involved sampling point(s). For the case that the element  $e$  does not contain any sampling points, the element volume fraction  $c_f(e)$  is set to be the value of the sampling point at a nearest distance from the element.

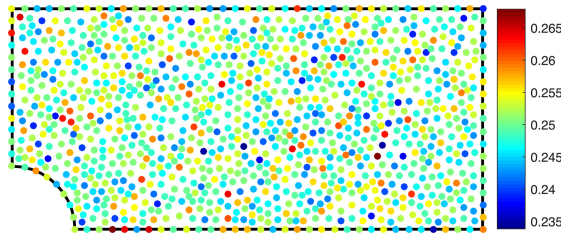


Figure 14: Macroscopically random composite - Illustration of the heterogeneous distribution of the fiber volume fraction  $c_f$  on chosen sampling points

The adaptive computations with the same parameterization as the previous sections 4.3 and 4.4 are done. The final adaptive results by different methods after 14 adaptive steps are summarized in Fig. 15, supporting the same statements as in the sections 4.3 and 4.4. The main difference is that the achieved highest hierarchical order (5) is relatively low in comparison with the previous examples in sections 4.3 and 4.4. This might be due to the fact that the element volume fraction distributions based on the statistical sampling shown in Fig. 14 largely changes in the course of the adaptive refinement, thus increasing the change of the regions with the peak values of the local indicators  $|\eta_m^e|$ .

Finally, we investigate the quantity of interest  $Q$ , the actual and the estimated global errors ( $\hat{E}$  and  $\tilde{E}$ ) in Fig. 16, where we make use of a reference solution computed with the fine mesh shown in Fig. 3c and the uniform model distribution  $n_e = \text{const.} = 9$ . Similarly to sections 4.3 and 4.4, Fig. 13b shows a satisfactory convergence behavior of all methods. By a comparison of the estimated error  $\tilde{E}$  in Fig. 16c with  $\hat{E}$  in Fig. 16b, patch recovery provides an improved accuracy on error

estimate, amongst all the considered recovery methods.

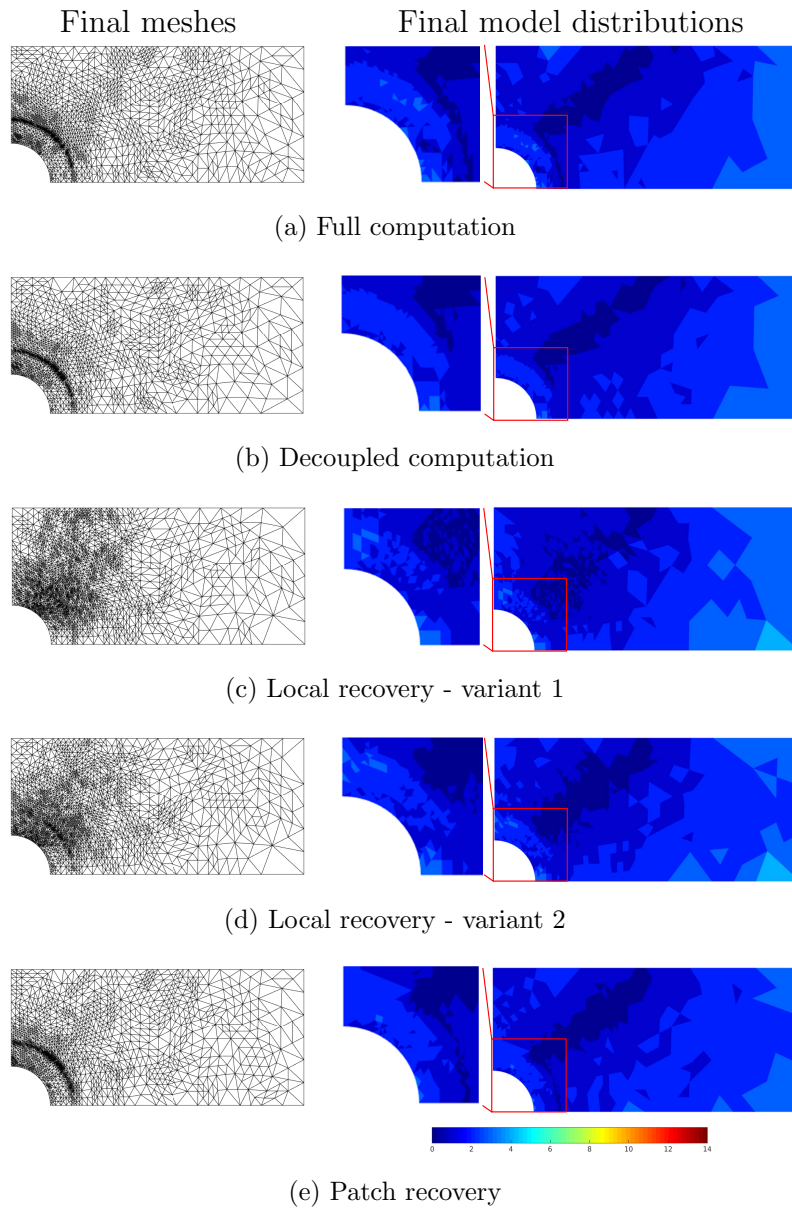
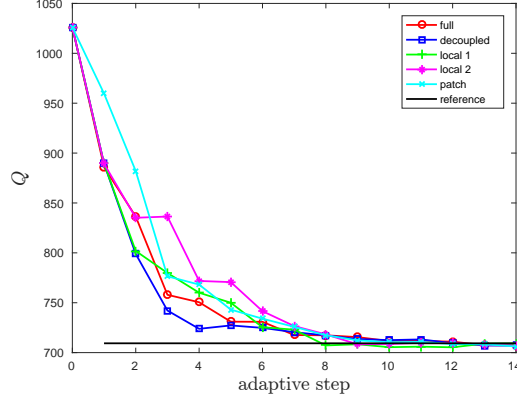
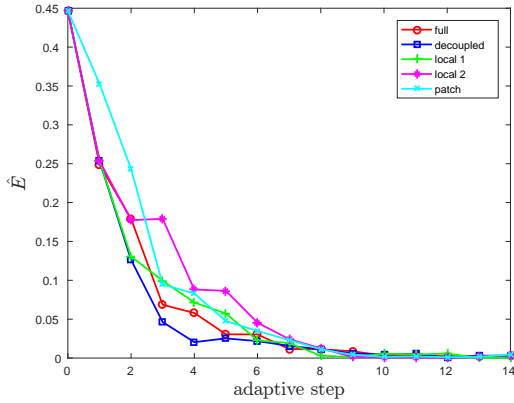


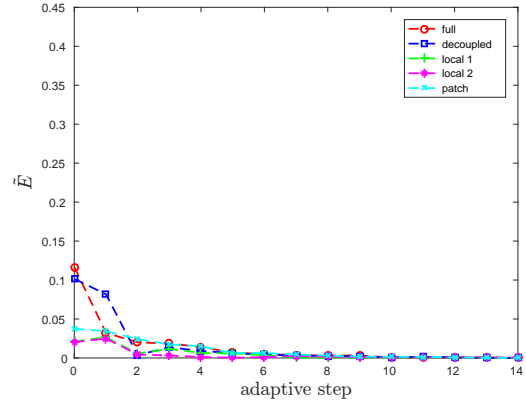
Figure 15: Macroscopically random composite - Comparison of final adaptive results



(a) Quantity of interest  $Q$



(b) Error measure  $\hat{E}$  of  $Q$



(c) Estimated error  $\tilde{E}$  of  $Q$  (normalized)

Figure 16: Macroscopically random composite - Comparison of the quantity of interest  $Q$

## 5 Conclusion and outlook

In this work, the well established model adaptivity has been applied to a class of homogenization problems for linear elastic materials. Analytical methods, as an important class of homogenization methods, have been considered. Meeting the requirement of model adaptivity with convergence properties, we chose the classical bounding theory. As an efficient solver of the terms in the Neumann series for higher order bounds, the classical singular approximation is made. The convergence of these bounds has been checked by a comparison with a reference solution. It is also found that a (slight) overlap effect, as a deficiency, may occur, since the singular approximation may violate the compatibility condition for the minimum energy principle. As a remedy, we proposed a simple correction in this work. However, the development of a better approximation method avoiding this overlap effect is not an objective of this work, hence, still remains for future work. Based on the results of the bounding theory, we have then shown how a model hierarchy is established.

Furthermore, the model adaptivity has been coupled to the well established adaptive FEM, such that the macro discretization errors are additionally controlled. An efficient goal-oriented a posteriori error estimator based on duality techniques,

driving the adaptive procedure, has been derived. For efficient computation of the enhanced dual solution, a patch-based recovery technique has been tailored for the present case, where a detailed comparison with other existing methods has also been given. According to the numerical results, the effectivity of the proposed recovery technique has been confirmed. Among these considered recovery techniques, we prefer the most recent patch-based recovery technique. However, it is still difficult to decide on the most reliable technique, hence, further investigations are required. By comparison with a reference solution, a good convergence behavior of the proposed adaptive procedure, using all the considered methods for the enhanced dual solution, has been observed. Nevertheless, we summarize possible reasons for the underestimate effect w.r.t. the global error as follows:

- linearization of the exact dual problem in (60) or (64)
- discretization of the linearized dual problem in Section 3.3
- replacement of the exact model by a fine model in (59)
- the fact that the local domain involved in the quantity of interest is rather crudely reproduced in the previous steps.

Obviously, our work is still in the initial stage. The work [25] sheds some light on numerical evaluation of bounds of effective elastic properties for a high level of accuracy, which is of our great interest. Moreover, in order to arrive at an accurate fine-scale solution, we will make use of certain numerical methods, e.g. FEM- or FFT-based methods. Based on straightforward extensions of the present work, we will also consider nonlinear homogenization problems, taking large deformations or plasticity into account and including the aspects of model adaptivity for reduced order homogenization schemes.

## Acknowledgment

This paper is based on investigations supported by the Deutsche Forschungsgemeinschaft (DFG) under grant MA 1979/30-1.

## References

- [1] Ainsworth M, Oden JT (2000) A posteriori error estimation in finite analysis. Pure and applied mathematics, John Wiley & Sons, New York
- [2] Babuska I, Whiteman J, Strouboulis T (2011) Finite Elements: An Introduction to the Methods and Error Estimation. Oxford University Press, New York
- [3] Becker R, Rannacher R (1996) A Feed-back approach to error control in finite element methods: basic analysis and examples. East-West Journal of Numerical Mathematics 4(4):237–264

- [4] Beran M, McCoy J (1970) Mean field variations in a statistical sample of heterogeneous linearly elastic solids. *Int J Solids Struct* 6 (8):1035–1054
- [5] Berveiller M, Zaoui A (1978) An extension of the self-consistent scheme to plastically-flowing polycrystals. *J Mech Phys Solids* 26:325–344
- [6] Böhlke T, Jöchen K, Langhoff TA (2008) Homogenization of linear elastic properties of silicon nitride. *Proc Appl Math Mech* 8:10,535–10,536
- [7] Braack M, Ern A (2003) A posteriori control of modeling errors and discretization errors. *Multiscale Model Simul* 1(2):221–238
- [8] Cirak F, Ramm E (1998) A posteriori error estimation and adaptivity for linear elasticity using the reciprocal theorem. *Comput Methods Appl Mech Engrg* 156:351–362
- [9] Dederichs PH, Zeller R (1973) Variational treatment of the elastic constants of disordered materials. *Zeitschrift für Physik* 259(2):103–116
- [10] Du DX, Zheng QS (2002) A further exploration on the effective self-consistent scheme and IDD estimate for the effective properties of multiphase composites which accounts for inclusion distribution. *Acta Mech*
- [11] Dvorak GJ, Benveniste Y (1992) On transformation strains and uniform fields in multiphase elastic media. *Proc R Soc A* 437:291–310
- [12] Eriksson K, Estep D, Hansbo P, Johnson C (1995) Introduction to Adaptive Methods for Differential Equations. *Acta Numerica* 4:150–158
- [13] Eshelby JD (1957) The determination of the elastic field of an ellipsoidal inclusion, and related problems. *Proc R Soc A* 241:376–396
- [14] Fish J (2013) Practical multiscale. John Wiley & Sons, The Atrium
- [15] Fokin AG (1972) Solution of statistical problems in elasticity theory in the singular approximation. *J Appl Mech Tech Phys* 13:85–89
- [16] Fokin AG (1973) Singular approximation for the calculation of the elastic properties of reinforced systems. *Mech Compos Mater* 9 (3):445–449
- [17] Ghosh S, Lee K, Moorthy S (1996) Two scale analysis of heterogeneous elastic–plastic materials with asymptotic homogenization and Voronoi cell finite element model. *Comput Methods Appl Mech Eng* 132:63–116
- [18] Hill R (1952) The elastic behaviour of a crystalline aggregate. *Proceedings of the Physical Society Section A* 65(5):349
- [19] Hill R (1963) Elastic properties of reinforced solids: some theoretical principles. *Journal of the mechanics and physics of solids* 11:357–372
- [20] Hornung U (1996) Homogenization and porous media. Springer, New York

- [21] Jöchen K (2013) Homogenization of the linear and non-linear mechanical behavior of polycrystals. PhD thesis, Karlsruher Institut für Technologie
- [22] Ju X, Mahnken R (2016) An NTFA-based homogenization framework considering softening effects. *Mechanics of Materials* 96:106–125
- [23] Ju X, Mahnken R (2016) Two accuracy improvements on nonuniform transformation field analysis for plasticity coupled to softening. *Proceedings in Applied Mathematics and Mechanics* 16:527–528
- [24] Ju X, Mahnken R (2017) Goal-oriented adaptivity for linear elastic micromorphic continua based on primal and adjoint consistency analysis. *International Journal for Numerical Methods in Engineering*, accepted
- [25] Kabel M, Andrä H (2013) Fast numerical computation of precise bounds of effective elastic moduli. Report of the Fraunhofer ITWM 224
- [26] Kröner E (1958) Berechnung der elastischen Konstanten des Vielkristalls aus den Konstanten des Einkristalls. *Z Phys* 151:504–518
- [27] Kröner E (1972) *Statistical continuum mechanics*. 92, Springer, Wien
- [28] Kröner E (1977) Bounds for effective elastic moduli of disordered materials. *J Mech Phys Solids* 25:137–155
- [29] Ladevèze P, Pelle J (2005) *Mastering calculations in linear and non linear mechanics*. Mechanical Engineering Series, Springer, New York
- [30] Lagoudas DC, Gavazzi AC, Nigam H (1991) Elastoplastic behavior of metal matrix composites based on incremental plasticity and the Mori–Tanaka averaging scheme. *Comput Mech* 8:193–203
- [31] Lahellec N, Suquet P (2007) On the effective behavior of nonlinear inelastic, composites: I. Incremental variational principles. *Journal of the Mechanics and Physics of Solids* 55:1932–1963
- [32] Lahellec N, Suquet P (2007) On the effective behavior of nonlinear inelastic, composites: II. A second-order procedure. *Journal of the Mechanics and Physics of Solids* 55:1964–1992
- [33] Larsson F, Runesson K (2004) Modeling and discretization errors in hyperelasto-(visco-)plasticity with a view to hierarchical modeling. *Comput Methods Appl Mech Engrg* 193:5283–5300
- [34] Larsson F, Runesson K (2006) Adaptive computational meso-macro-scale modeling of elastic composites. *Comput Methods Appl Mech Engrg* 195:324–338
- [35] Larsson F, Runesson K (2007) RVE computation with error control and adaptivity: the power of duality. *Comp Meths* 39:647–661

- [36] Larsson F, Hansbo P, Runesson K (2002) Strategies for computing goal-oriented a posteriori error measures in non-linear elasticity. *Int J Numer Mech Engng* 55:879–894
- [37] Mahnken R (2013) Goal-oriented adaptive refinement for phase field modeling with finite elements. *International Journal for Numerical Methods in Engineering* 94(4):418–440
- [38] Maier M (2015) Duality-based adaptivity of model and discretization in multi-scale finite-element methods. PhD thesis, Ruprecht Karl University of Heidelberg
- [39] Michel J, Suquet P (2003) Nonuniform transformation field analysis. *International Journal for Solids and Structures* 40:6937–6955
- [40] Miehe C, Schröder J, Schotte J (1999) Computational homogenization analysis in finite plasticity. Simulation of texture development in polycrystalline materials. *Comput Methods Appl Mech Eng* 171:387–418
- [41] Mori T, Tanaka K (1973) Average stress in matrix and average elastic energy of materials with misfitting inclusions. *Acta Metall* 21:571–574
- [42] Müller V, Kabel M, Andrä H, Böhlke T (2015) Homogenization of linear elastic properties of short-fiber reinforced composites—a comparison of mean field and voxel-based methods. *International Journal of Solids and Structures* 67:56–70
- [43] Mura T (1987) *Micromechanics of defects in solids*. Martinus Nijhoff Publishers, The Hague
- [44] Oden JT, Prudhomme S (2002) Estimation of Modeling Error in Computational Mechanics. *Journal of Computational Physics* 182:496–515
- [45] Oden JT, Vemaganti KS (2000) Estimation of local modeling error and goal-oriented adaptive modeling of heterogeneous materials; Part I: Error Estimates and Adaptive Algorithms. *Journal of Computational Physics* 164:22–47
- [46] Oden JT, Prudhomme S, Hammerand D, Kuczma M (2001) Modeling error and adaptivity in nonlinear continuum mechanics. *Comput Methods Appl Mech Eng* 190:6663–6684
- [47] Oden JT, Prudhomme S, Romkes A, Bauman P (2006) Multiscale modelling of physical phenomena: adaptive control of models. *SAIM J SCI Comput* 28:2359–2389
- [48] Paraschivoiu M, Peraire J, Patera A (1997) A posteriori finite element bounds for linear-functional outputs of elliptic partial differential equations. *Comput Methods Appl Mech Engrg* 150(1):289–312, DOI 10.1016/S0045-7825(97)00086-8

- [49] Ponte-Castañeda P (2012) A finite-strain constitutive theory for electro-active polymer composites via homogenization. *International Journal of Non-Linear Mechanics* 47(2):293–306
- [50] Ponte Castañeda P, Suquet P (1998) Nonlinear composites. *Advances in Applied Mechanics* 34:171–302
- [51] Prudhomme S, Oden JT (1999) On goal-oriented error estimation for elliptic problems: application to the control of pointwise errors. *Comput Methods Appl Mech Engrg* 176(1–4):313–331, DOI 10.1016/S0045-7825(98)00343-0
- [52] Qu J, Cherkaoui M (2006) *Fundamentals of Micromechanics of Solids*. Wiley, Hoboken, New Jersey
- [53] Rüter M (2003) *Error-controlled Adaptive Finite Element Methods in Large Strain Hyperelasticity and Fracture Mechanics*. PhD thesis, University of Hannover, Hannover
- [54] Schmich M, Vexler B (2008) Adaptivity with dynamic meshes for space-time finite element discretizations of parabolic equations. *SIAM J Sci Comput* 30(1):369–393
- [55] Stein E (ed) (2003) *Error-controlled Adaptive Finite Elements in Solid Mechanics*. Wiley, Chichester
- [56] Stein E, Ohnibus S, Rüter M (2001) Hierarchical model-and discretization-error estimation of elasto-plastic structures. In: *Mechanics for a New Millennium*, Kluwer Academic Publishers, Netherlands, pp 373–388
- [57] Vemaganti KS, Oden JT (2001) Estimation of local modeling error and goal-oriented adaptive modeling of heterogeneous materials; Part II: a computational environment for adaptive modeling of heterogeneous elastic solids. *Comput Methods Appl Mech Engrg* 190:6089–6124
- [58] Verfürth R (1996) *A Review of A Posteriori Error Estimation and Adaptive Mesh-Refinement Techniques*. Wiley-Teubner, Stuttgart
- [59] Widany KU, Mahnken R (2012) Adaptivity for parameter identification of incompressible hyperelastic materials using stabilized tetrahedral elements. *Comput Methods Appl Mech Engrg* 245-246:117–131
- [60] Widany KU, Mahnken R (2016) Dual-based adaptive FEM for inelastic problems with standard FE implementations. *Int J Numer Meth Engng* 107:127–154
- [61] Willis JR (1977) Bounds and self-consistent estimates for the overall properties of anisotropic composites. *Journal of the Mechanics and Physics of Solids* 25(3):185–202
- [62] Yvonnet J, He QC (2007) The reduced model multiscale method (R3M) for the non-linear homogenization of hyperelastic media at finite strains. *Journal of Computational Physics* 223:341–368

- [63] Zeller R, Dederichs P (1973) Elastic constants of polycrystals. *phys stat sol (b)* 55:831–842
- [64] Zienkiewicz O, Zhu J (1992) Superconvergent patch recovery and a posteriori error estimates. Part 1: the recovery technique. *Int J Num Meth Eng* 33(7):1331–1364
- [65] Zohdi TI, Wriggers P (2008) *Introduction to computational micromechanics*. Springer, Berlin
- [66] Zohdi TI, Oden JT, Rodin GJ (1996) Hierarchical modeling of heterogeneous bodies. *Comput Methods Appl Mech Eng* 138:273–298



---

## **Paper B**

Rolf Mahnken and Xiaozhe Ju

*Goal-oriented adaptivity based on a model hierarchy of mean-field and full-field  
homogenization methods in linear elasticity*

submitted

---



# Goal-oriented adaptivity based on a model hierarchy of mean-field and full-field homogenization methods in linear elasticity

Rolf Mahnken and Xiaozhe Ju

Chair of Engineering Mechanics, University of Paderborn,  
Warburger Str. 100, 33098 Paderborn, Germany

## Abstract

Homogenization methods are drawing increasing attention for simulation of heterogeneous materials like composites. For balancing the accuracy and the numerical efficiency of such strategies, we deal with both model and discretization errors of the finite element method (FEM) on a macro scale. Within a framework of goal-oriented adaptivity, we consider linear elastic heterogeneous materials, for which first order homogenization schemes apply. A novel model hierarchy is proposed based on mean-field and full-field homogenization methods. For the former we consider several well-established schemes like Mori-Tanaka or self-consistent as basic models, and for the latter, as superior models, unit cell problems are solved via the FEM under an a priori chosen boundary condition. For a further stage of the model hierarchy, we consider hierarchical unit cells within the frame of the FEM towards an adaptive selection of the unit cell size. By means of several numerical examples, we illustrate the effectiveness of the proposed adaptive approach.

**Keywords:** model adaptivity, unit cell size, mean-field methods, full-field methods, adaptive finite element method, goal-oriented error estimate

## 1 Introduction

Many engineering materials like steel, alloy and composites are heterogeneous, when viewed on a certain (for instance micro) scale. On that scale, several constituents of different material properties can be distinguished. Under the premise that the individual material properties as well as the distribution of the different constituents are known, homogenization methods provide a powerful tool to predict their overall behavior, which is often of engineering interest. Another advantage of homogenization methods is their potential on optimum material design by avoiding high experimental cost. For a comprehensive overview, the interested reader is referred to [15, 65, 55, 20]. In this work, we limit our attention to methods assuming a clear

scale separation, that is, the characteristic length of the subscale is much smaller than that of the macro scale. Otherwise, one has to resort to certain higher order homogenization schemes, see e.g. [17, 16, 18]. Within the framework of first order homogenization, we distinguish two main groups of homogenization methods:

- Mean-field methods: They are established on the basis of the Eshelby solution [13] to an ellipsoidal inclusion embedded in an infinite matrix, see e.g. Mori-Tanaka [41], self-consistent [27] and interaction direct derivative [10], and also find applications to nonlinear materials, see e.g. [27, 30, 4]. By means of analytical solutions, this kind of methods is most efficient. As a drawback, they are not able to account for complex microstructures and some fine effects like unit cell size or periodic boundary conditions. As an important feature, they resolve the microscopic fields only to their means over the individual material phases.
- Full-field methods: They achieve a much higher resolution of the microscopic fields than the mean-field methods. A most straightforward way is to adopt computational methods at the expense of a large computational cost, see e.g. [14, 65] for the FE<sup>2</sup> method and [42, 39] for fast fourier transformation (FFT) based methods. For a numerical efficiency, model order reduction methods focus on an effective reduction of the number the degrees of freedom, see e.g. the transformation field analysis (TFA) [11], its nonuniform extension (NTFA) [38] and proper orthogonal decomposition (POD) [63].

It is also worth mentioning another kind of homogenization methods, which relies on variational principles and provides a powerful tool to derive bounds of effective properties, see e.g. [8, 28] for linear elasticity. For nonlinear cases, the concept of *linear comparison material* is introduced, such that classical bounds or estimates of linear materials can be used to derive those of the nonlinear one, see e.g. [52, 53, 31, 32]. Depending on what microscopic resolution they achieve, they also may fall into one of the above two categories.

Furthermore, the influence of different micro boundary conditions on the effective properties are examined e.g. in [21, 22, 50]. The Dirichlet type and the Neumann type boundary condition are shown to provide the upper and the lower bounds, respectively. The periodic boundary condition usually shows the fastest convergence behavior, when the size of the chosen *unit cell* is enlarged, see e.g. [48, 26]. In this context, we refer to a *unit cell* as an arbitrary sample of microstructure, which does not necessarily meet the requirements of a representative volume element (RVE) according to Hill [19]:

- An RVE is entirely typical of the whole mixture on average.
- An RVE contains a sufficient number of inclusions for the *apparent* effective properties to be independent of the surface values of traction and displacement.

The apparent effective properties refer to those provided by a unit cell. For a unit cell to be an RVE, its size should be sufficiently large. The issue of a minimum RVE size is addressed e.g. in [9].

To address the issue of model validation, the notion of model adaptivity has been well established, see e.g. [66, 45, 60, 59, 44, 46, 47, 5, 33, 34] for both linear and nonlinear problems. It aims at an adaptive model selection to efficiently achieve a preset level of accuracy, for which an assessment of model error is required. In this context, a model hierarchy, consisting of a series of mathematical models, from the simplest to the most complex (state-of-the-art) model with an ascending hierarchical order, plays a central role. A model, which is of a higher hierarchical order than the current one, can be used for both, error estimate and a possible model refinement. If the error estimate is directed to a user-defined *quantity of interest*, the resulted adaptivity is called *goal-oriented* adaptivity, see e.g. [3, 49, 7, 54]. For applications to multiscale problems, we refer to [45, 60, 47, 37, 34, 35].

The issue of numerical verification is addressed by the adaptive FEM, which is developed to estimate and adaptively control the discretization error, see e.g. [12, 61, 1, 29, 2, 58] for the general framework of a posteriori error estimate and [3, 49, 7, 54, 36, 24] for goal-oriented error estimate.

In our recent work [25], a general coupled framework of model adaptivity and adaptive FEM was developed for linear elastic heterogeneous materials. For a model hierarchy, a bounding theory according to [8, 28] was used. On this basis, in this work, we intend to establish a single model hierarchy, which consistently addresses the following issues:

- For an adaptive approach to start, a basic model is required, which should be computationally efficient with an improvement potential. Meeting this requirement, several well-established mean-field methods are considered. For an accuracy improvement, they are replaced by a full-field approximation, where a unit cell problem is solved via the FEM under an appropriate boundary condition. To avoid the need of computational methods for error estimation of the basic model, hierarchical models, as an intermediate stage of the model hierarchy, are established within the frame of mean-field methods using a priori knowledge.
- Since an arbitrary choice of a unit cell does not necessarily meet the requirements of an RVE, it should have a sufficient size for a pursued accuracy level. As a larger unit cell gives rise to increasing computational cost in view of the FEM, adaptive selection of unit cell size is crucial for a numerical efficiency. This is achieved by integrating the unit cell size into the model hierarchy. For a fast convergence behavior with respect to the unit cell size, different micro boundary conditions are examined. One of them is selected prior to the adaptive approach.

This paper is structured as follows: In Section 2, the general framework of a two-scale modeling is introduced including the aspects of scale separation, scale transition and related boundary conditions as well as a full-field formulation towards effective properties. An equivalent mean-field formulation to the full-field formulation is established at the beginning of Section 3. Subsequently, several well-established mean-field and FE-based full-field methods are revisited and interpreted as two different approximations of full-field formulations. Section 4 briefly reviews the coupled adaptive strategy developed in our previous work [25] for a structural

analysis. As a highlight, a novel model hierarchy is proposed for model adaptivity based on mean-field and full-field homogenization methods, including an additional aspect of hierarchical unit cells. Its generality is discussed in some detail. Several numerical experiments are presented in Section 5, while Section 6 gives a conclusion and an outlook on further research.

Notation: The scalar products of two vectors  $\mathbf{a}$  and  $\mathbf{b}$ , and two second-order tensors  $\mathbf{A}$  and  $\mathbf{B}$  are

$$\mathbf{a} \cdot \mathbf{b} = a_i b_i, \quad \mathbf{A} : \mathbf{B} = A_{ij} B_{ij}, \quad (1)$$

respectively, using the Einstein summation convention for repeated indices. The gradient operator  $\nabla$  is introduced as

$$\nabla \mathbf{c} := \mathbf{c} \otimes \nabla = c_{i,j} \mathbf{e}_i \otimes \mathbf{e}_j, \quad \text{with } c_{i,j} = \frac{\partial c_i}{\partial X_j}, \quad (2)$$

where  $\mathbf{e}_i$ ,  $i = 1, 2, 3$  is a Cartesian orthonormal basis and  $X_i$  are coordinates of the reference position  $\mathbf{X}$ . The divergence operator  $\text{Div}(\bullet)$  is defined as

$$\text{Div}(\boldsymbol{\sigma}) := \boldsymbol{\sigma} \cdot \nabla = \sigma_{ij,j} \mathbf{e}_i, \quad \text{with } \sigma_{ij,j} = \frac{\partial \sigma_{ij}}{\partial X_j}. \quad (3)$$

Additionally, the volume averaging operator on a domain  $\Omega$  is defined as

$$\langle \bullet \rangle = \frac{1}{\Omega} \int_{\Omega} \bullet dv. \quad (4)$$

Gâteaux differentiation of a linear form  $F$  and a bilinear form  $B$  w.r.t. the argument  $\mathbf{u}$  is denoted as

$$D_{\mathbf{u}} F(\mathbf{u}; \mathbf{v}) = \lim_{\theta \rightarrow 0} \frac{1}{\theta} [F(\mathbf{u} + \theta \mathbf{v}) - F(\mathbf{u})], \quad (5a)$$

$$D_{\mathbf{u}} B(\mathbf{u}; \mathbf{w}, \mathbf{v}) = \lim_{\theta \rightarrow 0} \frac{1}{\theta} [B(\mathbf{u} + \theta \mathbf{v}; \mathbf{w}) - B(\mathbf{u}; \mathbf{w})], \quad (5b)$$

respectively.

## 2 A full-field formulation for two-scale problems

### 2.1 Scale separation and transition

By means of the asymptotic homogenization theory [57, 15], we consider a two-scale mechanical problem of first order, making the assumption of scale separation, i.e.  $l/L \ll 1$ , as depicted in Fig. 1. To each material point of the macro domain  $\bar{\Omega}$  a micro domain  $\Omega$ , i.e. the RVE, is associated, where the subscripts 0 and  $t$  denote the reference and the current configuration, respectively.

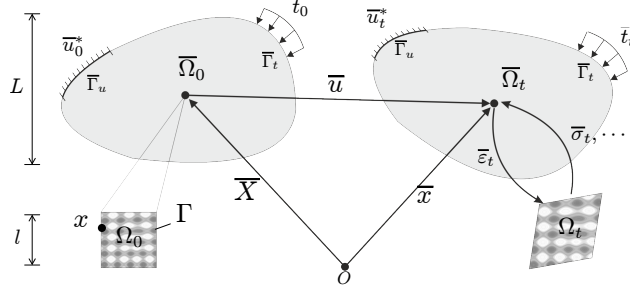


Figure 1: Illustration of a two-scale problem

Neglecting the difference between the reference and the current configuration, we assume a framework of small strains, with the macro displacement vector and the macro small strain tensor as

$$\bar{\mathbf{u}} = \bar{\mathbf{x}} - \bar{\mathbf{X}}, \quad (6a)$$

$$\bar{\boldsymbol{\varepsilon}} = \nabla^{\text{sym}} \bar{\mathbf{u}}, \quad (6b)$$

respectively. In Eq. (6a),  $\bar{\mathbf{X}}$  and  $\bar{\mathbf{x}}$  are the position vectors with respect to a reference point  $O$ , respectively in the reference and the current state. Moreover, the macroscopic equilibrium problem  $\bar{P}$  and the underlying microscopic equilibrium problem  $P$  read

$$\bar{P}: \begin{cases} \text{Div}(\bar{\boldsymbol{\sigma}}) + \bar{\mathbf{b}} = \mathbf{0}, & \text{in } \bar{\Omega} \\ \bar{\boldsymbol{\sigma}}\mathbf{N} = \bar{\mathbf{t}}, & \text{on } \bar{\Gamma}_t \\ \bar{\mathbf{u}} = \bar{\mathbf{u}}^*, & \text{on } \bar{\Gamma}_u \end{cases}, \quad (7a)$$

$$P: \begin{cases} \text{Div}(\boldsymbol{\sigma}) = \mathbf{0}, & \text{in } \Omega \\ + \text{ boundary conditions} \end{cases}, \quad (7b)$$

respectively. In problem  $\bar{P}$ ,  $\bar{\boldsymbol{\sigma}}$  denotes the macroscopic stress tensor and  $\bar{\mathbf{t}}$  represents the tractions imposed on  $\bar{\Gamma}_t$  satisfying the Neumann boundary condition. The body force is symbolized by  $\bar{\mathbf{b}}$ , while  $\bar{\mathbf{u}}^*$  indicates the prescribed displacements on the Dirichlet boundary  $\bar{\Gamma}_u$  with the properties  $\bar{\Gamma}_u \cup \bar{\Gamma}_t = \bar{\Gamma}$  and  $\bar{\Gamma}_u \cap \bar{\Gamma}_t = \emptyset$ , where  $\bar{\Gamma}$  symbolizes the total boundary for the macroscopic problem. To solve the macro problem  $\bar{P}$  with the FEM, let us establish its weak form:

$$\underbrace{\int_{\bar{\Omega}} \bar{\boldsymbol{\varepsilon}}[\delta\bar{\mathbf{u}}] : \bar{\boldsymbol{\sigma}}(\bar{\boldsymbol{\varepsilon}}[\bar{\mathbf{u}}]) dV}_{:=\bar{B}(\bar{\mathbf{u}}; \delta\bar{\mathbf{u}})} = \underbrace{\int_{\bar{\Omega}} \delta\bar{\mathbf{u}} \cdot \bar{\mathbf{b}} dv + \int_{\bar{\Gamma}_t} \delta\bar{\mathbf{u}} \cdot \bar{\mathbf{t}} dA}_{:=\bar{F}(\delta\bar{\mathbf{u}})}, \quad \forall \delta\bar{\mathbf{u}} \in \bar{\mathcal{V}}^0, \quad (8)$$

where  $\bar{\mathbf{u}}$  and  $\delta\bar{\mathbf{u}}$  are the macro displacement vector and its variation, respectively.  $\bar{\mathcal{V}}^0$  is an appropriate Sobolev space. For linear elasticity,  $\bar{B}(\cdot; \cdot)$  is a bilinear form, while  $\bar{F}(\cdot)$  is a linear form. We shall rewrite Eq. (8) in a residual form as

$$\bar{\varrho}(\bar{\mathbf{u}}; \delta\bar{\mathbf{u}}) := \bar{F}(\delta\bar{\mathbf{u}}) - \bar{B}(\bar{\mathbf{u}}; \delta\bar{\mathbf{u}}) = 0. \quad (9)$$

The micro problem  $P$  is completed with some proper boundary conditions. This will be separately discussed in Section 2.2. Moreover,  $\boldsymbol{\sigma}$  and  $\boldsymbol{\varepsilon}$  are, respectively,

the microscopic stress and the microscopic strain tensor, which are generally heterogeneously distributed within the RVE, while  $\bar{\boldsymbol{\varepsilon}}$  denotes the macroscopic strain tensor.

Additionally, the scale transition, which couples both problems  $\bar{P}$  and  $P$ , is established by

$$\bar{\boldsymbol{\varepsilon}} = \langle \boldsymbol{\varepsilon}(\mathbf{x}) \rangle, \quad (10a)$$

$$\bar{\boldsymbol{\sigma}} = \langle \boldsymbol{\sigma}(\mathbf{x}) \rangle, \quad (10b)$$

$$\langle \boldsymbol{\sigma} : \boldsymbol{\varepsilon} \rangle = \langle \boldsymbol{\sigma} \rangle : \langle \boldsymbol{\varepsilon} \rangle = \bar{\boldsymbol{\sigma}} : \bar{\boldsymbol{\varepsilon}}, \quad (10c)$$

where Eq. (10c) is nothing else but the well-established Hill-Mandel condition [19].

## 2.2 Micro boundary conditions

In this work, we consider the following three micro boundary conditions, which are consistent with the Hill-Mandel condition (10c).

1. *Linear displacement boundary condition:* As depicted in Fig. 2b, this Dirichlet type boundary condition takes the form

$$\mathbf{u}(\mathbf{x}) = \bar{\boldsymbol{\varepsilon}} \mathbf{x}, \quad \forall \mathbf{x} \in \Gamma. \quad (11)$$

2. *Constant traction boundary condition:* As shown in Fig. 2c, a Neumann type boundary condition is established by

$$\mathbf{t}(\mathbf{x}) = \bar{\boldsymbol{\sigma}} \mathbf{n}(\mathbf{x}), \quad \forall \mathbf{x} \in \Gamma, \quad (12)$$

where  $\mathbf{n}$  is the outward normal vector at the micro boundary point  $\mathbf{x} \in \Gamma$ .

3. *Periodic boundary condition:* As illustrated in Fig. 2d, while the entire boundary is decomposed into two parts  $\Gamma = \Gamma^+ \cup \Gamma^-$  with associated point pairs  $\mathbf{x}^+ \in \Gamma^+$  and  $\mathbf{x}^- \in \Gamma^-$ , we assume periodic displacements and antiperiodic tractions on  $\Gamma$  as

$$\mathbf{u}(\mathbf{x}^+) - \mathbf{u}(\mathbf{x}^-) = \bar{\boldsymbol{\varepsilon}} (\mathbf{x}^+ - \mathbf{x}^-), \quad (13a)$$

$$\mathbf{t}(\mathbf{x}^+) + \mathbf{t}(\mathbf{x}^-) = \mathbf{0}, \quad \forall \mathbf{x}^+ \in \Gamma^+, \mathbf{x}^- \in \Gamma^-, \quad (13b)$$

respectively. Eq. (13a) guarantees the kinematical conformity of the deformed boundary with neighboring RVEs, while the statical equilibrium is ensured by Eq. (13b).

An FE implementation of these boundary conditions will be discussed in some detail in Section 3.3.2.

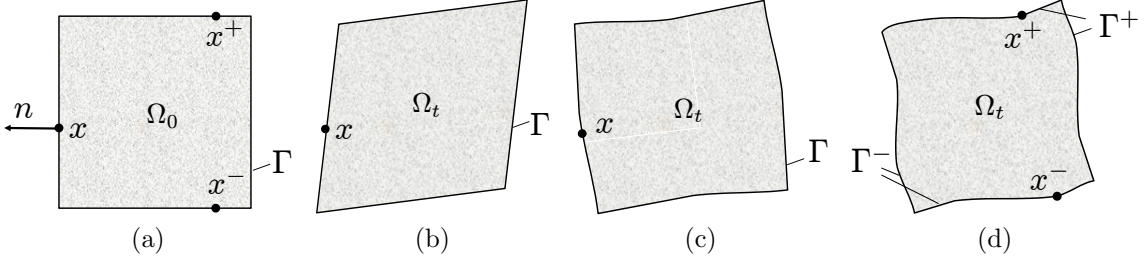


Figure 2: Illustration of different boundary conditions (b.c.): a) undeformed RVE, b) linear displacement b.c., c) constant traction b.c. and d) periodic b.c.

## 2.3 Full-field localization operators and effective properties

For linear elastic materials, the following two equivalent linear constitutive relations apply

$$\boldsymbol{\sigma}(\mathbf{x}) = \mathbb{C}(\mathbf{x})\boldsymbol{\varepsilon}(\mathbf{x}), \quad (14a)$$

$$\boldsymbol{\varepsilon}(\mathbf{x}) = \mathbb{S}(\mathbf{x})\boldsymbol{\sigma}(\mathbf{x}), \quad (14b)$$

with the micro elasticity tensor  $\mathbb{C}$  and the micro compliance tensor  $\mathbb{S} = \mathbb{C}^{-1}$ , respectively. A common approach towards a structural (macroscopic) analysis consists of two steps: 1. solve the micro problem (7b) and 2. perform the scale transition (10a) or (10b). For the first step, the micro problem (7b) can be defined either via a prescribed macro strain  $\bar{\boldsymbol{\varepsilon}}$  or via a prescribed macro stress  $\bar{\boldsymbol{\sigma}}$ . Accordingly, there exist linear localization operations

$$\boldsymbol{\varepsilon}(\mathbf{x}) = \mathbb{A}(\mathbf{x}) \bar{\boldsymbol{\varepsilon}}, \quad (15a)$$

$$\boldsymbol{\sigma}(\mathbf{x}) = \mathbb{B}(\mathbf{x}) \bar{\boldsymbol{\sigma}}, \quad (15b)$$

where  $\mathbb{A}$  and  $\mathbb{B}$  are referred to as the micro strain and the micro stress localization tensor, respectively. Moreover, inserting Eq. (15a) into Eq. (10a) renders the identity

$$\langle \mathbb{A}(\mathbf{x}) \rangle = \mathbb{I}^S, \quad (16)$$

where  $\mathbb{I}^S$  denotes the fourth-order symmetric identity tensor. Similarly, by inserting Eq. (15b) into Eq. (10b) we obtain

$$\langle \mathbb{B}(\mathbf{x}) \rangle = \mathbb{I}^S. \quad (17)$$

The equations (15a) and (15b) can be interpreted as formal solutions of the micro problem (7b).

For the second step, we combine the equations (15a), (14a) and (10b) and obtain

$$\bar{\boldsymbol{\sigma}} = \underbrace{\langle \mathbb{C}(\mathbf{x})\mathbb{A}(\mathbf{x}) \rangle}_{:=\bar{\mathbb{C}}} \bar{\boldsymbol{\varepsilon}}, \quad (18)$$

for a prescribed  $\bar{\boldsymbol{\varepsilon}}$ , where we refer to  $\bar{\mathbb{C}}$  as the effective elasticity tensor. If  $\bar{\boldsymbol{\sigma}}$  is prescribed, one may use Eq. (15b) in combination with the equations (14b) and (10a), and obtain

$$\bar{\boldsymbol{\varepsilon}} = \underbrace{\langle \mathbb{S}(\mathbf{x})\mathbb{B}(\mathbf{x}) \rangle}_{:=\bar{\mathbb{S}}} \bar{\boldsymbol{\sigma}}, \quad (19)$$

where  $\bar{\mathbb{S}}$  is nothing else but the effective compliance tensor.

### 3 Approximations of full-field formulations

The exact solution of the micro problem (7b), formally in Eq. (15a) or Eq. (15b), is generally intractable. In the following, we first show that the full-field formulation in Section 2.3 may equivalently reduce to a mean-field formulation, which forms a basis for the mean-field methods. Subsequently, well-established mean-field and full-field methods are revisited and interpreted as two different approximations of full-field formulations. As a full-field method, we adopt the FEM to achieve a full-field approximation.

#### 3.1 An equivalent mean-field formulation to full-field

In contrast to the full-field representations in Section 2.3, the mean-field methods resolve the relevant microscopic fields to their means over  $N$  individual material phases distinguished by a subscript  $r = 0, 1, \dots, N - 1$ . Correspondingly, the localization rules (15a) and (15b) reduce to

$$\boldsymbol{\varepsilon}_r = \mathbb{A}_r \bar{\boldsymbol{\varepsilon}}, \quad (20a)$$

$$\boldsymbol{\sigma}_r = \mathbb{B}_r \bar{\boldsymbol{\sigma}}, \quad (20b)$$

where  $\mathbb{A}_r$  and  $\mathbb{B}_r$  are the average strain and the average stress localization tensor, respectively, and

$$\boldsymbol{\varepsilon}_r = \langle \boldsymbol{\varepsilon} \rangle_{\Omega_r}, \quad (21a)$$

$$\boldsymbol{\sigma}_r = \langle \boldsymbol{\sigma} \rangle_{\Omega_r}, \quad (21b)$$

are the average strain and the average stress tensor over the local domain  $\Omega_r$  occupied by the  $r$ -th material phase, respectively. By inserting the equations (15a) and (20a) into Eq. (21a) and inserting the equations (15b) and (20b) into Eq. (21b) we obtain

$$\mathbb{A}_r = \langle \mathbb{A} \rangle_{\Omega_r}, \quad (22a)$$

$$\mathbb{B}_r = \langle \mathbb{B} \rangle_{\Omega_r}, \quad (22b)$$

respectively. The mean-field version of effective properties are obtained from the equations (18) and (19) as

$$\bar{\mathbb{C}} = \sum_{r=0}^{N-1} c_r \mathbb{C}_r \mathbb{A}_r, \quad (23a)$$

$$\bar{\mathbb{S}} = \sum_{r=0}^{N-1} c_r \mathbb{S}_r \mathbb{B}_r, \quad (23b)$$

respectively. Here,  $c_r$ ,  $\mathbb{C}_r$  and  $\mathbb{S}_r$  represent the volume fraction, the elasticity tensor and the compliance tensor of the phase  $r$ , respectively. Correspondingly, the equations (16) and (17) become

$$\sum_{r=0}^{N-1} c_r \mathbb{A}_r = \mathbb{I}^S, \quad (24a)$$

$$\sum_{r=0}^{N-1} c_r \mathbb{B}_r = \mathbb{I}^S, \quad (24b)$$

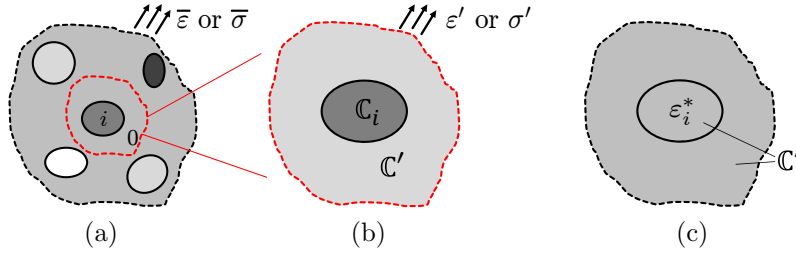


Figure 3: Basic concepts of mean-field methods: a) actual composite problem, b) single inclusion problem and c) Eshelby's problem

respectively.

In the following subsections, we will consider some composite materials of matrix-inclusion type as shown in Fig. 3a. For our convenience, a subscript 0 is assigned to the matrix material, while the subscript  $i = 1, \dots, N_i$  denotes the  $i$ -th inclusion. Consequently, we have  $r = [0, i]$  and  $N_i = N - 1$ . In combination with the equations (24a) and (24b), the equations (23a) and (23b) become

$$\bar{\mathbb{C}} = \mathbb{C}_0 + \sum_{i=1}^{N_i} c_i (\mathbb{C}_i - \mathbb{C}_0) \mathbb{A}_i, \quad (25a)$$

$$\bar{\mathbb{S}} = \mathbb{S}_0 + \sum_{i=1}^{N_i} c_i (\mathbb{S}_i - \mathbb{S}_0) \mathbb{B}_i, \quad (25b)$$

respectively.

**Remark 1.** The above mean-field representations are equivalent to the full-field ones in Section 2.3 in the sense of determining effective properties. For its formulations, no approximations have been made.

## 3.2 Mean-field approximations of full-field formulations

The mean-field methods are fundamental in micromechanics [43, 55, 20]. In this section, we review some well-established mean-field methods based on the mean-field formulation in Section 3.1. It is obvious from the equations (25a) and (25b) that the effective properties  $\bar{\mathbb{C}}$  or  $\bar{\mathbb{S}}$  require the knowledge about the localization tensors  $\mathbb{A}_i$  or  $\mathbb{B}_i$  of each single inclusion  $i = 1, \dots, N_i$ . These localization tensors are determined by means of a single inclusion problem illustrated in Fig. 3b, see Section 3.2.2 below for details.

### 3.2.1 Eshelby's solution

The origin of the mean-field approximate methods may be traced back to the seminal work of Eshelby [13], who considered an infinite matrix material with an ellipsoidal inclusion  $i$  which is made of the same material with the property  $\mathbb{C}'$  but with a uniform eigenstrain  $\boldsymbol{\varepsilon}_i^*$ , see Fig. 3c. No remote load is applied. The strain field in

that inclusion induced by the release of  $\boldsymbol{\varepsilon}_i^*$  is uniform, and can be expressed as

$$\boldsymbol{\varepsilon}_i^e = \mathcal{S}'_i \boldsymbol{\varepsilon}_i^*, \quad (26)$$

where  $\mathcal{S}'_i$  is the Eshelby tensor depending on the material property  $\mathbb{C}'$  as well as the shape and orientation of the inclusion  $i$ . Additionally, the superscript  $e$  stands for this eigenstrain problem for a distinction from the problems considered in Section 3.2.2 below. The corresponding stress is obtained from

$$\boldsymbol{\sigma}_i^e = \mathbb{C}'(\boldsymbol{\varepsilon}_i^e - \boldsymbol{\varepsilon}_i^*) = \mathbb{C}'(\mathcal{S}'_i \boldsymbol{\varepsilon}_i^* - \boldsymbol{\varepsilon}_i^*) = -\mathbb{C}'_i \boldsymbol{\varepsilon}_i^*, \quad (27)$$

where the eigenstiffness tensor is defined as

$$\mathbb{C}'_i := \mathbb{C}'(\mathbb{I}^S - \mathcal{S}'_i). \quad (28)$$

### 3.2.2 The equivalent inclusion concept

For the actual composite material in Fig. 3a with  $N_i$  inclusions, the localization tensors  $\mathbb{A}_i$  in Eq. (25a) or  $\mathbb{B}_i$  in Eq. (25b) are determined by  $N_i$  single inclusion problems in Fig. 3b. The interaction between different inclusions may be considered by modifying the matrix material properties  $\mathbb{C}'$  or the remote load  $\boldsymbol{\varepsilon}'$  or  $\boldsymbol{\sigma}'$ , see A.2–A.4. As shown in Fig. 3b, the inclusion  $i$  is made of a material with  $\mathbb{C}_i$  other than  $\mathbb{C}'$  of the matrix material, where we do not assume an eigenstrain. For the Eshelby's solution of the problem in Fig. 3c to apply, we may find a proper eigenstrain  $\boldsymbol{\varepsilon}_i^*$  for a prescribed strain  $\boldsymbol{\varepsilon}'$ , such that the stresses in the inclusion of both cases are equivalent, i.e.

$$\boldsymbol{\sigma}_i^e = \mathbb{C}'(\boldsymbol{\varepsilon}' + \boldsymbol{\varepsilon}_i^e - \boldsymbol{\varepsilon}_i^*) = \mathbb{C}_i(\boldsymbol{\varepsilon}' + \boldsymbol{\varepsilon}_i^e), \quad (29)$$

which in combination with Eq. (26) suggests the claimed eigenstrain

$$\boldsymbol{\varepsilon}_i^* = ((\mathbb{C}_i - \mathbb{C}')\mathcal{S}'_i + \mathbb{C}')^{-1}(\mathbb{C}' - \mathbb{C}_i)\boldsymbol{\varepsilon}', \quad (30)$$

where we have splitted the strain within the inclusion  $i$  into a constant and a fluctuation part, i.e.  $\boldsymbol{\varepsilon}_i = \boldsymbol{\varepsilon}' + \boldsymbol{\varepsilon}_i^e$ . Together with the equations (26) and (30), we have

$$\boldsymbol{\varepsilon}_i = \boldsymbol{\varepsilon}' + \boldsymbol{\varepsilon}_i^e = \boldsymbol{\varepsilon}' + \mathcal{S}'_i \boldsymbol{\varepsilon}_i^* = \mathbb{A}'_i \boldsymbol{\varepsilon}', \quad (31)$$

where we identify

$$\mathbb{A}'_i = (\mathbb{I}^S + \mathcal{S}'_i \mathbb{C}'^{-1}(\mathbb{C}_i - \mathbb{C}'))^{-1}. \quad (32)$$

Correspondingly, the stress in the inclusion  $i$  reads

$$\boldsymbol{\sigma}_i = \mathbb{C}_i \mathbb{A}'_i \boldsymbol{\varepsilon}' = \mathbb{C}_i \mathbb{A}'_i \mathcal{S}'_i \boldsymbol{\sigma}' = \mathbb{B}'_i \boldsymbol{\sigma}', \quad (33)$$

where we identify

$$\mathbb{B}'_i = \mathbb{C}_i \mathbb{A}'_i \mathcal{S}'_i = (\mathbb{S}_i - \mathcal{S}_i(\mathbb{S}_i - \mathbb{S}'))^{-1} \mathcal{S}'_i. \quad (34)$$

In A, we consider some well-established mean-field methods by specifying the single inclusion problem in Fig. 3b.

**Remark 2.** The mean-field methods in Appendix A include approximations and simplifications. For instance, the subdivision of the actual composite problem into  $N_i$  single inclusion problems in Fig. 3b is an approximation, which together with the dilute method in A.1 completely neglects the inclusion interaction. The inclusion interaction can be considered to a certain extent, but not exactly, by some advanced schemes in A.2–A.4. Additionally, the mean-field methods in A.1–A.3 do not account for possible anisotropic inclusion distributions, while the interaction direct derivative (IDD) method in A.4 is restricted to ellipsoidal distributions. Hence, in contrast to the mean-field formulation in Section 3.1, the effective properties determined by the mean-field methods are not equivalent to those of the full-field formulation in Section 2.3, but approximations.

### 3.3 FE approximation of full-field formulations

In this subsection, we consider the FEM as a further approximation of the micro problem (7b).

#### 3.3.1 Weak formulation and FE discretization

For the FEM to apply, we introduce a weak residual form of the micro problem (7b)

$$\varrho(\mathbf{u}; \delta\mathbf{u}) = \underbrace{\int_{\Gamma} \delta\mathbf{u} \cdot \mathbf{t} dA}_{:=F(\delta\mathbf{u})} - \underbrace{\int_{\Omega} \boldsymbol{\varepsilon}[\delta\mathbf{u}] : \boldsymbol{\sigma}(\boldsymbol{\varepsilon}[\mathbf{u}]) dV}_{:=B(\mathbf{u}; \delta\mathbf{u})} = 0, \quad \forall \delta\mathbf{u} \in \mathcal{V}^0, \quad (35)$$

where  $B$ ,  $F$  and  $\mathcal{V}^0$  are a bilinear form, a linear form and an appropriate Sobolev space, respectively. Clearly, the primal solution of (35) is the micro displacement vector  $\mathbf{u}$ . By introducing a regular FE-space  $\mathcal{V}_h^0$ , we may further arrive at a discretized version of (35)

$$\varrho(\mathbf{u}_h; \delta\mathbf{u}_h) = F(\delta\mathbf{u}_h) - B(\mathbf{u}_h; \delta\mathbf{u}_h) = 0, \quad \forall \delta\mathbf{u}_h \in \mathcal{V}_h^0. \quad (36)$$

#### 3.3.2 Implementation of different boundary conditions

Now, we consider the different micro boundary conditions introduced in Section 2.2:

1. *Linear displacement boundary condition:* the load term in Eq. (35) vanishes, i.e  $F(\delta\mathbf{u}) = 0$ . Formally, we have

$$\varrho(\mathbf{u}; \delta\mathbf{u}) = -B(\mathbf{u}; \delta\mathbf{u}) = 0, \quad \forall \delta\mathbf{u} \in \mathcal{V}^0, \quad (37)$$

with the constraint (11).

2. *Constant traction boundary condition:* using Eq. (12), the load term in Eq. (35) becomes

$$F(\delta\mathbf{u}) = \int_{\Gamma} \delta\mathbf{u} \cdot \bar{\boldsymbol{\sigma}} \cdot \mathbf{n} dA. \quad (38)$$

Note that for a strain-driven approach additional effort has to be paid to ensure a prescribed macro strain  $\bar{\boldsymbol{\varepsilon}}$  instead of  $\bar{\boldsymbol{\sigma}}$ , see e.g. [40] for an approach based on Lagrange multipliers.

3. *Periodic boundary condition:* with the strain polarization  $\boldsymbol{\varepsilon} = \bar{\boldsymbol{\varepsilon}} + \tilde{\boldsymbol{\varepsilon}}$  in mind, where  $\tilde{\boldsymbol{\varepsilon}}$  is a fluctuation part, we correspondingly split the micro displacement vector into two parts, i.e.  $\mathbf{u}(\mathbf{x}) = \mathbf{u}^0(\mathbf{x}) + \tilde{\mathbf{u}}(\mathbf{x})$ , where  $\mathbf{u}^0 = \bar{\boldsymbol{\varepsilon}} \mathbf{x}$ . In this manner, using Eq. (10a), the primal micro problem (7b) or (35) becomes an equivalent eigenstrain problem of the strong form

$$\begin{cases} \text{Div}(\boldsymbol{\sigma}) = \text{Div}(\mathbb{C}(\tilde{\boldsymbol{\varepsilon}} + \bar{\boldsymbol{\varepsilon}})) = \mathbf{0}, & \text{in } \Omega \\ \langle \tilde{\boldsymbol{\varepsilon}} \rangle = \mathbf{0}, \end{cases}, \quad (39)$$

and of the weak residual form

$$\varrho(\tilde{\mathbf{u}}; \delta \tilde{\mathbf{u}}) = - \underbrace{\int_{\Omega} \tilde{\boldsymbol{\varepsilon}}[\delta \tilde{\mathbf{u}}] : \mathbb{C}(\tilde{\boldsymbol{\varepsilon}}(\tilde{\mathbf{u}}) + \bar{\boldsymbol{\varepsilon}}) dV}_{:=B(\tilde{\mathbf{u}}; \delta \tilde{\mathbf{u}})} = 0, \quad \forall \delta \tilde{\mathbf{u}} \in \tilde{\mathcal{V}}^0, \quad (40)$$

where  $F(\delta \tilde{\mathbf{u}}) = 0$ . Note that the fluctuation part of the micro displacement vector  $\tilde{\mathbf{u}}$  is the primal solution of the eigenstrain problem (40), while the homogeneous part  $\mathbf{u}^0$  constitutes the constant eigenstrain  $\bar{\boldsymbol{\varepsilon}}$ . Then, we split the micro displacement vector into three parts as  $\tilde{\mathbf{u}}(\mathbf{x}) = [\tilde{\mathbf{u}}^{in} \ \tilde{\mathbf{u}}^+ \ \tilde{\mathbf{u}}^-]$ . While  $\tilde{\mathbf{u}}^{in}$  corresponds to the displacement in the interior domain,  $\tilde{\mathbf{u}}^+$  and  $\tilde{\mathbf{u}}^-$  are the displacements at  $\mathbf{x}^+ \in \Gamma^+$  and  $\mathbf{x}^- \in \Gamma^-$ , respectively. On this basis, we arrive at an alternative version of (13a)

$$\tilde{\mathbf{u}}^+(\mathbf{x}^+) = \tilde{\mathbf{u}}^-(\mathbf{x}^-). \quad (41)$$

In the context of the FEM, the combination of the equations (40) and (41) leads to a reduced equation system for solving  $\tilde{\mathbf{u}}_h^{in}$  and  $\tilde{\mathbf{u}}_h^+$ , see e.g. [51] for details.

For detailed FE algorithms, the interested reader is referred to [40, 51].

**Remark 3.** Fig. 4a schematically depicts the relation between solution spaces of mean-field and FE approximations as well as an exact solution. For illustration purposes, material properties and microstructural information (like inclusion shape or distribution) are chosen as independent variables. In particular, we assume that the solution space of the mean-field approximation is completely included within that of the FE approximation. Since the FEM allows to consider some fine micromorphology effects, which cannot be considered analytically via a mean-field approximation, it is expected to be more accurate than the mean-field methods in general. However, the FE approximation is still not exact due to the underlying discretization errors or due to the lack of knowledge about an RVE.

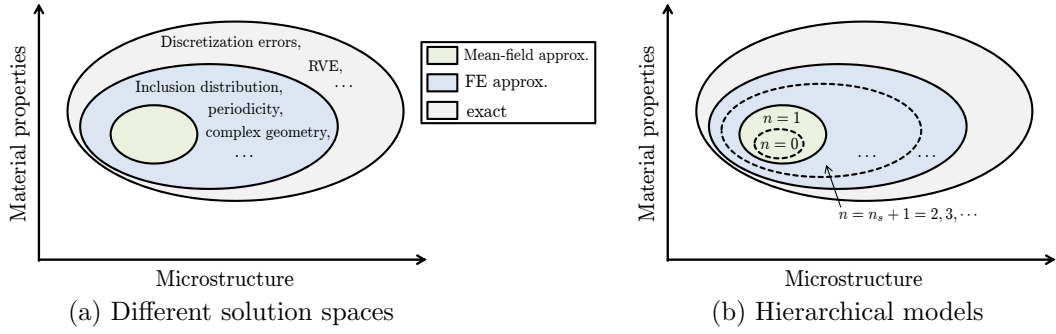


Figure 4: Schematic illustration of the relations between mean-field and FE approximations for determining effective properties

## 4 Goal-oriented adaptivity on the macro scale

With the different approximation methods for homogenization introduced in the previous sections 3.2 and 3.3 at hand, we are now in a position to establish the macro scale adaptivity. To this end, we first briefly recall the general goal-oriented adaptive approach developed in our previous work [25]. Then, we propose a novel model hierarchy, including the aspects of mean-field and full-field homogenization methods as well as unit cell size.

### 4.1 Quantity of interest and dual problem

For the exact model (9) to be practically solved, we need to introduce two additional models: the working (surrogate) model

$$\bar{\rho}^{(n)}(\bar{\mathbf{u}}^{(n)}; \delta\bar{\mathbf{u}}) = \bar{F}(\delta\bar{\mathbf{u}}) - \bar{B}^{(n)}(\bar{\mathbf{u}}^{(n)}; \delta\bar{\mathbf{u}}) = 0, \quad \forall \delta\bar{\mathbf{u}} \in \bar{\mathcal{V}}^0 \quad (42)$$

with a hierarchical order  $n \geq 0$  and the computable model

$$\bar{\rho}^{(n)}(\bar{\mathbf{u}}_h^{(n)}; \delta\bar{\mathbf{u}}_h) = \bar{F}(\delta\bar{\mathbf{u}}_h) - \bar{B}^{(n)}(\bar{\mathbf{u}}_h^{(n)}; \delta\bar{\mathbf{u}}_h) = 0, \quad \forall \delta\bar{\mathbf{u}}_h \in \bar{\mathcal{V}}_h^0. \quad (43)$$

Here  $\mathcal{V}_h^0 \subset \bar{\mathcal{V}}^0$  represents the approximate FE-space. In the case where the quality of the simulation is measured by a *quantity of interest*  $Q(\bar{\mathbf{u}})$  depending on a macroscale solution  $\bar{\mathbf{u}}$ , we define the total error  $E$  as

$$E(\bar{\mathbf{u}}, \bar{\mathbf{u}}_h^{(n)}) := Q(\bar{\mathbf{u}}) - Q(\bar{\mathbf{u}}_h^{(n)}). \quad (44)$$

For duality techniques [33, 34, 35] to apply, we first formulate a residuum as

$$\bar{\rho}(\bar{\mathbf{u}}_h^{(n)}; \delta\bar{\mathbf{u}}) = \bar{F}(\delta\bar{\mathbf{u}}) - \bar{B}(\bar{\mathbf{u}}_h^{(n)}; \delta\bar{\mathbf{u}}) = \bar{B}(\bar{\mathbf{u}}; \delta\bar{\mathbf{u}}) - \bar{B}(\bar{\mathbf{u}}_h^{(n)}; \delta\bar{\mathbf{u}}) = \bar{B}(\bar{\mathbf{e}}; \delta\bar{\mathbf{u}}), \quad (45)$$

with the error of the primal solution  $\bar{\mathbf{e}} = \bar{\mathbf{u}} - \bar{\mathbf{u}}_h^{(n)}$ , where we used the Galerkin orthogonality (9) for the second equality and the last equality is ensured by the fact that  $\bar{B}$  is bilinear. Since the quantity of interest  $Q$  in Eq. (44) does not necessarily have to be linear, we rewrite Eq. (44) as

$$E(\bar{\mathbf{u}}, \bar{\mathbf{u}}_h^{(n)}) = Q(\bar{\mathbf{u}}) - Q(\bar{\mathbf{u}}_h^{(n)}) = Q_S(\bar{\mathbf{u}}, \bar{\mathbf{u}}_h^{(n)}; \bar{\mathbf{e}}), \quad (46)$$

where we introduce a secant form as

$$Q_S(\bar{\mathbf{u}}, \bar{\mathbf{u}}_h^{(n)}; \bar{\mathbf{e}}) = \int_0^1 D_{\bar{\mathbf{u}}} Q(\bar{\mathbf{u}}_h^{(n)} + s\bar{\mathbf{e}}; \bar{\mathbf{e}}) ds, \quad (47)$$

with  $0 \leq s \leq 1$ , see also [56]. To set a link between the equations (45) and (47), we introduce a *dual Lagrangian functional*  $\mathcal{L}$  as

$$\mathcal{L}(\bar{\mathbf{u}}, \bar{\mathbf{u}}_h^{(n)}, \bar{\mathbf{z}}; \delta \bar{\mathbf{z}}) := Q_S(\bar{\mathbf{u}}, \bar{\mathbf{u}}_h^{(n)}; \delta \bar{\mathbf{z}}) - \bar{B}^*(\bar{\mathbf{z}}; \delta \bar{\mathbf{z}}), \quad (48)$$

where  $\bar{B}^*$  is the adjoint form of  $\bar{B}$ , satisfying  $\bar{B}^*(\bar{\mathbf{z}}; \delta \bar{\mathbf{z}}) = \bar{B}(\delta \bar{\mathbf{z}}; \bar{\mathbf{z}})$ . Furthermore,  $\delta \bar{\mathbf{z}} \in \bar{\mathcal{V}}^0$  and  $\bar{\mathbf{z}} \in \bar{\mathcal{V}}^0$  are test functions. The dual problem is then established by

$$\text{stat}_{\delta \bar{\mathbf{z}}} \left\{ \mathcal{L}(\bar{\mathbf{u}}, \bar{\mathbf{u}}_h^{(n)}, \bar{\mathbf{z}}; \delta \bar{\mathbf{z}}) \right\} \implies Q_S(\bar{\mathbf{u}}, \bar{\mathbf{u}}_h^{(n)}; \delta \bar{\mathbf{u}}) - \bar{B}^*(\bar{\mathbf{z}}; \delta \bar{\mathbf{u}}) = 0, \quad (49)$$

with the dual solution  $\bar{\mathbf{z}}$ . For self-adjoint problems (true for the present case), we have

$$\bar{B}(\bar{\mathbf{z}}; \delta \bar{\mathbf{u}}) = Q_S(\bar{\mathbf{u}}, \bar{\mathbf{u}}_h^{(n)}; \delta \bar{\mathbf{u}}). \quad (50)$$

## 4.2 Exact error representations

To distinguish two different error sources, we rewrite the residuum (45) as

$$\begin{aligned} \bar{\varrho}(\bar{\mathbf{u}}_h^{(n)}; \delta \bar{\mathbf{u}}) &= \bar{F}(\delta \bar{\mathbf{u}}) - \bar{B}(\bar{\mathbf{u}}_h^{(n)}; \delta \bar{\mathbf{u}}) \\ &= \underbrace{\bar{F}(\delta \bar{\mathbf{u}}) - \bar{B}^{(n)}(\bar{\mathbf{u}}_h^{(n)}; \delta \bar{\mathbf{u}})}_{:= \bar{\varrho}_h} + \underbrace{\bar{B}^{(n)}(\bar{\mathbf{u}}_h^{(n)}; \delta \bar{\mathbf{u}}) - \bar{B}(\bar{\mathbf{u}}_h^{(n)}; \delta \bar{\mathbf{u}})}_{:= \bar{\varrho}_m}, \end{aligned} \quad (51)$$

which defines the discretization error  $\bar{\varrho}_h$  and the model error  $\bar{\varrho}_m$ , see also [34, 35]. Note that the special cases  $\bar{\varrho} = \bar{\varrho}_m$  and  $\bar{\varrho} = \bar{\varrho}_h$  are obtained for  $h \rightarrow 0$  and  $n \rightarrow \infty$ , respectively. Finally, by combining the equations (44), (45), (46), (50) and (51), we obtain

$$E(\bar{\mathbf{u}}, \bar{\mathbf{u}}_h^{(n)}) = \underbrace{\bar{\varrho}_h(\bar{\mathbf{u}}_h^{(n)}, \bar{\mathbf{z}} - \pi \bar{\mathbf{z}})}_{:= E_h} + \underbrace{\bar{\varrho}_m(\bar{\mathbf{u}}_h^{(n)}, \bar{\mathbf{z}})}_{:= E_m}, \quad (52)$$

where  $E_h$  and  $E_m$  are the discretization error and the model error of the quantity of interest  $Q$ , respectively. In Eq. (52) for  $E_h$ , the Galerkin orthogonality (43) is used, and  $\pi \bar{\mathbf{z}} \in \mathcal{V}_h^0$  is a projection of  $\bar{\mathbf{z}}$  onto the FE-space  $\bar{\mathcal{V}}_h^0$ .

## 4.3 Approximations for a computable error representation

To arrive at a computable error representation, we make the following three approximations:

1. The exact model of hierarchical order  $n \rightarrow \infty$  is replaced by a *fine* model of a hierarchical order  $n^+ > n$ . Hence, we obtain for Eq. (51)

$$\bar{\varrho}_m(\bar{\mathbf{u}}_h^{(n)}, \bar{\mathbf{z}}) \approx \bar{\varrho}_m^+(\bar{\mathbf{u}}_h^{(n)}, \bar{\mathbf{z}}) := \bar{B}^{(n)}(\bar{\mathbf{u}}_h^{(n)}; \bar{\mathbf{z}}) - \bar{B}^{(n^+)}(\bar{\mathbf{u}}_h^{(n)}; \bar{\mathbf{z}}). \quad (53)$$

2. The exact dual problem (50) also depends on the exact primal solution  $\bar{\mathbf{u}}$  and requires knowledge of the exact model. Hence, we introduce an approximate dual problem

$$\bar{B}^{(n)}(\bar{\mathbf{z}}; \delta\bar{\mathbf{u}}) = Q_S^{(n)}(\bar{\mathbf{u}}_h^{(n)}, \bar{\mathbf{u}}_h^{(n)}; \delta\bar{\mathbf{u}}) \quad (54)$$

by the replacements  $\bar{B} \approx \bar{B}^{(n)}$ ,  $Q_S \approx Q_S^{(n)}$  and  $\bar{\mathbf{u}} \approx \bar{\mathbf{u}}_h^{(n)}$ , leading to a linearization of (50).

3. In practice, the approximate dual problem (54) is not solved exactly. Instead a spatially discretized version of (54), i.e.

$$\bar{B}^{(n)}(\bar{\mathbf{z}}_h; \delta\bar{\mathbf{u}}_h) = Q_S^{(n)}(\bar{\mathbf{u}}_h^{(n)}, \bar{\mathbf{u}}_h^{(n)}; \delta\bar{\mathbf{u}}_h), \quad (55)$$

is solved via the FEM, using the same mesh as for the primal problem and thus preserving an analogous structure of the primal problem (see e.g. [62]). Here  $\bar{\mathbf{z}}_h$  is the FE solution of the approximate dual problem (54), which is not directly useful for the error representation (52) due to the Galerkin orthogonality. For this reason, we use, in this work, a patch recovery approach developed in our previous works [25, 24] to construct an approximate solution of

$$\bar{B}^{(n)}(\bar{\mathbf{z}}_{h+}; \delta\bar{\mathbf{u}}_{h+}) = Q_S^{(n)}(\bar{\mathbf{u}}_{h+}^{(n)}, \bar{\mathbf{u}}_{h+}^{(n)}; \delta\bar{\mathbf{u}}_{h+}), \quad (56)$$

on an enhanced FE-space  $\delta\bar{\mathbf{u}}_{h+} \in \bar{\mathcal{V}}_{h+}^0$  satisfying  $\bar{\mathcal{V}}_h^0 \subset \bar{\mathcal{V}}_{h+}^0 \subset \bar{\mathcal{V}}^0$ , using the hierarchical FE structure by increasing the polynomial interpolation order.

#### 4.4 A model hierarchy based on mean-field and full-field homogenization methods

To obtain a computable error estimate, we specify the exact, the working and the fine model as

$$\bar{B}(\bar{\mathbf{u}}; \delta\bar{\mathbf{u}}) = \int_{\bar{\Omega}} \bar{\boldsymbol{\varepsilon}}[\delta\bar{\mathbf{u}}] : (\bar{\mathbb{C}}\bar{\boldsymbol{\varepsilon}}[\bar{\mathbf{u}}]) dv, \quad (57a)$$

$$\bar{B}^{(n)}(\bar{\mathbf{u}}; \delta\bar{\mathbf{u}}) = \int_{\bar{\Omega}} \bar{\boldsymbol{\varepsilon}}[\delta\bar{\mathbf{u}}] : (\bar{\mathbb{C}}^{(n)}\bar{\boldsymbol{\varepsilon}}[\bar{\mathbf{u}}]) dv, \quad (57b)$$

$$\bar{B}^{(n+)}(\bar{\mathbf{u}}; \delta\bar{\mathbf{u}}) = \int_{\bar{\Omega}} \bar{\boldsymbol{\varepsilon}}[\delta\bar{\mathbf{u}}] : (\bar{\mathbb{C}}^{(n+)}\bar{\boldsymbol{\varepsilon}}[\bar{\mathbf{u}}]) dv, \quad (57c)$$

respectively. To complete the working model (57b), we recall the solution spaces of mean-field and FE approximation in Fig. 4a. On this basis, we propose a model hierarchy consisting of the following stages:

1. The basic model of hierarchical order  $n = 0$  is chosen as one of the mean-field methods presented in A.
2. As an accuracy improvement, a further mean-field method is chosen as  $n = 1$ . Due to the lack of a hierarchical model structure, this method does not have to be computationally more expensive than the basic one. Most importantly, this choice eliminates the need of a full-field method for an error estimate of

the basic model for  $n = 0$ . For a structural analysis, it is expected that the use of the two mean-field methods  $n = 0$  and  $n = 1$  is sufficient for a comparably large domain of the whole structure, and for both purposes of modeling and the error estimate to be specified in the equations (59), (60) and (61).

3. For a further accuracy improvement, the FE-based method in Eq. (36) with an appropriately chosen boundary condition is adopted for  $n > 1$  towards a full-field approximation. Here, the key role is played by hierarchical unit cells with increasing sizes  $n = n_s + 1 = 2, 3, \dots$ , see Remark 4.

Furthermore, we choose  $n^+ = n + 1 > n$  for the fine model (57c).

**Remark 4.** As a representative example, a model hierarchy used in Section 5 is as follows:

1.  $n = 0$  : Self-consistent in Eq. (A.12),
2.  $n = 1$  : IDD in Eq. (A.14), (58)
3.  $n = n_s + 1 = 2, 3, \dots$  : FEM (periodic) in Eq. (40).

**Remark 5.** Based on the solution spaces of mean-field and FE approximations in Fig. 4a, the resulting hierarchical models are schematically illustrated in Fig. 4b.

**Remark 6.** In Tab. 1, we recall the accuracy level of some mean-field methods from the literature [10, 64], where  $c = \sum_{i=1}^{N_i} c_i$  denotes the total volume fraction of all inclusions. A function  $f(c)$  is said to be  $o(c^m)$ , if there exist two  $c$ -independent positive constants  $A$  and  $m$  such that  $|f(c)| \leq Ac^m$  as  $c \rightarrow 0$ . The accuracy level given in Tab. 1 provides a two-step model hierarchy, however, is only restricted to a limit case of a very low inclusion volume fraction  $c \rightarrow 0$  and does not have a generality for all possible inclusion volume fractions. Therefore, the special choice for  $n = 0, 1$  in the model hierarchy (58) does not have generality due to the lack of a hierarchical model structure. The choice should be tailored for the problem under study.

Methods	Accuracy
Eshelby (dilute)	$o(c)$
Mori-Tanaka	$o(c^2)$
Self-consistent	$o(c)$
IDD	$o(c^2)$

Table 1: Comparative properties of several mean-field methods [10]

**Remark 7.** For an alternative approach to model adaptivity based on a clear hierarchical model structure, we refer to our recent work [25].

**Remark 8.** The switch from Stage 2 to Stage 3 of the above model hierarchy is based on the hierarchical model structure in Fig. 4b. As already discussed in Remark 3, the FEM is capable of considering some fine micromorphology effects, which cannot be considered analytically via the mean-field methods. Therefore, it may be considered as a more accurate method than the mean-field methods in view of determining effective properties. A mathematical proof of this assumption is still lacking.

**Remark 9.** Additionally to the effective properties in Remark 8, for some scenarios like a damage analysis, a localization in the equations (15a) and (15b) is of interest. The basis of the mean-field methods used for Stage 2 is the mean-field formulation in Section 3.1, leading to a rather low microscopic resolution that might suffice for uncritical regions of a structure. In contrast to that, at the expense of a larger computational effort, the FEM used in Stage 3 provides a much more detailed localization, which becomes useful for the critical region. Therefore, a clear model structure also preserves in view of a localization.

**Remark 10.** An RVE is defined as a statistical representative of the microstructure of the material under study. The choice of an RVE is not unique, but by definition any RVE should return the same effective properties  $\overline{\mathbb{C}}$  in Eq. (18) or  $\overline{\mathbb{S}}$  in Eq. (19). However, this is not always practicable, such that, instead of an RVE, a unit cell is used for formulation of the micro problem (7b), as already mentioned in Section 1. Fig. 5a schematically depicts some possible choices of a unit cell for a given microstructure, which do not necessarily meet the requirements of an RVE. With increasing unit cell size, a better estimate of effective properties is expected, as illustrated in Fig. 5b for different boundary conditions, see e.g. [15]. When unit cell size  $n_s$  is fixed, the linear displacement boundary condition gives the stiffest prediction, whereas the constant traction boundary condition provides the most compliant behavior. In most cases, the periodic boundary condition gives the best prediction, such that the fastest convergence rate may be expected. The unit cell corresponds to an RVE, when a certain size is reached, such that the exact effective properties can be reproduced. In this work, we consider hierarchical unit cells  $n_s = 1, 2, \dots$ , starting with a basic unit cell  $n_s = 1$  and enlarging their size with an increasing  $n_s$ . Additionally, a unit cell of a size  $n_s$  contains all microstructural information of the one of  $n_s - 1$ . The hierarchical unit cells are considered within Stage 3 of the above model hierarchy by means of the FEM. Since a clear hierarchical model structure is obtained by enlarging the unit cell size, this ansatz is quite general.

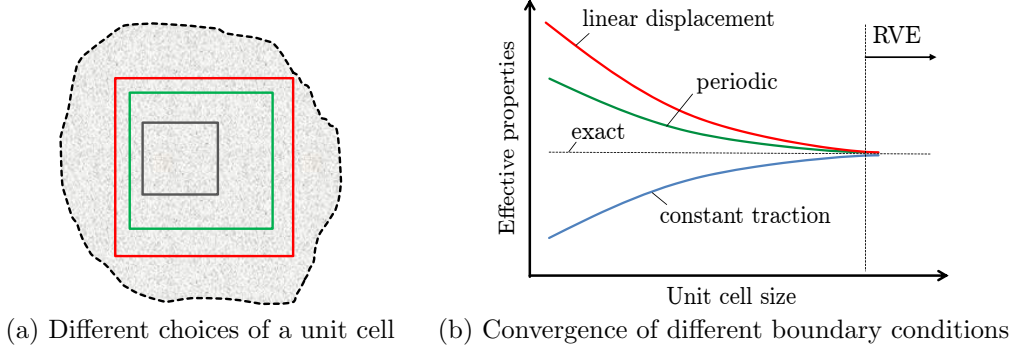


Figure 5: Schematic illustration of the influence of unit cell size

**Remark 11.** An adaptive selection of micro boundary conditions is not included in the model hierarchy, and a selection is suggested to be done prior to the adaptive approach, since, for our case, a switch of boundary conditions does not have a significant influence on the numerical effort associated with the FEM.

**Remark 12.** It is remarkable that the aspects of mean-field and full-field methods as well as hierarchical unit cells can be consistently included in one single model hierarchy as shown above.

## 4.5 A computable error estimator

Using the enhanced dual solution  $\bar{\mathbf{z}}_{h+}$  of the dual problem (56) and combining the equations (51), (52), (53) and (57), we finally obtain the model error estimate

$$E_m = \bar{\varrho}_m(\bar{\mathbf{u}}_h^{(n)}, \bar{\mathbf{z}}) \approx \int_{\bar{\Omega}} \bar{\boldsymbol{\varepsilon}}[\bar{\mathbf{z}}_{h+}] : \left( (\bar{\mathbb{C}}^{(n)} - \bar{\mathbb{C}}^{(n+)}) \bar{\boldsymbol{\varepsilon}}[\bar{\mathbf{u}}_h^{(n)}] \right) dv =: \tilde{E}_m \quad (59)$$

and the discretization error estimate

$$\begin{aligned} E_h &= \bar{\varrho}_h(\bar{\mathbf{u}}_h^{(n)}, \bar{\mathbf{z}} - \pi \bar{\mathbf{z}}) \\ &\approx \bar{F}(\bar{\mathbf{z}}_{h+} - \pi \bar{\mathbf{z}}_{h+}) - \int_{\bar{\Omega}} \bar{\boldsymbol{\varepsilon}}[\bar{\mathbf{z}}_{h+} - \pi \bar{\mathbf{z}}_{h+}] : (\bar{\mathbb{C}}^{(n)} \bar{\boldsymbol{\varepsilon}}[\bar{\mathbf{u}}_h^{(n)}]) dv =: \tilde{E}_h, \end{aligned} \quad (60)$$

respectively. The local error indicators  $\eta_m^e$  and  $\eta_h^e$  for each single element  $e$  are then obtained from the corresponding element contributions of their global counterparts (59) and (60), respectively, i.e.

$$\tilde{E}_m = \sum_{e=1}^{N_{el}} \eta_m^e, \quad \eta_m^e = \int_{\bar{\Omega}^e} \bar{\boldsymbol{\varepsilon}}[\bar{\mathbf{z}}_{h+}] : \left( (\bar{\mathbb{C}}^{(n)} - \bar{\mathbb{C}}^{(n+)}) \bar{\boldsymbol{\varepsilon}}[\bar{\mathbf{u}}_h^{(n)}] \right) dv, \quad (61a)$$

$$\tilde{E}_h = \sum_{e=1}^{N_{el}} \eta_h^e, \quad \eta_h^e = - \int_{\bar{\Omega}^e} \bar{\boldsymbol{\varepsilon}}[\bar{\mathbf{z}}_{h+} - \pi \bar{\mathbf{z}}_{h+}] : (\bar{\mathbb{C}}^{(n)} \bar{\boldsymbol{\varepsilon}}[\bar{\mathbf{u}}_h^{(n)}]) dv, \quad (61b)$$

$$\tilde{E} := \tilde{E}_m + \tilde{E}_h, \quad (61c)$$

where  $\bar{\Omega} = \bigcup_{e=1}^{N_{el}} \bar{\Omega}^e$ . In Eq. (61c), we introduce  $\tilde{E}$  as an error estimate of the total error  $E$  in Eq. (44).

**Remark 13.** For the second equation in Eq. (61b), the load term  $\bar{F}$  in Eq. (60) is neglected for a localization. This does not have any influence on the effectivity for a displacement-controlled approach in Section 5, where  $\bar{F}(\bar{\mathbf{z}}_{h^+} - \pi\bar{\mathbf{z}}_{h^+}) = 0$ . Otherwise, for an effectivity improvement, one could use the Galerkin orthogonality

$$\bar{F}(\bar{\mathbf{z}}_{h^+}) - \int_{\Omega} \bar{\boldsymbol{\varepsilon}}[\bar{\mathbf{z}}_{h^+}] : (\bar{\mathbb{C}}^{(n)} \bar{\boldsymbol{\varepsilon}}[\bar{\mathbf{u}}_{h^+}^{(n)}]) dv = 0, \quad (62)$$

which suggests to solve the primal problem (43) on an enhanced FE-space  $\bar{\mathcal{V}}_{h^+}^0$  for an enhanced primal solution  $\bar{\mathbf{u}}_{h^+}^{(n)}$ . In this manner, the load term  $\bar{F}$  can be equivalently replaced by the second term in Eq. (62), which can be easily localized into its element contributions. For a numerical efficiency, the patch recovery [25, 24] can be used to approximate the enhanced primal problem (62) in a similar manner as for the enhanced dual solution  $\bar{\mathbf{z}}_{h^+}$  in Section 4.3.

**Remark 14.** The sign of  $\eta_m^e$  and  $\eta_h^e$  in the equations (61) indicates the direction of the deviation w.r.t. the quantity of interest  $Q$ , hence, only their absolute values are considered as local indicators in the adaptive algorithm, which will be described in the subsequent section.

## 4.6 Adaptive algorithm

For both model and discretization errors to be controlled in a systematic and automated manner, we adopt Algorithm 1.

Initialization: set the initial mesh  $\mathcal{V}_{h^0}^0$  with the initial (uniform) elastic property  $\bar{\mathbb{C}}^{(n=0)}$  and adaptive step  $i = 0$ ;  
 Define a stopping criterion  $\tilde{E} = \tilde{E}_h + \tilde{E}_m \leq TOL$  for the adaptive refinement loop, where  $TOL$  is a user-defined threshold value related to the desired accuracy;  
**while**  $\tilde{E} = \tilde{E}_h + \tilde{E}_m > TOL$  **do**  
     Solve the computable working model problem (43) with (57b);  
     Solve the approximate dual problem (55) on the current mesh and compute the enhanced dual solution  $\bar{\mathbf{z}}_{h^+}$  in Eq. (56) using the patch recovery technique [25, 24];  
     Compute the local fine models  $\bar{\mathbb{C}}^{(n_e^+)}$ ;  
     Compute the error representations  $\eta_m^e$ ,  $\eta_h^e$ ,  $\tilde{E}_m$ ,  $\tilde{E}_h$  and  $\tilde{E}$  according to the equations (59), (60) and (61);  
     Adaptive refinement: a fixed refinement ratio, such as  $\alpha = 3\%$ , of the elements with the largest  $|\eta_h^e|$  and  $|\eta_m^e|$  is spatially refined and enhanced by  $\bar{\mathbb{C}}^{(n_e)} \rightarrow \bar{\mathbb{C}}^{(n_e^+)}$ , respectively; update the local hierarchical order  $n_e \rightarrow n_e^+$  for enhanced elements and adaptive step  $i \rightarrow i + 1$ .  
**end**

**Algorithm 1:** Adaptive algorithm

**Remark 15.** For linear elasticity, the effective properties need to be computed only once for a certain microstructure. For macroscopically homogeneous materials,

in each adaptive step  $i = 0, 1, 2, \dots$ , the (maximal reachable) fine model  $\overline{\mathbb{C}}^{(n^+=i+1)}$  is computed only once for all and stored for a possible call by subsequent steps.

**Remark 16.** The computational cost cannot be saved in this manner, when the considered material is macroscopically heterogeneous, see e.g. a random composite in Section 5.3, or when the mechanical problem is coupled to an additional problem such as phase transformation.

## 5 Numerical examples

### 5.1 Preliminaries

In this section, a compact tension (CT) specimen is investigated, where no crack is assumed. As shown in Fig. 6a, we consider a half model. The specimen is stretched by a displacement  $\bar{u}^* = 0.01$  mm in the vertical direction, which is uniformly distributed on the entire boundary of the hole. The indices 1 and 2 represent the horizontal and the vertical direction, respectively. We restrict ourselves to a two-dimensional case following the notations given in B, where a plane strain state is assumed.

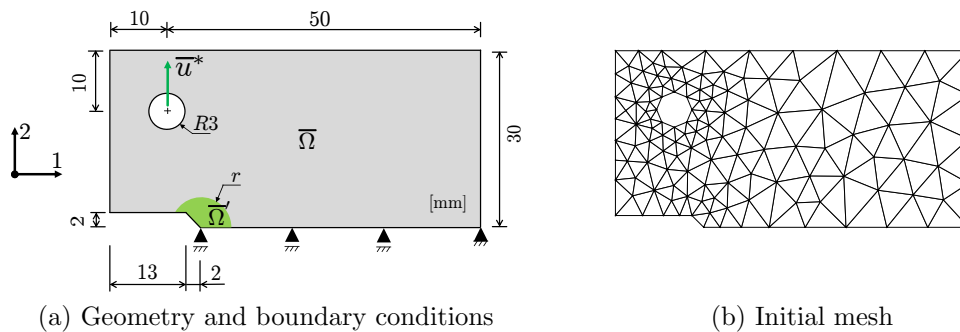


Figure 6: A CT specimen in linear elasticity

The specimen is made of a composite material, consisting of a matrix material and fibers of respective properties given in Tab. 2. In the subsequent examples, we will consider two different classes of materials as follows:

- **Periodic composite:** The macrostructure is made of a periodic repetition of the microstructure. As illustrated in Fig. 7a, the basic unit cell with  $n_s = 1$  is assumed to be a square matrix (white) with a centrally located circular fiber (black). Higher order unit cells ( $n_s > 1$ ) are generated by a repetition of the basic unit cell in such a way that the same number  $n_s$  of basic unit cells is contained for both rows  $i$  and columns  $j$ . In this manner, any unit cell with  $n_s > 1$  remains a square and automatically contains all microstructural information of the one with  $n_s = 1$ . Since size effects (in the context of generalized continuum mechanics [18]) are not considered by the present approach, the absolute size of the unit cell does not play a role for computation of the effective properties. For this reason, a specification of the

volume fraction of the fibers  $c_f$  suffices for a microscopic geometric description in this case. Due to the fiber arrangement in Fig. 7a, the resulting effective material is orthotropic.

- **Random composite:** It contains randomly distributed fibers. Local periodicity is assumed such that homogenization schemes apply. As illustrated in Fig. 7b, the fibers are randomly deviated from the center position, such that the effective properties can be expected to be isotropic. For simplicity, the deviations are controlled in such a way that the fibers do not cross the boundaries of the square unit.

	Young's modulus $E$ [MPa]	Poisson's ratio $\nu$ [-]
matrix	$7 \cdot 10^4$	0.25
fiber	$7 \cdot 10^5$	0.25

Table 2: Summary of material parameters

In order to solve the underlying micro problem (7b), we will consider the following two classes of methods:

- **Mean-field methods:** Eshelby (A.3), Mori-Tanaka (A.9), Self-consistent (A.12) and IDD (A.14) in Section 3.2.
- **Full-field methods:** FEM (linear displacement) in Eq. (37), FEM (constant traction) in Eq. (38) and FEM (periodic) in Eq. (40) in Section 3.3.

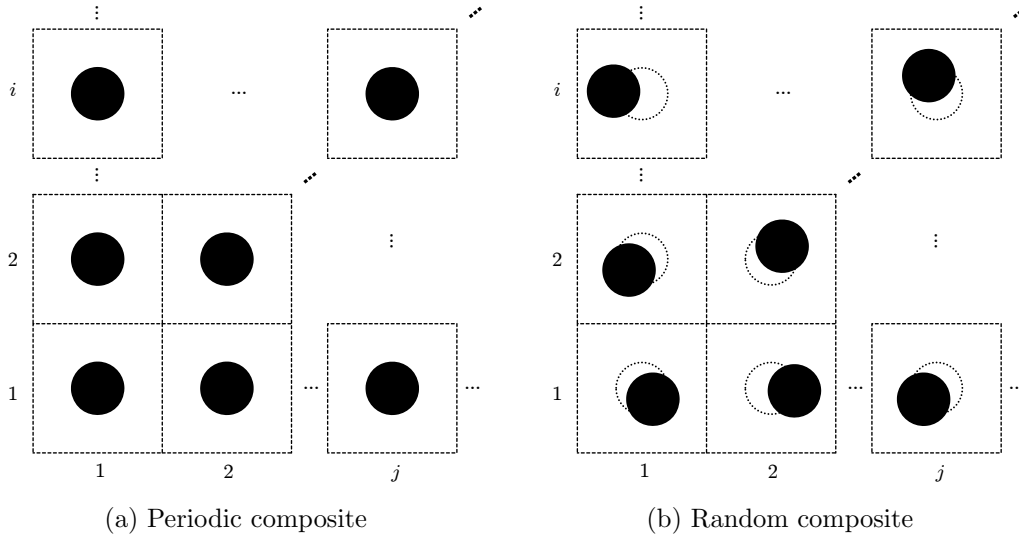


Figure 7: Artificial generation of hierarchical unit cells

Algorithm 1 starts with the initial mesh  $\mathcal{V}_{h^0}^0$  shown in Fig. 6b, consisting of linear triangular elements, and with a uniform model distribution  $n(\bar{\mathbf{x}}) = \text{const.} = 0$ . An

artificial constraint is added to avoid a mesh refinement around the hole boundary for two reasons: 1. the hole is made for imposing a load and does not correspond to our investigation region, 2. this avoids a varying mesh quantity for reproducing the hole geometry, thus enabling a pure effectiveness study of our error estimate (61).

To illustrate the power of goal-oriented adaptivity, we define the quantity of interest  $Q$  as a local type quantity

$$Q := \int_{\bar{\Omega}'} \bar{\sigma}_{ij} dv, \quad (63)$$

where  $\bar{\sigma}_{ij}$  represents coefficients of the macro stress tensor  $\bar{\sigma}$ . For this work, we choose  $i = j = 2$ . Furthermore,  $\bar{\Omega}'$  is a local domain out of the whole domain  $\bar{\Omega}$ , i.e. the green area marked in Fig. 6a, with  $r = 4$  mm.

For an effectiveness study of the proposed adaptive approach, we introduce an accurate estimate of the exact global error  $E^i$  in Eq. (44), called the *actual* error  $\hat{E}^i$ , as

$$E^i = Q - Q_h^{(n),i} \approx Q_{ref} - Q_h^{(n),i} =: \hat{E}^i, \quad i = 0, 1, \dots, N_s. \quad (64)$$

Here  $Q_h^{(n),i}$  represents the quantity of interest computed on the current ( $i$ -th) mesh with a corresponding ( $i$ -th) model distribution, where  $N_s$  denotes the number of adaptive refinement steps. Furthermore,  $Q_{ref}$  represents a reference solution, which is independent of  $i$ . Additionally, we introduce a relative actual error

$$\hat{E}_{rel}^i := \frac{\hat{E}^i}{Q_{ref}}, \quad (65)$$

and a relative error estimate

$$\tilde{E}_{rel}^i := \frac{\tilde{E}^i}{Q_{ref}}, \quad (66)$$

respectively.

## 5.2 Example 1: Periodic composite

In this example, we deal with the periodic composite illustrated in Fig. 7a. The volume fraction of the fibers is assumed to be  $c_f = 40\%$ .

### 5.2.1 Example 1.1: Model hierarchy

Fig. 8 shows several hierarchical unit cells discretized with linear triangular elements for the FEM with different micro boundary conditions (37), (38) and (40). Using the mesh in Fig. 8c, different results are obtained for different boundary conditions, as exemplarily shown in Fig. 9 for contour plots of the von Mises stresses  $\sigma_v$  under a pure shear loading  $\bar{\varepsilon}_{12} = 0.005$ . A maximum von Mises stress is locally achieved by the linear displacement boundary condition (11), while a periodic stress distribution is ensured by the periodic boundary condition (13) as expected. Additionally, the stress distribution obtained by the constant traction boundary condition (12) is quite similar to that for the periodic boundary condition.

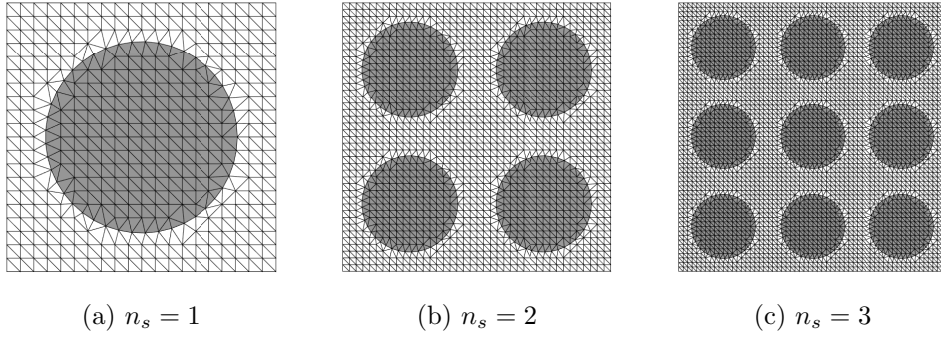


Figure 8: Example 1.1: A sequence of FE-discretized unit cells with different sizes  $n_s$

As stated in Section 5.1, different methods are used to obtain the effective elasticity matrix  $\bar{\mathbf{C}}$  in Eq. (B.1). As the considered effective material is orthotropic, the effective moduli  $\bar{K}$ ,  $\bar{G}_1$  and  $\bar{G}_2$  defined in Eq. (B.4) are shown in Figs. 10a–10c, respectively, where we consider the unit cell size  $n_s$ . Since all four mean-field methods, i.e. Eshelby (A.3), Mori-Tanaka (A.9), self-consistent (A.12) and IDD (A.14), are not able to account for unit cell size effect, their courses remain constant versus  $n_s$  in Fig. 10. Moreover, Eshelby (A.3), Mori-Tanaka (A.9) and self-consistent (A.12) method are not able to consider the fiber distribution, thus leading to isotropic predictions of effective properties as can be seen from a comparison between Figs. 10b and 10c for  $\bar{G}_1 = \bar{G}_2$ , which is not the case for the FEM. As discussed in A.4, the IDD method may account for ellipsoidal distribution, which does not correspond to the present case. The underlying inclusion-matrix cell is assumed to be of the same shape of the corresponding inclusion, leading to an isotropic prediction of effective properties. As a result, the IDD estimate coincides with the Mori-Tanaka one as also reported e.g. in [64, 10]. Interestingly, the Eshelby estimate performs very well when compared to the FEM for the effective shear modulus  $\bar{G}_2$  in Fig. 10c, whereas a relative large deviation can be observed for the effective moduli  $\bar{K}$  and  $\bar{G}_1$  in Figs. 10a and 10b, respectively. Additionally, its prediction becomes poor, running outside of the Reuss bound, for a higher fiber concentration like  $c_f > 50\%$ .

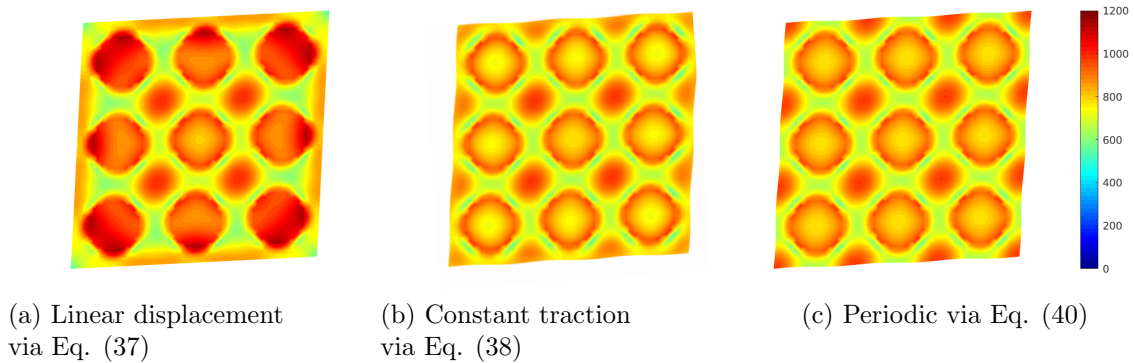


Figure 9: Example 1.1: Contour plots of von Mises stress  $\sigma_v$  [MPa] under different micro boundary conditions (deformation scaling factor of 10)

As depicted in Figs. 10a–10c, using the FEM, the linear displacement boundary

condition (11) provides an upper bound of the effective elastic moduli, while the constant traction one (12) renders a lower bound. With increasing unit cell size  $n_s$ , the bounds become narrower. Most strikingly, the estimate made by the periodic boundary condition (13) lies between the bounds and holds constant with increasing unit cell size  $n_s$ . In this case, it stays rather close to the lower bound (the constant traction boundary condition) for the effective shear modulus  $\overline{G}_2$  in Fig. 10c, which is quite reasonable due to the similar stress distributions in Figs. 9b and 9c for a pure shear loading. In contrast to that, Fig. 10b shows that the periodic estimate is very close to the upper bound (the linear displacement boundary condition) for the effective shear modulus  $\overline{G}_1$ , while the periodic estimate approximately lies in the middle of the bounds for the effective bulk modulus  $\overline{K}$  in Fig. 10a. Most importantly, as illustrated in Fig 10, the basic unit cell  $n_s = 1$  can be used along with the periodic boundary condition to compute an accurate estimate of the effective elasticity matrix  $\overline{\mathcal{C}}$  at a comparably low computational cost. Once a periodic boundary condition is chosen, there is no need to enlarge the unit cell size  $n_s$  for an accuracy improvement. This illustrates the power of the periodic boundary condition for periodic composites. Note that the effective elasticity matrix  $\overline{\mathcal{C}}$  obtained by the FEM (periodic) in Eq. (40) is still not exact due to the discretization errors.

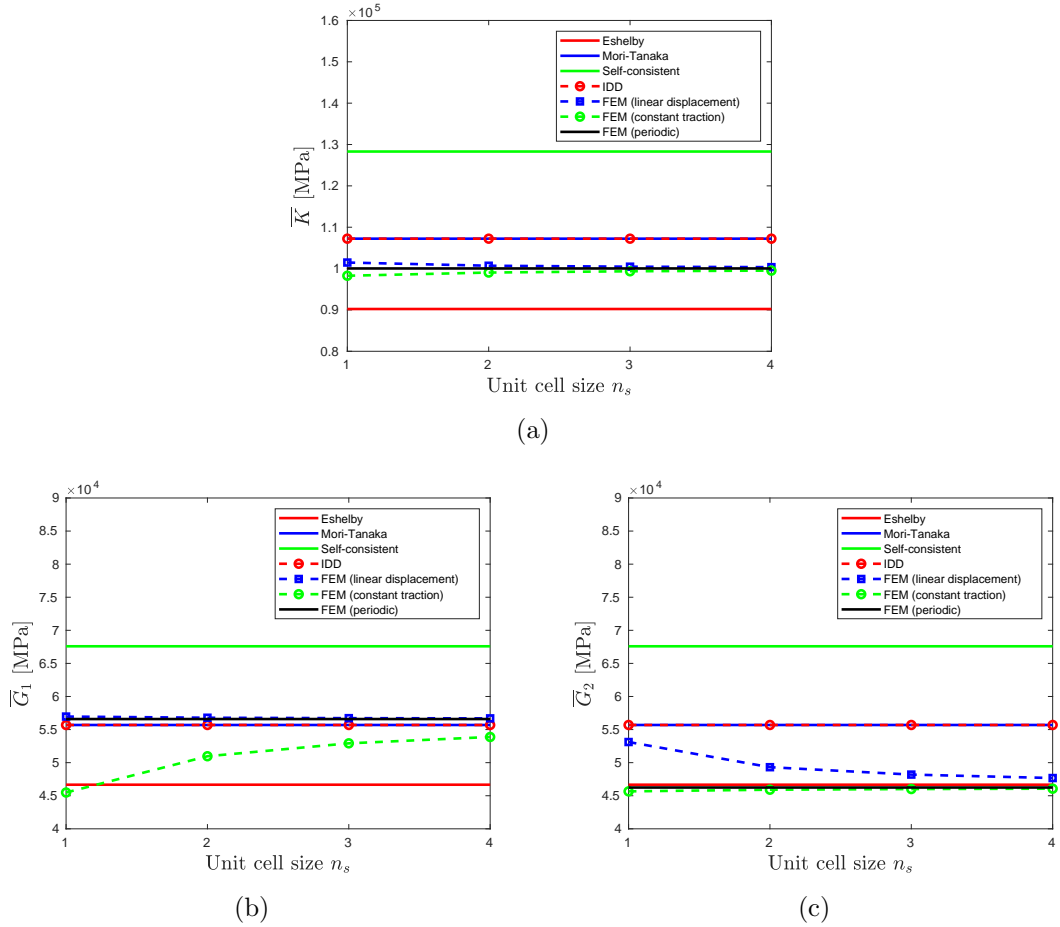


Figure 10: Example 1.1: Comparison between different methods for different unit cell sizes  $n_s$

Correspondingly, we establish the model hierarchy in Eq. (58), which is illustrated for the effective elastic moduli  $\bar{K}$ ,  $\bar{G}_1$  and  $\bar{G}_2$  in Figs. 11a–11c, respectively. For  $n = 0$  and  $n = 1$ , mean-field methods are used, while a switch to full-field methods follows by  $n \geq 2$ . Compared to the results of full-field methods, a large deviation is observed for the basic model (self-consistent)  $n = 0$ , which is significantly enhanced by the IDD estimate  $n = 1$ . At the expense of a much larger computational effort, the IDD estimate is further enhanced by a full-field approximation via the FEM for a basic unit cell problem  $n_s = 1$  or  $n = 2$ . As discussed above, since a periodic boundary condition is chosen, no further accuracy improvement can be made by enlarging the unit cell size  $n_s$  for  $n > 2$ .

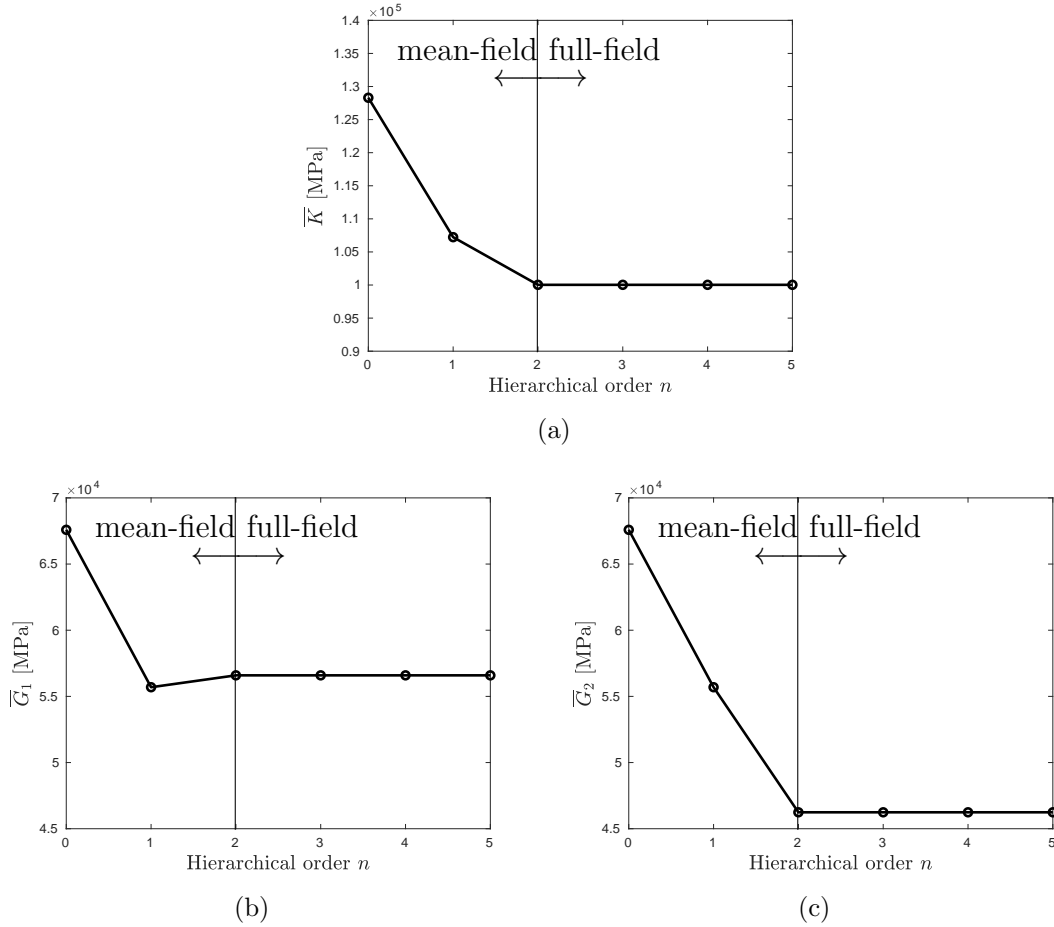


Figure 11: Example 1.1: Illustration of hierarchical models

### 5.2.2 Example 1.2: Pure model adaptivity

Based on the model hierarchy in Eq. (58), we investigate a special case of pure model adaptivity on the initial mesh in Fig. 6b, which is not refined during the adaptive approach. For an effectiveness study, we introduce an estimate of the exact model error  $E_m^i$  in Eq. (52), called the *actual* model error  $\hat{E}_m^i$ , as

$$E_m^i \approx Q_{h,ref} - Q_h^{(n),i} =: \hat{E}_m^i, \quad i = 0, 1, \dots, N_s. \quad (67)$$

Here  $Q_h^{(n),i}$  represents the quantity of interest computed on the initial mesh with the  $i$ -th model distribution, where  $N_s$  denotes the number of adaptive refinement steps. Furthermore,  $Q_{h,ref}$  represents a reference solution, which is computed on the initial mesh in Fig. 6b with a uniform model distribution  $n(\bar{\mathbf{x}}) = const. = 2$ . Similarly to the equations (65) and (66), we introduce a *relative* actual model error

$$\hat{E}_{m,rel}^i := \frac{\hat{E}_m^i}{Q_{h,ref}}, \quad (68)$$

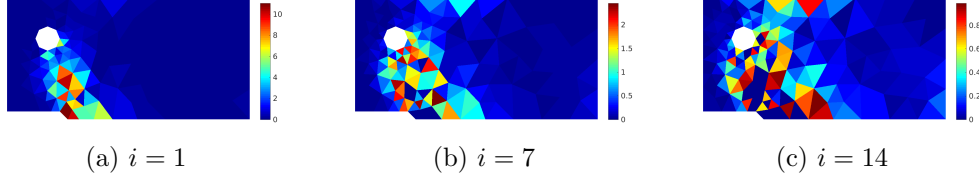
and a *relative* model error estimate

$$\tilde{E}_{m,rel}^i := \frac{\tilde{E}_m^i}{Q_{h,ref}}, \quad (69)$$

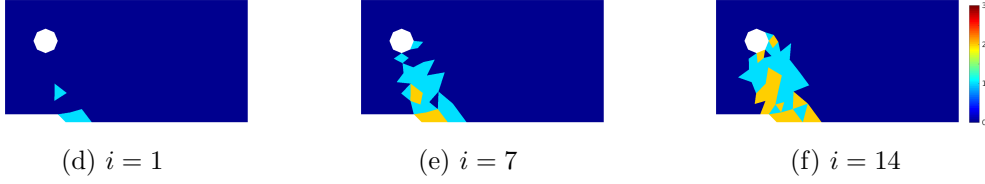
respectively. The adaptive approach is stopped until the actual model error  $\hat{E}_m^i$  completely vanishes, where  $N_s = 86$  adaptive steps are needed. Exemplarily, Figs. 12a–12c show several distributions of the local model errors  $|\eta_m^e|$  in Eq. (61a) for different adaptive steps, while the resulting model distributions are depicted in Figs. 12d–12f, respectively. In the course of the adaptive model refinements, the local model errors  $|\eta_m^e|$  are balanced and significantly reduced.

Furthermore, Fig. 13a shows the quantity of interest  $Q_h^{(n),i}$  versus adaptive steps, where a convergence to the reference value  $Q_{h,ref}$  can be clearly observed. For a numerical efficiency of a structural analysis, it is preferable to limit the use of the FEM for the underlying unit cell computation as strongly as possible. Fig. 13b depicts the relation between the fraction  $c_{fem}$  of elements using the FEM and the relative actual model error  $\hat{E}_{m,rel}$ , where a comparison to the relative model error estimate  $\tilde{E}_{m,rel}$  is additionally given. The reduction of the relative actual model error  $\hat{E}_{m,rel}$  is rapid at the beginning for  $c_{fem} < 30\%$ , then becomes somewhat slower until a sudden jump to zero for  $c_{fem} = 100\%$ . The relative model error estimate  $\tilde{E}_{m,rel}$  somewhat underestimates the relative actual model error  $\hat{E}_{m,rel}$ , but with a very good effectivity. Additionally,  $\tilde{E}_{m,rel}$  correctly predicts the sign of  $\hat{E}_{m,rel}$  except for only 2 out of 86 adaptive steps at the end of the model refinements. Most strikingly, the zero actual model error  $\hat{E}_{m,rel} = 0$  for  $c_{fem} = 100\%$  is reproduced by  $\tilde{E}_{m,rel}$  to working precision. Finally, Figs. 12g–12i show several model distributions obtained by the adaptive approach for different error levels. We observe that the actual model error  $\hat{E}_{m,rel}$  can be reduced from 26.4% for the initial step to 0.24% by a use of the FEM in a comparably small region, showing the effectiveness of the proposed adaptive approach.

Localization of macro model error  $|\eta_m^e|$



Adaptively refined model distributions  $n$



Model distributions for different error levels  
(green: mean-field and red: full-field FEM)

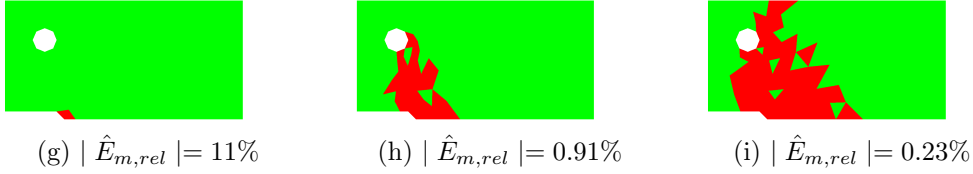


Figure 12: Example 1.2: Results of pure model adaptivity – Part I

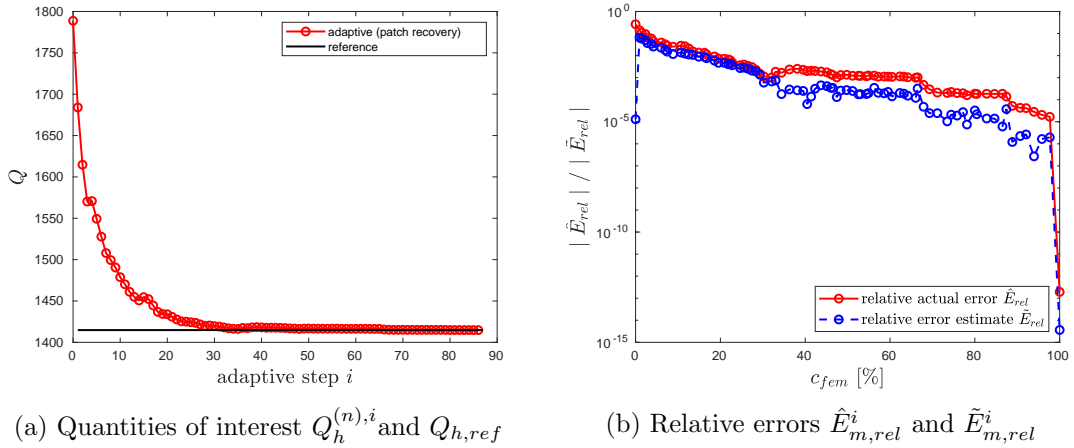


Figure 13: Example 1.2: Results of pure model adaptivity – Part II

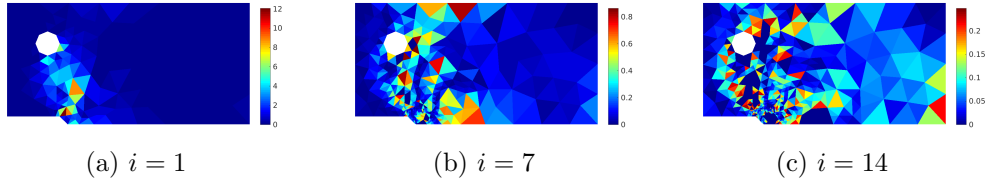
### 5.2.3 Example 1.3: Coupled model and mesh adaptivity

Now, we consider a fully coupled adaptivity using Algorithm 1, where model adaptivity and adaptive FEM are simultaneously applied. Local model error indicators  $|\eta_m^e|$  and local discretization error indicators  $|\eta_h^e|$  in Eq. (61) are depicted in Figs.

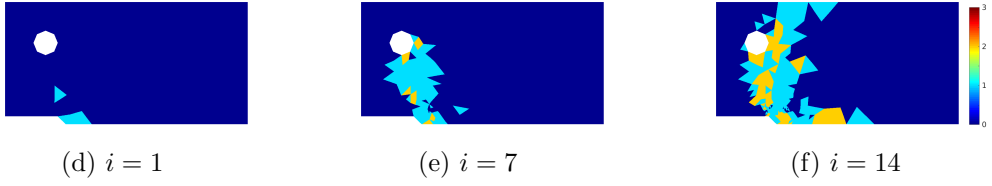
14a–14c and Figs. 14g–14i for different adaptive steps, respectively. In the course of the adaptive refinements, both of them are balanced and significantly reduced. The balance effect is weaker around the hole due to the artificial constraint avoiding a mesh refinement there, see Figs. 14h and 14i. As shown in Figs. 14j–14l, the local mesh refinements are mainly located within the local domain  $\overline{\Omega}'$  in the quantify of interest (63). Similar trends can also be found for model refinements shown in Figs. 14d–14f. Since Algorithm 1 aims at a balanced model error distribution, as a coupling effect to the adaptive mesh refinements, the model on coarsest meshes (sooner or later) starts to be refined as can be seen from Fig. 14f. Compared to Figs. 12d–12f for a pure model adaptivity, Figs. 14d–14f show a different model refinement pattern due to the coupling effect with the adaptive mesh refinements. More precisely, the mesh adaptivity results into a varying distribution of element size, which has a further influence on the model error distribution. Additionally, a hierarchical order  $n > 2$  is not achieved, since it does not provide any accuracy improvement to the model  $n = 2$  due to the periodic boundary condition. This is also reflected by the local model error distributions in Figs. 14b and 14c, where  $\eta_h^e = 0$  holds for regions using the model  $n = 2$  (yellow regions in Figs. 14e and 14f).

Fig. 15a shows the quantity of interest  $Q_h^{(n),i}$  versus adaptive steps, where a convergence to a reference value  $Q_{ref}$  can be clearly observed. The reference value  $Q_{ref}$  is obtained by using a mesh, that is refined uniformly from the last adaptive mesh in Fig. 14l, with a uniform model distribution  $n(\overline{\mathbf{x}}) = const. = 2$ . In Fig. 15b, the relative actual error  $\hat{E}_{rel}^i$  in Eq. (65) is shown to be effectively reduced by the adaptive approach, where an additional comparison to the relative error estimate  $\tilde{E}_{rel}^i$  in Eq. (66) is given. The error estimate  $\tilde{E}^i$  appears to somewhat underestimate the actual error  $\hat{E}^i$ , and is able to mimic the decreasing trend of the actual error  $\hat{E}^i$ . These observations are quite similar to those obtained from our previous work [25] for a different model hierarchy, where a more detailed discussion on the error estimator was given. Finally, Figs. 14m–14o show several model distributions obtained by the adaptive approach for different error levels. We observe that the actual error  $\hat{E}_{rel}$  can be reduced from 35.9% for the initial step to 4.61% by a use of the FEM in a comparably small region, confirming the effectiveness of the proposed adaptive approach. Compared to Figs. 12g–12i for a pure model adaptivity, a different model refinement pattern is obtained here due to the coupling effect with the adaptive mesh refinements, as already discussed above.

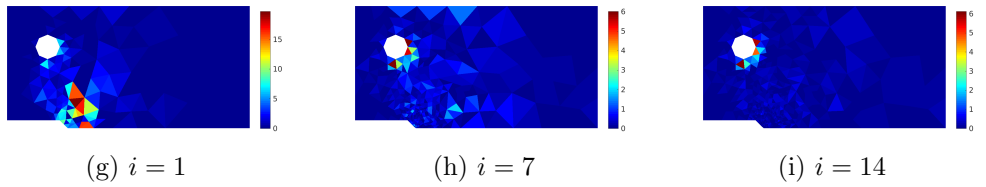
Localization of macro model error  $|\eta_m^e|$



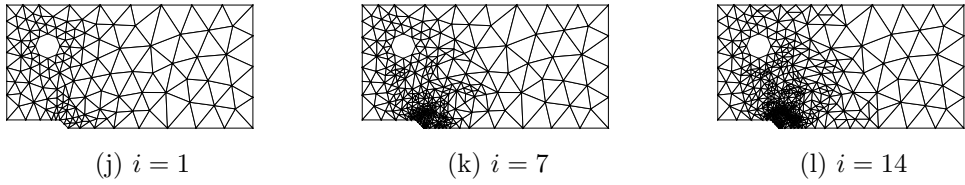
Adaptively refined model distributions  $n$



Localization of macro discretization error  $|\eta_h^e|$



Adaptively refined meshes



Model distributions for different error levels  
(green: mean-field and red: full-field FEM)

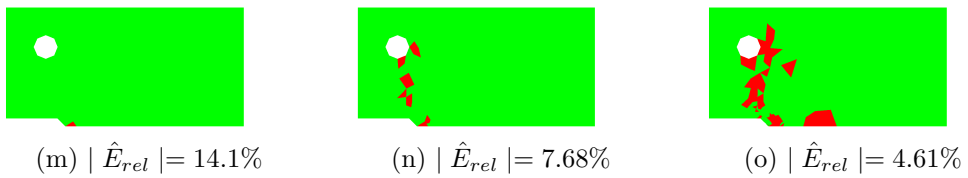


Figure 14: Example 1.3: Results of coupled adaptivity – Part I

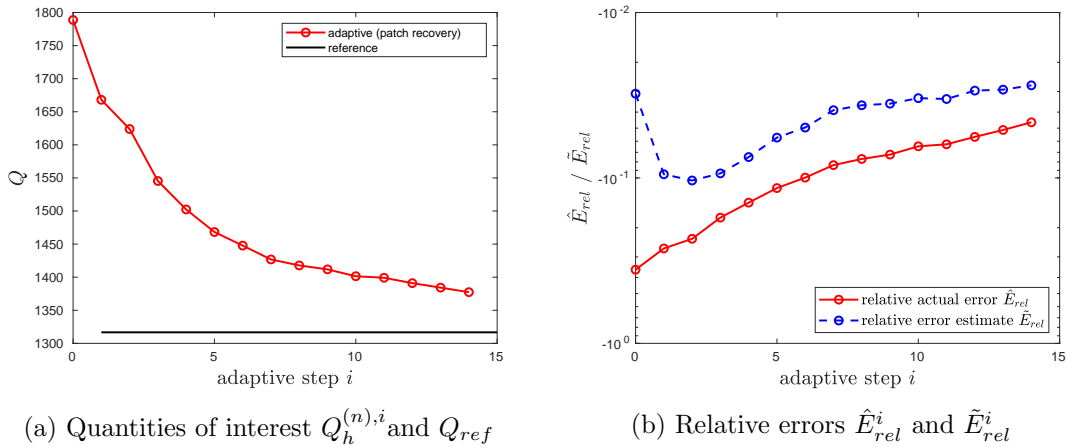


Figure 15: Example 1.3: Results of coupled adaptivity – Part II

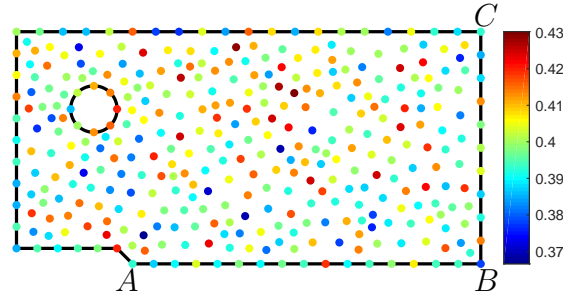
### 5.3 Example 2: Random composite

In this example, we deal with the random composite illustrated in Fig. 7b. The distribution of the fiber volume fraction  $c_f$  is macroscopically random and assumed to satisfy some statistical properties like the statistical mean  $\text{mean}(c_f) = 40\%$  and the standard deviation  $\text{dev}(c_f) = 0.012$ . We consider one specific realization shown in Fig. 16a for 357 given sampling points. Additionally, the distribution of fibers is random for each sampling point, as exemplarily shown for the sampling points  $A$ ,  $B$  and  $C$  in Figs. 16b–16d, respectively. This sampling procedure is done once for all the following FE computations and serves as a basis for determining the underlying microstructure for each macro element. In our calculations, the underlying microstructure for each element is assumed to be the same as of the sampling point with a nearest distance from the element center. Furthermore, all fibers are assumed to have a same diameter, such that different volume fractions can be reached by adapting the size of the matrix. As for Example 1, the model hierarchy in Eq. (58) is used. Despite of the random composite rather than a periodic one, the periodic boundary condition (13) is chosen for a fast convergence rate, see e.g. [48, 26, 15].

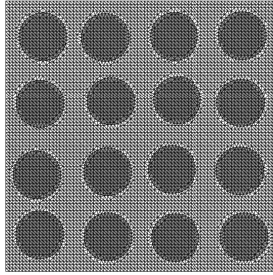
On this basis, as for Example 1.3, we consider a fully coupled adaptivity using Algorithm 1. For an investigation of hierarchical unit cells, a larger refinement ratio  $\alpha = 6\%$  is used. Local model error indicators  $|\eta_m^e|$  and local discretization error indicators  $|\eta_h^e|$  in Eq. (61) are depicted in Figs. 17a–17c and Figs. 17g–17i for different adaptive steps  $i$ , respectively. In the course of the adaptive refinements, both of them are balanced and significantly reduced. The balance effect is weaker around the hole due to the artificial constraint avoiding a mesh refinement there, see Figs. 17h and 17i. As shown in Figs. 17j–17l, the local mesh refinements are mainly located within the local domain  $\bar{\Omega}'$  in the quantify of interest (63) at the beginning and then spread to surrounding regions for a balanced discretization error distribution. Similar trends can also be found for model refinements shown in Figs. 17d–17f. A maximal hierarchical order  $n = 4$  is achieved in Fig. 17f for a very small region, whereas for a comparably large region a basic unit cell  $n = 2$  suffices to consider hierarchical unit cells. This illustrates the power of the periodic boundary condition even for the random composite under study.

For an effectiveness study, Fig. 18a shows the quantity of interest  $Q_h^{(n),i}$  versus adaptive steps, where a convergence to the reference value  $Q_{ref}$  can be clearly observed. Here,  $Q_{ref}$  is obtained by using a mesh, that is refined uniformly once from the last adaptive mesh in Fig. 17l, with a uniform model distribution  $n(\bar{\mathbf{x}}) = const. = 5$ . In Fig. 18b, the relative actual error  $\hat{E}_{rel}^i$  in Eq. (65) is shown to be effectively reduced by the adaptive approach, where an additional comparison to the relative error estimate  $\tilde{E}_{rel}^i$  in Eq. (66) showing a good effectivity is given. Additionally, Figs. 17m–17o depict several model distributions obtained by the adaptive approach for different error levels, showing that the actual error  $\hat{E}_{rel}$  can be reduced from 37.1% for the initial step to 4.98% by a use of the FEM in a comparably small region. A similar model refinement pattern as for Example 1.3 in Figs. 17m–17o is obtained here due to the coupling effect with the adaptive mesh refinements. The effectiveness of the proposed adaptive approach is confirmed again.

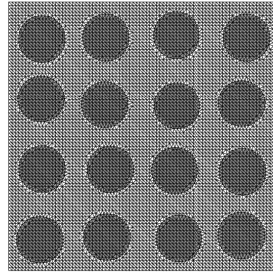
In view of a numerical efficiency, compared to a uniform model distribution  $n(\bar{\mathbf{x}}) = const. = 2$ , the model distributions in Figs. 17m–17o achieve a speed-up factor of 13, 4.8 and 2.9, respectively.



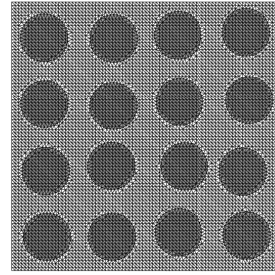
(a) Heterogeneous distribution of the fiber volume fraction  $c_f$  on chosen sampling points



(b) Point A for  $n_s = 4$



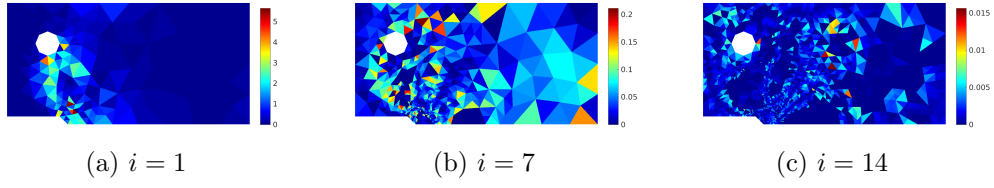
(c) Point B for  $n_s = 4$



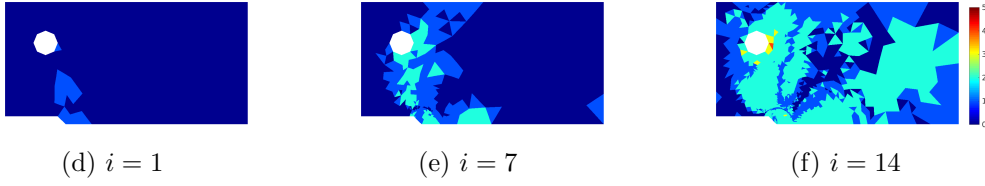
(d) Point C for  $n_s = 4$

Figure 16: Example 2: Illustration of a random composite

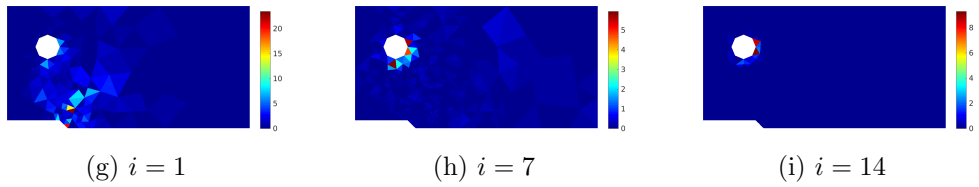
Localization of macro model error  $|\eta_m^e|$



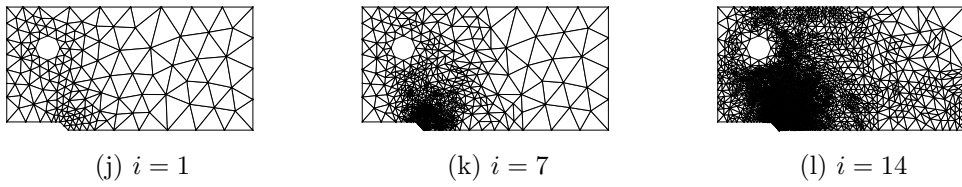
Adaptively refined model distributions  $n$



Localization of macro discretization error  $|\eta_h^e|$



Adaptively refined meshes



Model distributions for different error levels  
(green: mean-field and red: full-field FEM)

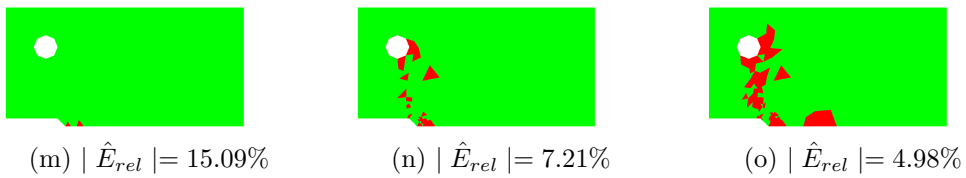


Figure 17: Example 2: Results of coupled adaptivity – Part I

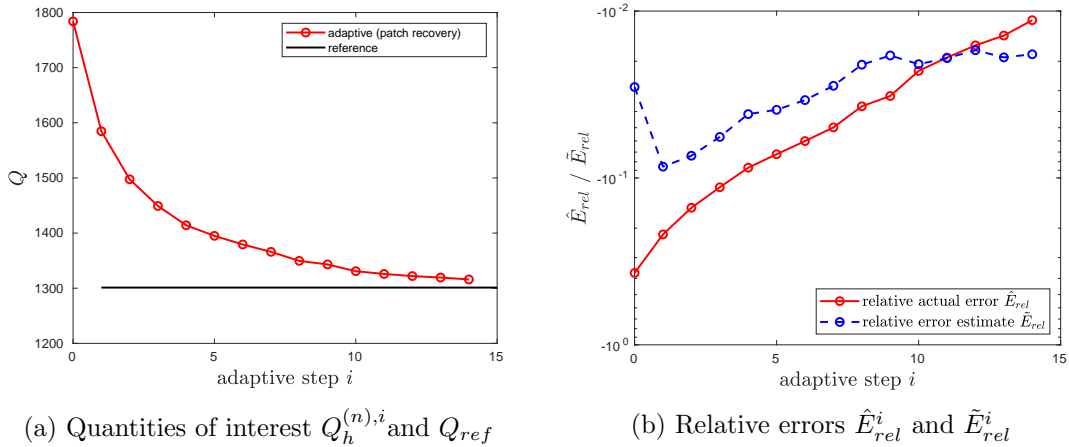


Figure 18: Example 2: Results of coupled adaptivity – Part II

## 6 Conclusion and outlook

This work presents a continuation of our previous work [25] by considering two major concerns arising in homogenization of linear elastic heterogeneous materials:

- The need for a full-field approximation obtained by a computational method (here FEM) where an analytical (mean-field) method does not suffice for the pursued accuracy level.
- An adaptive selection of unit cell size for a further accuracy improvement of computational methods.

We have shown that these two concerns can be simultaneously addressed by an appropriately formulated model hierarchy within the framework of goal-oriented adaptivity. Three typical micro boundary conditions have been examined and suggested to be chosen prior to the adaptive approach. Considering both model and discretization errors, the proposed adaptive approach has been shown to be effective for two different classes of materials. Compared to a uniform  $FE^2$  approach, a promising speed-up factor is achieved by the model distribution obtained from model adaptivity.

The proposed methodology provides a basis for an extension to nonlinear homogenization problems, like large deformations or plasticity, for future work. Model adaptivity for reduced order homogenization schemes is of our particular interest. Our previous work [23] developed an adaptive reduced order homogenization scheme on an empirical basis. For an error control, a framework of goal-oriented adaptivity should be incorporated in future. Furthermore, an eventuell mathematical proof of the assumption in Fig. 4b is another challenging task.

## Acknowledgment

This paper is based on investigations supported by the Deutsche Forschungsgemeinschaft (DFG) under grant MA 1979/30-1.

## A Several well-established mean-field methods

In the following, we describe some well-established mean-field methods by specifying the single inclusion problem in Fig. 3b.

### A.1 Eshelby (dilute) method

Typically in micromechanics, a prescribed macro strain tensor  $\bar{\boldsymbol{\varepsilon}}$  is ensured by the linear displacement boundary condition (11), while a prescribed macro stress tensor  $\bar{\boldsymbol{\sigma}}$  is imposed by the traction boundary condition (12). The Eshelby method considers a single inclusion problem by defining

$$\mathbb{C}' := \mathbb{C}_0, \quad \boldsymbol{\varepsilon}' := \bar{\boldsymbol{\varepsilon}}, \quad (\text{A.1})$$

where the inclusion interaction is completely neglected. It follows from Eq. (32) that

$$\mathbb{A}_i^{\text{dilute}} = (\mathbb{I}^S + \mathcal{S}_i^0 \mathbb{C}_0^{-1} (\mathbb{C}_i - \mathbb{C}_0))^{-1}, \quad (\text{A.2})$$

where  $\mathcal{S}_i^0$  is the Eshelby tensor depending on the matrix material property  $\mathbb{C}_0$  and the shape of the inclusion  $i$ . Inserting Eq. (A.2) into Eq. (25a) renders the *dilute* estimate of  $\bar{\mathbb{C}}$  as

$$\bar{\mathbb{C}}^{\text{dilute}} = \mathbb{C}_0 + \sum_{i=1}^{N_i} c_i (\mathbb{C}_i - \mathbb{C}_0) (\mathbb{I}^S + \mathcal{S}_i^0 \mathbb{C}_0^{-1} (\mathbb{C}_i - \mathbb{C}_0))^{-1}. \quad (\text{A.3})$$

Alternatively, one may proceed with Eq. (12) and have  $\boldsymbol{\sigma}' = \bar{\boldsymbol{\sigma}}$ . Then, it follows from Eq. (34) that

$$\mathbb{B}_i^{\text{dilute}} = (\mathbb{S}_i - \mathcal{S}_i^0 (\mathbb{S}_i - \mathbb{S}_0))^{-1} \mathbb{S}_0, \quad (\text{A.4})$$

together with Eq. (25b), leading to the dilute estimate of  $\bar{\mathbb{S}}$  as

$$\bar{\mathbb{S}}^{\text{dilute}} = \mathbb{S}_0 + \sum_{i=1}^{N_i} c_i (\mathbb{S}_i - \mathbb{S}_0) (\mathbb{S}_i - \mathcal{S}_i^0 (\mathbb{S}_i - \mathbb{S}_0))^{-1} \mathbb{S}_0. \quad (\text{A.5})$$

It is not difficult to identify  $\bar{\mathbb{C}}^{\text{dilute}} \bar{\mathbb{S}}^{\text{dilute}} \neq \mathbb{I}^S$ , such that the dilute estimate is not *reciprocal-invariant*. In other words, the dilute method gives different predictions on effective properties, depending on the applied boundary conditions (11) or (12). In contrast to that, the methods introduced in the subsequent subsections are all reciprocal-invariant.

### A.2 Mori-Tanaka method

To take into account the inclusion interaction, the work [41] suggests a single inclusion problem by defining

$$\mathbb{C}' := \mathbb{C}_0, \quad \boldsymbol{\varepsilon}' := \boldsymbol{\varepsilon}_0, \quad (\text{A.6})$$

where  $\boldsymbol{\varepsilon}_0$  is the average strain in the matrix material. It is shown that the strain localization tensor for the inclusion  $i$  in Eq. (32) becomes

$$\mathbb{A}_i^{\text{MT}} = \mathbb{A}_i^0 (c_0 \mathbb{I}^S + \sum_{j=1}^{N_i} c_j \mathbb{A}_j^0)^{-1}, \quad (\text{A.7})$$

where the local localization tensor  $\mathbb{A}_i^0$  is the same as Eq. (A.2), i.e.

$$\mathbb{A}_i^0 = (\mathbb{I}^S + \mathcal{S}_i^0 \mathbb{C}_0^{-1} (\mathbb{C}_i - \mathbb{C}_0))^{-1}. \quad (\text{A.8})$$

Finally, inserting Eq. (A.7) into Eq. (25a) renders

$$\bar{\mathbb{C}}^{\text{MT}} = \mathbb{C}_0 + \sum_{i=1}^{N_i} c_i (\mathbb{C}_i - \mathbb{C}_0) \left( \mathbb{A}_i^0 (c_0 \mathbb{I}^S + \sum_{j=1}^{N_i} c_j \mathbb{A}_j^0)^{-1} \right). \quad (\text{A.9})$$

### A.3 Self-consistent method

The self-consistent method [27] assumes

$$\mathbb{C}' := \bar{\mathbb{C}}, \quad \boldsymbol{\varepsilon}' := \bar{\boldsymbol{\varepsilon}}, \quad (\text{A.10})$$

such that Eq. (32) becomes

$$\mathbb{A}_i^{\text{SC}} = \left( \mathbb{I}^S + \bar{\mathcal{S}}_i (\bar{\mathbb{C}}^{\text{SC}})^{-1} (\mathbb{C}_i - \bar{\mathbb{C}}^{\text{SC}}) \right)^{-1}, \quad (\text{A.11})$$

where  $\bar{\mathcal{S}}_i$  differs from  $\mathcal{S}_i^0$  by using the effective elasticity tensor  $\bar{\mathbb{C}}^{\text{SC}}$  rather than the elasticity tensor of the matrix  $\mathbb{C}_0$ . Inserting Eq. (A.11) into Eq. (25a) renders the self-consistent estimate of  $\bar{\mathbb{C}}$  as

$$\bar{\mathbb{C}}^{\text{SC}} = \mathbb{C}_0 + \sum_{i=1}^{N_i} c_i (\mathbb{C}_i - \mathbb{C}_0) \left( \mathbb{I}^S + \bar{\mathcal{S}}_i (\bar{\mathbb{C}}^{\text{SC}})^{-1} (\mathbb{C}_i - \bar{\mathbb{C}}^{\text{SC}}) \right)^{-1}. \quad (\text{A.12})$$

Clearly, Eq. (A.12) is an implicit equation, which has to be solved iteratively.

### A.4 Interaction direct derivative (IDD)

The so-called interaction direct derivative (IDD) method of [64, 10] possesses the following features:

- It has an explicit structure.
- It is valid for multiphase composites with various inclusion geometries and isotropic or anisotropic properties.
- It accounts for interaction between inclusions and matrix as well as inclusion distributions.

The IDD method is an explicit version of the effective self-consistent method, which is deduced from the generalized self-consistent method [6] based on a three-phase model. As shown in [64], it may be interpreted as the single inclusion problem in Fig. 3b with

$$\mathbb{C}' := \mathbb{C}_0, \quad \boldsymbol{\sigma}' := \boldsymbol{\sigma}^E = \left( \mathbb{I}^S - \sum_{i=1}^{N_i} \left( c_i \mathcal{C}_{D_i} \sum_{j=1}^{N_i} ((\mathbb{S}_j - \mathbb{S}_0)^{-1} + \mathcal{C}_j) \right) \right)^{-1} \bar{\boldsymbol{\sigma}}. \quad (\text{A.13})$$

Here  $\mathcal{C}_j$  is the eigenstiffness tensor computed by using the matrix material property  $\mathbb{C}_0$  and the geometry of the inclusion  $j$ , while the eigenstiffness tensor  $\mathcal{C}_{D_i}$  is computed by using the matrix material property  $\mathbb{C}_0$  and the geometry of the so-called *inclusion-matrix cell*  $D_i$ , which is designed to account for inclusion distributions. The effective elasticity tensor of the IDD estimate reads

$$\bar{\mathbb{C}}^{\text{IDD}} = \mathbb{C}_0 + \left( \mathbb{I}^S - \sum_{j=1}^{N_i} c_j (\mathbb{C}_j - \mathbb{C}_0) \mathbb{A}_j^* \mathcal{S}_{D_j}^0 \mathbb{S}_0 \right)^{-1} \sum_{i=1}^{N_i} c_i (\mathbb{C}_i - \mathbb{C}_0) \mathbb{A}_i^*, \quad (\text{A.14})$$

where

$$\mathbb{A}_i^* = (\mathbb{I}^S + \mathcal{S}_i^0 \mathbb{C}_0^{-1} (\mathbb{C}_i - \mathbb{C}_0))^{-1}, \quad (\text{A.15})$$

and  $\mathcal{S}_i^0$  is the Eshelby tensor computed by using the matrix material property  $\mathbb{C}_0$  and the geometry of the inclusion  $i$ , while the Eshelby tensor  $\mathcal{S}_{D_j}^0$  is computed by using the matrix material property  $\mathbb{C}_0$  and the geometry of an inclusion-matrix cell  $D_j$ . By comparing Eq. (A.14) with Eq. (25a), we conclude that

$$\mathbb{A}_i^{\text{IDD}} = (\mathbb{C}_i - \mathbb{C}_0)^{-1} \left( \mathbb{I}^S - \sum_{j=1}^{N_i} c_j (\mathbb{C}_j - \mathbb{C}_0) \mathbb{A}_j^* \mathcal{S}_{D_j}^0 \mathbb{S}_0 \right)^{-1} (\mathbb{C}_i - \mathbb{C}_0) \mathbb{A}_i^*. \quad (\text{A.16})$$

According to [64, 10], the geometry of the inclusion-matrix cell  $D_j$  accounts for the inclusion distribution. For anisotropic distributions, additional effort has to be paid to identify the correct geometry of  $D_j$ . For the orthotropic effective material in Fig. 7a, the inclusion-matrix cell would be a square rather than an ellipsoidal, thus violating the requirement of the IDD, i.e. ellipsoidal distribution given in [10]. For the model hierarchy in Eq. (58), the inclusion-matrix cell is assumed to be of the same shape of the corresponding inclusion for simplicity. As shown in Section 5.2, this simplification still provides a sufficient accuracy improvement to the self-consistent estimate in Eq. (A.12) for the considered example.

## B Some notations for a two-dimensional implementation

In the following, we declare some notations used in Section 5. In a two-dimensional case, a matrix representation of Eq. (18) takes the form

$$\bar{\underline{\sigma}} = \bar{\underline{\mathbb{C}}} \bar{\underline{\varepsilon}}, \quad (\text{B.1})$$

or more precisely

$$\begin{bmatrix} \bar{\sigma}_{11} \\ \bar{\sigma}_{22} \\ \bar{\sigma}_{12} \end{bmatrix} = \begin{bmatrix} \bar{C}_{11} & \bar{C}_{12} & \bar{C}_{14} \\ & \bar{C}_{22} & \bar{C}_{24} \\ \text{sym.} & & \bar{C}_{44} \end{bmatrix} \begin{bmatrix} \bar{\varepsilon}_{11} \\ \bar{\varepsilon}_{22} \\ 2 \cdot \bar{\varepsilon}_{12} \end{bmatrix}. \quad (\text{B.2})$$

For a plane strain state, we have  $\bar{\varepsilon}_{33} = 0$  and  $\bar{\sigma}_{33} \neq 0$  for the strain and the stress component normal to the plane, respectively. For an orthotropic material, Eq. (B.2) reduces to

$$\begin{bmatrix} \bar{\sigma}_{11} \\ \bar{\sigma}_{22} \\ \bar{\sigma}_{12} \end{bmatrix} = \begin{bmatrix} \bar{C}_{11} & \bar{C}_{12} & 0 \\ & \bar{C}_{22} & 0 \\ \text{sym.} & & \bar{C}_{44} \end{bmatrix} \begin{bmatrix} \bar{\varepsilon}_{11} \\ \bar{\varepsilon}_{22} \\ 2 \cdot \bar{\varepsilon}_{12} \end{bmatrix}. \quad (\text{B.3})$$

For the periodic composite in Fig. 7a, the relation  $\bar{C}_{11} = \bar{C}_{22}$  holds. Following the line of [50], we define three independent effective material parameters for this two-dimensional case, i.e. a bulk modulus and two shear moduli, as

$$\bar{K} := (\bar{C}_{11} + \bar{C}_{12})/2, \quad (\text{B.4a})$$

$$\bar{G}_1 := (\bar{C}_{11} - \bar{C}_{12})/2, \quad (\text{B.4b})$$

$$\bar{G}_2 := \bar{C}_{44}, \quad (\text{B.4c})$$

respectively. For an isotropic material like the random composite in Fig. 7b, the number of independent effective material parameters further reduces to two, due to the relation  $\bar{G}_1 = \bar{G}_2$ .

## References

- [1] Ainsworth M, Oden JT (2000) A posteriori error estimation in finite analysis. Pure and applied mathematics, John Wiley & Sons, New York
- [2] Babuska I, Whiteman J, Strouboulis T (2011) Finite Elements: An Introduction to the Methods and Error Estimation. Oxford University Press, New York
- [3] Becker R, Rannacher R (1996) A Feed-back approach to error control in finite element methods: basic analysis and examples. East-West Journal of Numerical Mathematics 4(4):237–264
- [4] Berveiller M, Zaoui A (1978) An extension of the self-consistent scheme to plastically-flowing polycrystals. J Mech Phys Solids 26:325–344
- [5] Braack M, Ern A (2003) A posteriori control of modeling errors and discretization errors. Multiscale Model Simul 1(2):221–238
- [6] Christensen R, Lo K (1979) Solutions for effective shear properties in three phase sphere and cylinder models. Journal of the Mechanics and Physics of Solids 27(4):315–330
- [7] Cirak F, Ramm E (1998) A posteriori error estimation and adaptivity for linear elasticity using the reciprocal theorem. Comput Methods Appl Mech Engrg 156:351–362
- [8] Dederichs PH, Zeller R (1973) Variational treatment of the elastic constants of disordered materials. Zeitschrift für Physik 259(2):103–116
- [9] Drugan W, Willis J (1996) A micromechanics-based nonlocal constitutive equation and estimates of representative volume element size for elastic composites. Journal of the Mechanics and Physics of Solids 44(4):497–524
- [10] Du DX, Zheng QS (2002) A further exploration of the interaction direct derivative (IDD) estimate for the effective properties of multiphase composites taking into account inclusion distribution. Acta Mechanica 157(1-4):61–80

- [11] Dvorak GJ, Benveniste Y (1992) On transformation strains and uniform fields in multiphase elastic media. *Proc R Soc A* 437:291–310
- [12] Eriksson K, Estep D, Hansbo P, Johnson C (1995) Introduction to Adaptive Methods for Differential Equations. *Acta Numerica* 4:150–158
- [13] Eshelby JD (1957) The determination of the elastic field of an ellipsoidal inclusion, and related problems. *Proc R Soc Lond A* 241(1226):376–396
- [14] Feyel F, Chaboche JL (2000) Fe2 multiscale approach for modelling the elastoviscoplastic behaviour of long fibre sic/ti composite materials. *Computer methods in applied mechanics and engineering* 183(3-4):309–330
- [15] Fish J (2013) Practical multiscale. John Wiley & Sons, The Atrium
- [16] Forest S (2002) Homogenization methods and mechanics of generalized continua-part 2. *Theoretical and applied mechanics* (28-29):113–144
- [17] Forest S, Sab K (1998) Cosserat overall modeling of heterogeneous materials. *Mechanics Research Communications* 25(4):449–454
- [18] Geers M, Kouznetsova V, Brekelmanns W (2010) Multi-scale computational homogenization: Trends and challenges. *Journal of Computational and Applied Mathematics* 234:2175–2182
- [19] Hill R (1963) Elastic properties of reinforced solids: some theoretical principles. *Journal of the mechanics and physics of solids* 11:357–372
- [20] Hornung U (1996) Homogenization and porous media. Springer, New York
- [21] Jiang M, Alzebedeh K, Jasiuk I, Ostoja-Starzewski M (2001) Scale and boundary conditions effects in elastic properties of random composites. *Acta Mechanica* 148(1-4):63–78
- [22] Jiang M, Ostoja-Starzewski M, Jasiuk I (2001) Scale-dependent bounds on effective elastoplastic response of random composites. *Journal of the Mechanics and Physics of Solids* 49(3):655–673
- [23] Ju X, Mahnken R (2016) An NTFA-based homogenization framework considering softening effects. *Mechanics of Materials* 96:106–125
- [24] Ju X, Mahnken R (2017) Goal-oriented adaptivity for linear elastic micromorphic continua based on primal and adjoint consistency analysis. *International Journal for Numerical Methods in Engineering* 112(8):1017–1039
- [25] Ju X, Mahnken R (2017) Model adaptivity on effective elastic properties coupled with adaptive FEM. *Computer methods in Applied Mechanics and Engineering* 322:208–237
- [26] Khisaeva Z, Ostoja-Starzewski M (2006) On the size of RVE in finite elasticity of random composites. *Journal of elasticity* 85(2):153

- [27] Kröner E (1958) Berechnung der elastischen Konstanten des Vielkristalls aus den Konstanten des Einkristalls. *Z Phys* 151:504–518
- [28] Kröner E (1977) Bounds for effective elastic moduli of disordered materials. *J Mech Phys Solids* 25:137–155
- [29] Ladevèze P, Pelle J (2005) Mastering calculations in linear and non linear mechanics. Mechanical Engineering Series, Springer, New York
- [30] Lagoudas DC, Gavazzi AC, Nigam H (1991) Elastoplastic behavior of metal matrix composites based on incremental plasticity and the Mori–Tanaka averaging scheme. *Comput Mech* 8:193–203
- [31] Lahellec N, Suquet P (2007) On the effective behavior of nonlinear inelastic, composites: I. Incremental variational principles. *Journal of the Mechanics and Physics of Solids* 55:1932–1963
- [32] Lahellec N, Suquet P (2007) On the effective behavior of nonlinear inelastic, composites: II. A second-order procedure. *Journal of the Mechanics and Physics of Solids* 55:1964–1992
- [33] Larsson F, Runesson K (2004) Modeling and discretization errors in hyperelasto-(visco-)plasticity with a view to hierarchical modeling. *Comput Methods Appl Mech Engrg* 193:5283–5300
- [34] Larsson F, Runesson K (2006) Adaptive computational meso-macro-scale modeling of elastic composites. *Comput Methods Appl Mech Engrg* 195:324–338
- [35] Larsson F, Runesson K (2007) RVE computation with error control and adaptivity: the power of duality. *Comp Meths* 39:647–661
- [36] Mahnken R (2013) Goal-oriented adaptive refinement for phase field modeling with finite elements. *International Journal for Numerical Methods in Engineering* 94(4):418–440
- [37] Maier M (2015) Duality-based adaptivity of model and discretization in multi-scale finite-element methods. PhD thesis, Ruprecht Karl University of Heidelberg
- [38] Michel J, Suquet P (2003) Nonuniform transformation field analysis. *International Journal for Solids and Structures* 40:6937–6955
- [39] Michel JC, Moulinec H, Suquet P (1999) Effective properties of composite materials with periodic microstructure: a computational approach. *Computer methods in applied mechanics and engineering* 172(1-4):109–143
- [40] Miehe C, Koch A (2002) Computational micro-to-macro transitions of discretized microstructures undergoing small strains. *Archive of Applied Mechanics* 72(4-5):300–317

- [41] Mori T, Tanaka K (1973) Average stress in matrix and average elastic energy of materials with misfitting inclusions. *Acta Metall* 21:571–574
- [42] Moulinec H, Suquet P (1998) A numerical method for computing the overall response of nonlinear composites with complex microstructure. *Computer methods in applied mechanics and engineering* 157(1-2):69–94
- [43] Mura T (1987) *Micromechanics of defects in solids*. Martinus Nijhoff Publishers, The Hague
- [44] Oden JT, Prudhomme S (2002) Estimation of Modeling Error in Computational Mechanics. *Journal of Computational Physics* 182:496–515
- [45] Oden JT, Vemaganti KS (2000) Estimation of local modeling error and goal-oriented adaptive modeling of heterogeneous materials; Part I: Error Estimates and Adaptive Algorithms. *Journal of Computational Physics* 164:22–47
- [46] Oden JT, Prudhomme S, Hammerand D, Kuczma M (2001) Modeling error and adaptivity in nonlinear continuum mechanics. *Comput Methods Appl Mech Eng* 190:6663–6684
- [47] Oden JT, Prudhomme S, Romkes A, Bauman P (2006) Multiscale modelling of physical phenomena: adaptive control of models. *SAIM J SCI Comput* 28:2359–2389
- [48] Ostoja-Starzewski M (2007) *Microstructural randomness and scaling in mechanics of materials*. Chapman and Hall/CRC, London
- [49] Paraschivoiu M, Peraire J, Patera A (1997) A posteriori finite element bounds for linear-functional outputs of elliptic partial differential equations. *Comput Methods Appl Mech Engrg* 150(1):289–312, DOI 10.1016/S0045-7825(97)00086-8
- [50] Pecullan S, Gibiansky L, Torquato S (1999) Scale effects on the elastic behavior of periodic and hierarchical two-dimensional composites. *Journal of the Mechanics and Physics of Solids* 47(7):1509–1542
- [51] Perić D, de Souza Neto E, Feijóo R, Partovi M, Molina A (2011) On micro-to-macro transitions for multi-scale analysis of non-linear heterogeneous materials: unified variational basis and finite element implementation. *International Journal for Numerical Methods in Engineering* 87(1-5):149–170
- [52] Ponte Castañeda P, Suquet P (1998) Nonlinear composites. *Advances in Applied Mechanics* 34:171–302
- [53] Ponte-Castañeda P (2012) A finite-strain constitutive theory for electro-active polymer composites via homogenization. *International Journal of Non-Linear Mechanics* 47(2):293–306

- [54] Prudhomme S, Oden JT (1999) On goal-oriented error estimation for elliptic problems: application to the control of pointwise errors. *Comput Methods Appl Mech Engrg* 176(1–4):313–331, DOI 10.1016/S0045-7825(98)00343-0
- [55] Qu J, Cherkaoui M (2006) *Fundamentals of Micromechanics of Solids*. Wiley, Hoboken, New Jersey
- [56] Rüter M (2003) *Error-controlled Adaptive Finite Element Methods in Large Strain Hyperelasticity and Fracture Mechanics*. PhD thesis, University of Hannover, Hannover
- [57] Sanchez-Palencia E (1987) General introduction to asymptotic methods. In: *Homogenization techniques for composite media*, Springer, pp 121–136
- [58] Stein E (ed) (2003) *Error-controlled Adaptive Finite Elements in Solid Mechanics*. Wiley, Chichester
- [59] Stein E, Ohnibus S, Rüter M (2001) Hierarchical model-and discretization-error estimation of elasto-plastic structures. In: *Mechanics for a New Millennium*, Kluwer Academic Publishers, Netherlands, pp 373–388
- [60] Vemaganti KS, Oden JT (2001) Estimation of local modeling error and goal-oriented adaptive modeling of heterogeneous materials; Part II: a computational environment for adaptive modeling of heterogeneous elastic solids. *Comput Methods Appl Mech Engrg* 190:6089–6124
- [61] Verfürth R (1996) *A Review of A Posteriori Error Estimation and Adaptive Mesh-Refinement Techniques*. Wiley-Teubner, Stuttgart
- [62] Widany KU, Mahnken R (2016) Dual-based adaptive FEM for inelastic problems with standard FE implementations. *Int J Numer Meth Engng* 107:127–154
- [63] Yvonnet J, He QC (2007) The reduced model multiscale method (R3M) for the non-linear homogenization of hyperelastic media at finite strains. *Journal of Computational Physics* 223:341–368
- [64] Zheng QS, Du DX (2001) An explicit and universally applicable estimate for the effective properties of multiphase composites which accounts for inclusion distribution. *Journal of the Mechanics and Physics of Solids* 49(11):2765–2788
- [65] Zohdi TI, Wriggers P (2008) *Introduction to computational micromechanics*. Springer, Berlin
- [66] Zohdi TI, Oden JT, Rodin GJ (1996) Hierarchical modeling of heterogeneous bodies. *Comput Methods Appl Mech Eng* 138:273–298



---

## Paper C

Xiaozhe Ju and Rolf Mahnken

*An NTFA-based homogenization framework considering softening effects*

Mechanics of Materials 96 (2016), 106-125

---



# An NTFA-based homogenization framework considering softening effects

Xiaozhe Ju and Rolf Mahnken

Chair of Engineering Mechanics, University of Paderborn,  
Warburger Str. 100, 33098 Paderborn, Germany

## Abstract

In this work, we consider a two-scale mechanical problem of solids, where a microscopic heterogeneity is taken into account. In addition to plasticity, another irreversible process is our focus: softening, which is introduced on the micro scale and homogenized on the macro scale by model reduction with the so-called nonuniform transformation field analysis (NTFA, originally proposed by Michel and Suquet, 2003). Based on dissipative considerations, new NTFA constitutive equations with even model structure, accounting for softening effects, are proposed and validated theoretically and numerically for a homogeneous microstructure. For an accuracy improvement, we propose two new methods: the 'uneven NTFA' method and the 'adaptive NTFA' method, which introduce the additional aspects of parameter identification and adaptive modeling, respectively. The related numerical issues of both new methods are outlined. Two procedures for mode identification are studied for the present case, where the modes are actually basis functions for the reduced homogenization scheme. By means of the finite element method (FEM), numerical examples with regard to a fiber-reinforced composite are presented, where the accuracy and the numerical efficiency of the NTFA methods are investigated by comparison with the FEM solution. The mesh dependence of the different NTFA methods is also studied.

**Keywords:** finite element method, multiscale simulation, nonuniform transformation field analysis, continuum damage mechanics, parameter identification, adaptive modeling

## 1 Introduction

In general, solid materials in industrial engineering are treated as homogeneous, from a structural point of view. Thus, with the finite element method (FEM), they are constitutively modeled solely on the macro scale, under the assumption of homogeneity. However, upon increasing the resolution on a much smaller scale, the homogeneity is lost due to a heterogeneous microstructure. Therefore, the enhancement of the modern computational level in the last decades has led to a so-called

multiscale simulation. Here the heterogeneity, optionally at a micro level, is considered in a separate domain, which is attached to the macro domain. The macro domain is usually assumed to be homogeneous, whose effective quantities such as stresses are obtained by averaging quantities of the underlying micro domain.

In recent years the international research tends to develop accurate approaches for the homogenization. A so-called  $FE^2$  method drew some attentions, because of the outstanding accuracy as well as the simplicity of the theory. Several researches focused on, e.g. the boundary condition (see [16, 33]) or the gradient extensions (see [17, 18]) etc. For instance, an overview on these issues can be found in [13]. However, the major drawback of this method is the enormous computational cost, which makes a structural computation impracticable. Therefore, proper procedures of model reduction are required.

To this end, a so-called nonuniform transformation field analysis (NTFA) was introduced by [26], where the consideration of the nonuniform plastic strain fields in the underlying micro domain is simplified, such that the computational effort can be significantly reduced. This approximate model is a generalization of the transformation field analysis (TFA) proposed by Dvorak and coworkers (see [2, 3]), where the microscopic fields of internal variables are assumed to be piecewise uniform. The NTFA overcomes the extremely stiff prediction of the effective stresses by the TFA, leading to an improved accuracy, as demonstrated by [26, 27] for two-dimensional computations of composites. In combination with the outstanding computational efficiency, a remarkable efficiency-accuracy ratio of the NTFA is striking, which was also confirmed for the three-dimensional implementation e.g. by [7, 6].

In the context of the NTFA, most of the present research is focused on the extension or generalization of its theory to allow for more microscopic material models. Amongst them, [37] dealt with incompressible and compressible viscoplasticity and proposed firstly a Karhunen-Loève decomposition based approach to identify a set of basis functions. A further application to cyclic loading conditions and life time predictions was addressed in [28]. Pressure-dependent materials were considered in [15], while a generalization to viscoelastic composites was addressed by [8]. Subsequently, an extended version of [8] accounting for more viscoelastic phases in the presence of aging and swelling effects was proposed by [19]. Furthermore, an approach using a mixed incremental formulation that handles e.g. nonlinear viscous materials and crystal plasticity was developed by [9] and numerically implemented with an GPU acceleration in [11]. Moreover, a so-called nonuniform TFA technique, tailored for shape memory alloys, was proposed by [40], while a comparison between this approach and the one of [9, 11] was given in [12]. Most recently, a so-called potential-based reduced basis model order reduction procedure considering materials with cohesive interfaces was developed by [10]. To the authors knowledge, very few contributions in literature are provided for consideration of the additional effect of damage or softening at present. In this work, we intend to give an adaptation of the NTFA to consider plasticity coupled with softening effects.

Our preparatory work by [39, 38] implements a thermo-mechanical coupled two scale framework, which is applied to reproduce the damage effect of a coating system. However, as the underlying scale problem, a mesomodel is chosen, where the Taylor assumption is adopted, i.e. a homogeneous distribution of the mesoscopic strain

fields is assumed. The NTFA-based framework proposed in this work considers a two scale problem undergoing small strains, under an isothermal condition. The major improvement is the additional consideration of heterogeneous microstructures.

Based on the assumption of even micro and macro model structures, where the macroscopic variables such as damage variable have the same evolution functions as their microscopic counterparts, a prototype model with uneven micro and macro model structures is proposed. More precisely, the accuracy of the NTFA predictions is improved at the expense of introduction of three additional correction parameters. In order to identify these new parameters, a gradient-free approach based on the Downhill-Simplex method (see e.g. [29]) is provided.

Moreover, for accuracy improvement, an alternative method based on the idea of adaptive modeling is proposed. It will be referred to as the adaptive NTFA method, where a reduced homogenization scheme is merely applied to those regions where sufficient accuracy is expected. The proposed adaptive method belongs to the class of a priori methods, sharing the common ideas with e.g. [36, 35, 34] in the context of POD (Proper Orthogonal Decomposition). Another class of error estimates based methods can be additionally found in the homogenization context (see e.g. [5, 31, 30, 20]).

The outline of this work is as follows: In Section 2, the multiscale problem is described and the constitutive equations applied on the micro scale are summarized; the theory of the NTFA is briefly reviewed, then, a new coupled model accounting for additional softening effects is derived; a prototype model with even model structure is described; for accuracy improvement, the *uneven NTFA* and the *adaptive NTFA* method are proposed. Subsequently, the framework of the numerical implementation based on the FEM is summarized in Section 3. Finally, Section 4 presents several numerical examples.

Notation: All quantities on the macro scale are symbolized by overlined letters like  $\overline{A}$ , and quantities on the micro scale are not overlined. The norm of a tensor or a vector  $\mathbf{a}$  is operated by  $\|\mathbf{a}\|$ . Additionally, the volume averaging operator on a domain  $\Omega$  is defined as

$$\langle \dots \rangle_{\Omega} = \frac{1}{\Omega} \int_{\Omega} \dots dv.$$

## 2 NTFA-based multiscale modeling considering softening effects

### 2.1 Multiscale problem

We consider a two scale problem of solids, where each material point at the macro level is associated with an additional microscopic problem. These relations are shown in Fig. 1, where  $\overline{\Omega}_0$  and  $\overline{\Omega}_t$  represent the macroscopic domains with respect to the initial and the current configuration, respectively. An analogous notation is used for the microscopic problems with the underlying domains  $\Omega_0$  and  $\Omega_t$ , called the representative volume elements (RVE).

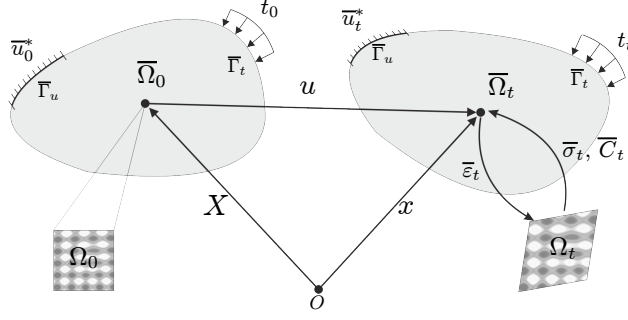


Figure 1: Illustration of a two scale problem

The displacement of a material point and the small strain tensor are defined as

$$1. \mathbf{u} = \mathbf{x} - \mathbf{X}, \quad 2. \boldsymbol{\varepsilon} = \text{sym}(\nabla_{\mathbf{x}} \mathbf{u}), \quad (1)$$

respectively. In Eq. (1.1),  $\mathbf{X}$  and  $\mathbf{x}$  are the location vectors with respect to a reference point  $O$ , respectively in the initial and the current state. Moreover, the macroscopic equilibrium problem  $\bar{P}$  and the underlying microscopic equilibrium problem  $P$  read

$$1. \bar{P}: \begin{cases} \text{Div}(\bar{\boldsymbol{\sigma}}) = \mathbf{0}, & \text{in } \bar{\Omega} \\ \bar{\boldsymbol{\sigma}} \bar{\mathbf{n}} = \bar{\mathbf{t}}, & \text{on } \bar{\Gamma}_t \\ \bar{\mathbf{u}} = \bar{\mathbf{u}}^*, & \text{on } \bar{\Gamma}_u \end{cases}, \quad 2. P: \begin{cases} \text{Div}(\boldsymbol{\sigma}) = \mathbf{0}, & \text{in } \Omega \\ \langle \boldsymbol{\varepsilon} \rangle = \bar{\boldsymbol{\varepsilon}} \end{cases}, \quad (2)$$

respectively. In problem  $\bar{P}$ ,  $\bar{\boldsymbol{\sigma}}$  denotes the macroscopic stress tensor and  $\bar{\mathbf{t}}$  represents the tractions imposed on  $\bar{\Gamma}_t$  satisfying the Neumann boundary condition.  $\bar{\mathbf{u}}^*$  indicates the prescribed displacements on the Dirichlet boundary  $\bar{\Gamma}_u$  with the properties  $\bar{\Gamma}_u \cup \bar{\Gamma}_t = \bar{\Gamma}$  and  $\bar{\Gamma}_u \cap \bar{\Gamma}_t = \emptyset$ , where  $\bar{\Gamma}$  symbolizes the total boundary for the macroscopic problem. For problem  $P$ , the boundary condition of the RVE is assumed to be linear, i.e. the displacement in spatial and temporal dependence  $\mathbf{u}_b(\mathbf{x}, t)$ , on the RVE boundary  $\Gamma$ , takes the form

$$\mathbf{u}_b(\mathbf{x}, t) = \bar{\boldsymbol{\varepsilon}}(t) \mathbf{x}, \quad \text{for } \mathbf{x} \in \Gamma. \quad (3)$$

Additionally, the scale transition, which couples both problems  $\bar{P}$  and  $P$ , is established by

$$1. \bar{\boldsymbol{\varepsilon}} = \langle \boldsymbol{\varepsilon}(\mathbf{x}) \rangle, \quad 2. \bar{\boldsymbol{\sigma}} = \langle \boldsymbol{\sigma}(\mathbf{x}) \rangle, \quad 3. \langle \boldsymbol{\sigma} : \dot{\boldsymbol{\varepsilon}} \rangle = \langle \boldsymbol{\sigma} \rangle : \langle \dot{\boldsymbol{\varepsilon}} \rangle = \bar{\boldsymbol{\sigma}} : \dot{\bar{\boldsymbol{\varepsilon}}}, \quad (4)$$

where  $\boldsymbol{\sigma}$  and  $\boldsymbol{\varepsilon}$  are the microscopic stress and the microscopic strain tensor, which are generally heterogeneously distributed within the RVE. The effective quantities  $\bar{\boldsymbol{\sigma}}$  and  $\bar{\boldsymbol{\varepsilon}}$  denote the macroscopic stress and the macroscopic strain tensor, respectively. For any microscopic statically admissible stress fields and any microscopic compatible strain fields, the so-called Hill-Mandel condition (4.3) is valid (see [14]).

## 2.2 Constitutive modeling at the micro level

It is assumed that the microscopic material behavior of each constituent resulting into a heterogeneous microstructure can be constitutively modeled. For an inelastic

constituent, the following typical continuum damage mechanic model, considering a rate-independent von Mises plasticity coupled with an isotropic damaging effect, is adopted:

1. Hooke's law:  $\boldsymbol{\sigma} = \mathbf{C}\boldsymbol{\varepsilon}^e = \boldsymbol{\sigma}^{vol} + \boldsymbol{\sigma}^{dev},$
2. Yield function:  $\phi = \|\boldsymbol{\sigma}_{eff}^{dev}\| - \sqrt{\frac{2}{3}}Y(q),$   
where  $\boldsymbol{\sigma}_{eff}^{dev} = \frac{\boldsymbol{\sigma}^{dev}}{W}, Y = Y_0 + R,$
3. Flow rule:  $\dot{\boldsymbol{\varepsilon}}^p = \dot{\lambda} \frac{\partial \phi}{\partial \boldsymbol{\sigma}^{dev}} = \frac{\dot{\lambda}}{W} \mathbf{n},$  where  $\mathbf{n} = \frac{\boldsymbol{\sigma}^{dev}}{\|\boldsymbol{\sigma}^{dev}\|},$  (5)
4. Strain like internal variable:  $\dot{q} = \sqrt{\frac{2}{3}}\dot{\lambda},$
5. Isotropic hardening stress:  $R = R(q),$
6. Isotropic damage variable:  $W = W(q).$

Here  $\boldsymbol{\sigma}^{vol}, \boldsymbol{\sigma}^{dev}$  and  $\mathbf{C}$  represent the volumetric, the deviatoric part of the stress tensor  $\boldsymbol{\sigma}$  and the elasticity tensor, respectively. The elastic strain tensor  $\boldsymbol{\varepsilon}^e$  is given by  $\boldsymbol{\varepsilon}^e = \boldsymbol{\varepsilon} - \boldsymbol{\varepsilon}^p,$  where  $\boldsymbol{\varepsilon}$  and  $\boldsymbol{\varepsilon}^p$  are the total and the plastic strain tensor. By means of the effective stress concept, the effective deviatoric stress tensor  $\boldsymbol{\sigma}_{eff}^{dev}$  is introduced, whereas  $Y$  and  $W$  represent the yield stress and the independent damage variable, both depending on the strain like internal variable  $q$ . Additionally, the dependent damage variable is defined as  $D = 1 - W,$  where  $0 \leq D \leq 1.$  Moreover,  $\lambda$  is a plastic multiplier satisfying the Karush-Kuhn-Tucker complementary conditions

$$\dot{\lambda}\phi = 0, \quad \phi \leq 0, \quad \dot{\lambda} \geq 0. \quad (6)$$

According to the second law of thermodynamics, considering inelastic cases ( $\dot{\lambda} > 0$  and  $\phi = 0$ ) and combining the equations (5.2), (5.3) and (5.4), we write the dissipation inequality as

$$\begin{aligned} \mathcal{D} = \boldsymbol{\sigma} : \dot{\boldsymbol{\varepsilon}}^p - R\dot{q} &= \frac{\dot{\lambda}}{W} \boldsymbol{\sigma} : \frac{\boldsymbol{\sigma}^{dev}}{\|\boldsymbol{\sigma}^{dev}\|} - R\dot{q} = \frac{\dot{\lambda}}{W} \|\boldsymbol{\sigma}^{dev}\| - R\dot{q} \\ &= \frac{\dot{\lambda}}{W} W \sqrt{\frac{2}{3}}Y - R\dot{q} = \sqrt{\frac{2}{3}}\dot{\lambda}(Y_0 + R) - \sqrt{\frac{2}{3}}R\dot{\lambda} = \sqrt{\frac{2}{3}}\dot{\lambda}Y_0 > 0, \end{aligned} \quad (7)$$

thus proving thermodynamic consistency of the present model.

### Remarks 2.1.

1. The model (5) is a simplified version of the model proposed by [23] and does not account for strength difference effects and damage caused by volumetric stresses, which are highlighted in [23]. An extension of the NTFA theory to consider these additional issues still remains an aspect of our work.
2. A typical model in continuum damage mechanics, where the damage state has impact on the elasticity tensor  $\mathbf{C},$  is not considered here for simplicity. It

would make the application of the superposition principle in the NTFA theory (see equations (9), (10.1) and (10.2) in Section 2.3) difficult, because of the dependence of the elasticity tensor on the changing damage state.

3. An alternative formulation for the yield function (5.2) that also accounts for softening effects is

$$\phi = \|\boldsymbol{\sigma}^{dev}\| - \sqrt{\frac{2}{3}}W(q)Y(q).$$

However, it would render a different associated flow rule.

4. A typical plasticity model with isotropic hardening can be simply recovered by setting  $W = 1 \neq W(q)$ . Hence, the present model may be considered as a generalized model of that.

### 2.3 Nonuniform transformation field analysis

The NTFA proposed by [26] is an order reduction based homogenization method, originally for plasticity problems, where the number of internal variables is significantly reduced to enhance the computational efficiency. This section intends to adapt this method to consider the additional softening effect introduced in Section 2.2. The key idea of the NTFA is the assumption that the initial space-time dependency of the plastic strain  $\boldsymbol{\varepsilon}^p(\mathbf{x}, t)$  can be approximately decomposed as

$$\boldsymbol{\varepsilon}^p(\mathbf{x}, t) \approx \sum_{i=1}^N \xi_i(t) \boldsymbol{\mu}^i(\mathbf{x}). \quad (8)$$

Here  $\xi^i$  is a set of time dependent variables named *mode activity coefficients*, while  $\boldsymbol{\mu}^i$  represents several spatial heterogeneous plastic strain fields, which are called *plastic modes*, having the same number  $N$  as  $\xi^i$ . Thereby, fairly large number of degrees of freedom in the case of the initial microscopic problem described in Eq. (2.2) is reduced to  $N$ , which is generally of the order of ten. Consequently, there are two essential tasks for the NTFA: 1. identification of plastic modes  $\boldsymbol{\mu}^i$  and 2. determination of the evolution of the mode activity coefficients  $\xi_i(t)$ .

According to the proposal of [26, 27] under consideration of the modification by [7], the choice of the plastic modes is free, provided the following four requirements are satisfied: 1. normalization condition, i.e.  $\langle \|\boldsymbol{\mu}^i\| \rangle_{\Omega_p} = 1$ ; 2. the support of each mode is entirely contained in one single material phase, for which macroscopic constitutive equations will be defined (see equations (23) and (24)); 3. incompressibility, i.e.  $\text{tr}(\boldsymbol{\mu}^i) = 0$ ; 4. orthogonality, i.e.  $\langle \boldsymbol{\mu}^i : \boldsymbol{\mu}^j \rangle = 0$ , when  $i \neq j$ .

In this work, we deal with microstructures, which contain merely one inelastic constituent (phase). Hence, a specific notation for the inelastic phases is not necessary.

We move on to the second task, under the assumption that the modes are known. In combination with Hooke's law (5-1), we rewrite the initial microscopic problem  $P$  in Eq. (2.2) as

$$P: \begin{cases} \text{Div}(\mathbf{C}(\boldsymbol{\varepsilon} - \boldsymbol{\varepsilon}^p)) = \mathbf{0}, & \text{in } \Omega \\ \langle \boldsymbol{\varepsilon} \rangle = \bar{\boldsymbol{\varepsilon}}. \end{cases} \quad (9)$$

According to the superposition principle under consideration of the approximation (8), similarly to e.g. [7, 6], the problem  $P$  becomes approximately the superposition of an elastic problem  $P_e$  and  $N$  eigenstress problems  $P_\sigma^i$  as

$$\begin{aligned} 1. P_e: & \begin{cases} \text{Div}(\mathbf{C}\boldsymbol{\varepsilon}_e) = \mathbf{0}, & \text{in } \Omega \\ \langle \boldsymbol{\varepsilon}_e \rangle = \bar{\boldsymbol{\varepsilon}} \end{cases}, \\ 2. P_\sigma^i: & \begin{cases} \text{Div}(\mathbf{C}(\boldsymbol{\varepsilon}_*^i - \boldsymbol{\mu}^i)) = \mathbf{0} \\ \langle \boldsymbol{\varepsilon}_*^i \rangle = \mathbf{0} \end{cases}, \quad i = 1, \dots, N, \end{aligned} \quad (10)$$

respectively. Here  $\boldsymbol{\varepsilon}_e$  and  $\boldsymbol{\varepsilon}_*^i$  denote the elastic strain and the eigenstrain tensor, respectively, thus leading to the localization rule for the microscopic strain field as

$$\boldsymbol{\varepsilon}(\mathbf{x}, t) = \boldsymbol{\varepsilon}_e(\mathbf{x}, t) + \sum_{i=1}^N \xi_i(t) \boldsymbol{\varepsilon}_*^i(\mathbf{x}) = \mathbf{A}(\mathbf{x}) \bar{\boldsymbol{\varepsilon}}(t) + \sum_{i=1}^N \xi_i(t) \boldsymbol{\varepsilon}_*^i(\mathbf{x}). \quad (11)$$

Furthermore, the fourth-order tensor  $\mathbf{A}(\mathbf{x})$  symbolizes the *elastic strain localization operator*, with  $\boldsymbol{\varepsilon}_e(\mathbf{x}, t) = \mathbf{A}(\mathbf{x}) \bar{\boldsymbol{\varepsilon}}(t)$  and  $\langle \mathbf{A}(\mathbf{x}) \rangle = \mathbf{1}$ . In principle,  $\mathbf{A}(\mathbf{x})$  can be determined either analytically or numerically. In this work, it will be determined numerically by several elastic computations (see Section 3.2 on more details). According to Hooke's law (5-1), in combination with the approximation (8) and Eq. (11), the localization rule for the microscopic stress field is derived by

$$\boldsymbol{\sigma}(\mathbf{x}, t) = \mathbf{C}(\mathbf{x}) \boldsymbol{\varepsilon}^e(\mathbf{x}, t) \approx \mathbf{C}(\mathbf{x}) \mathbf{A}(\mathbf{x}) \bar{\boldsymbol{\varepsilon}}(t) + \sum_{i=1}^N \xi_i(t) \boldsymbol{\sigma}_*^i(\mathbf{x}), \quad (12)$$

$$\text{where } \boldsymbol{\sigma}_*^i = \mathbf{C}(\boldsymbol{\varepsilon}_*^i - \boldsymbol{\mu}^i),$$

where  $\boldsymbol{\sigma}_*^i$  is the eigenstress tensor. Then, we formulate the macroscopic dissipation power  $\bar{\mathcal{D}}$  at a macroscopic material point by volume averaging of Eq. (7) and combine equations (8) and (12) as

$$\begin{aligned} \bar{\mathcal{D}} &= \langle \mathcal{D} \rangle = \langle \boldsymbol{\sigma} : \dot{\boldsymbol{\varepsilon}}^p - R\dot{q} \rangle \\ &= \sum_{i=1}^N \dot{\xi}_i \left( \langle \mathbf{A}^T \mathbf{C} \boldsymbol{\mu}^i \rangle : \bar{\boldsymbol{\varepsilon}} + \sum_{j=1}^N \xi_j \langle \boldsymbol{\sigma}_*^j : \boldsymbol{\mu}^i \rangle \right) - \langle R\dot{q} \rangle = \hat{\underline{\tau}} \cdot \dot{\hat{\underline{\xi}}} - \langle R\dot{q} \rangle. \end{aligned} \quad (13)$$

Here the mode activity coefficients are represented in vector form  $\hat{\underline{\xi}} = [\xi_1 \cdots \xi_i \cdots \xi_N]^T$  and their thermodynamic conjugates are denoted by a vector  $\hat{\underline{\tau}}$  as

$$\begin{aligned} \hat{\underline{\tau}} &= [\hat{\tau}_1 \quad \cdots \quad \hat{\tau}_i \quad \cdots \quad \hat{\tau}_N]^T, \\ \text{where } \hat{\tau}_i &= \langle \mathbf{A}^T \mathbf{C} \boldsymbol{\mu}^i \rangle : \bar{\boldsymbol{\varepsilon}} + \sum_{j=1}^N \xi_j \langle \boldsymbol{\sigma}_*^j : \boldsymbol{\mu}^i \rangle. \end{aligned} \quad (14)$$

Fritzen and Böhlke [7] suggest the orthonormal basis

$$\boldsymbol{\Sigma} = \begin{cases} \boldsymbol{\Sigma}^i = \mathbf{e}_i \otimes \mathbf{e}_i, & \text{for } i = 1, 2, 3 \\ \boldsymbol{\Sigma}^4 = \sqrt{2} \text{sym}(\mathbf{e}_1 \otimes \mathbf{e}_2), \\ \boldsymbol{\Sigma}^5 = \sqrt{2} \text{sym}(\mathbf{e}_1 \otimes \mathbf{e}_3), \\ \boldsymbol{\Sigma}^6 = \sqrt{2} \text{sym}(\mathbf{e}_2 \otimes \mathbf{e}_3), \end{cases} \quad (15)$$

defined by [4], primarily for their three-dimensional implementation, whereby any symmetric second-order tensor can be represented by a convenient vector notation. Note that the orthonormal basis  $\Sigma$  can be simply adapted for two-dimensional cases by omitting the components  $\Sigma^5$  and  $\Sigma^6$ . The macroscopic strain tensor  $\bar{\varepsilon}$  obtains its vector representation  $\widehat{\underline{\underline{\varepsilon}}}$  with coefficients  $\widehat{\underline{\underline{\varepsilon}}}_i = \bar{\varepsilon} : \Sigma^i$ ,  $i = 1, \dots, n_{st}$ . Here  $n_{st}$  denotes the number of stress components,  $n_{st} = 4$  and  $n_{st} = 6$  hold for two-dimensional and three-dimensional problems, respectively. Moreover, the system matrices  $\widehat{\underline{\underline{A}}}$  and  $\widehat{\underline{\underline{D}}}$  are defined with the coefficients

$$1. \widehat{A}_{ik} = \langle \mathbf{A}^T \mathbf{C} \boldsymbol{\mu}^i \rangle : \Sigma^k, \quad 2. \widehat{D}_{ij} = \langle \boldsymbol{\sigma}_*^j : \boldsymbol{\mu}^i \rangle, \quad i, j = 1, \dots, N, \quad k = 1, \dots, n_{st}, \quad (16)$$

respectively, such that the conjugate forces  $\widehat{\tau}$  can be rewritten in a simplified form as

$$\widehat{\tau} = \widehat{\underline{\underline{A}}}\widehat{\underline{\underline{\varepsilon}}} + \widehat{\underline{\underline{D}}}\widehat{\underline{\underline{\xi}}}. \quad (17)$$

Furthermore, the macroscopic stress tensor  $\bar{\boldsymbol{\sigma}}$  is obtained from volume averaging of Eq. (12) as

$$\bar{\boldsymbol{\sigma}}(t) = \langle \boldsymbol{\sigma}(\mathbf{x}, t) \rangle = \langle \mathbf{C}(\mathbf{x}) \mathbf{A}(\mathbf{x}) \rangle \bar{\boldsymbol{\varepsilon}}(t) + \sum_{i=1}^N \xi_i(t) \langle \boldsymbol{\sigma}_*^i \rangle = \bar{\mathbf{C}} \bar{\boldsymbol{\varepsilon}}(t) + \sum_{i=1}^N \xi_i(t) \langle \boldsymbol{\sigma}_*^i \rangle, \quad (18)$$

where  $\bar{\mathbf{C}} = \langle \mathbf{C}(\mathbf{x}) \mathbf{A}(\mathbf{x}) \rangle$  is the macroscopic elasticity tensor. By means of the orthonormal basis (15), the macroscopic stress tensor  $\bar{\boldsymbol{\sigma}}$  can be represented by the stress vector  $\widehat{\underline{\underline{\sigma}}}$  with coefficients  $\widehat{\underline{\underline{\sigma}}}_i = \bar{\boldsymbol{\sigma}} : \Sigma^i$ ,  $i = 1, \dots, n_{st}$ . Then, Eq. (18) obtains its convenient vector-matrix representation as

$$1. \widehat{\underline{\underline{\sigma}}} = \widehat{\underline{\underline{C}}}\widehat{\underline{\underline{\varepsilon}}} + \widehat{\underline{\underline{R}}}\widehat{\underline{\underline{\xi}}}, \quad \text{where} \quad 2. \widehat{R}_{ij} = \Sigma^i : \langle \boldsymbol{\sigma}_*^j \rangle, \quad i = 1, \dots, n_{st}, \quad j = 1, \dots, N, \quad (19)$$

where the system matrix  $\widehat{\underline{\underline{C}}}$  is the symmetric macroscopic elasticity matrix corresponding to the macroscopic elasticity tensor  $\bar{\mathbf{C}}$ . It will be evaluated numerically (see Section 3.2 for more details). Note that the relation

$$\widehat{\underline{\underline{R}}} = -\widehat{\underline{\underline{A}}}^T, \quad \text{for} \quad \mathbf{C} = \mathbf{C}^T, \quad (20)$$

holds (see e.g. [6]), indicating that the system matrices  $\widehat{\underline{\underline{A}}}$  and  $\widehat{\underline{\underline{R}}}$  do not need to be determined individually for the considered class of materials.

In accordance with the coupled model proposed by [26], we introduce the macroscopic hardening variable  $\bar{R}$  and the macroscopic independent damage variable  $\bar{W}$  representing the state of the whole inelastic phase. They both depend on the macroscopic equivalent plastic strain  $\bar{q}$ , whose rate is given by

$$\dot{\bar{q}} = \sqrt{\frac{2}{3}} \dot{\bar{\lambda}}, \quad (21)$$

where  $\bar{\lambda}$  is the macroscopic inelastic multiplier. Then, we can rewrite the macroscopic dissipative power in Eq. (13) as

$$\bar{D} = \widehat{\underline{\underline{\tau}}} \cdot \widehat{\underline{\underline{\dot{\xi}}}} - \frac{1}{\Omega} \int_{\Omega} R \dot{q} dv = \widehat{\underline{\underline{\tau}}} \cdot \widehat{\underline{\underline{\dot{\xi}}}} - \frac{1}{\Omega} \int_{\Omega_p} R \dot{q} dv = \widehat{\underline{\underline{\tau}}} \cdot \widehat{\underline{\underline{\dot{\xi}}}} - \frac{\Omega_p}{\Omega} \langle R \dot{q} \rangle_{\Omega_p} \approx \widehat{\underline{\underline{\tau}}} \cdot \widehat{\underline{\underline{\dot{\xi}}}} - c_p \bar{R} \dot{\bar{q}}, \quad (22)$$

where  $c_p$  denotes the volume fraction of the inelastic constituent in the total RVE, i.e.  $c_p = \Omega_p/\Omega$ . It shall be noted that the initial heterogeneous variable fields  $R(\mathbf{x})$  and  $q(\mathbf{x})$  are approximately treated as homogeneous here, i.e.  $\bar{R} = R(\mathbf{x}) = \text{const}$  and  $\bar{q} = q(\mathbf{x}) = \text{const}$ . Similarly to [26] and [7], the macroscopic yield function  $\bar{\phi}$  is proposed as

$$\bar{\phi}(\hat{\underline{\tau}}, \bar{q}) = \frac{\|\hat{\underline{\tau}}\|}{\bar{W}(\bar{q})} - \sqrt{\frac{2}{3}}c_p\bar{Y}(\bar{q}), \quad \text{where} \quad \bar{Y} = Y_0 + \bar{R}(\bar{q}), \quad (23)$$

where  $\bar{Y}$ ,  $Y_0$  and  $\bar{R}$  are the macroscopic flow stress, the microscopic initial flow stress and the macroscopic hardening variable, respectively. Consequently, we define the rate of the mode activity coefficient vector  $\hat{\underline{\xi}}$  as

$$\hat{\underline{\xi}} = \dot{\lambda} \frac{\partial \bar{\phi}}{\partial \hat{\underline{\tau}}} = \frac{\dot{\lambda}}{\bar{W}} \frac{\hat{\underline{\tau}}}{\|\hat{\underline{\tau}}\|}, \quad (24)$$

where  $\hat{\underline{\tau}}/\|\hat{\underline{\tau}}\|$  returns the direction of the evolution.

Additionally, a dependent damage variable  $\bar{D}$  is defined by

$$\bar{D} = 1 - \bar{W}, \quad 0 \leq \bar{D} \leq 1, \quad (25)$$

where  $\bar{D} = 0$  and  $\bar{D} = 1$  indicate the undamaged and the fully damaged state at the macro level, respectively.

Similarly to the microscopic case in Eq. (7), combining the equations (21), (23) and (24) with Eq. (22), one obtains the result

$$\bar{\mathcal{D}} = \sqrt{\frac{2}{3}}c_p Y_0 \dot{\lambda} > 0, \quad (26)$$

proving thermodynamic consistency of the coupled model for inelastic cases ( $\bar{\phi} = 0$  and  $\dot{\lambda} > 0$ ).

In order to verify our coupled model, we assume that the RVE is homogeneous without any cavities and fully occupied by the inelastic constituent, i.e.  $c_p = 1$ . Consequently, all microscopic and macroscopic quantities are identical. Inserting Eq. (24) into Eq. (22), the macroscopic dissipation power becomes

$$\bar{\mathcal{D}} = \frac{\dot{\lambda}}{\bar{W}} \frac{\hat{\underline{\tau}}}{\|\hat{\underline{\tau}}\|} \cdot \hat{\underline{\tau}} - \bar{R}\dot{q} = \dot{\lambda} \frac{\|\hat{\underline{\tau}}\|}{\bar{W}} - \bar{R}\dot{q}. \quad (27)$$

For comparison with the microscopic model, we recall the microscopic dissipation power from Eq. (7) in the form

$$\mathcal{D} = \dot{\lambda} \frac{\|\boldsymbol{\sigma}^{dev}\|}{W} - R\dot{q}. \quad (28)$$

Due to the equivalence of microscopic and macroscopic quantities, we conclude

$$\mathcal{D} = \bar{\mathcal{D}} \Rightarrow \|\boldsymbol{\sigma}^{dev}\| = \|\hat{\underline{\tau}}\| \Rightarrow \phi = \bar{\phi}, \quad (29)$$

indicating that the coupled model is exact for the homogeneous case (see Section 4.1 for numerical verification).

## Remarks 2.2.

1. An important feature of the NTFA theory is that it is merely available (in its present form) to problems where the superposition principle applies. For our present case in a geometrically linear context, the main framework of [26, 27] does not change and the notion of system matrices primarily used in [7, 6] is adopted.
2. Based on dissipative considerations, a new coupled model, including both the yield function (23) and the evolution law (24), is derived. It differs from both [26] and [7] by introducing the independent macroscopic damage variable  $\bar{W}$  accounting for additional softening effects.

## 2.4 Prototype model

Up to now, the microscopic hardening variable  $R$  and the microscopic damage variable  $W$  as well as their macroscopic counterparts  $\bar{R}$  and  $\bar{W}$  introduced in Section 2.2 and Section 2.3 remain to be specified. In principle, the specification is free to users according to their needs. In the following we propose a prototype model, which will be investigated in the examples in Section 4.

In order to specify the framework of Section 2.3, we assume that the microscopic material behavior of the inelastic constituent is characterized by the mixed isotropic hardening law

$$R(q) = Hq + c(1 - \exp(-bq)) \quad (30)$$

and a damage evolution function based on the proposal of [23] as

$$W(q) = \begin{cases} 1, & \text{if } q \leq e \\ \exp((e - q)^n \tilde{w}), & \text{if } q > e, \end{cases} \quad (31)$$

where  $\tilde{w} = \begin{cases} \frac{q - e}{d} w, & \text{if } e < q \leq e + d \\ w, & \text{if } q > e + d. \end{cases}$

Here  $H$ ,  $b$ ,  $c$ ,  $e$ ,  $d$ ,  $w$  and  $n$  are material parameters, which, generally, may not have a specific physical meaning. They are usually identified by comparison with proper experimental data (e.g. stress-strain-curve from a uniaxial tensile experiment). For an overview of parameter identification for more general cases we refer to [21, 22]. The hardening law (30) is of large practical meaning and was used e.g. in [24, 38], for simulation of an adhesive material (Betamate 1496) and an NiCr alloy coating, respectively. Here,  $H$  and  $c$  are factors for the linear and the nonlinear part, respectively, whereas  $b$  is an exponential factor. The damage evolution function (31) is a non-increasing function with range  $[0, 1]$ . It was postulated primarily by [23] for softening representation of glue materials, where  $e$  is a threshold value,  $n$  is an exponent,  $d$  and  $w$  are additional parameters for the scalar value  $\tilde{w}$ , respectively. The function (31) finds also its application, e.g. on simulating the damaging behavior of a coating system under transient thermomechanical loading conditions (see [39, 38]).

Comparing to previous publications on the NTFA, e.g. [26, 27, 7] amongst others, the constitutive equations are complemented with an *even* micro and macro model structure. More precisely, the macroscopic hardening variable  $\bar{R}$  and the macroscopic damage variable  $\bar{W}$  coincide with their microscopic counterparts  $R$  and  $W$ , respectively, i.e.

$$\text{even NTFA: } \bar{R}(\bar{q}) = R(\bar{q}), \quad \bar{W}(\bar{q}) = W(\bar{q}). \quad (32)$$

Hence, the NTFA computations done via Eq. (32) will be referred to as *even NTFA* computations.

On the micro scale, the hardening law (30), in combination with the damage function (31), leads to three different material stages: a pure elastic stage, a plastic hardening stage and an inelastic stage coupled to softening. The latter two stages are related to the plastic strain fields approximated via Eq. (8). Because of the additional softening effects, the nonlinearity of the material becomes much more stronger (compared to a pure hardening type plasticity case). The state of the plastic strain fields changes largely by loading as well as localization effects. Therefore, it becomes difficult to identify a set of universal modes that are simultaneously suitable for representing both plastic hardening and softening. Hence, theoretically it is expected that the even NTFA predictions become (more or less) inaccurate (see Section 4.4 for details).

## 2.5 Methods for accuracy improvement

In order to improve the accuracy of the even NTFA predictions, we present, in the following, two methods: the *uneven NTFA method* and the *adaptive NTFA method*, which will be described in Section 2.5.1 and Section 2.5.2, respectively. Additionally, a comparative adjustment of both methods will be given in Section 2.5.3

### 2.5.1 The uneven NTFA method

The first method is based on the idea of parameter identification, which is, in general cases, applied to fit experimental data for a given constitutive model. To compensate the approximation error made in Eq. (8), we introduce an additional correction parameter set

$$\underline{p}^{uneven} = [\vartheta > 0 \quad \alpha > 0 \quad \beta > 0], \quad (33)$$

leading to a modified macroscopic yield function

$$\bar{\phi}^*(\hat{\underline{\tau}}, \bar{q}) = \frac{\|\hat{\underline{\tau}}\|}{\bar{W}(\bar{q})} - \sqrt{\frac{2}{3}} c_p \vartheta \bar{Y}(\bar{q}), \quad (34)$$

and a modified macroscopic damage function

$$\bar{W}^*(\bar{q}) = \begin{cases} 1, & \text{if } \bar{q} \leq \beta e \\ \exp((e - \bar{q})^n \tilde{w} \alpha), & \text{if } \bar{q} > \beta e, \end{cases} \quad (35)$$

$$\text{where } \tilde{w} = \begin{cases} \frac{\bar{q} - e}{d} w, & \text{if } \beta e < \bar{q} \leq \beta e + d \\ w, & \text{if } \bar{q} > \beta e + d. \end{cases}$$

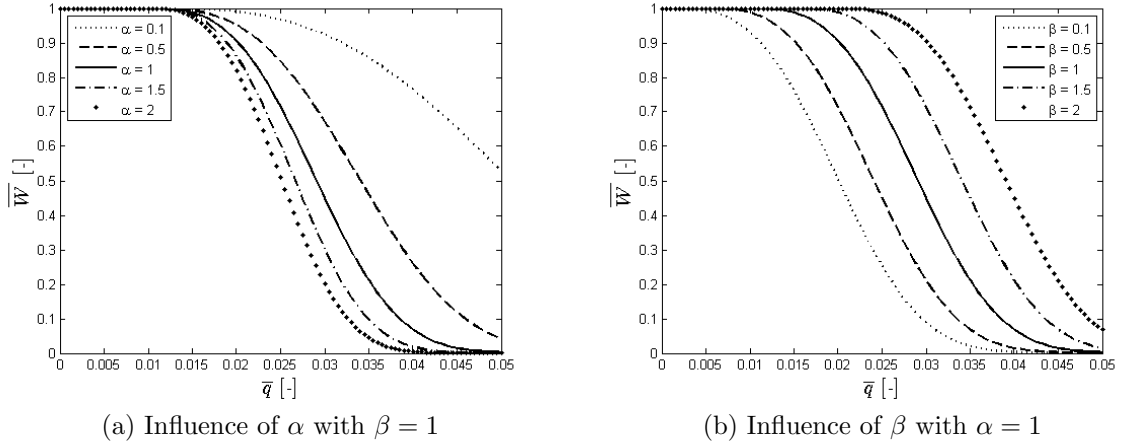


Figure 2: Influence on the macroscopic damage function

Contrary to the *even NTFA* in Eq. (32), this results into *uneven* micro and macro model structures. Here  $\vartheta$  has an influence on the initiation of macroscopic flow, whereas  $\alpha$  and  $\beta$  have the task to fit the rate and the initiation of the macroscopic damage evolution, as illustrated in figures 2a and 2b respectively. The other parameters used here are  $e = 10^{-2}$ ,  $d = 10^{-3}$ ,  $w = 10^5$  and  $n = 3$ , respectively. For simplicity, the macroscopic hardening law  $\bar{R}(\bar{q})$  still has the same model structure as the microscopic one  $R(q)$ . Note also that the parameter set  $\underline{p}^{uneven} = [1 \ 1 \ 1]$  returns the NTFA computation in the sense of an even model structure. Otherwise, the NTFA predictions are referred to as *uneven NTFA*, meaning the NTFA predictions with uneven micro and macro model structures.

In principle, the additional correction parameter set  $\underline{p}^{uneven}$  can be identified in several ways (see e.g. [21, 22] for an overview). In the sense of least-squares, we consider a minimization problem

$$\text{find } \underline{p}_*^{uneven} \in \kappa : f(\underline{p}^{uneven}) := \frac{1}{2} \|\underline{s}^{NTFA}(\underline{p}^{uneven}) - \underline{s}^{full}\| \rightarrow \min, \quad (36)$$

where  $\underline{p}_*^{uneven}$  is referred to as an *ordinary least squares estimate* and  $f$  is a function representing the sum of the errors between the NTFA predictions and full-field simulations.  $\kappa = \{\vartheta, \alpha, \beta > 0\}$  denotes the permissible parameter space of  $\underline{p}^{uneven}$ .  $\underline{s}^{NTFA}$  and  $\underline{s}^{full}$  are the predictions by the (uneven) NTFA computation and by the full-field simulation via FEM, respectively. To generate problem (36), any strain path loading can be used. One can also use several different loadings that the material is likely subjected to. Here,  $\underline{s}$  is defined as the vector of macroscopic powers, calculated by Eq. (4.3) through a given strain path, although it could also be the norms of macroscopic stresses. Note that the vector  $\underline{s}^{full}$  is computed once for all. Given the outstanding numerical efficiency of the NTFA, the numerical effort of the parameter identification procedure is acceptable.

Furthermore, the newly introduced fitting parameter set  $\underline{p}^{uneven}$  depends on the overall loading direction and on the overall load amplitude (see Section 4.5 for more details). Due to this limitation, the uneven NTFA has only an approximation property.

### 2.5.2 The adaptive NTFA method

In order to overcome the approximation property of the uneven NTFA method, we propose a more accurate, however more expensive, method: the *adaptive NTFA method*. Here the (even) NTFA procedure is merely applied to suitable regions, whereas a full-field computation is performed, e.g. via FEM, for the remaining 'unsuitable' regions. For selection of the different regions, a proper indicator has to be developed first. Given the good suitability of the even NTFA shown in the literature (see e.g. [26, 27, 7]) for pure hardening plasticity case, we replace the (even) NTFA by full-field computations, when the microscopic softening is initialized. Based on the plastic strain fields approximated by NTFA via Eq. (8), a spurious microscopic strain like variable field  $\tilde{q}(\mathbf{x}, t)$  is reconstructed by

$$\dot{\tilde{q}}(\mathbf{x}, t) = \sqrt{\frac{2}{3}} \|\dot{\epsilon}^p(\mathbf{x}, t)\| \approx \sqrt{\frac{2}{3}} \left\| \sum_{i=1}^N \dot{\xi}_i(t) \boldsymbol{\mu}^i(\mathbf{x}) \right\|. \quad (37)$$

This relation can be easily concluded from the microscopic constitutive equations (5.3) and (5.4), for the case of  $W = 1$  representing the absence of softening. Then, we propose an empirical indicator for replacement by full-field computations as

$$\max(\tilde{q}(\mathbf{x}, t)) \geq e, \quad (38)$$

where  $\max(\bullet)$  represents the maximum operator returning the maximal value of the field  $\tilde{q}(\mathbf{x})$  at time  $t$ . In order to initialize the full-field computation properly, direct after the switch, a localization approach has to be performed, which is not necessary for the even NTFA. More details will be revealed in Section 3.6. As already stated in Section 1, a methodologically similar approach using adaptive sub-structuring criteria was proposed in a slightly different context for the so-called adaptive selective POD in [35, 34]. However, a different model reduction method (POD) in relation to plasticity problems was applied and homogenization problems were not considered.

### 2.5.3 Comparative adjustment of uneven NTFA and adaptive NTFA

For accuracy improvement, we have introduced two new different alternatives to the even NTFA theory: parameter identification and adaptive modeling, leading to the *uneven NTFA* and the *adaptive NTFA* method, respectively.

The uneven NTFA method is more suitable for structural computations where only the macroscopic quantities are of interest, since it is an empirical method on the macro scale and does not account for accuracy improvements of localization. However, accurate microscopic predictions are usually not necessary for most homogenization problems (see e.g. Eshelby-solution based methods). Moreover, the fitting parameter set  $\underline{p}^{uneven}$  introduced in Eq. (33) is dependent on the concerning microstructure (geometry and material properties) and the modes used in the NTFA theory (see Eq. (8)). The dependence of loading cases will be studied and discussed in Section 4.5.

The adaptive NTFA method is particularly useful for those cases where the softening region of a structure is small (compared to the whole region) or where

the softening stage is merely activated in a limited extent. The adaptive NTFA method is more accurate however more expensive than the uneven NTFA method (see Section 4.3).

### 3 Numerical implementation

This section focuses on the numerical implementation of the NTFA methods and is structured as follows: In Section 3.1, we give an overview on the framework of the numerical implementation based on the FEM. Then, further details are given in the referred subsections.

#### 3.1 Algorithmic steps

As illustrated in Fig. 3, the framework implemented by our self-programmed code in MATLAB [25] is subdivided into the following algorithmic steps:

1. *Microscopic modeling*, which consists of FE-discretization (meshing) and material modeling.
2. *Numerical experiments* (see Section 3.2), including the linear elastic analysis to investigate the elastic properties, the linear eigenstress analysis preparing the eigenstress and the eigenstrain field data as well as the inelastic analysis preparing the field data required by mode identification (see Section 3.3).
3. Determination of *system matrices* (via equations (16.1), (41), (16.2) and (19.2)), based on the field data obtained from the numerical experiments described in Section 3.2. Note that, due to Eq. (20), the number of independent system matrices is reduced to three for the present case.
4. *Local integration procedure* (see Section 3.4), optionally for the even, uneven and adaptive NTFA method, where the evolution of the mode activity coefficients is computed and the homogenization is done, for each integration point at the macro level. Section 3.5 provides a gradient-free approach for parameter identification of the uneven NTFA, whereas numerical implementation of the adaptive NTFA method and the related localization procedure are described in Section 3.6.
5. *Macroscopic (structural) problem*, which is solved using the Newton-Raphson method at the macro level.

#### 3.2 Numerical experiments

Similarly to e.g. [7] amongst others, several numerical experiments are performed to investigate the elastic and inelastic properties of the microstructures. Those numerical experiments are also called *strain path computations*. The elastic and the inelastic strain path computations are respectively as follows for two-dimensional plane strain cases ( $n_{st} = 4$ ):

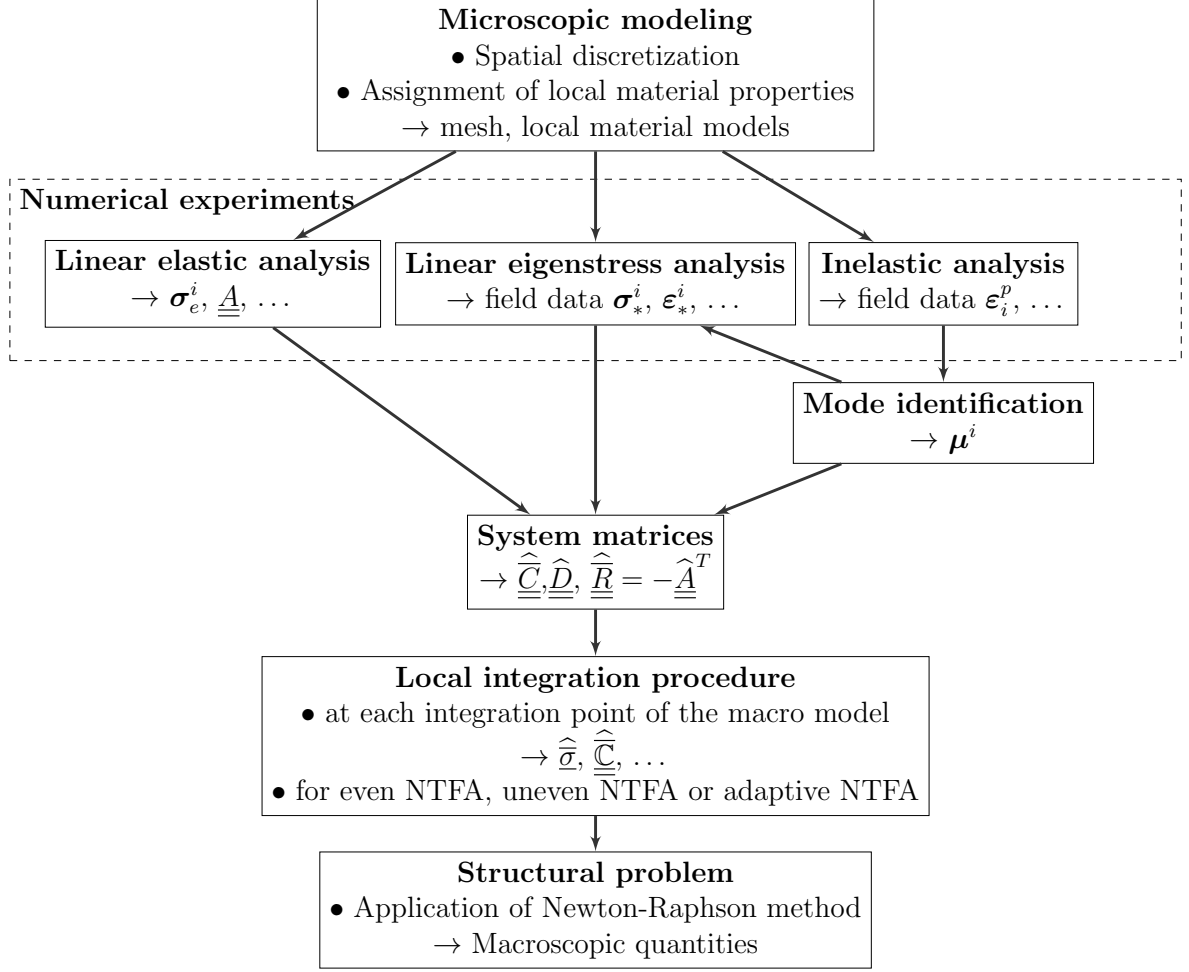


Figure 3: Framework of algorithmic steps

- *Linear elastic strain path computations:*

The linear elastic properties are identified by three linear FE computations of the RVE as

$$\text{Div}(\boldsymbol{\sigma}_e^i) = \text{Div}(\mathbf{C}\boldsymbol{\varepsilon}_e^i) = \mathbf{0}, \quad \langle \boldsymbol{\varepsilon}_e^i \rangle = \varepsilon_0 \boldsymbol{\Sigma}^i, \quad i = 1, 2, n_{st}, \quad (39)$$

where  $\boldsymbol{\sigma}_e^i$  and  $\boldsymbol{\varepsilon}_e^i$  denote respectively the elastic stress and the elastic strain tensor.  $\varepsilon_0$  is a positive constant. Then, the linear strain localization operator  $\mathbf{A}(\mathbf{x})$  of Eq. (11) is computed as

$$\mathbf{A}(\mathbf{x}) = \frac{1}{\varepsilon_0} \sum_{i=1}^{n_{st}} \boldsymbol{\varepsilon}_e^i(\mathbf{x}) \otimes \boldsymbol{\Sigma}^i. \quad (40)$$

According to Eq. (19), the macroscopic elasticity matrix  $\widehat{\underline{\underline{C}}}$  is assembled with the coefficients computed by

$$\widehat{C}_{ij} = \frac{1}{\varepsilon_0} \boldsymbol{\Sigma}^i : \langle \boldsymbol{\sigma}_e^j \rangle = \widehat{C}_{ji}, \quad i, j = 1, \dots, n_{st}. \quad (41)$$

Additionally, the eigenstress field data  $\boldsymbol{\sigma}_*^i$ , required for computation of the NTFA system matrices via equations (16.2) and (19.2), are obtained from the  $N$  eigenstress problems in Eq. (10.2), as soon as the modes are identified.

- *Inelastic strain path computations:*

The inelastic computations prepare the field data required for the mode identification in Section 3.3. In general, any strain path directions can be chosen. One can also choose several strain paths that the structure is likely subjected to. To hold the generality, the following three simple strain loading directions are used here:

$$\Sigma_*^1 = \mathbf{e}_1 \otimes \mathbf{e}_1, \quad \Sigma_*^2 = \mathbf{e}_2 \otimes \mathbf{e}_2, \quad \Sigma_*^3 = \mathbf{e}_1 \otimes \mathbf{e}_2 + \mathbf{e}_2 \otimes \mathbf{e}_1, \quad (42)$$

leading to three individual computations with the corresponding strain loading directions

$$\dot{\boldsymbol{\varepsilon}}^i = \dot{\varepsilon}^i \Sigma_*^i, \quad i = 1, \dots, 3, \quad \text{where } \dot{\varepsilon}^i \neq 0. \quad (43)$$

Each single inelastic strain path computation is temporally discretized into  $N_f$  frames, such that the  $i$ -th computation returns plastic strain fields  $\boldsymbol{\varepsilon}_i^{p(n)}(\boldsymbol{x})$ ,  $n = 1, \dots, N_f$  with chronological sequence. Here  $i = 1, \dots, N_p$  and  $N_p$  represents the number of the strain path computations (for the present case  $N_p = 3$ ). We note that both these inelastic strain path computations and the FE computations for reference solutions require solving the inelastic problem in Eq. (9). This is done using a two-level (local and global) Newton method. On the local level, a return-mapping algorithm is applied (see e.g. [41] amongst others). Since this is not the main objective of this paper, we will omit more details on it.

### 3.3 Mode identification

In order to identify a set of modes  $\boldsymbol{\mu}^i$ , which are essential for the NTFA, two approaches are used and studied here: the Karhunen-Loève decomposition (see [37, 19]) and the modified Gram-Schmidt procedure (see [7]) in the NTFA context. They both rely on *snapshots* that are, in the present case, several spatially heterogeneous plastic strain fields  $\boldsymbol{\varepsilon}_i^{p(n)}(\boldsymbol{x})$  obtained from the inelastic strain path computations described in Section 3.2. The number of snapshots totals  $N_p \cdot N_f$ . The two approaches are briefly described below.

According to the experience published in [19], most accurate NTFA predictions can be obtained from modes identified using two successive applications of Karhunen-Loève decomposition. Hence, we apply first such a procedure and refer it to as the *two-level Karhunen-Loève decomposition*. The total snapshots are divided into several partitions with a number of  $N_{par}$ , where each partition contains  $N^s$  snapshots.  $N^s$  with  $s = 1, \dots, N_{par}$  can differ from each other. Criteria of the partitioning can be different strain path loading or/and activity of the damage state. For each partition, a Karhunen-Loève decomposition is done and modes are individually obtained. These modes are naturally orthogonal to each other within one partition, while the modes from different partitions do not necessarily fulfill

the orthogonality condition. Therefore, a second application of the Karhunen-Loève decomposition needs to be done to these modes.

Alternatively, a modified Gram-Schmidt procedure proposed by [7] is also applied here for study purpose. This procedure has an improved numerical efficiency compared to the Karhunen-Loève decomposition, since the number of the computations of  $\langle \boldsymbol{\varepsilon}^{p(i)} : \boldsymbol{\varepsilon}^{p(j)} \rangle$  is significantly reduced and the computation of eigenvalue problems of correlation matrices is avoided (see [7]). One important feature of this procedure is the use of the snapshots in opposite direction per strain path loading.

For detailed algorithms of the two-level Karhunen-Loève decomposition and the modified Gram-Schmidt procedure, we refer to [19] and [7], respectively. Moreover,  $\delta_k$  (' $\alpha$ ' in [19]) and  $\delta_0$  (' $r_{min}$ ' in [7]) are the algorithm parameters for the threshold criterion of the two-level Karhunen-Loève decomposition and the modified Gram-Schmidt procedure, respectively, which determine the number  $N$  of modes.

### 3.4 Local integration procedure of NTFA

The local integration is the key part of the implementation of the NTFA, which determines the evolution of the mode activity vector  $\hat{\underline{\xi}}$ . To this end, the  $N$  conjugate forces  $\hat{\underline{\tau}}$  in addition to the increment of the plastic multiplier  $\Delta\bar{\lambda}$  have to be computed. Similarly to the approach in [7], an  $(N + 1)$ -dimensional root finding problem is adopted:

$$\hat{\underline{r}}(\hat{\underline{x}}) = \begin{bmatrix} \hat{\underline{\tau}} - \hat{\underline{\tau}}_{tr} - \frac{\Delta\bar{\lambda}}{\bar{W}(\bar{q}_{n+1})} \frac{\hat{D}\hat{\underline{\tau}}}{\|\hat{\underline{\tau}}\|} \\ \frac{\|\hat{\underline{\tau}}\|}{\bar{W}(\bar{q}_{n+1})} - \sqrt{2/3}c_p\vartheta\bar{Y}(\bar{q}_{n+1}) \end{bmatrix} = \mathbf{0}, \quad \text{where} \quad \hat{\underline{x}} = \begin{bmatrix} \hat{\underline{\tau}} \\ \Delta\bar{\lambda} \end{bmatrix}. \quad (44)$$

Here the internal variable  $\bar{q}$  is updated as

$$\bar{q}_{n+1} = \bar{q}_n + \sqrt{2/3}\Delta\bar{\lambda}, \quad (45)$$

The Newton-Raphson iteration scheme solving Eq. (44) reads

$$\hat{\underline{x}}^i = \hat{\underline{x}}^{i-1} - \hat{\underline{J}}^{-1}\hat{\underline{r}}(\hat{\underline{x}}^{i-1}), \quad (46)$$

with the initial guess  $\hat{\underline{\tau}}_0 = \hat{\underline{\tau}}_{tr}$  and  $\Delta\bar{\lambda}_0 = 0$  for the iteration step  $i = 1$ , where the trial state of  $\hat{\underline{\tau}}$ , under the assumption of linear elastic behavior for the current strain increment  $\Delta\hat{\underline{\varepsilon}}$ , reads

$$\hat{\underline{\tau}}_{tr} = \hat{\underline{\tau}}_n + \hat{\underline{A}}\Delta\hat{\underline{\varepsilon}}. \quad (47)$$

Moreover,  $\hat{\underline{J}}$  denotes the Jacobi matrix given by

$$\hat{\underline{J}} = \frac{\partial \hat{\underline{r}}}{\partial \hat{\underline{x}}} = \begin{bmatrix} \hat{\underline{I}} - \frac{\Delta\bar{\lambda}\hat{D}}{\bar{W}\|\hat{\underline{\tau}}\|} \left( \hat{\underline{I}} - \frac{\hat{\underline{\tau}}\hat{\underline{\tau}}^T}{\hat{\underline{\tau}}^T\hat{\underline{\tau}}} \right) & -\frac{\bar{W} - \sqrt{2/3}\Delta\bar{\lambda}\frac{\partial\bar{W}}{\partial\bar{q}}}{\bar{W}^2} \frac{\hat{D}\hat{\underline{\tau}}}{\|\hat{\underline{\tau}}\|} \\ \frac{\hat{\underline{\tau}}^T}{\bar{W}\|\hat{\underline{\tau}}\|} & -\sqrt{2/3}\frac{\|\hat{\underline{\tau}}\|}{\bar{W}^2}\frac{\partial\bar{W}}{\partial\bar{q}} - \frac{2}{3}c_p\vartheta\frac{\partial\bar{Y}}{\partial\bar{q}} \end{bmatrix}. \quad (48)$$

The iteration is completed, when the predefined tolerance (here  $TOL = 1e - 8$ ) is achieved, i.e.  $\|\hat{\underline{\tau}}\| < TOL$ . Furthermore, the macroscopic stress  $\hat{\underline{\sigma}}$  is updated as

$$\hat{\underline{\sigma}}_{n+1} = \hat{\underline{\sigma}} + \hat{\underline{\underline{C}}}\Delta\hat{\underline{\varepsilon}} + \hat{\underline{\underline{R}}}\Delta\hat{\underline{\xi}}. \quad (49)$$

The macroscopic consistent stiffness matrix  $\hat{\underline{\underline{C}}}$ , required for application of the Newton-Raphson method at the macro level, is obtained from a straightforward differentiation of Eq. (49) as

$$\hat{\underline{\underline{C}}} = \frac{\partial\hat{\underline{\sigma}}}{\partial\hat{\underline{\varepsilon}}} = \hat{\underline{\underline{C}}} + \hat{\underline{\underline{R}}}\frac{\partial\Delta\hat{\underline{\xi}}}{\partial\hat{\underline{x}}}\frac{\partial\hat{\underline{x}}}{\partial\hat{\underline{\varepsilon}}}. \quad (50)$$

Here the partial derivative  $\partial\Delta\hat{\underline{\xi}}/\partial\hat{\underline{x}}$  is given by

$$\frac{\partial\Delta\hat{\underline{\xi}}}{\partial\hat{\underline{x}}} = \left[ \begin{array}{c} \Delta\bar{\lambda} \\ \frac{\Delta\bar{\lambda}}{\bar{W}\|\hat{\underline{\tau}}\|} \left( \hat{\underline{\underline{I}}} - \frac{\hat{\underline{\tau}}\hat{\underline{\tau}}^T}{\hat{\underline{\tau}}^T\hat{\underline{\tau}}} \right) \end{array} \quad \frac{\bar{W} - \sqrt{\frac{2}{3}}\Delta\bar{\lambda}\frac{\partial\bar{W}}{\partial q}}{\bar{W}^2} \frac{\hat{\underline{\tau}}}{\|\hat{\underline{\tau}}\|} \right] \quad (51)$$

and the partial derivative  $\partial\hat{\underline{x}}/\partial\hat{\underline{\varepsilon}}$  is obtained from

$$\begin{aligned} 1. \quad \frac{d\hat{\underline{r}}}{d\hat{\underline{\varepsilon}}} &= \frac{\partial\hat{\underline{r}}}{\partial\hat{\underline{\varepsilon}}} + \frac{\partial\hat{\underline{r}}}{\partial\hat{\underline{x}}}\frac{\partial\hat{\underline{x}}}{\partial\hat{\underline{\varepsilon}}} = \begin{bmatrix} -\hat{\underline{A}} \\ \underline{\underline{0}}^T \end{bmatrix} + \hat{\underline{\underline{J}}}\frac{\partial\hat{\underline{x}}}{\partial\hat{\underline{\varepsilon}}} = \underline{\underline{0}} \\ \Rightarrow 2. \quad \frac{\partial\hat{\underline{x}}}{\partial\hat{\underline{\varepsilon}}} &= -\hat{\underline{\underline{J}}}^{-1}\frac{\partial\hat{\underline{r}}}{\partial\hat{\underline{\varepsilon}}} = \hat{\underline{\underline{J}}}^{-1}\begin{bmatrix} \hat{\underline{A}} \\ \underline{\underline{0}}^T \end{bmatrix}. \end{aligned} \quad (52)$$

The matrix  $\hat{\underline{\underline{C}}}$  computed via Eq. (50) is found to be symmetric for the considered class of materials (see e.g. [6] on a detailed proof for a material without softening). We remark that our approach differs from [7] by the macroscopic damage variable  $\bar{W}$ , which makes the integration procedure somewhat more complicated. Note also that this integration procedure is simultaneously valid to the even, uneven and adaptive NTFA method. The only difference is that different parameters ( $\underline{p}^{uneven}$ ) are used in the uneven NTFA method for an empirical correction (see Section 3.5). For a replacement by full-field computations, a localization procedure needs to be performed by the adaptive NTFA method (see Section 3.6).

### 3.5 Parameter identification for the uneven NTFA method

In this section, the parameter identification procedure for the uneven NTFA method is described. To solve the minimization problem (36), we choose a gradient-free approach, i.e. Downhill-Simplex or Nelder-Mead procedure (see e.g. [29]). This algorithm is quite simple and robust, and requires no gradients. Let  $N_d = 3$  be the number of the parameter set  $\underline{p}^{uneven}$ . In the following, the index 'uneven' will be omitted for simplicity. The parameters  $\alpha_d$ ,  $\gamma_d$ ,  $\beta_d$  and  $\sigma_d$  are the algorithm control parameters for the reflection, expansion, contraction and compression procedure, respectively. To initialize the Downhill-Simplex procedure,  $(N_d + 1)$  permissible initial parameter sets  $\underline{p}^i$ , forming an initial simplex, have to be chosen. Note that the choice of the initial parameters has an influence on the efficiency and quality of

this algorithm. For the present case,  $\underline{p}^1 = [1 \ 1 \ 1]$  is fixed. Then, we give each parameter a second permissible value, such that each other parameter set  $\underline{p}^i$ , for  $i = 2, \dots, 4$ , is formed on the basis of  $\underline{p}^1$ , but replacing the value 1 by the second value for each of all three parameters, respectively. Examples will be given in Section 4.5 and the detailed algorithm can be found elsewhere e.g. in [29].

### 3.6 Numerical implementation of the adaptive NTFA method

In this section, details about the adaptive NTFA method are revealed. For regions, where the indication condition (38) is not fulfilled, the local integration procedure of Section 3.4 for the even NTFA is performed. Additionally, the spurious variable field reconstruction via Eq. (37) is performed for evaluation of (38) by the backward Euler time integration

$$\tilde{q}^i(\mathbf{x}) = \tilde{q}^{i-1}(\mathbf{x}) + \sqrt{\frac{2}{3}} \left\| \sum_{j=1}^N \Delta \xi_j^i(t) \boldsymbol{\mu}^j(\mathbf{x}) \right\|, \quad (53)$$

for the current time step  $i$ , where the index  $(i - 1)$  denotes the previous time step. Once the condition (38) is fulfilled for the time step  $i$ , the replacement of the even NTFA by a full-field computation has to be performed. To initialize the full-field computation properly, the state variable field  $q^{full}(\mathbf{x})$ , the plastic strain field  $\boldsymbol{\varepsilon}_{full}^p(\mathbf{x})$ , and the displacement field  $\underline{u}^{full}$  are reconstructed as

$$\begin{aligned} 1. \quad q^{full}(\mathbf{x}) &\approx \tilde{q}^{i-1}(\mathbf{x}), & 2. \quad \boldsymbol{\varepsilon}_{full}^p(\mathbf{x}) &\approx \sum_{j=1}^N \xi_j^{i-1} \boldsymbol{\mu}^j(\mathbf{x}), \\ 3. \quad \underline{u}^{full}(\mathbf{x}) &\approx \frac{1}{\varepsilon_0} \sum_{j=1}^{n_{st}} \bar{\varepsilon}_j^{i-1} \underline{u}_j^e(\mathbf{x}) + \sum_{j=1}^N \xi_j^{i-1} \underline{u}_j^*(\mathbf{x}), \end{aligned} \quad (54)$$

respectively. In Eq. (54.3),  $\underline{u}_j^e$  and  $\underline{u}_j^*$  are the displacement fields obtained from the linear elastic and the elastic eigenstress computations (via equations (39) and (10.2)), respectively. Note that the localization procedure, performed by the equations (54), has to be done only once for the replacement. This is achieved straightforward with function evaluations based on known quantities. Hence, the computational effort for the additional localization procedure is acceptable. This localization procedure is of great practical interest, since the Newton-Raphson method used for solving full-field FE-problem converges (as well-known) merely locally. The accuracy gains of the adaptive NTFA method, both on the macroscopic and on the microscopic (fields) predictions, will be illustrated in Section 4.3.

Furthermore, the time integration (53) requires only the state variable field  $\tilde{q}(\mathbf{x})$  from the previous step. More precisely, the field  $\tilde{q}(\mathbf{x})$  on each macro integration point is updated step by step and a storage of the whole history is not necessary (though optional). Hence, the additional storage memory requirement is limited.

## 4 Numerical examples

In order to illustrate and validate the methods presented in this work, we provide in the following several numerical examples. This section is organized as follows: First, the even NTFA method explained in Section 2.3 is validated by means of a simple microscopic computation of a homogeneous microstructure. With regard to a fiber-reinforced composite, the mesh dependence is studied via FEM, even NTFA and adaptive NTFA, respectively. Subsequently, the adaptive NTFA method is illustrated. The influence of different approaches of mode identification (see Section 3.3) on the accuracy of the even NTFA predictions is investigated. Then, the uneven NTFA approach is illustrated and discussed. Finally, a macroscopic example demonstrating future structural applications is given, where the different approaches are investigated with a structural loading condition selected at a macroscopic integration point.

The results are presented in Voigt notation, that is the vector representations of the stress tensor  $\boldsymbol{\sigma}$  and the strain tensor  $\boldsymbol{\varepsilon}$  for the two-dimensional case as

$$\underline{\boldsymbol{\sigma}} = [\sigma_{11} \quad \sigma_{22} \quad \sigma_{33} \quad \tau_{12}]^T, \quad \underline{\boldsymbol{\varepsilon}} = [\varepsilon_{11} \quad \varepsilon_{22} \quad \varepsilon_{33} \quad \gamma_{12}]^T, \quad \text{where } \gamma_{12} = 2\varepsilon_{12}. \quad (55)$$

Here the indices 1 and 2 represent the horizontal and the vertical direction, respectively. Due to the plane strain state assumed throughout all examples, the third strain component  $\varepsilon_{33}$  implying the strain in the thickness direction is always zero. Additionally, a scale factor of 5 is used for presentation of deformations. The linear displacement boundary condition (3) is applied for all examples. For illustration purpose, we will employ a pseudo-time axis for individual computations, although no time dependence of the plasticity and softening is considered.

### 4.1 Example 1: Homogeneous microstructure

Firstly, we consider a homogeneous microstructure fully occupied by a nonlinear component constitutively modeled by the equations (5). This is simply done with two linear triangular elements as shown in Fig. 4a. For spatial discretization, one could also use more elements, but the same results are obtained for this case. The material parameters are identical with the matrix material shown in Table 1. For mode identification, three inelastic strain path computations are carried out with the three loading directions defined by Eq. (43), where  $\dot{\varepsilon}^1 = \dot{\varepsilon}^2 = \dot{\varepsilon}^3 = 0.05/s$  for a simulation time of 1s. Snapshots are captured every 0.02s, leading totally to 150 snapshots. Based on the snapshots, both the two-level Karhunen-Loève decomposition and the modified Gram-Schmidt procedure (see Section 3.3) return the same modes in Voigt notation

$$\underline{\boldsymbol{\mu}}^1(\boldsymbol{x}) = \begin{bmatrix} 0.9164 \\ -0.4082 \\ -0.4082 \\ 0 \end{bmatrix}, \quad \underline{\boldsymbol{\mu}}^2(\boldsymbol{x}) = \begin{bmatrix} 0 \\ 0.7071 \\ -0.7071 \\ 0 \end{bmatrix}, \quad \underline{\boldsymbol{\mu}}^3(\boldsymbol{x}) = \begin{bmatrix} 0 \\ 0 \\ 0 \\ 1.4142 \end{bmatrix},$$

where each of the modes is a homogeneous field. For verification purpose, we define a macroscopic strain path computation with two different strain rates

$$\dot{\bar{\boldsymbol{\varepsilon}}}^1 = \begin{bmatrix} 0.03 & 0 \\ 0 & -0.03 \\ & & 0 \end{bmatrix} \frac{\mathbf{e}_i \otimes \mathbf{e}_j}{s}, \quad \dot{\bar{\boldsymbol{\varepsilon}}}^2 = \begin{bmatrix} -0.01 & 0.015 \\ 0.015 & 0.01 \\ & & 0 \end{bmatrix} \frac{\mathbf{e}_i \otimes \mathbf{e}_j}{s}, \quad (56)$$

where each of these strain rates holds constant for 0.5s. The computation is done by even NTFA and FEM, respectively, where identical results are obtained. In Fig. 4, the macroscopic stress coefficients and the macroscopic damage evolution are shown, respectively. Note that the macroscopic damage variable for the FEM full-field computation is computed by  $\bar{D}^{FEM} = \langle D(\mathbf{x}) \rangle_{\Omega_p}$ . Here, for the homogeneous case, there is no difference between the microscopic and the macroscopic quantities. This simple example is a numerical verification for the conclusion derived by the equations (27), (28) and (29) in Section 2.3.

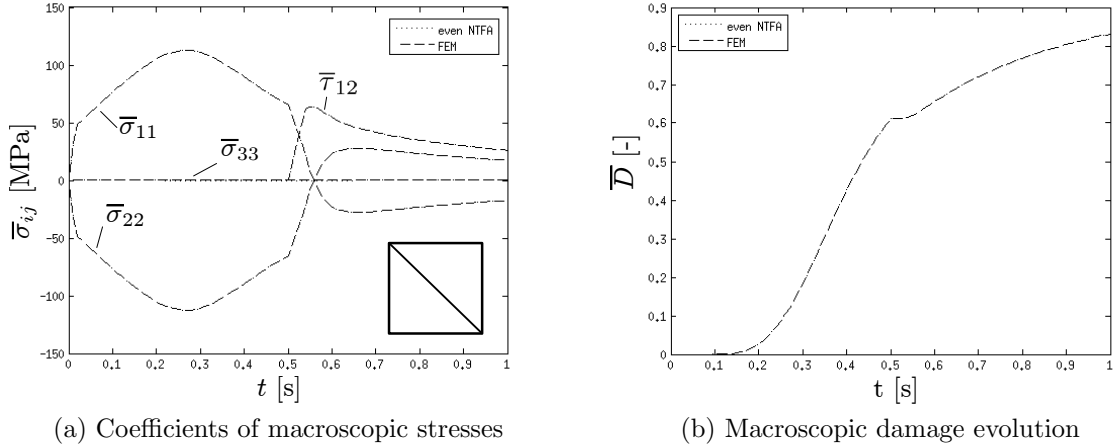


Figure 4: Example 1; results for the homogeneous case

Material	$E$ [MPa]	$\nu$ [-]	$Y_0$ [MPa]	$H$ [MPa]	$b$ [-]	$c$ [MPa]	$e$ [-]	$d$ [-]	$w$ [-]	$n$ [-]
<i>inelastic</i>										
Matrix	70000	0.3	80	1500	25	360	$5 \cdot 10^{-3}$	$10^{-3}$	$10^5$	3
<i>elastic</i>										
Fiber	210000	0.24	-	-	-	-	-	-	-	-

Table 1: Example 2; summary of material parameters

## 4.2 Example 2: A study of mesh dependence

In this example, we deal with a fiber-reinforced composite. In order to study the mesh dependence, we provide three different FE discretizations of the RVE, where

linear triangular elements are used. They are spatially discretized with three different meshes, as shown in Fig. 5. The fibers (the dark-displayed phase, volume fraction 18.54%) are elastic with relatively high Young’s modulus and distributed randomly in the matrix, while the matrix (gray-displayed, volume fraction  $c_p = 81.46\%$ ) is assumed to be inelastic. Moreover, the inelastic material behavior of the matrix is characterized by the prototype model described in Section 2.4. The corresponding material parameters are summarized in Table 1.

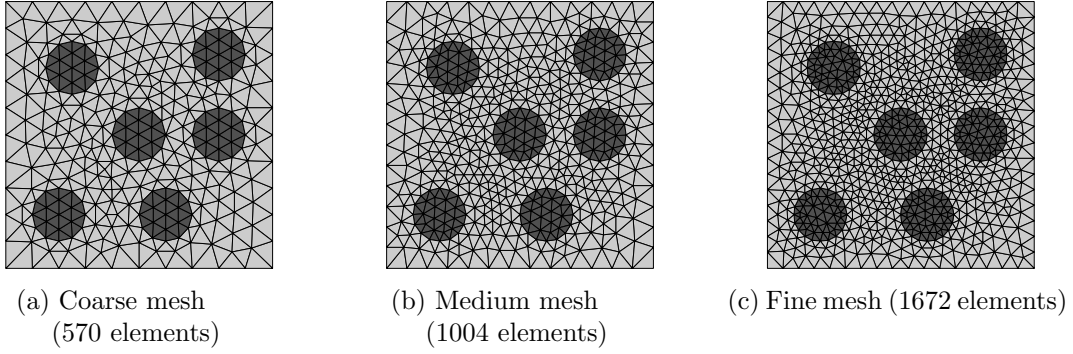


Figure 5: Example 2; different FE discretizations of the RVE for fiber-reinforced composite

With respect to all three different FE meshes shown in Fig. 5, the strain path computation defined by Eq. (56) is done by the even NTFA, the adaptive NTFA and the FEM, respectively, leading totally to nine single computations. For all three meshes, the mode identification procedures for the even NTFA and the adaptive NTFA approach are equally parameterized, respectively. For the even NTFA, three inelastic strain path computations are carried out with the three loading directions defined by Eq. (43), where  $\dot{\varepsilon}^1 = \dot{\varepsilon}^2 = \dot{\varepsilon}^3 = 0.05/s$  for a simulation time of 1s. Snapshots are captured every 0.02s, leading totally to 150 snapshots for the mode identification procedure. For the adaptive NTFA, the three inelastic strain path computations, defined by Eq. (43), are performed without damage evolution. This is simply done by setting the parameter  $e$  to a sufficient large value like e.g.  $10^2$ . With  $\dot{\varepsilon}^1 = \dot{\varepsilon}^2 = \dot{\varepsilon}^3 = 0.02/s$  for a simulation time of 1s, 150 snapshots are also captured. Then, the modified Gram-Schmidt procedure returns different number of plastic modes, as summarized in Table 2. Here the cut-off parameters  $\delta_0 = 10^{-7}$  and  $\delta_0 = 10^{-8}$  are used for the even NTFA and the adaptive NTFA computation, respectively.

	coarse mesh	medium mesh	fine mesh
even NTFA	21 modes	23 modes	28 modes
adaptive NTFA	9 modes	9 modes	9 modes

Table 2: Example 2; results of mode identification

Two components of the first mode, related to the even NTFA computation of the fine mesh, are depicted in Fig. 6. The regions of fibers are displayed in gray,

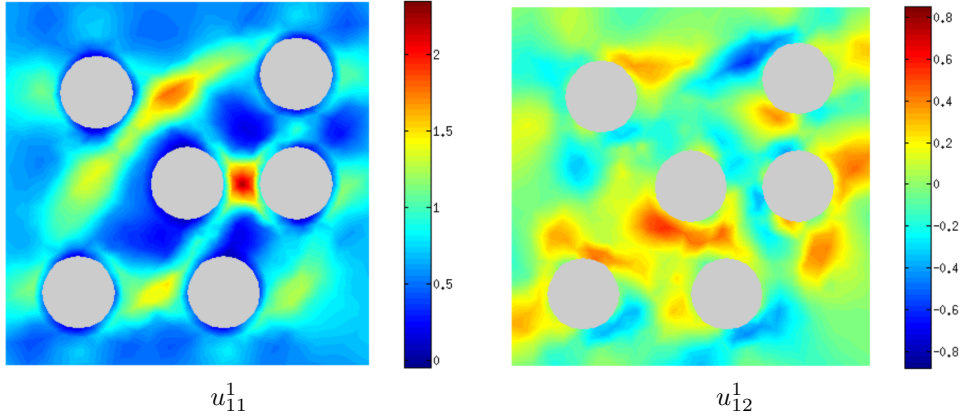


Figure 6: Example 2; a representative example of plastic modes:  $\mathbf{u}^1$

since the modes have their support merely in the matrix. The results of all nine computations are summarized in Fig. 7. Fig. 7a shows the macroscopic von Mises stress plot over the time, while the damage evolutions are summarized in Fig. 7b. From all three FEM computations, a mesh dependence is obviously observed. This is also theoretically expected, since no non-local damage models is considered in this work. One can clearly see that the same mesh dependence is preserved by the reduced schemes, i.e. the even and the adaptive NTFA. Furthermore, the predictions of the adaptive NTFA are very accurate, whereas an obvious deviation of the even NTFA predictions (from  $t \approx 0.1$ s) is observed. Further studies on the adaptive NTFA and the even NTFA will be done in Section 4.3 and Section 4.4, respectively.

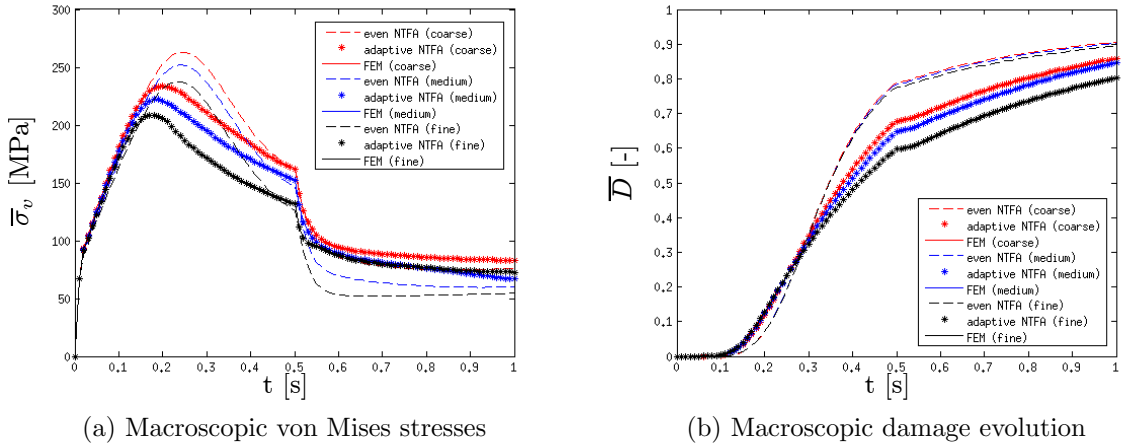


Figure 7: Example 2; results of mesh dependence study

### 4.3 Example 3: A study of the adaptive NTFA method

Without loss of generality, we choose the fine mesh in Fig. 5c for a further study of the adaptive NTFA method. The strain path computations of Section 4.2 are recalled. In Fig. 8, the individual components of the macroscopic stresses are shown, where the results of the adaptive NTFA computation coincide with the reference FEM solutions. In the adaptive NTFA computation, an even NTFA computation

is done at the beginning of loading up to 0.05s, where no microscopic damage is initialized. The final time steps up to 1s are computed via FEM, where damage evolution is activated. For both the even NTFA and the FEM procedure, a quadratic convergence rate is observed.

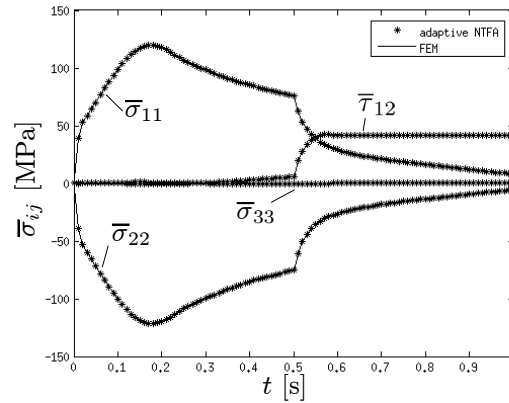


Figure 8: Example 3; comparison of macroscopic stresses

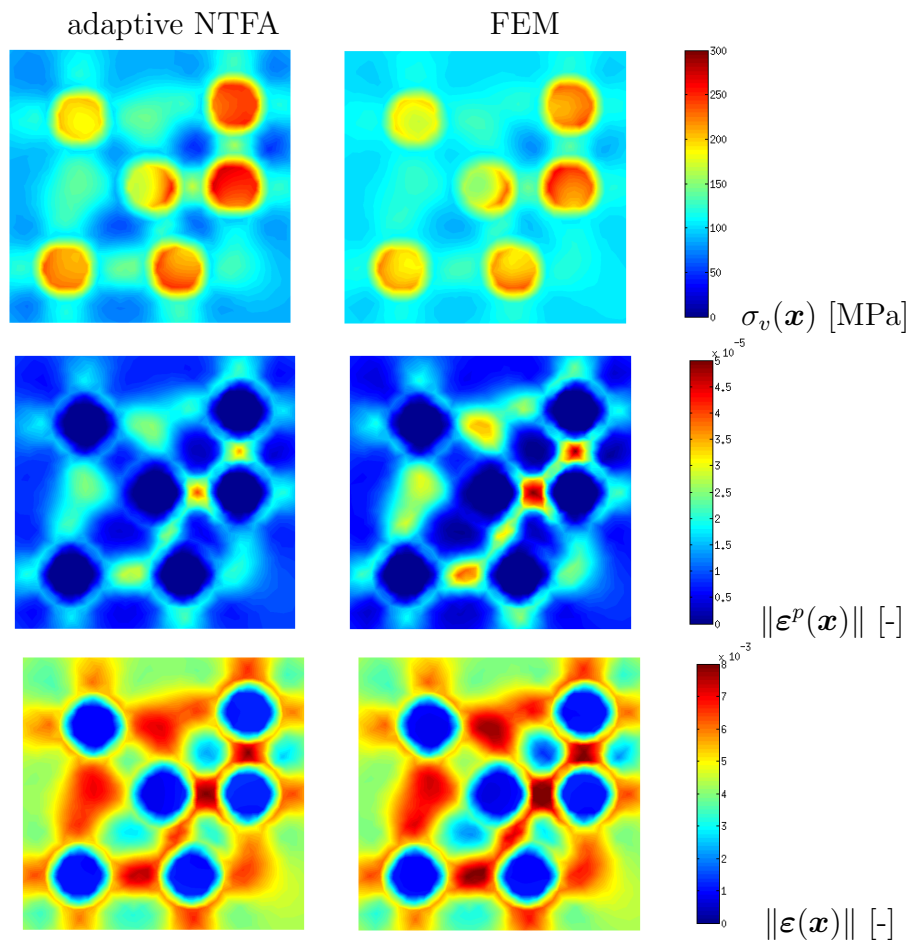


Figure 9: Example 3; comparison of the micro fields reconstructed by the adaptive NTFA to the FEM reference fields selected at  $t = 0.05s$

By a simple post-processing via equations (12), (11) and (8), a micro field reconstruction is done for the microscopic stress, strain and plastic strain field, respectively. For a comparison between the micro field reconstructions and the FEM reference fields, we select the time  $t = 0.05\text{s}$  where an even NTFA procedure is performed. The comparison is illustrated in Fig. 9, where a good accordance is obtained. Fig. 9 shows also that the stress concentration is overpredicted by the even NTFA. This effect coincides with the results in e.g. [7] for a three-dimensional computation with a pure hardening type plasticity.

Furthermore, Fig. 10 gives a comparison of the microscopic von Mises stress fields between the adaptive NTFA and the FEM at the end of the computation. Interestingly, the fields are almost identical, the error made in the microscopic reconstructions by the even NTFA computation (see Fig. 9) is almost completely compensated.

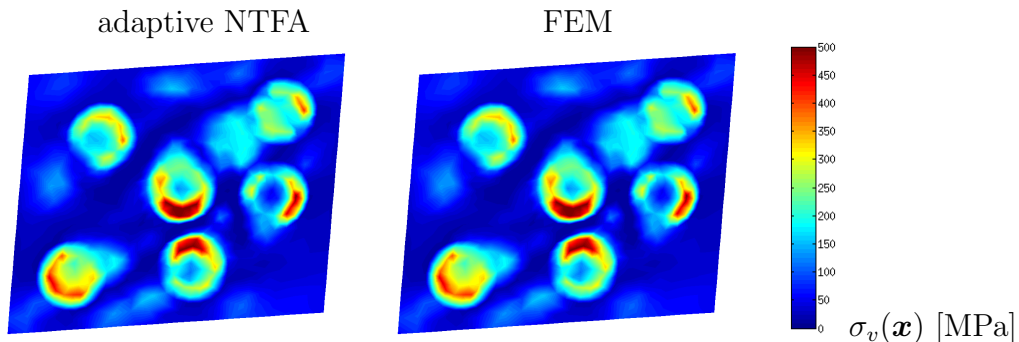


Figure 10: Example 3; comparison of the stress field reconstructed by the adaptive NTFA to the FEM reference field at the end of the computation ( $t = 1\text{s}$ )

#### 4.4 Example 4: Several even NTFA computations with different modes

The aim of this example is to investigate which approach of mode identification provides a better primary prediction for an even NTFA computation. Without loss of generality, we choose the fine mesh of the fiber-reinforced composite shown in Fig. 5c. Then, six even NTFA strain path computations (described by Eq. (56)) are performed using six different sets of modes, respectively as summarized in Table 3. Two approaches for mode identification (see Section 3.3) are studied here. They are used three times with three different parameterizations, based on the same snapshots (obtained in Section 4.2), respectively. For the two-level Karhunen-Loève decomposition (KL), the same threshold parameter  $\delta_k = 0.9999$  but different partitions are used. In the test 'even NTFA 01', the snapshots are subdivided according to three different strain paths, leading to three partitions. In 'even NTFA 02' and 'even NTFA 03', the individual partitions from 'even NTFA 01' are evenly subdivided into 2 and 5 sections again, resulting into 6 and 15 partitions, respectively. Interestingly, with more partitions, the KL procedure needs less CPU time, but returns larger number of modes. For the modified Gram-Schmidt procedure (GS), different cut-off parameters  $\delta_0$  are used. Using a smaller  $\delta_0$ , the GS procedure renders larger number of modes, at the expense of a longer CPU time. With a proper value of  $\delta_0$

(see e.g. 'even NTFA 04'), a considerable numerical efficiency, compared to the KL procedure, is achieved.

Test	Mode identification	Number of modes	CPU time (normalized) for mode identification	Error [%]
even NTFA 01	KL (3 partitions)	13	0.8190	15.28
even NTFA 02	KL (6 partitions)	15	0.3290	14.95
even NTFA 03	KL (15 partitions)	19	0.2016	14.96
even NTFA 04	GS ( $\delta_0 = 10^{-6}$ )	17	0.1230	15.83
even NTFA 05	GS ( $\delta_0 = 10^{-7}$ )	28	0.2094	15.92
even NTFA 06	GS ( $\delta_0 = 10^{-8}$ )	44	0.3483	15.51

Table 3: Example 4; summary of results for different even NTFA computations

Furthermore, the results of the six even NTFA computations are compared with the FEM reference solution in Fig. 11. For clarity, the components of macroscopic stresses are subdivided in Fig. 11a and Fig. 11b. Fig. 11c and Fig. 11d show the macroscopic von Mises stresses and the macroscopic damage evolutions, respectively. No strong difference between the even NTFA computations is observed. Similar mean errors, defined as  $\text{Error} = \|\underline{P}^{NTFA} - \underline{P}^{FEM}\| / \|\underline{P}^{FEM}\|$ , are made by the even NTFA computations (see Table 3). Here  $\underline{P}^{NTFA}$  and  $\underline{P}^{FEM}$  denote the vectors of the macroscopic stress powers through the strain path (via Eq. (4.3)) obtained from the even NTFA and the FEM, respectively. An obvious deviation from the FEM reference solution can be clearly seen, particularly since  $t \approx 0.15\text{s}$  where the damage evolution is activated considerably. The damage evolution is somewhat delayed, whereas the macroscopic damage is overpredicted from  $t \approx 0.3\text{s}$  (see Figure 11d). Additionally, a speed-up factor up to 2000 compared to the FE computations is observed.

Besides the reasons already stated in Section 2.4, the delay effect might have another reason that the (even) NTFA method is merely driven by the macroscopic quantities, unlike the fully microscopically motivated full-field computation. One can see the fact that the additional consideration of softening effects leads to inaccurate (even) NTFA predictions, particularly when the damage evolution is activated to a certain extent. The performance of the uneven NTFA method, which corrects the macroscopic predictions empirically, will be shown in the subsequent section.

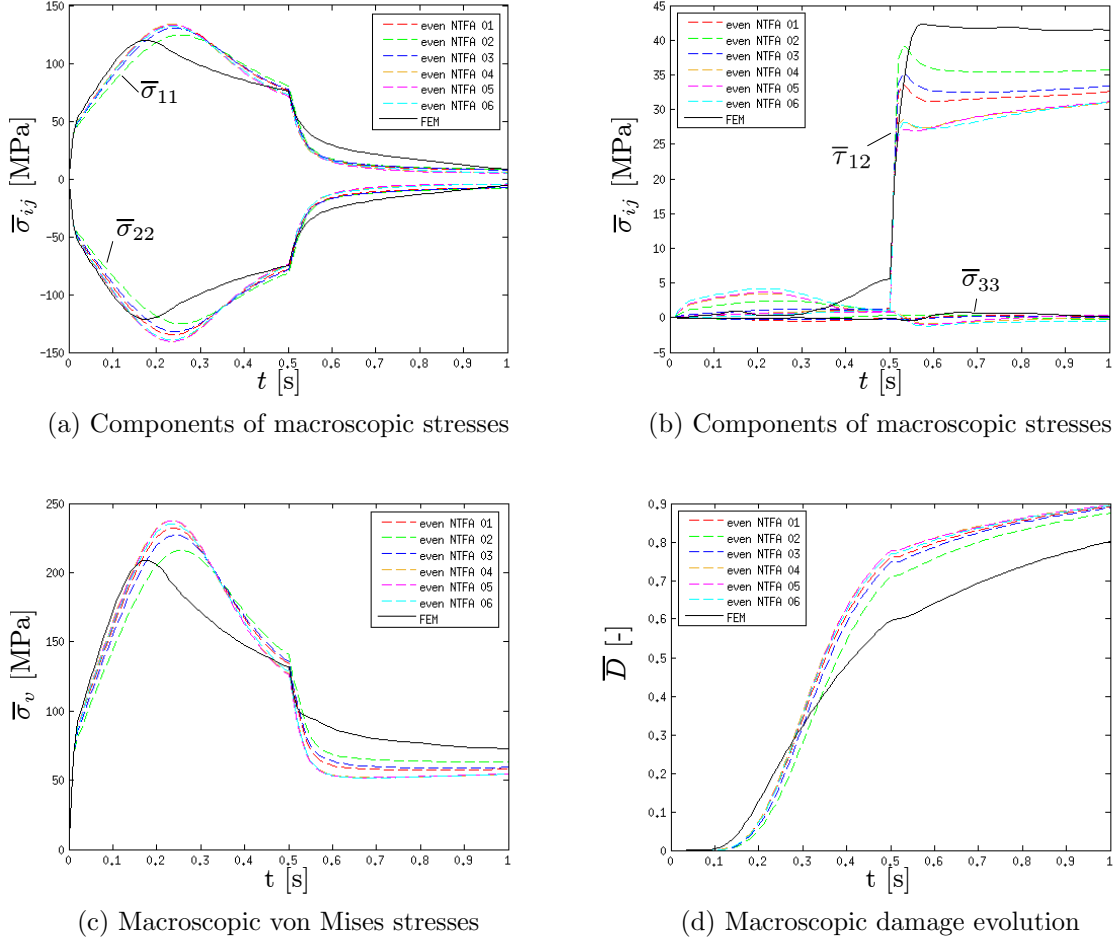


Figure 11: Example 4; influence of different modes on the accuracy of the even NTFA method

#### 4.5 Example 5: A study of the uneven NTFA method

In this example, we intend to show the performance of the uneven NTFA method. Without loss of generality, we choose the 'even NTFA 01' in Section 4.5. For simplicity, we consider the following three simple cases with three constant strain path directions

$$\text{Case 1: } \dot{\underline{\epsilon}}^1 = \begin{bmatrix} 0.02 & 0 \\ 0 & -0.02 \\ & & 0 \end{bmatrix} \frac{\mathbf{e}_i \otimes \mathbf{e}_j}{s}, \quad \text{Case 2: } \dot{\underline{\epsilon}}^2 = \begin{bmatrix} 0 & 0.015 \\ 0.015 & 0 \\ & & 0 \end{bmatrix} \frac{\mathbf{e}_i \otimes \mathbf{e}_j}{s},$$

$$\text{Case 3: } \dot{\underline{\epsilon}}^3 = \begin{bmatrix} -0.01 & 0.01 \\ 0.01 & 0.015 \\ & & 0 \end{bmatrix} \frac{\mathbf{e}_i \otimes \mathbf{e}_j}{s},$$

respectively. Each loading takes 1s. The initial parameter sets for initialization of the Downhill-Simplex procedure (see Section 3.5) are  $\underline{p}^1 = [1 \ 1 \ 1]$ ,  $\underline{p}^2 = [2 \ 1 \ 1]$ ,  $\underline{p}^3 = [1 \ 0.1 \ 1]$  and  $\underline{p}^4 = [1 \ 1 \ 0.1]$ , respectively. The corresponding algorithm parameters are  $\alpha_d = 1$ ,  $\gamma_d = 2$ ,  $\beta_d = 0.5$  and  $\sigma_d = 0.5$ , respectively. The results of parameter

identification are summarized in Table 4. All of them are returned by the Downhill-Simplex procedure within 100 iteration steps.

uneven NTFA	$\vartheta$ [-]	$\alpha$ [-]	$\beta$ [-]
Case 1	1.0886	1.7987	0.5440
Case 2	1.2277	2.3222	0.3516
Case 3	1.1203	1.9645	0.4356

Table 4: Example 5; results of parameter identification for different uneven NTFA computations

The results of all three uneven NTFA computations, using the parameter sets in Table 4, are shown in Fig. 12a, Fig. 12b and Fig. 12c, respectively. A comparison with the FEM reference solutions and the even NTFA predictions is given. Considerable corrections are made by the uneven NTFA method, leading to an improved accuracy.

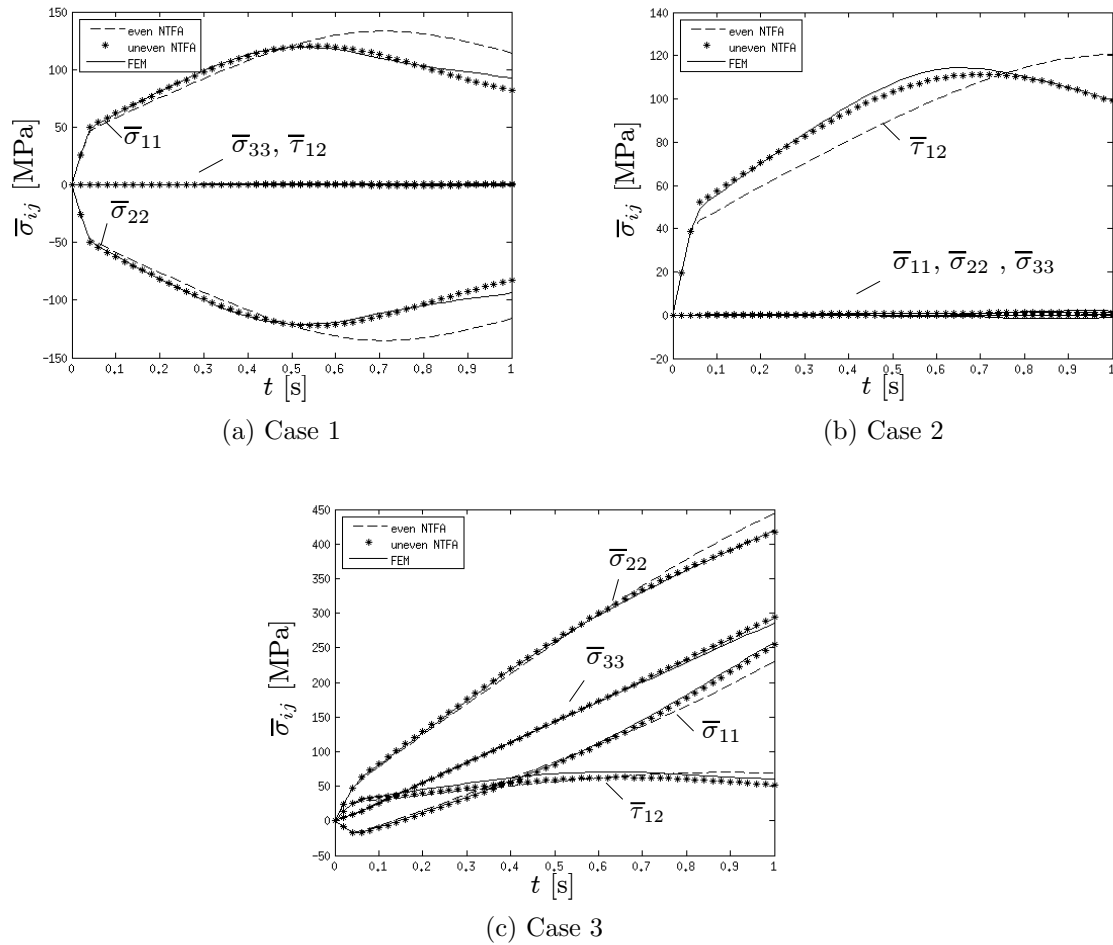


Figure 12: Example 5; results of three uneven NTFA computations

In Fig. 13, the micro von Mises stress fields reconstructed by the even and uneven NTFA, at the end of the 'case 1' computation, are compared with the FEM reference field. An obvious deviation of both the even and uneven NTFA computation from the FEM reference solution is observed, while a difference between the even and the uneven NTFA computation is also given. It becomes obvious that the uneven NTFA does not account for an accuracy improvement on the micro field reconstructions.

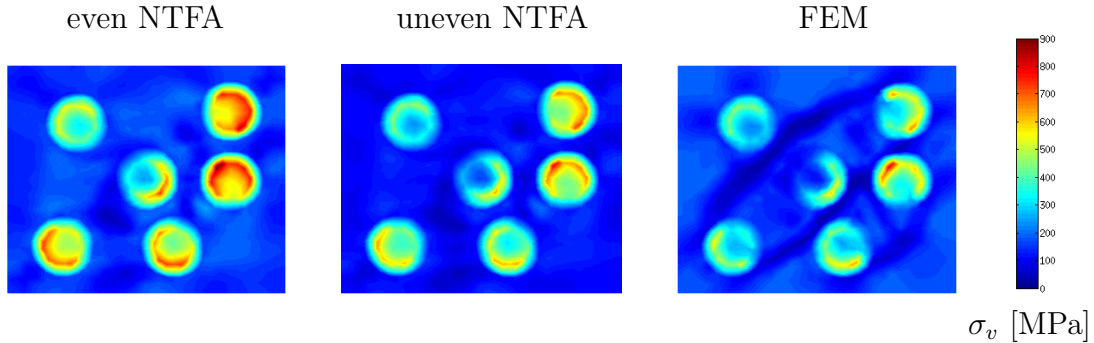


Figure 13: Example 5; comparison of the stress field reconstructed by the even and uneven NTFA to the FEM reference field at the end of the computation ( $t = 1\text{s}$ )

Furthermore, the parameter sets, identified for the different loading conditions in Table 4, are not identical, unfortunately. This means that the fitting parameter set depends also on different loading conditions. Therefore, the use of the uneven NTFA method for structural applications still remains a challenging task for future research.

#### 4.6 Example 6: Macroscopic computations

In order to verify the macroscopic stiffness matrix derived in Section 3.4, we perform a macroscopic example of a tensile-shear test, as illustrated in Fig. 14a. Two equal-sized rods are glued together with a thin layer, which is characterized by the homogenized (NTFA) material. The microstructure of the layer is represented by the RVE with the fine mesh shown in Fig. 5c. The corresponding material parameters are those of Table 1. The rods are assumed to be elastic, with  $E = 2 \cdot 10^6$  MPa and  $\nu = 0.25$ . A displacement-driven algorithm is applied, where the displacement  $u$  is initialized by  $u_0 = 0$  mm and grows with a constant rate  $\dot{u} = 0.05$  mm/s. Additionally, the thickness of rod and the computation time are defined as 10 mm and 1 s, respectively. For a macroscopic computation, the geometry is spatially discretized with 560 quadratic triangular elements, as shown in Fig. 14b.

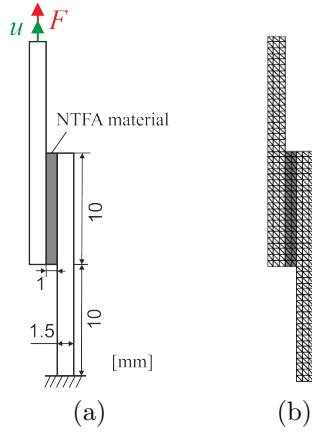


Figure 14: Example 6; a tensile-shear test: (a) Schematic representation; (b) FE discretization

Two computations are performed using the even NTFA and the uneven NTFA method for case 1 in Section 4.5, respectively. For both computations, a quadratic convergence rate is observed for the Newton-Raphson method. The FE results of both computations with regard to the von Mises stress  $\bar{\sigma}_v$  and the damage variable  $\bar{D}$  are presented in Fig. 15. The force-displacement ( $F$ - $u$ ) diagrams for both computations are shown in Fig. 16a, where a softening effect of the force  $F$  due to the damage evolution is present. The even NTFA and the uneven NTFA render completely different results, where the damage evolution is empirically advanced by the uneven NTFA method (see figures 15 and 16a).

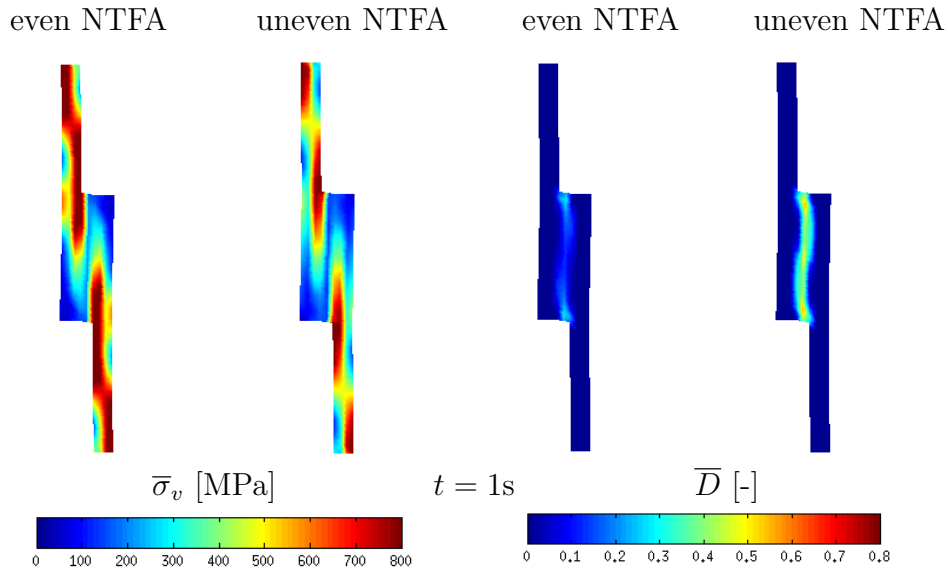
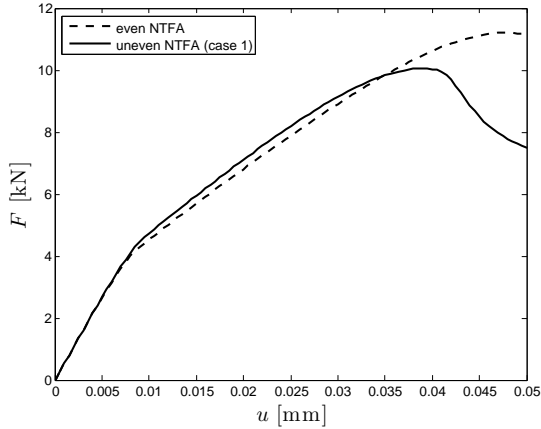
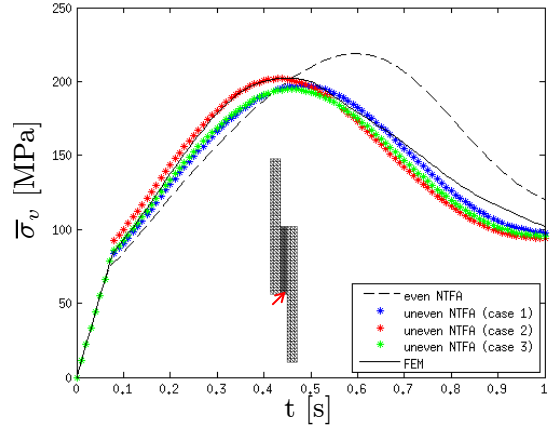


Figure 15: Example 6; FE results of the macroscopic NTFA computations: contour plot of von Mises stress  $\bar{\sigma}_v$  and damage variable  $\bar{D}$



(a) Force  $F$  vs. displacement  $u$



(b) Macroscopic von Mises stresses obtained by different methods with respect to a strain path record

Figure 16: Example 6; results of the macroscopic NTFA computations

Based on the recorded strain path on a selected integration point of the macroscopic even NTFA (see Fig. 16b), five strain path computations are done using the even NTFA, the uneven NTFA with the three different parameter sets in Table 4 and the FEM, respectively. Their results with respect to the macroscopic von Mises stress are summarized in Fig. 16b. The delay effect of the damage evolution is compensated by all three uneven NTFA computations, whereas slight deviations of the stress amplitudes are observed.

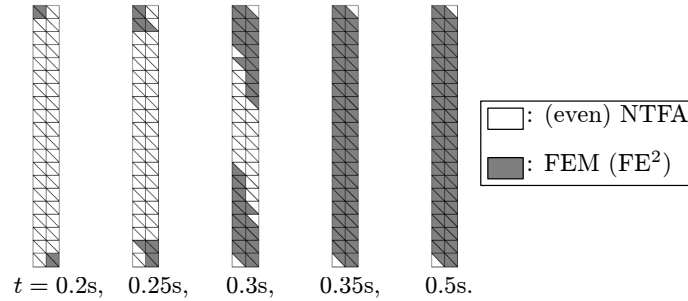


Figure 17: Example 6; illustration of selection within the thin layer of different regions according to Eq. (38) for the adaptive NTFA method

Additionally, to illustrate the structural application of the adaptive NTFA method, the macroscopic example shown in Fig. 14 is performed, where the thin layer is homogenized by the even NTFA with the same parameterization as in Section 4.3. According to the indication condition (38) proposed in the adaptive NTFA method, the selection of different regions is illustrated in Fig. 17, which adaptively changes over the time. Here those quadratic triangular elements, whose integration points (at least one) require a microscopic full-field FE-computation, are displayed in dark gray, leading to a partial  $FE^2$  problem. A complete computation saving could be made by the even NTFA from the beginning of the computation up to  $t \approx 0.2$  s, whereas the adaptive NTFA computation would become a complete  $FE^2$  computation since a certain time ( $t > 0.5$  s).

Note also that the selection of different regions, shown in Fig. 17, approximately illustrates that of a macroscopic adaptive NTFA computation, since only the even NTFA is performed for the homogenization of the thin layer, for an acceptable computation time. However, due to the full-field computation regions, resulting into a (partial) FE<sup>2</sup> problem that is beyond the scope of this work, macroscopic examples by means of the adaptive NTFA method are not provided.

## 5 Conclusion and outlook

In this work, an extension on the classical NTFA has been given to consider an additional softening effect. Based on dissipative considerations, a new coupled model for the even NTFA has been derived, where large part of the NTFA theory, such as the approximation of the plastic strains and the localization rules, remains unchanged. Subsequently, the new coupled model has been theoretically and numerically verified for a homogeneous microstructure. This new model is actually a generalization of the classical one with a pure hardening type plasticity, where softening effects are additionally coupled to isotropic hardening type plasticity and a pure hardening type plasticity can be simply recovered by deactivating the damage evolution. It has also been found by the authors that the additional introduction of softening effects gives rise to inaccurate predictions using the even NTFA method. One reason is that the strong material nonlinearity makes the mode identification procedures difficult. More precisely, a set of universal modes may be hardly found for an ideal representation throughout the damaging course. Another reason is that the (even) NTFA for the homogenized material is macroscopically driven, whereas the full-field FE-computations are fully microscopically motivated.

For an accuracy improvement based on the even NTFA predictions, we have presented two new methods. The first method is based on the idea of parameter identification, which fits, in more general cases, experimental data for a given constitutive material model. With this in mind, we have introduced three additional empirical fitting parameters, resulting into uneven micro and macro model structures. Hence, this method has been referred to as the *uneven NTFA method*. The corresponding parameter identification problem has been formulated in the sense of least-squares and numerically solved by the Downhill-Simplex method. The use of the uneven NTFA method has also been illustrated by several numerical examples. A considerable accuracy improvement for the macroscopic predictions has been achieved for different loading conditions. However, the success of the uneven NTFA method (in its present form) is merely limited to one or a group of loading condition(s) on an integration point level, due to the dependence of loadings. Therefore, the structural application of the uneven NTFA method still remains a challenging task for our future research.

Moreover, the second method for accuracy improvement has been referred to as the *adaptive NTFA method*, which is motivated by adaptive modeling. In this method, the reduced homogenization scheme by the even NTFA procedure is merely applied to the elastic and the plastic region. The remaining inelastic region coupled with softening effects, which causes inaccurate NTFA predictions, has to be solved via the FEM. The related localization procedure, required for the numerical im-

plementation, has been proposed. A microscopically motivated indicator has been developed and checked with an example for a fiber-reinforced composite. It has been found that the adaptive NTFA method renders very accurate results of both macroscopic predictions and the microscopic field reconstructions. The main drawback of this method might be the additional computational effort for regions where FEM has been performed for a full-field computation. Given that the damage zone is usually localized in a comparably small region in the case of structural applications, considerable computational savings can be made by the adaptive NTFA method.

Additionally, two-dimensional macroscopic examples have been done by the even and the uneven NTFA method, respectively, to validate the derived macroscopic consistent stiffness matrix. A quadratic convergence rate of the Newton method has been obtained. Furthermore, the numerical efficiency of the NTFA method has been confirmed. A speed-up factor up to 2000 compared to the FE computations has been observed. Another point is that the NTFA procedures have a noticeably better convergence behavior than the full-field FE-computations, since the NTFA procedures are macroscopically driven. The full-field computations need usually more time steps to converge. Note also that our approaches can be extended to three-dimensional applications without any methodological gains.

The gradient theory conventionally used in continuum damage mechanics simulating localization phenomena (see e.g. [32] amongst others) is not considered in this work so far. Additional consideration of damage caused by volumetric stresses is also one of the priorities of our future work.

In last decades, many model reduction schemes, e.g. POD for more general cases (see e.g. [42, 1]), have been developed. Amongst them, the NTFA method still remains an attractive method for homogenization of nonlinear composites. The main limitation of the NTFA is the superposition principle, which is no longer valid e.g. for problems with large deformations. An additional application of the NTFA in adaptive modeling is of our interest.

## Acknowledgment

This work is based on investigations of the collaborative research centre SFB/TR TRR 30, which is kindly supported by the Deutsche Forschungsgemeinschaft (DFG) (grant no.: INST 159/11-3), Germany.

## References

- [1] Berkooz G, Holmes P, Lumley J (1993) The proper orthogonal decomposition in the analysis of turbulent flows. *Annu Rev Fluid Mech* 25:539–575
- [2] Dvorak G, Benveniste Y (1992) On transformation strains and uniform fields in multiphase elastic media. *Proceedings of the Royal Society of London* 437(A):291–310
- [3] Dvorak G, Bahei-El-Din Y, Wafa A (1994) The modeling of inelastic composite

material with the transformation field analysis. *Modelling and simulation in materials science and engineering* 2:571–586

- [4] Federov F (1968) *Theory of elastic waves in crystals*. Plenum Press: New York
- [5] Fish J, Shek K (1999) Finite deformation plasticity for composite structures: Computational models and adaptive strategies. *Comput Methods Appl Mech Engrg* 172:145–174
- [6] Fritzen F (2011) *Microstructural modeling and computational homogenization of the physically linear and nonlinear constitutive behavior of micro-heterogeneous materials*. PhD thesis, Karlsruher Institut für Technologie
- [7] Fritzen F, Böhlke T (2010) Three-dimensional finite element implementation of the nonuniform transformation field analysis. *International Journal for Numerical Methods in Engineering* 84:803–829
- [8] Fritzen F, Böhlke T (2013) Reduced basis homogenization of viscoelastic composites. *Composites Science and Technology* 76:84–91
- [9] Fritzen F, Leuschner M (2013) Reduced basis hybrid computational homogenization based on a mixed incremental formulation. *Comput Methods Appl Mech Engrg* 260:143–154
- [10] Fritzen F, Leuschner M (2015) Nonlinear reduced order homogenization of materials including cohesive interfaces. *Comput Mech* 56:131–151
- [11] Fritzen F, Hodapp M, Leuschner M (2014) Gpu accelerated computational homogenization based on a variational approach in a reduced basis framework. *Comput Methods Appl Mech Engrg* 278:186–217
- [12] Fritzen F, Marfia S, Sepe V (2015) Reduced order modeling in nonlinear homogenization: A comparative study. *Computers and Structures* 157:114–131
- [13] Geers M, Kouznetsova V, Brekelmanns W (2010) Multi-scale computational homogenization: Trends and challenges. *Journal of Computational and Applied Mathematics* 234:2175–2182
- [14] Hill R (1963) Elastic properties of reinforced solids: some theoretical principles. *Journal of the mechanics and physics of solids* 11:357–372
- [15] Jiang T, Shao J, Xu W (2013) A non-uniform transformation field analysis for frictional cohesive geomaterials. *European Journal of Mechanics A/Solids* 42:97–111
- [16] Koch A, Miehe C (2002) Computational micro-to-macro transitions of discretized microstructures undergoing small strains. *Archive of Applied Mechanics* 72(2002):300–317

- [17] Kouznetsova V, Geers M, Brekelmanns W (2002) Multi-scale constitutive modelling of heterogeneous materials with a gradient-enhanced computational homogenization scheme. *International Journal for Numerical Methods in Engineering* 54:1235–1260
- [18] Kouznetsova V, Geers M, Brekelmanns W (2004) Multi-scale second-order computational homogenization of multi-phase materials: a nested finite element solution strategy. *Comput Methods Appl Mech Engrg* 193(48-51):5525–5550
- [19] Largeton R, Michel JC, Suquet P (2014) Extension of the nonuniform transformation field analysis to linear viscoelastic composites in the presence of aging and swelling. *Mechanics of Materials* 73:76–100
- [20] Larsson F, Runesson K (2006) Adaptive computational meso-macro-scale modeling of elastic composites. *Comput Methods Appl Mech Engrg* 195:324–338
- [21] Mahnken R (1998) Theoretische und numerische Aspekte zur Parameteridentifikation und Modellierung bei metallischen Werkstoffen. PhD thesis, Inst. für Baumechanik und Numerische Mechanik, University of Hannover
- [22] Mahnken R (2004) Identification of material parameter for constitutive equations. In: Stein E, deBorst R, Hughes J (eds) *Encyclopedia of Computational Mechanics*, John Wiley & Sons, Ltd., chap 19
- [23] Mahnken R (2012) Simulation of strength difference coupled to softening in elasto-plasticity for adhesive materials. *International Journal of Adhesion and Adhesives* 32:1–14
- [24] Mahnken R, Schlimmer M (2005) Simulation of strength difference in elasto-plasticity for adhesive materials. *International Journal for Numerical Methods in Engineering* 63:1461–1477
- [25] MATLAB (2012) version 8.0.0.783 (R2012b). The MathWorks Inc., Natick, Massachusetts
- [26] Michel J, Suquet P (2003) Nonuniform transformation field analysis. *International Journal for Solids and Structures* 40:6937–6955
- [27] Michel J, Suquet P (2004) Computational analysis of nonlinear composite structures using the nonuniform transformation field analysis. *Computer Methods in Applied Mechanics and Engineering* 193:5477–5502
- [28] Michel JC, Suquet P (2009) Nonuniform transformation field analysis: a reduced model for multiscale nonlinear problems in solid mechanics. In: *Multi-scale Modelling in Solid Mechanics - Computational Approaches*, chap 4, pp 159–206
- [29] Nelder JA, Mead R (1965) A simplex method for function minimization. *Computer Journal* 7:308–313

- [30] Oden J, Vemaganti K (2000) Estimation of local modeling error and goal-oriented adaptive modeling of heterogeneous materials. *Journal of Computational Physics* 164:22–47
- [31] Oden J, Vemaganti K, Moes N (1999) Hierarchical modeling of heterogeneous solids. *Comput Methods Appl Mech Engrg* 172:3–25
- [32] Peerlings R, de Borst R, Brekelmanns W, Geers M (1998) Gradient-enhanced damage modelling of concrete fracture. *Mechanics of Cohesive-frictional Materials* 3(4):323–342
- [33] Preric D, de Souza Neto EA, Feijoo RA, Partovi M, Carneiro Molina AJ (2011) On micro-to-macro transitions for multi-scale analysis of non-linear heterogeneous materials: unified variational basis and finite element implementation. *International Journal for Numerical Methods in Engineering* 87:149–170
- [34] Radermacher A (2015) Proper orthogonal decomposition-based model reduction in nonlinear solid mechanics. PhD thesis, RWTH Aachen University
- [35] Radermacher A, Reese S (2014) Model reduction in elastoplasticity: proper orthogonal decomposition combined with adaptive sub-structuring. *Computational Mechanics* 54(3):677–687
- [36] Radermacher A, Reese S, Hadoush A (2013) Selective proper orthogonal decomposition model reduction for forming simulations. *PAMM* 13(1):115–116
- [37] Roussette S, Michel J, Suquet P (2009) Nonuniform transformation field analysis of elastic-viscoplastic composites. *Composite Science and Technology* 69:22–27
- [38] Sauerland K (2013) Phenomenological process simulation and multiscale tool simulation directed to a hybrid forming process. PhD thesis, University of Paderborn
- [39] Sauerland K, Mahnken R (2012) Two scale fe simulation of coated forming tools under thermo-mechanical loading. *Technische Mechanik* 32,1:84–101
- [40] Sepe V, Marfia S, Sacco E (2013) A non uniform tfa homogenization technique based on piecewise interpolation functions of the inelastic field. *International Journal for Solids and Structures* 50:725–742
- [41] Simo JC, Hughes TJR (1987) General return mapping algorithms for rate-independent plasticity. *Constitutive laws for engineering materials: theory and applications* 1:221–232
- [42] Sirovich L (1987) Turbulence and the dynamics of coherent structures. *Q Appl Math* 45:561–590

---

## Paper D

Xiaozhe Ju and Rolf Mahnken

*Goal-oriented adaptivity for linear elastic micromorphic continua based on primal  
and adjoint consistency analysis*

International Journal for Numerical Methods in Engineering 112 (2017), 1017-1039

---

**Note:** This version slightly differs from the paper by correcting two minor errors pointed out in a corrigendum [68].



# Goal-oriented adaptivity for linear elastic micromorphic continua based on primal and adjoint consistency analysis

Xiaozhe Ju and Rolf Mahnken

Chair of Engineering Mechanics, University of Paderborn,  
Warburger Str. 100, 33098 Paderborn, Germany

## Abstract

Microscopic considerations are drawing increasing attention for modern simulation techniques. Micromorphic continuum theories, considering micro degrees of freedom (DoFs), are usually adopted for simulation of localization effects like shear bands. The increased number of DoFs clearly motivates an application of adaptive methods. In this work, the adaptive FEM is tailored for micromorphic elasticity. The proposed adaptive procedure is driven by a goal-oriented a posteriori error estimator based on duality techniques. For efficient computation of the dual solution, a patch-based recovery technique is proposed and compared to a reference approach. In order to theoretically ensure optimal convergence order of the proposed adaptive procedure, adjoint consistency of the FE-discretized solution for the linear elastic micromorphic continua is shown. For illustration, numerical examples are provided.

**Keywords:** finite element method, micromorphic continuum, goal-oriented adaptivity, error estimate, recovery techniques, primal and adjoint consistency

## 1 Introduction

Many materials show size-dependent behavior, e.g. for metals and ceramics the indentation hardness increases with decreasing indenter size for micro-size indents, see [48, 37, 42, 6]. Additionally, there are localization phenomena, such as shear bands, which occur under softening. The classical continuum theory is not able to account for these phenomena, which is why different extensions of classical continuum theory have been developed. Supplementary quantities are introduced, that lead to nonlocal behavior, meaning that the stresses of a material point are dependent on a finite neighborhood. To govern the nonlocality an internal length scale is introduced. This leads to a regularization of the boundary value problem, when localization phenomena arise, and the internal length scale can be used to represent size dependence. When higher order gradients of strain or internal variables are used to account for nonlocal behavior, the theories are called gradient theories [41, 31].

The so-called micromorphic theories were originally introduced by Eringen in [12], who intends to capture the microstructure of a material by introducing additional degrees of freedom (DoFs), labeled as micro DoFs. In doing so, an additional micro continuum representing a deformation of this point is attached to each material point. As well known, the micromorphic theories incorporate micropolar and microstrain theories as special cases. The subsequent publications, e.g. [13], focused on micropolar continua, which have a rigid micro continuum that can only rotate, whereas a micromorphic continuum has fully deformable micro continua. The micropolar continuum is covered extensively in the literature, see e.g. [47, 10, 9, 39] for the aspects of plasticity and parameter identification. Microstrain theories are treated, e.g. in [18]. Plasticity for micromorphic continua has been the subject of various publications in recent years, see e.g. [16, 15, 29, 23, 24, 25]. The papers [15, 24, 25] are also concerned with damage. A detailed comparison of micromorphic, micropolar and microstrain continua is given in [36]. As shown in [38], these theories can be seen as special cases within the framework of generalized stresses [20, 21, 26, 19, 2].

Adaptive refinement is a systematic methodology to find a proper mesh for the simulations and thus save computational costs compared to uniform refinement. The basis for adaptive refinement is error estimate, for which there are different possibilities. In this paper goal-oriented a posteriori error estimate is considered, where an auxiliary dual (adjoint) problem is required. On the one hand, this procedure can be employed to calculate an estimate of a quantity of the solution. In this step, no mesh refinement is involved. On the other hand, one can use the local residuals calculated from the goal-oriented error estimate procedures to steer optimal mesh refinement with respect to that quantity. Both procedures can be effectively combined. For the general framework of a posteriori error estimate, we refer to [11, 49, 1, 34, 4, 46]. The term “goal-oriented” means that the refinement is governed with respect to a quantity of interest. Usually, the aim of a simulation is to find solutions for a certain quantity. Adaptive mesh refinement is then governed by error indicators which are localizations of the global error to elements. It is then advantageous to refine the mesh with the goal of minimizing the error in this quantity of interest. Contributions to this topic can be found in [5, 40, 7, 43]. To the authors’ knowledge goal-oriented error estimate has not been applied to micromorphic continua, and subsequently, no literature exists on this kind of problem. The present paper intends to close this gap. For efficient computation of the dual solution, which is essential for the error estimate, a patch-based recovery technique is proposed and compared to a reference approach. For a more detailed comparison of the proposed recovery technique w.r.t. model adaptivity of multiscale problems, we refer to our recent work [33].

In addition to consistency in the numerical analysis for the primal problem, the so-called adjoint consistency is drawing increasing attention, see e.g. [3, 27] for discontinuous Galerkin methods. Adjoint consistency is a key property of discretizations, which ensures optimal order of convergence of the error measured in an energy norm as well as in terms of a specific quantity of interest. A general framework for adjoint consistency analysis was suggested by Hartmann [28]. According to [28], we perform, in this work, a primal and an adjoint consistency analysis for the linear elastic micromorphic continua.

The paper is structured as follows: In Section 2, the classical micromorphic continuum framework is revisited, including kinematic relations, balance laws in strong and weak form as well as a linear elastic constitutive model. Section 3 is concerned with goal-oriented adaptivity, for which a dual problem is introduced and a computable error representation for discretization errors is derived. For illustration purposes, three numerical examples are presented in Section 4. A conclusion and an outlook on further research are given in Section 5. Finally, a primal and an adjoint consistency analysis are performed in Appendix A.

Notation: The scalar products of two vectors  $\mathbf{a}$  and  $\mathbf{b}$ , two second-order tensors  $\mathbf{A}$  and  $\mathbf{B}$  and two third-order tensors  $\mathbf{Q}$  and  $\mathbf{R}$  are

$$\mathbf{a} \cdot \mathbf{b} = a_i b_i, \quad \mathbf{A} : \mathbf{B} = A_{ij} B_{ij}, \quad \mathbf{Q} \cdot \mathbf{R} = Q_{ijk} R_{ijk}, \quad (1)$$

respectively, using the Einstein summation convention for repeated indices. Additionally, we define a modified scalar product  $\overset{(\bullet)}{\cdot}$ , for instance,  $\nabla \overset{(2)}{\cdot} \mathbb{C} := \nabla_j C_{ijkl} \mathbf{e}_i \otimes \mathbf{e}_k \otimes \mathbf{e}_l$ , using the Einstein summation convention for repeated indices. By  $\otimes$  we denote the standard dyadic product and by  $\overset{(\bullet, \bullet)}{\otimes}$  a modified one. There holds, for instance,  $\mathbf{Q} \overset{(2,4)}{\otimes} \mathbf{A} := Q_{ikm} A_{jl} \mathbf{e}_i \otimes \mathbf{e}_j \otimes \mathbf{e}_k \otimes \mathbf{e}_l \otimes \mathbf{e}_m$ . The gradient operator  $\nabla$  is introduced as

$$\nabla \mathbf{c} := \mathbf{c} \otimes \nabla = c_{i,j} \mathbf{e}_i \otimes \mathbf{e}_j, \quad \text{with } c_{i,j} = \frac{\partial c_i}{\partial X_j}, \quad (2)$$

where  $\mathbf{e}_i$ ,  $i = 1, 2, 3$  is a Cartesian orthonormal basis and  $X_i$  are coordinates of the reference placement  $\mathbf{X}$ . The divergence operator  $\text{Div}(\bullet)$  is defined as

$$\text{Div}(\boldsymbol{\sigma}) := \boldsymbol{\sigma} \cdot \nabla = \sigma_{ij,j} \mathbf{e}_i, \quad \text{with } \sigma_{ij,j} = \frac{\partial \sigma_{ij}}{\partial X_j}. \quad (3)$$

Partial derivatives are denoted as  $\partial_x(\bullet) := \partial(\bullet)/\partial x$ . Gâteaux differentiation of a linear form  $F$  and a (generally) semilinear form  $B$  w.r.t. the argument  $\mathbf{u}$  is denoted as

$$\begin{aligned} 1. \quad D_{\mathbf{u}} F(\mathbf{u}; \mathbf{v}) &= \lim_{\theta \rightarrow 0} \frac{1}{\theta} [F(\mathbf{u} + \theta \mathbf{v}) - F(\mathbf{u})], \\ 2. \quad D_{\mathbf{u}} B(\mathbf{u}; \mathbf{w}, \mathbf{v}) &= \lim_{\theta \rightarrow 0} \frac{1}{\theta} [B(\mathbf{u} + \theta \mathbf{v}; \mathbf{w}) - B(\mathbf{u}; \mathbf{w})], \end{aligned} \quad (4)$$

respectively.

## 2 Linear elasticity in micromorphic continuum

### 2.1 Kinematics

As illustrated in Fig. 1, a classical framework of micromorphic continuum is considered. The macro deformation gradient is defined as

$$\mathbf{F}(\mathbf{X}) = \nabla \varphi(\mathbf{X}), \quad (5)$$

with the operator  $\varphi$  mapping the initial coordinates  $\mathbf{X}$  to the current coordinates  $\mathbf{x} = \varphi(\mathbf{X})$ . The macro displacement is given by  $\mathbf{u} = \mathbf{x} - \mathbf{X}$ . For simplicity, small strains

$$\boldsymbol{\varepsilon} := \nabla^{\text{sym}} \mathbf{u} = \frac{1}{2}(\mathbf{H} + \mathbf{H}^T) \quad (6)$$

are assumed, where

$$\mathbf{H} = \nabla \mathbf{u} = \mathbf{F} - \mathbf{1} \quad (7)$$

is the displacement gradient, and where  $\mathbf{1}$  represents the second-order identity tensor. The underlying microstructure is assumed to undergo an affine micro deformation gradient  $\bar{\mathbf{F}}$ , which is related to the micro displacement gradient  $\bar{\mathbf{H}}$  by  $\bar{\mathbf{H}} = \bar{\mathbf{F}} - \mathbf{1}$ . Hence, an introduction of a specific microstructure, unlike homogenization schemes [44, 14, 32], is not required. Furthermore, we define two additional strain measures: the relative deformation (second-order)

$$\bar{\mathbf{e}}(\mathbf{X}) = \mathbf{H}(\mathbf{X}) - \bar{\mathbf{H}}(\mathbf{X}) \quad (8)$$

and the gradient of the micro displacement gradient being a third-order tensor

$$\bar{\mathbf{G}}(\mathbf{X}) = \nabla \bar{\mathbf{H}}(\mathbf{X}), \quad (9)$$

respectively, depending merely on the macro coordinates  $\mathbf{X}$ .

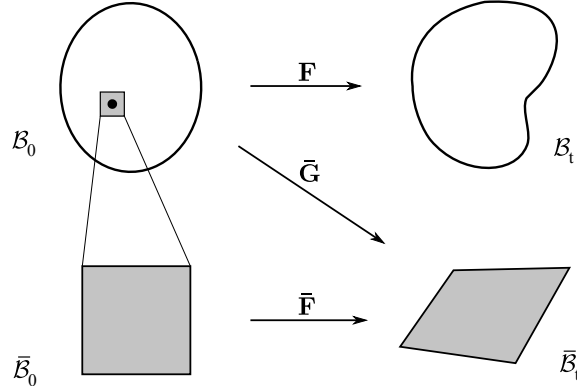


Figure 1: Kinematics of a micromorphic continuum

## 2.2 Balance laws and weak formulations

According to [8, 17] within the small strain framework, the following coupled balance laws for momentum and moment of momentum must be satisfied:

$$1. \text{Div}(\boldsymbol{\sigma} + \bar{\mathbf{s}}) = \mathbf{0}, \quad 2. \text{Div}(\bar{\mathbf{S}}) + \bar{\mathbf{s}} = \mathbf{0}. \quad (10)$$

Here  $\boldsymbol{\sigma}$  is the (symmetric) Cauchy stress tensor,  $\bar{\mathbf{s}}$  the generally nonsymmetric relative stress tensor and  $\bar{\mathbf{S}}$  the third-order hyperstress tensor. Their thermodynamic counterparts, i.e. the corresponding strain tensors, are the small strain tensor  $\boldsymbol{\varepsilon}$ , the relative strain tensor  $\bar{\mathbf{e}}$  and the third-order tensor  $\bar{\mathbf{G}}$ , respectively. Note that body

forces, couples and double forces are not considered here. The following boundary conditions, acting on  $\mathcal{B} = \mathcal{B}_0 = \mathcal{B}_t$  for small strains, apply:

$$\begin{aligned} 1. \quad & \mathbf{u} = \mathbf{u}^{pre} && \text{on } \partial\mathcal{B}^u, & 2. \quad & \overline{\mathbf{H}} = \overline{\mathbf{H}}^{pre} && \text{on } \partial\mathcal{B}^{\overline{\mathbf{H}}}, \\ 3. \quad & (\boldsymbol{\sigma} + \overline{\mathbf{s}}) \cdot \mathbf{N} = \mathbf{t} && \text{on } \partial\mathcal{B}^t, & 4. \quad & \overline{\mathbf{S}} \cdot \mathbf{N} = \overline{\mathbf{T}} && \text{on } \partial\mathcal{B}^{\overline{\mathbf{Q}}}. \end{aligned} \quad (11)$$

Here  $\mathbf{N}$  is the outward normal vector on the boundary  $\partial\mathcal{B}$  and  $\mathbf{t}$  the macro traction on the Neumann boundary  $\partial\mathcal{B}^t$ . The micro traction on the boundary  $\partial\mathcal{B}^{\overline{\mathbf{Q}}}$  in Eq. (11.4) is denoted as  $\overline{\mathbf{T}}$ . A possible micro traction  $\overline{\mathbf{T}}$  is here neglected, i.e.  $\overline{\mathbf{T}} = \mathbf{0}$ , since it can be hardly identified by an experimental setup.

Upon introducing test functions  $\delta\mathbf{u}$  and  $\delta\overline{\mathbf{H}}$ , the final expressions for the weak forms of the balance laws (10) are established as

$$\begin{aligned} 1. \quad & \int_{\mathcal{B}} (\boldsymbol{\varepsilon}[\delta\mathbf{u}] : \boldsymbol{\sigma}[\mathbf{u}] + \mathbf{H}[\delta\mathbf{u}] : \overline{\mathbf{s}}[\mathbf{u}, \overline{\mathbf{H}}]) dV - \int_{\partial\mathcal{B}^t} \delta\mathbf{u} \cdot \mathbf{t} dA = 0, \quad \forall \delta\mathbf{u} \in \mathcal{V}_u, \\ 2. \quad & \int_{\mathcal{B}} (\overline{\mathbf{G}}[\delta\overline{\mathbf{H}}] : \overline{\mathbf{S}}[\overline{\mathbf{H}}] - \delta\overline{\mathbf{H}} : \overline{\mathbf{s}}[\mathbf{u}, \overline{\mathbf{H}}]) dV - \underbrace{\int_{\partial\mathcal{B}^{\overline{\mathbf{Q}}}} \delta\overline{\mathbf{H}} : \overline{\mathbf{T}} dA}_{=0} = 0, \quad \forall \delta\overline{\mathbf{H}} \in \mathcal{V}_H, \end{aligned} \quad (12)$$

respectively, where  $\mathcal{V}_u$  and  $\mathcal{V}_H$  are appropriate Sobolev spaces. A simple combination of the coupled weak forms (12) renders a compact representation

$$\begin{aligned} & \underbrace{\int_{\mathcal{B}} (\boldsymbol{\varepsilon}[\delta\mathbf{u}] : \boldsymbol{\sigma}[\mathbf{u}] + \overline{\mathbf{e}}[\delta\mathbf{u}, \delta\overline{\mathbf{H}}] : \overline{\mathbf{s}}[\mathbf{u}, \overline{\mathbf{H}}] + \overline{\mathbf{G}}[\delta\overline{\mathbf{H}}] : \overline{\mathbf{S}}[\overline{\mathbf{H}}]) dV}_{:=B(\mathbf{u}, \overline{\mathbf{H}}; \delta\mathbf{u}, \delta\overline{\mathbf{H}})} \\ & = \underbrace{\int_{\partial\mathcal{B}^t} \mathbf{t} \cdot \delta\mathbf{u} dA + \int_{\partial\mathcal{B}^{\overline{\mathbf{Q}}}} \delta\overline{\mathbf{H}} : \overline{\mathbf{T}} dA}_{:=F(\delta\mathbf{u}, \delta\overline{\mathbf{H}})} \quad \forall \delta\mathbf{u} \in \mathcal{V}_u, \delta\overline{\mathbf{H}} \in \mathcal{V}_H, \end{aligned} \quad (13)$$

whose left hand side clearly shows three work conjugate pairs. Finally, upon introducing the notion of the generalized solution  $\widehat{\mathbf{u}}$  and its variation  $\delta\widehat{\mathbf{u}}$  as

$$\widehat{\mathbf{u}} := \begin{bmatrix} \mathbf{u} \\ \overline{\mathbf{H}} \end{bmatrix}, \quad \delta\widehat{\mathbf{u}} := \begin{bmatrix} \delta\mathbf{u} \\ \delta\overline{\mathbf{H}} \end{bmatrix}, \quad (14)$$

Eq.(13) rewrites in a compact residual form as

$$\rho(\widehat{\mathbf{u}}; \delta\widehat{\mathbf{u}}) = F(\delta\widehat{\mathbf{u}}) - B(\widehat{\mathbf{u}}; \delta\widehat{\mathbf{u}}) = 0, \quad \forall \delta\widehat{\mathbf{u}} \in \mathcal{V} := \mathcal{V}_u \cup \mathcal{V}_H. \quad (15)$$

### 2.3 Constitutive relations for linear elastic micromorphic continua

We restrict ourselves to linear isotropic elasticity, where the following constitutive equations apply:

$$\begin{aligned} 1. \quad & \boldsymbol{\sigma} = K \text{tr}(\boldsymbol{\varepsilon}) \mathbf{1} + 2G \boldsymbol{\varepsilon}^{\text{dev}} =: \mathbb{C} : \boldsymbol{\varepsilon}, \\ 2. \quad & \overline{\mathbf{s}} = \lambda_s \text{tr}(\overline{\mathbf{e}}) \mathbf{1} + 2\mu_s \overline{\mathbf{e}}^s + 2\mu_{cs} \overline{\mathbf{e}}^a =: \mathbb{A} : \mathbf{H} + \mathbb{B} : \overline{\mathbf{H}}, \\ 3. \quad & \overline{\mathbf{S}} = l^2 (\lambda_m \mathbf{1} \otimes \nabla \text{tr}(\overline{\mathbf{H}}) + 2\mu_m \overline{\mathbf{G}}) =: \mathbb{D} : \overline{\mathbf{G}}. \end{aligned} \quad (16)$$

In Eq. (16.1),  $\boldsymbol{\varepsilon}^{\text{dev}}$  represents the deviatoric part of the strain tensor  $\boldsymbol{\varepsilon}$ , where  $\boldsymbol{\varepsilon}^{\text{dev}} = \boldsymbol{\varepsilon} - \frac{1}{3}\text{tr}(\boldsymbol{\varepsilon})\mathbf{1}$  holds, while  $\mathbb{C}$  is the fourth-order elasticity tensor, described by two material parameters  $K$  and  $G$ . In Eq. (16.2),  $\bar{\boldsymbol{e}}^s$  and  $\bar{\boldsymbol{e}}^a$  are the symmetric and the skew-symmetric part of  $\bar{\boldsymbol{e}}$  in Eq. (8), respectively. Furthermore,  $\mathbb{A}$  and  $\mathbb{B}$  are fourth-order tensors depending on three material parameters  $\lambda_s$ ,  $\mu_s$  and  $\mu_{cs}$ , whereas  $\mathbb{D}$  is a sixth-order tensor depending on three further material parameters  $l$ ,  $\lambda_m$  and  $\mu_m$ . The constant material tensors  $\mathbb{C}$ ,  $\mathbb{A}$ ,  $\mathbb{B}$  and  $\mathbb{D}$  are found as

$$\begin{aligned}
1. \quad \mathbb{C} &= \partial_{\boldsymbol{\varepsilon}} \boldsymbol{\sigma} = K \mathbf{1} \otimes \mathbf{1} + 2G \mathbb{I}^{\text{dev}}, \quad \text{where} \\
\mathbb{I}^{\text{dev}} &= \mathbb{I} - \frac{1}{3} \mathbf{1} \otimes \mathbf{1}, \\
\mathbb{I} &= \mathbf{1} \otimes \mathbf{1}, \\
2. \quad \mathbb{A} &= \partial_{\bar{\boldsymbol{e}}^s} \partial_{\mathbf{H}} \bar{\boldsymbol{e}}, \quad \text{where} \\
\partial_{\bar{\boldsymbol{e}}^s} &= \lambda_s \mathbf{1} \otimes \mathbf{1} + (\mu_s + \mu_{cs}) \mathbb{I} + (\mu_s - \mu_{cs}) \mathbb{I}^T, \\
\partial_{\mathbf{H}} \bar{\boldsymbol{e}} &= \mathbb{I}, \\
3. \quad \mathbb{B} &= \partial_{\bar{\boldsymbol{e}}^s} \partial_{\bar{\mathbf{H}}} \bar{\boldsymbol{e}}, \quad \text{where} \\
\partial_{\bar{\mathbf{H}}} \bar{\boldsymbol{e}} &= -\mathbb{I}, \\
4. \quad \mathbb{D} &= \partial_{\bar{\mathbf{G}}} \bar{\mathbf{S}} = l^2 \lambda_m \mathbf{1} \otimes \mathbf{1} \otimes \mathbf{1} + 2l^2 \mu_m \mathbf{1} \otimes \mathbf{1} \otimes \mathbf{1},
\end{aligned} \tag{17}$$

respectively. From the equations (17.2) and (17.3) we clearly observe that

$$\mathbb{A} = -\mathbb{B}. \tag{18}$$

Also note that all the material tensors  $\mathbb{C}$ ,  $\mathbb{A}$ ,  $\mathbb{B}$  and  $\mathbb{D}$  have major symmetry in the sense that

$$C_{ijkl} = C_{klij}, \quad A_{ijkl} = A_{klij}, \quad B_{ijkl} = B_{klij}, \quad D_{ijklmn} = D_{lmnijk}, \tag{19}$$

and the elasticity tensor  $\mathbb{C}$  also has minor symmetry such that

$$C_{ijkl} = C_{ijlk} = C_{jikl}. \tag{20}$$

## 2.4 Compact weak form for linear elastic micromorphic continua

In this section, we specify the compact representation defined in (13) for our specific model problem. Inserting the constitutive relation (16) into the weak form (12) renders a linear variational form

$$\begin{aligned}
1. \quad &\int_{\mathcal{B}} (\boldsymbol{\varepsilon}[\delta \mathbf{u}] : (\mathbb{C} \boldsymbol{\varepsilon}[\mathbf{u}]) + \mathbf{H}[\delta \mathbf{u}] : (\mathbb{A} \mathbf{H}[\mathbf{u}] + \mathbb{B} \bar{\mathbf{H}})) dV - \int_{\partial \mathcal{B}^t} \delta \mathbf{u} \cdot \mathbf{t} dA = 0, \\
2. \quad &\int_{\mathcal{B}} (\bar{\mathbf{G}}[\delta \bar{\mathbf{H}}] : (\mathbb{D} \bar{\mathbf{G}}[\bar{\mathbf{H}}]) - \delta \bar{\mathbf{H}} : (\mathbb{A} \mathbf{H}[\mathbf{u}] + \mathbb{B} \bar{\mathbf{H}})) dV = 0,
\end{aligned} \tag{21}$$

which, together with the underlying kinematic relations (6), (7) and (9), becomes

$$\begin{aligned}
1. \quad &\int_{\mathcal{B}} (\nabla^{\text{sym}} \delta \mathbf{u} : (\mathbb{C} \nabla^{\text{sym}} \mathbf{u}) + \nabla \delta \mathbf{u} : (\mathbb{A} \nabla \mathbf{u} + \mathbb{B} \bar{\mathbf{H}})) dV - \int_{\partial \mathcal{B}^t} \delta \mathbf{u} \cdot \mathbf{t} dA = 0, \\
2. \quad &\int_{\mathcal{B}} (\nabla \delta \bar{\mathbf{H}} : (\mathbb{D} \nabla \bar{\mathbf{H}}) - \delta \bar{\mathbf{H}} : (\mathbb{A} \nabla \mathbf{u} + \mathbb{B} \bar{\mathbf{H}})) dV = 0,
\end{aligned} \tag{22}$$

$\forall \delta \mathbf{u} \in \mathcal{V}_u, \delta \overline{\mathbf{H}} \in \mathcal{V}_H$ , where  $\int_{\partial \mathcal{B}^{\overline{Q}}} \delta \overline{\mathbf{H}} : \overline{\mathbf{T}} dA = 0$ . For our convenience, the scalar products used in the constitutive equations in (16) are omitted here and hereafter. Due to the minor symmetry of the elasticity tensor  $\mathbb{C}$  in (20), the relation

$$\mathbb{C} \nabla^{\text{sym}} \mathbf{u} = \mathbb{C} \nabla \mathbf{u} \quad (23)$$

holds. Then, the compact form (13) becomes

$$\begin{aligned} & \int_{\mathcal{B}} \begin{bmatrix} \delta \mathbf{u} \\ \delta \overline{\mathbf{H}} \end{bmatrix} : \underbrace{\begin{bmatrix} \nabla \cdot \overset{(2)}{\mathbb{C}} \cdot \nabla + \nabla \cdot \overset{(2)}{\mathbb{A}} \cdot \nabla & \nabla \cdot \overset{(2)}{\mathbb{B}} \\ -\mathbb{A} \cdot \nabla & \nabla \cdot \overset{(3)}{\mathbb{D}} \cdot \nabla - \mathbb{B} \end{bmatrix}}_{:=\mathcal{K}} : \begin{bmatrix} \mathbf{u} \\ \overline{\mathbf{H}} \end{bmatrix} dV \\ & - \int_{\partial \mathcal{B}^t} \begin{bmatrix} \delta \mathbf{u} \\ \delta \overline{\mathbf{H}} \end{bmatrix} : \underbrace{\begin{bmatrix} \mathbf{t} \\ \mathbf{0} \end{bmatrix}}_{:=\widehat{\mathbf{t}}} dA = 0, \end{aligned} \quad (24)$$

whereby the compact residual form (15) is specified as

$$\varrho(\widehat{\mathbf{u}}; \delta \widehat{\mathbf{u}}) = \underbrace{\int_{\partial \mathcal{B}^t} \delta \widehat{\mathbf{u}} \cdot \widehat{\mathbf{t}} dA}_{:=F(\delta \widehat{\mathbf{u}})} - \underbrace{\int_{\mathcal{B}} \delta \widehat{\mathbf{u}} * \mathcal{K} * \widehat{\mathbf{u}} dV}_{:=B(\widehat{\mathbf{u}}; \delta \widehat{\mathbf{u}})} = 0, \quad \forall \delta \widehat{\mathbf{u}} \in \mathcal{V}, \quad (25)$$

and where we make use of the notion of the generalized solution  $\widehat{\mathbf{u}}$  and its variation  $\delta \widehat{\mathbf{u}}$  in (14). We denote  $\mathcal{K}$  introduced in Eq. (24) as a *generalized stiffness operator* for the linear elastic micromorphic continuum. Additionally, the scalar products  $[\cdot : ]^T$  in Eq. (24) are denoted as  $*$  in the compact residual form (25). Furthermore, due to the equations (18) and (19), the identity

$$\delta \widehat{\mathbf{u}} * (\mathcal{K} * \widehat{\mathbf{u}}) = (\mathcal{K} * \delta \widehat{\mathbf{u}}) * \widehat{\mathbf{u}} \quad (26)$$

holds, which shows  $\mathcal{K} = \mathcal{K}^*$ , i.e. the considered problem is self-adjoint.

## 3 Goal-oriented adaptivity

### 3.1 The general abstract setting

Generally, the exact form (15) can not be solved (exactly). Hence, a numerical method like FEM, providing an approximate solution  $\widehat{\mathbf{u}}_h$ , has to be applied, where we introduce a proper approximate FE-space  $\mathcal{V}_h \subset \mathcal{V}$ . We may write the discretized version of (15) as

$$\varrho(\widehat{\mathbf{u}}_h; \delta \widehat{\mathbf{u}}_h) = F(\delta \widehat{\mathbf{u}}_h) - B(\widehat{\mathbf{u}}_h; \delta \widehat{\mathbf{u}}_h) = 0, \quad \forall \delta \widehat{\mathbf{u}}_h \in \mathcal{V}_h. \quad (27)$$

The error w.r.t. the primal solution  $\widehat{\mathbf{u}}$  is defined as  $\widehat{\mathbf{e}} := \widehat{\mathbf{u}} - \widehat{\mathbf{u}}_h$ .

Following the lines of goal-oriented adaptivity [35, 45], we introduce a *quantity of interest*  $Q$ , which has to be Gâteaux differentiable and can be chosen rather arbitrarily. We are then interested in the error  $E$  w.r.t.  $Q$  as

$$E(\widehat{\mathbf{u}}, \widehat{\mathbf{u}}_h) := Q(\widehat{\mathbf{u}}) - Q(\widehat{\mathbf{u}}_h), \quad (28)$$

which can also be formulated as a secant form (see e.g. [45])

$$E(\widehat{\mathbf{u}}, \widehat{\mathbf{u}}_h) = Q_S(\widehat{\mathbf{u}}, \widehat{\mathbf{u}}_h; \widehat{\mathbf{e}}) = \int_0^1 D_{\widehat{\mathbf{u}}} Q(\widehat{\mathbf{u}}_h + s\widehat{\mathbf{e}}; \widehat{\mathbf{e}}) ds, \quad (29)$$

with  $0 \leq s \leq 1$ . We may also construct a secant form w.r.t. the form  $B$  as

$$B_S(\widehat{\mathbf{u}}, \widehat{\mathbf{u}}_h; \delta\widehat{\mathbf{u}}, \widehat{\mathbf{e}}) = \bar{\varrho}(\widehat{\mathbf{u}}_h; \delta\widehat{\mathbf{u}}) = B(\widehat{\mathbf{u}}; \delta\widehat{\mathbf{u}}) - B(\widehat{\mathbf{u}}_h; \delta\widehat{\mathbf{u}}), \quad (30)$$

where

$$B_S(\widehat{\mathbf{u}}, \widehat{\mathbf{u}}_h; \delta\widehat{\mathbf{u}}, \widehat{\mathbf{e}}) := \int_0^1 D_{\widehat{\mathbf{u}}} B(\widehat{\mathbf{u}}_h + s\widehat{\mathbf{e}}; \delta\widehat{\mathbf{u}}, \widehat{\mathbf{e}}) ds. \quad (31)$$

To set a link between the two secant forms (29) and (31), we introduce a *dual Lagrangian functional*

$$L(\widehat{\mathbf{u}}, \widehat{\mathbf{u}}_h; \delta\widehat{\mathbf{z}}, \widehat{\mathbf{z}}) := Q_S(\widehat{\mathbf{u}}, \widehat{\mathbf{u}}_h; \delta\widehat{\mathbf{z}}) - B_S^*(\widehat{\mathbf{u}}, \widehat{\mathbf{u}}_h; \widehat{\mathbf{z}}, \delta\widehat{\mathbf{z}}), \quad (32)$$

where  $B_S^*(\widehat{\mathbf{u}}, \widehat{\mathbf{u}}_h; \widehat{\mathbf{z}}, \delta\widehat{\mathbf{z}})$  is the adjoint of  $B_S(\widehat{\mathbf{u}}, \widehat{\mathbf{u}}_h; \delta\widehat{\mathbf{z}}, \widehat{\mathbf{z}})$ , and where  $\delta\widehat{\mathbf{z}}$  and  $\widehat{\mathbf{z}}$  are test functions. The dual problem is then established by

$$\begin{aligned} \text{stat}_{\delta\widehat{\mathbf{z}}} \{L(\widehat{\mathbf{u}}, \widehat{\mathbf{u}}_h; \delta\widehat{\mathbf{z}}, \widehat{\mathbf{z}})\} &\implies \\ Q_S(\widehat{\mathbf{u}}, \widehat{\mathbf{u}}_h; \delta\widehat{\mathbf{u}}) - B_S^*(\widehat{\mathbf{u}}, \widehat{\mathbf{u}}_h; \widehat{\mathbf{z}}, \delta\widehat{\mathbf{u}}) &= 0, \quad \forall \delta\widehat{\mathbf{u}} \in \mathcal{V}, \end{aligned} \quad (33)$$

where we refer to  $\widehat{\mathbf{z}}$  as the dual solution. Combining equations (29), (30) and (33) renders

$$E(\widehat{\mathbf{u}}, \widehat{\mathbf{u}}_h) = \bar{\varrho}(\widehat{\mathbf{u}}_h, \widehat{\mathbf{z}}) = B(\widehat{\mathbf{u}}; \widehat{\mathbf{z}}) - B(\widehat{\mathbf{u}}_h; \widehat{\mathbf{z}}) = F(\widehat{\mathbf{z}}) - B(\widehat{\mathbf{u}}_h; \widehat{\mathbf{z}}) \quad (34)$$

as an exact error representation, where the last equality is obtained from (25). In combination with the Galerkin orthogonality (27), we finally obtain

$$E(\widehat{\mathbf{u}}, \widehat{\mathbf{u}}_h) = \bar{\varrho}(\widehat{\mathbf{u}}_h, \widehat{\mathbf{z}} - \pi\widehat{\mathbf{z}}) = F(\widehat{\mathbf{z}} - \pi\widehat{\mathbf{z}}) - B(\widehat{\mathbf{u}}_h; \widehat{\mathbf{z}} - \pi\widehat{\mathbf{z}}), \quad (35)$$

where  $\pi\widehat{\mathbf{z}} \in \mathcal{V}_h$  is the projection of  $\widehat{\mathbf{z}}$  onto the FE-space  $\mathcal{V}_h$ .

## 3.2 The special case of linear elastic micromorphic continua

The abstract setting described in Section 3.1 is general and thus valid for nonlinear cases. In the following, we specify the general setting to linear elastic micromorphic continua of Section 2.4. With the specific definition of the bilinear form  $B$  in Eq. (25), the secant form (31) becomes

$$\begin{aligned} B_S(\widehat{\mathbf{u}}, \widehat{\mathbf{u}}_h; \delta\widehat{\mathbf{u}}, \widehat{\mathbf{e}}) &= \int_0^1 D_{\widehat{\mathbf{u}}} B(\widehat{\mathbf{u}}_h + s\widehat{\mathbf{e}}; \delta\widehat{\mathbf{u}}, \widehat{\mathbf{e}}) ds \\ &= \int_0^1 \left( \int_{\mathcal{B}} \delta\widehat{\mathbf{u}} * \mathcal{K} * \widehat{\mathbf{e}} dV \right) ds \\ &= \int_{\mathcal{B}} \delta\widehat{\mathbf{u}} * \mathcal{K} * \widehat{\mathbf{e}} dV = B(\widehat{\mathbf{e}}; \delta\widehat{\mathbf{u}}). \end{aligned} \quad (36)$$

Observe that for  $\delta\hat{\mathbf{u}} = \delta\hat{\mathbf{u}}_h \in \mathcal{V}_h$ , the Galerkin orthogonality condition

$$\begin{aligned} B(\hat{\mathbf{e}}; \delta\hat{\mathbf{u}}_h) &= \int_{\mathcal{B}} \delta\hat{\mathbf{u}}_h * \mathcal{K} * \hat{\mathbf{e}} dV = B(\hat{\mathbf{u}}; \delta\hat{\mathbf{u}}_h) - B(\hat{\mathbf{u}}_h; \delta\hat{\mathbf{u}}_h) \\ &= F(\delta\hat{\mathbf{u}}_h) - B(\hat{\mathbf{u}}_h; \delta\hat{\mathbf{u}}_h) = 0 \end{aligned} \quad (37)$$

holds, where for the third equality we make use of (15) and the last equality corresponds to (27). This means that the error of the primal solution  $\hat{\mathbf{e}}$  is orthogonal to the variation  $\delta\hat{\mathbf{u}}_h$  w.r.t. the generalized stiffness operator  $\mathcal{K}$  in a volume integral sense.

Furthermore, we assume that the considered quantity of interest is also linear, such that the secant form (29) becomes

$$E(\hat{\mathbf{u}}, \hat{\mathbf{u}}_h) = Q_S(\hat{\mathbf{u}}, \hat{\mathbf{u}}_h; \hat{\mathbf{e}}) = \int_0^1 D_{\hat{\mathbf{u}}} Q(\hat{\mathbf{u}}_h + s\hat{\mathbf{e}}; \hat{\mathbf{e}}) ds = Q(\hat{\mathbf{e}}), \quad (38)$$

i.e. in this case the error of quantity of interest  $E(\hat{\mathbf{u}}, \hat{\mathbf{u}}_h) = Q(\hat{\mathbf{u}}) - Q(\hat{\mathbf{u}}_h)$  equals the quantity of error  $Q(\hat{\mathbf{e}})$ . Then, the dual problem (33) simplifies to

$$Q(\delta\hat{\mathbf{u}}) - B^*(\hat{\mathbf{z}}; \delta\hat{\mathbf{u}}) = 0, \quad \forall \delta\hat{\mathbf{u}} \in \mathcal{V}, \quad (39)$$

where  $B^*(\hat{\mathbf{z}}; \delta\hat{\mathbf{u}}) = B(\delta\hat{\mathbf{u}}; \hat{\mathbf{z}})$  is the adjoint of  $B$ . For self-adjoint problems (true for the present case, see Eq. (26)), we have

$$\begin{aligned} Q(\delta\hat{\mathbf{u}}) - B(\hat{\mathbf{z}}; \delta\hat{\mathbf{u}}) &= 0 \implies \\ Q(\delta\hat{\mathbf{u}}) &= B(\hat{\mathbf{z}}; \delta\hat{\mathbf{u}}) = \int_{\mathcal{B}} \delta\hat{\mathbf{u}} * \mathcal{K} * \hat{\mathbf{z}} dV, \quad \forall \delta\hat{\mathbf{u}} \in \mathcal{V}. \end{aligned} \quad (40)$$

In combination with the definitions in (25), the error representation (35) is specified as

$$E(\hat{\mathbf{u}}, \hat{\mathbf{u}}_h) = \int_{\partial\mathcal{B}^t} (\hat{\mathbf{z}} - \pi\hat{\mathbf{z}}) \cdot \hat{\mathbf{t}} dA - \int_{\mathcal{B}} (\hat{\mathbf{z}} - \pi\hat{\mathbf{z}}) * \mathcal{K} * \hat{\mathbf{u}}_h dV. \quad (41)$$

### 3.3 FE discretizations of the dual problem

Clearly, the exact error representation (41) requires the knowledge of the exact dual solution  $\hat{\mathbf{z}}$  obtained from (40), which in general is intractable. Hence, we have to resort to numerical methods (FEM in this case) again. Using the same FE-mesh as for the primal problem (27), one obtains the discretized version of (40) as

$$\begin{aligned} Q(\delta\hat{\mathbf{u}}_h) - B(\hat{\mathbf{z}}_h; \delta\hat{\mathbf{u}}_h) &= 0 \implies \\ Q(\delta\hat{\mathbf{u}}_h) &= \int_{\mathcal{B}} \delta\hat{\mathbf{u}}_h * \mathcal{K} * \hat{\mathbf{z}}_h dV, \quad \forall \delta\hat{\mathbf{u}}_h \in \mathcal{V}_h. \end{aligned} \quad (42)$$

Note that the working dual solution  $\hat{\mathbf{z}}_h$  is not directly useful for the error formula (41), because of its Galerkin orthogonality to the working primal solution  $\hat{\mathbf{u}}_h$  shown in Eq. (37), rendering it unable to give us information in the unresolved directions which contribute to the error representation (41). Hence, we need an *enhanced dual solution*  $\hat{\mathbf{z}}_{h+}$ , which replaces the exact one  $\hat{\mathbf{z}}$  in (41). To this end, we introduce

an enhanced FE-space  $\mathcal{V}_{h^+}$ , satisfying  $\mathcal{V}_h \subset \mathcal{V}_{h^+} \subset \mathcal{V}$ . Here we make use of the hierarchical FE structure, meaning that the enhanced FE-space  $\mathcal{V}_{h^+}$  is obtained by increasing the polynomial interpolation order on the basis of  $\mathcal{V}_h$ . Obviously, the exact enhanced dual solution  $\widehat{\mathbf{z}}_{h^+}$  can be computed from the enhanced discretized dual problem

$$\begin{aligned} Q(\delta\widehat{\mathbf{u}}_{h^+}) - B(\widehat{\mathbf{z}}_{h^+}; \delta\widehat{\mathbf{u}}_{h^+}) &= 0 \quad \implies \\ Q(\delta\widehat{\mathbf{u}}_{h^+}) &= \int_{\mathcal{B}} \delta\widehat{\mathbf{u}}_{h^+} * \mathcal{K} * \widehat{\mathbf{z}}_{h^+} dV, \quad \forall \delta\widehat{\mathbf{u}}_{h^+} \in \mathcal{V}_{h^+}. \end{aligned} \quad (43)$$

which is computationally much more expensive than (42).

### 3.4 Primal and adjoint consistency of the FE discretizations

In addition to consistency of the primal problem, adjoint consistency is a key property of discretizations, which ensures optimal order of convergence of the error in terms of a specific quantity of interest, see e.g. [3, 27] for discontinuous Galerkin methods. Therefore, following the general framework suggested by Hartmann [28], we perform a primal and an adjoint consistency analysis for the linear elastic micro-morphic continua of sections 2.4 and 3.3 in Appendix A.

### 3.5 Efficient computation of the enhanced dual solution

The computation of the enhanced dual solution  $\widehat{\mathbf{z}}_{h^+}$  directly from (43) is quite expensive, therefore, not practicable in general. There exist several contributions in the literature, focused on efficient methods replacing (43). Amongst them, the methods of decoupled computations and locally enhanced FE-space are proposed in [35]. Two variants of local recovery methods are suggested in our preparatory work [50], requiring merely information within one single element after a smoothing procedure.

In the following, we propose a recovery technique based on the idea of locally enhanced FE-space in [35]. Note that the computations on the locally enhanced FE-space in [35] rely on local formulations of the enhanced dual problem (43). Here, these local computations will be replaced by certain minimization problems, which do not require any knowledge about (43). Our approach is illustrated here for linear triangular elements, whose enhancement is the quadratic triangular element. As shown in Fig. 2a, we define a locally enhanced FE-space  ${}^e\mathcal{V}_{h^+}$  for each element  $e$ , which is associated to a *patch*. Hence, we refer to our approach as a patch-based recovery technique. Next, we use the notion  $\widehat{\mathbf{z}}_{h^+} \approx \widehat{\mathbf{z}}_{h^+} = [\widehat{\mathbf{z}}_1 \ \widehat{\mathbf{z}}_2]$ , where  $\widehat{\mathbf{z}}_1$  and  $\widehat{\mathbf{z}}_2$  are nodal values on existing nodes in  $\mathcal{V}_h$  and on additional nodes in  $\mathcal{V}_{h^+}$ , respectively. With the approximation  $\widehat{\mathbf{z}}_1 \approx \widehat{\mathbf{z}}_h$ , we focus on determining  $\widehat{\mathbf{z}}_2$ . To this end, we make a modification on the so-called superconvergent patch recovery [51]. In  ${}^e\mathcal{V}_{h^+}$ , each component  ${}^e\widehat{\mathbf{z}}_{h^+}^i$  of  ${}^e\widehat{\mathbf{z}}_{h^+}$  is assumed to be expressed as a higher order polynomial representation

$${}^e\widehat{\mathbf{z}}_{h^+}^i = \underline{p}(\mathbf{x}) \cdot \underline{a}^i \in {}^e\mathcal{V}_{h^+}, \quad \text{for } i = 1, \dots, n_{\text{dof}}, \quad (44)$$

where the index  $i$  is related to nodal DoFs. For three-dimensional cases, the number of nodal DoFs is  $n_{\text{dof}} = \text{Dim}(\mathbf{z}) + \text{Dim}(\bar{\mathbf{z}}) = 3 + 9 = 12$ , where  $\text{Dim}(\bullet)$  designates the number of coefficients of a vector or a tensor, respectively. For the present two-dimensional cases, we have  $n_{\text{dof}} = 2 + 4 = 6$ . For an enhanced quadratic representation, we define  $\underline{p}(\mathbf{x}) := [1 \ x_1 \ x_2 \ x_1^2 \ x_1x_2 \ x_2^2]$ , while  $\underline{a}^i := [a_1^i \cdots a_k^i \cdots a_6^i]^T$  contains six unknown coefficients. Here  $x_d$ , with  $d = 1, 2$ , corresponds to single components of the coordinate  $\mathbf{x}$ . To determine the unknown coefficients in  $\underline{a}^i$ , minimization problems are formulated as

$$f(\hat{z}_h^i, {}^e\hat{z}_{h+}^i) := \sum_{j=1}^{N^h} \left( \hat{z}_h^i(\mathbf{x}^j) - {}^e\hat{z}_{h+}^i(\mathbf{x}^j) \right)^2 \rightarrow \min, \quad \text{for } i = 1, \dots, n_{\text{dof}}, \quad (45)$$

where  $\hat{z}_h^i$  is the corresponding component of the dual solution obtained from (42). Further,  $N^h$  is the number of existing nodes on the patch. Combining (44) and (45) renders

$$f(\hat{z}_h^i, {}^e\hat{z}_{h+}^i) = \sum_{j=1}^{N^h} \left( \hat{z}_h^i(\mathbf{x}^j) - \underline{p}(\mathbf{x}^j) \cdot \underline{a}^i \right)^2 \rightarrow \min, \quad \text{for } i = 1, \dots, n_{\text{dof}}, \quad (46)$$

which has a simple analytical solution

1.  $\underline{a}^i = \underline{A}^{-1}\underline{b}^i$ , where
2.  $\underline{A} := \sum_{j=1}^{N^h} \underline{p}^T(\mathbf{x}^j)\underline{p}(\mathbf{x}^j)$ ,
3.  $\underline{b}^i := \sum_{j=1}^{N^h} \underline{p}^T(\mathbf{x}^j)\hat{z}_h^i(\mathbf{x}^j)$ .

(47)

Note that the matrix  $\underline{A}$  is independent on index  $i$ . With the result  $\underline{a}^i$ , the additional nodal values  ${}^e\hat{z}_2$  can be simply recovered by (44). Obviously, to obtain the global vector  $\hat{\mathbf{z}}_2$ , Eq. (47) has to be computed for all elements  $e = 1, \dots, N_{el}$  and all nodal DoFs  $i = 1, 2, \dots, 6$ . Given that different nodal values on the same node can be obtained by different computations of (47), the global vector  $\hat{\mathbf{z}}_2$  is calculated by weighted averaging of  ${}^e\hat{z}_2$  from adjacent elements. In our calculation, we use the arithmetic means in case of two adjacent elements as

$$\hat{z}_2^{n,i} = \frac{1}{2} \sum_{e=1}^2 {}^e\hat{z}_2^{n,i}, \quad (48)$$

where the indices  $n, i$  and  $e = 1, 2$  represent the global node, the coefficient of  $\hat{\mathbf{z}}_2$  and the two adjacent elements, respectively. As shown in Fig. 2b, special care must be paid for boundary elements, which do not have sufficient number of surrounding elements in the same manner as shown in Fig. 2a. Consequently, additional nodes have to be included to arrive at a sufficient number of surrounding elements. Additionally, the boundary values must be corrected correspondingly.

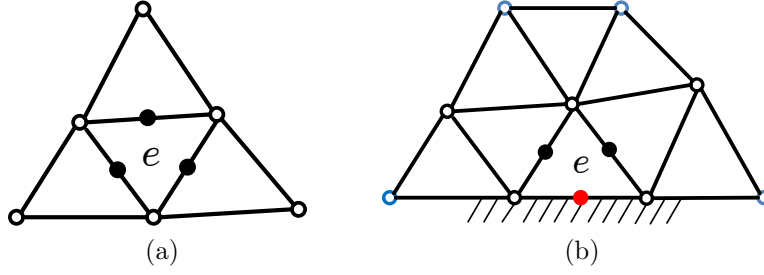


Figure 2: Illustration of patch based recovery approach: (a) Regular case for interior elements ( $\circ$ : existing nodes and  $\bullet$ : additional nodes in locally enhanced FE-space) and (b) special case for boundary elements ( $\circ$ : extended nodes and  $\bullet$ : boundary nodes in locally enhanced FE-space)

### 3.6 Adaptive algorithm

In order to adaptively control the discretization error, we adopt the following algorithm:

1. Initialization: set an initial mesh  $\mathcal{V}_{h^0}$ .
2. Solve the discretized model problem (27).
3. Solve the approximate dual problem (42) on the current mesh and compute the enhanced dual solution via the recovery technique (44)-(47).
4. Compute the estimated error representations (global and local) via

$$\tilde{E}(\hat{\mathbf{u}}, \hat{\mathbf{u}}_h) = F(\hat{\mathbf{z}}_{h^+} - \pi \hat{\mathbf{z}}_{h^+}) - B(\hat{\mathbf{u}}_h; \hat{\mathbf{z}}_{h^+} - \pi \hat{\mathbf{z}}_{h^+}) = \sum_{e=1}^{N_{el}} \eta^e, \quad (49)$$

which is obtained from (35) by the approximation  $\hat{\mathbf{z}} \approx \hat{\mathbf{z}}_{h^+}$ . Here,  $\eta^e$  is the contribution of element  $e$  for the estimated global error  $\tilde{E}$ .

5. Check the stopping criterion  $\tilde{E} < TOL$ , where  $TOL$  is a user-defined threshold value related to the desired accuracy. If the stopping criterion is fulfilled, then break and return the current solution.
6. Otherwise, do refinement: a fixed quota, here  $\alpha = 5\%$ , of the elements with the largest  $|\eta^e|$  is spatially refined; go to step 2.

## 4 Numerical examples

In this section, a perforated sheet is investigated as a linear elastic micromorphic continuum. As shown in Fig. 3a, we consider a quarter model of the sheet, which is stretched by a displacement  $u = 0.01$  mm in 1-direction. The indices 1 and 2 represent the horizontal and the vertical direction, respectively. We restrict ourselves to a two-dimensional case. The thickness of the sheet is 1 mm. A plane strain state is assumed, where the third strain component  $\varepsilon_{33}$  implying the strain in the

thickness direction is always zero. The used material parameters are summarized in Tab. 1. The adaptive FEM starts with the initial mesh  $\mathcal{V}_{h^0}$  shown in Fig. 3b, consisting of linear triangular elements. For an efficiency study of the proposed adaptive procedure, a comparison with uniform refinements will be done. Additionally, a comparison between the patch recovery technique proposed in Section 3.5 and a reference approach based on full computation of the enhanced discretized dual problem (43) will be performed.

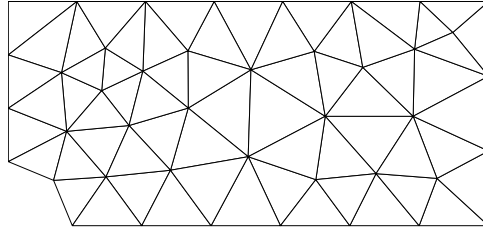
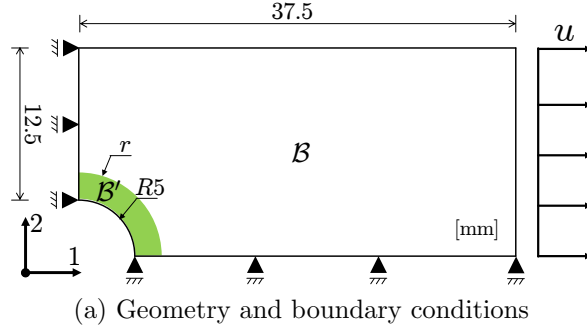


Figure 3: Perforated sheet in micromorphic elasticity

$K$	$G$	$\lambda_s$	$\mu_s$	$\mu_{cs}$	$l$	$\lambda_m$	$\mu_m$
[MPa]	[MPa]	[MPa]	[MPa]	[MPa]	[-]	[MPa]	[MPa]
175000	80769	175000	80769	80769	0.1	175000	80769

Table 1: Summary of material parameters

According to the results of the adjoint consistency analysis in Appendix A, it turns out that the used discretizations are adjoint-consistent only for certain quantities of interest. For simplicity, we consider, in this work, quantities of interest of a volume integral type, for which adjoint consistency is ensured. In practice, one might be interested in a particular quantity on a certain domain. For illustration, we will present three numerical examples, considering three different types for the

quantity of interest  $Q$

$$\begin{aligned}
1. \text{ global: } & Q(\mathbf{u}) := \int_{\mathcal{B}} \sigma_{ij} dV = \int_{\mathcal{B}} \{\mathbb{C} : \nabla \mathbf{u}\}_{ij} dV, \\
2. \text{ local: } & Q(\mathbf{u}) := \int_{\mathcal{B}'} \sigma_{ij} dV = \int_{\mathcal{B}} \phi(\mathbf{x}) \sigma_{ij} dV, \\
3. \text{ local: } & Q(\overline{\mathbf{H}}) := \int_{\mathcal{B}'} \overline{H}_{ij} dV = \int_{\mathcal{B}} \phi(\mathbf{x}) \overline{H}_{ij} dV,
\end{aligned} \tag{50}$$

respectively, with a regularization function

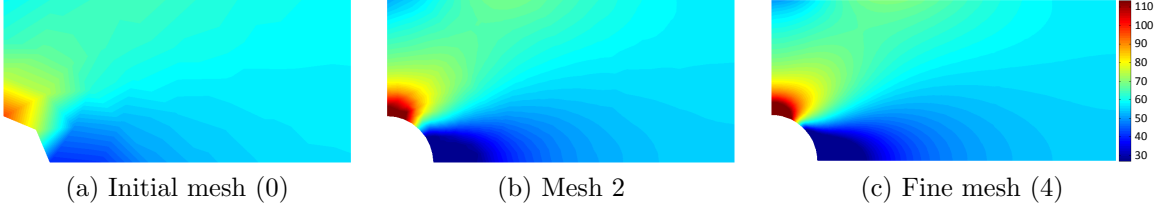
$$\phi(\mathbf{x}) = \begin{cases} 1, & \text{if } \mathbf{x} \in \mathcal{B}', \\ 0, & \text{otherwise.} \end{cases} \tag{51}$$

Here  $\sigma_{ij}$  and  $\overline{H}_{ij}$  are coefficients of the stress tensor  $\boldsymbol{\sigma}$  and the micro displacement gradient  $\overline{\mathbf{H}}$ , respectively. Note that (50.1) and (50.2) are concerned with stresses, which are of engineering interest, whereas (50.3) is more of academic interest, however, demonstrates the general applicability of the proposed methodology. Further,  $\mathcal{B}'$  is a local domain out of the whole domain  $\mathcal{B}$ , i.e. the green area marked in Fig. 3a, with  $r = 8$  mm.

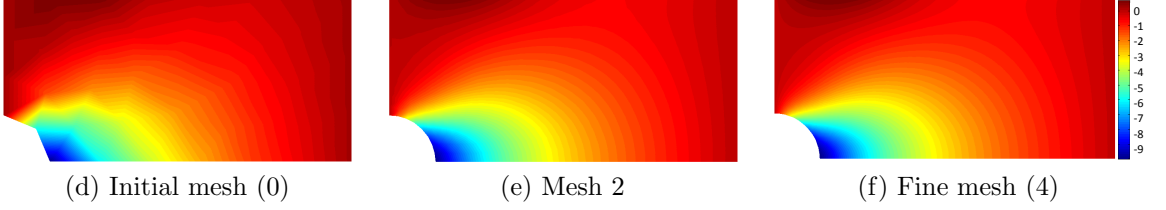
#### 4.1 Example 1: Global quantity of interest w.r.t. stresses

This example deals with the global quantity of interest defined in Eq. (50.1), with the choice  $i = j = 1$ . The primal solution  $\sigma_{11}$  and the dual solution  $\widehat{z}_1$  using uniform refinements are shown in Figs. 4a-4c and 4d-4f, respectively, where  $\widehat{z}_1$  represents the first component of  $\widehat{\mathbf{z}}_h$  computed from (42). Note that the working dual solution  $\widehat{\mathbf{z}}_h$  is not used in the error computation (see Section 3.3). For a computational saving of error estimate, we make use of an (approximate) enhanced dual solution  $\widehat{\mathbf{z}}_{h+}$  obtained by the recovery technique proposed in Section 3.5 on the basis of  $\widehat{\mathbf{z}}_h$ . As a representative example, a comparison of the working dual solution  $\widehat{\mathbf{z}}_h$  and the enhanced dual solution by full computation ( $\widehat{\mathbf{z}}_{h+}$ ) and by patch recovery described in Section 3.5 ( $\widehat{\mathbf{z}}_{h+}^1$ ) is given in Fig. 5. By *full computation* we mean the reference approach, where the enhanced dual solution  $\widehat{\mathbf{z}}_{h+}$  is fully computed from the enhanced discretized dual problem (43). The full computation approach is computationally expensive and only used here for a comparison with the proposed patch recovery technique. From the Figs. 5a and 5c we observe that the recovered enhanced dual solution  $\widehat{\mathbf{z}}_{h+}^1$  is smoother than the working dual solution  $\widehat{\mathbf{z}}_h^1$ . Moreover, a slight deviation of the recovered enhanced dual solution  $\widehat{\mathbf{z}}_{h+}^1$  from the actual enhanced dual solution  $\widehat{\mathbf{z}}_{h+}^1$  is revealed by a comparison of the Figs. 5c and 5b. Consequently, with the recovery technique we somehow extrapolate the working dual solution to an enhanced FE-space and expect to circumvent the issue of Galerkin orthogonality stated in Section 3.3. The following results substantiate our approach.

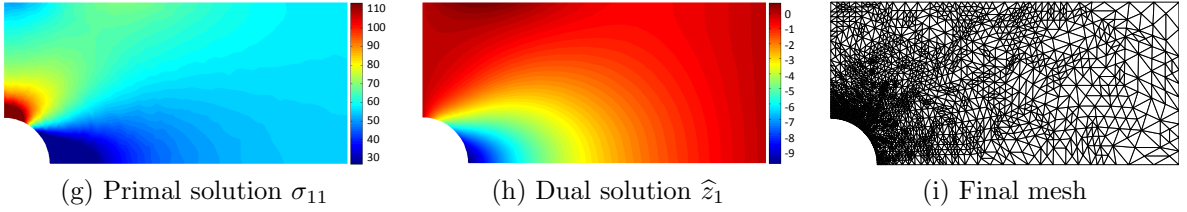
Primal solution  $\sigma_{11}$  for different meshes with uniform refinements



Dual solution  $\hat{z}_1$  for different meshes with uniform refinements



Results after 15 adaptive refinements (patch recovery)



Local error indicators  $|\eta^e|$  (patch recovery)

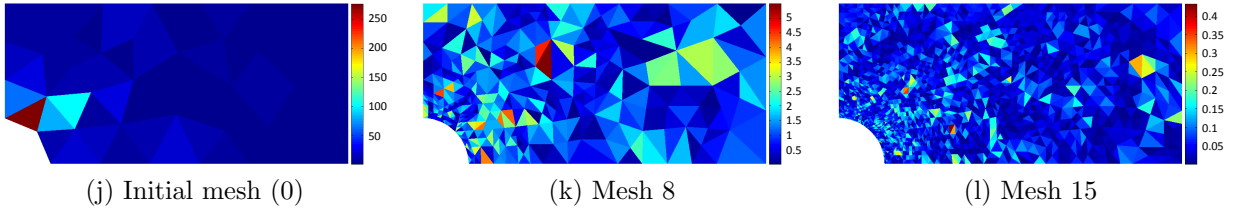


Figure 4: Example 1: Summary of results

Fig. 4i depicts the final mesh after 15 adaptive refinements based on the patch recovery technique. The primal solution  $\sigma_{11}$  and the dual solution  $\hat{z}_1$  of this mesh, shown in Figs. 4g and 4h, respectively, are rather close to their references in Figs. 4c and 4f. The distributions of the local error indicators  $|\eta^e|$  are depicted for different meshes in Fig. 4j-4l, showing that the discretization errors are strongly reduced by the adaptive procedure using patch recovery. From the local error indicator formular (49) we observe that the local error indicators  $|\eta^e|$  depend on the working primal solution  $\hat{\mathbf{u}}_h$ , the enhanced dual solution  $\hat{\mathbf{z}}_{h+}$  as dual weights and the magnitude of the element volume or area etc. Since the difference of the volume or area between individual elements on the initial mesh is much smaller than that on the subsequent nonuniformly refined meshes, a clear error distribution pattern is recognized in Fig. 4j, which is not observed in the Figs. 4k and 4l. Moreover, the Figs. 4j-4l illustrate a balanced error distribution with increasing refinement.

Finally, a comparison between the adaptive procedures (patch recovery and full computation) and uniform refinements is given in Fig. 6. Fig. 6a shows  $Q$  for different procedures versus the number of DoFs. In Fig. 6b, a normalized measure representing the global error  $E$  is defined as

$$\hat{E} := \left| \frac{Q_{ref} - Q_{FEM}}{Q_{ref}} \right|, \quad (52)$$

where  $Q_{ref}$  represents the reference value shown in Fig. 6a. In order to exploit our limited computation source for a highly accurate reference value, the reference solution is obtained by using a mesh that is refined uniformly once from the last adaptive mesh represented in Fig. 4i. Note that  $\hat{E}$  is still an estimate, since  $Q_{ref}$  is not exact. The efficiency of both adaptive procedures (in comparison with uniform refinements) is striking, while a good convergence behavior is also noticeable. Although the error  $\hat{E}$  by full computation is reduced slightly faster than that by patch recovery at the beginning of the adaptive steps, the results of patch recovery are quite reliable and satisfactory.

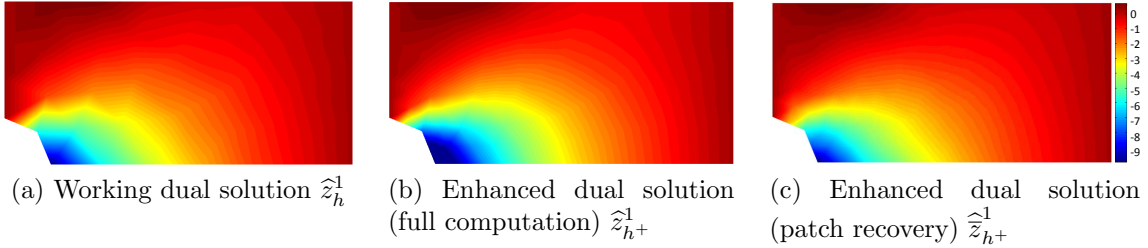


Figure 5: Example 1: Comparison of working and enhanced dual solutions for the initial mesh

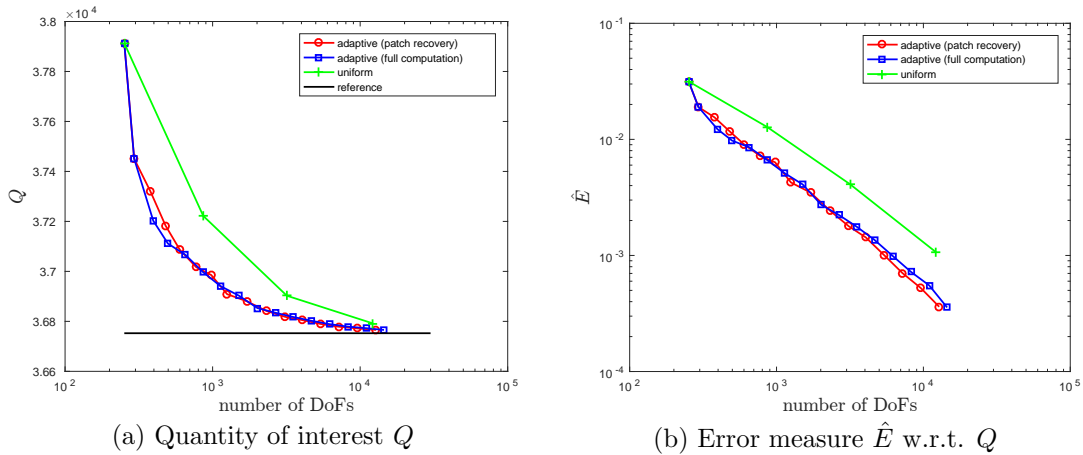


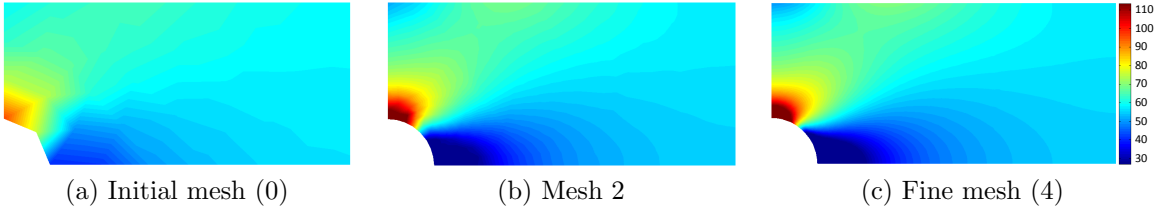
Figure 6: Example 1: Comparison with uniform refinements

## 4.2 Example 2: Local quantity of interest w.r.t. stresses

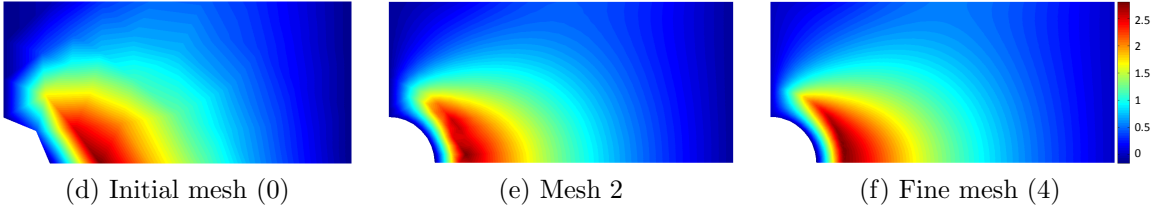
This example is concerned with the local quantity of interest defined in Eq. (50.2), with the choice  $i = j = 1$ . The only difference from Example 1 is that we now

consider  $\sigma_{11}$  in the local domain  $\mathcal{B}'$ . Naturally, the primal solution of uniform refinements remains unchanged, cf. Figs. 4a-4c and 7a-7c. The dual solution  $\hat{z}_1$  illustrated in Figs. 7d-7f shows large differences from Figs. 4d-4f, since the first term in the dual problem (42) differs from that of Example 1. In Fig. 7i, the final mesh after 15 adaptive refinements is presented, where the refinements are mainly concentrated in the local domain  $\mathcal{B}'$ , especially in its boundary regions. The primal solution  $\sigma_{11}$  and the dual solution  $\hat{z}_1$  shown in Figs. 7g and 7h, respectively, are also close to their references in Figs. 7c and 7f. The distributions of the local error indicators  $|\eta^e|$  are depicted for different meshes in Figs. 7j-7l, showing that the discretization errors are strongly reduced by the adaptive procedure.

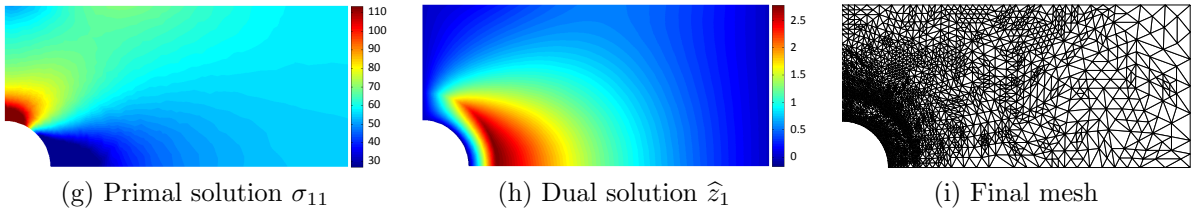
Primal solution  $\sigma_{11}$  for different meshes with uniform refinements



Dual solution  $\hat{z}_1$  for different meshes with uniform refinements



Results after 15 adaptive refinements (patch recovery)



Local error indicators  $|\eta^e|$  (patch recovery)

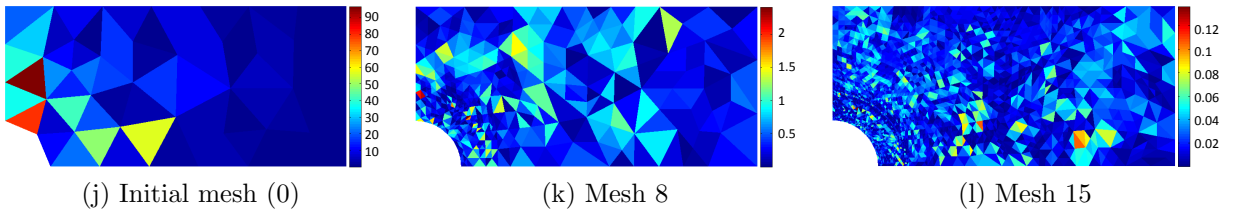


Figure 7: Example 2: Summary of results

As done in Example 1, a comparison with uniform refinements is given in Fig. 8, showing the effectiveness of the adaptive procedure. In contrast to Fig. 6b in

Example 1, the error curves of the adaptive procedures depicted in Fig. 8b is less smooth. This might be due to the fact that the local domain  $\mathcal{B}'$  is not exactly reproduced by the FE discretizations and the reproduction quality changes in the course of the adaptive refinement. In Fig. 8b, there is only a slight difference between the error curves of both adaptive procedures on the previous steps, whereas the difference becomes larger in the course of the adaptive refinements. Interestingly, the patch recovery technique converges faster than the full computation approach at the intermediate steps, however, slower at the end. Nevertheless, the patch recovery technique shows a good effectiveness and a satisfactory convergence behavior.

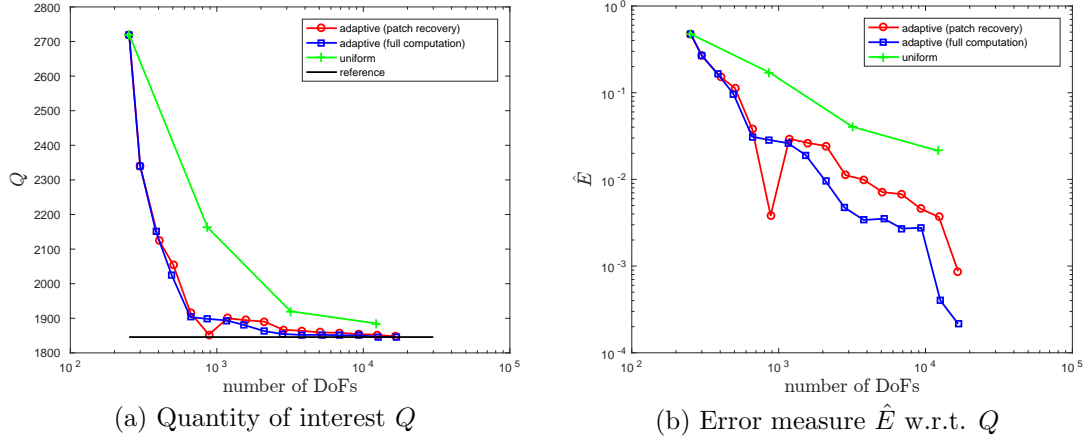
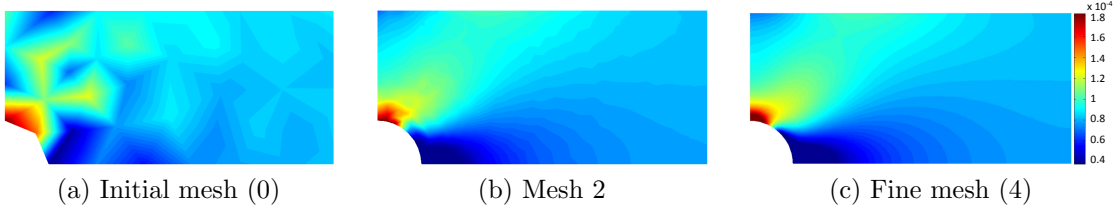


Figure 8: Example 2: Comparison with uniform refinements

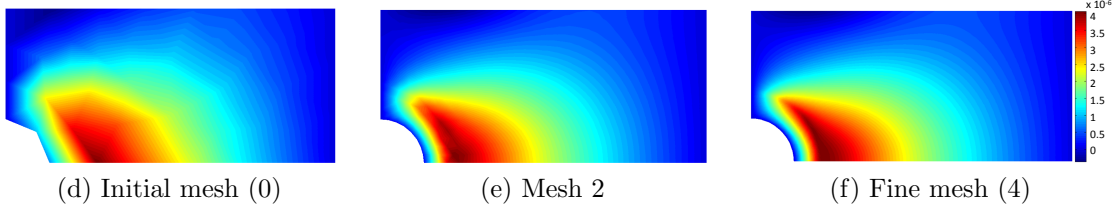
### 4.3 Example 3: Local quantity of interest w.r.t. the micro displacement gradient

In this example, we consider the local quantity of interest defined in Eq. (50.3), with the choice  $i = j = 1$ . The difference from Example 2 is that the quantity of interest is now related to a peculiar quantity in micromorphic continuum. As done in examples 1 and 2, we present the results of uniform refinements in Figs. 9a-9f. The adaptive results are shown in Figs. 9g-9l, supporting the same statements as Example 2. A comparison between the adaptive procedures and uniform refinements is given in Fig. 10, showing the effectiveness of the adaptive procedures. In Fig. 10b, it can be seen that a similar accuracy level is finally reached by both adaptive procedures (patch recovery and full computation), although the error convergence curve of the full computation is overall smoother than that of the patch recovery. Given the fact that the patch recovery technique converges all times much faster than uniform refinements, despite of a possible erratic error reduction pattern on the small error regions, the proposed patch recovery technique is a promising choice for an efficient computational saving.

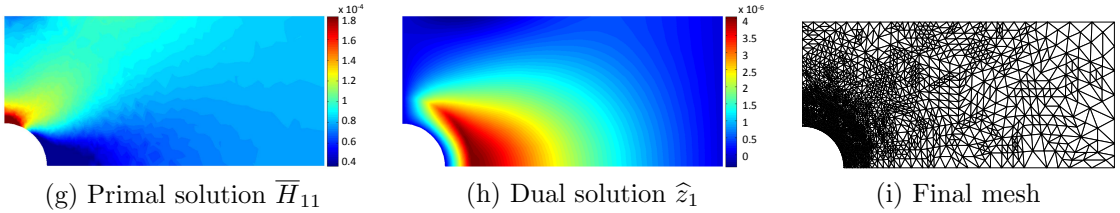
Primal solution  $\overline{H}_{11}$  for different meshes with uniform refinements



Dual solution  $\widehat{z}_1$  for different meshes with uniform refinements



Results after 15 adaptive refinements (patch recovery)



Local error indicators  $|\eta^e|$  (patch recovery)

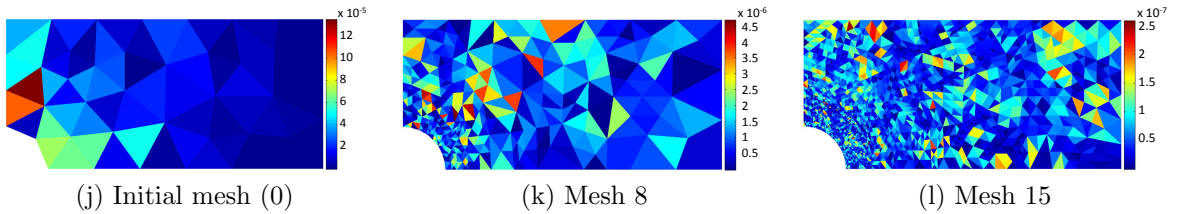


Figure 9: Example 3: Summary of results

## 5 Conclusion and outlook

In this work, the well established goal-oriented adaptivity has been applied to a class of micromorphic continuum problems. Using the notion of the generalized solution, the abstract setting preserves the classical format. An efficient a posteriori error estimator, driving the adaptive FEM, has been derived, where a tailored patch-based recovery technique is proposed and compared to the full computation approach. For illustration, three numerical examples have been presented, giving a comparison with uniform refinements. The results are quite satisfactory, showing the effectiveness of the proposed adaptive procedure, both for global and local quantities of interest. Furthermore, the FE discretizations are shown to be consistent for the primal problem and adjoint-consistent for the dual problem.

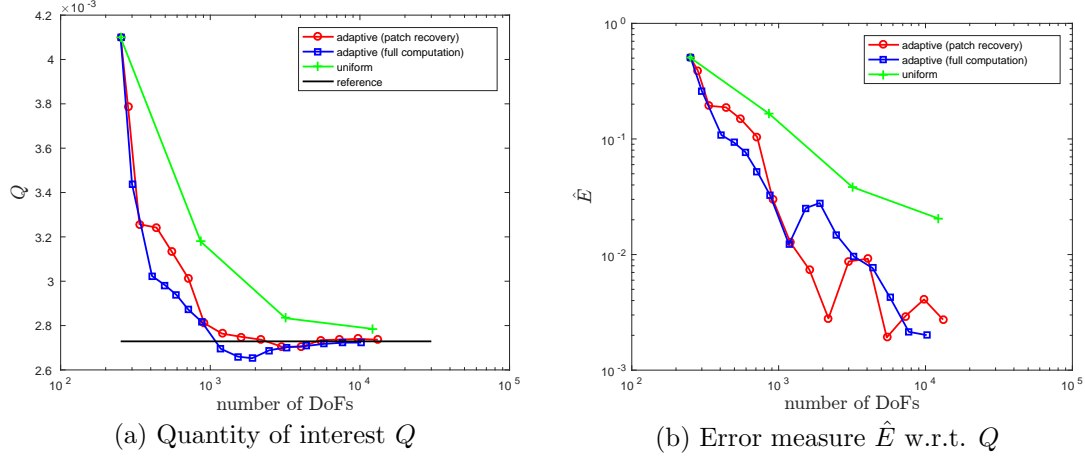


Figure 10: Example 3: Comparison with uniform refinements

In future, nonlinear problems, such as large deformations or plasticity, will be considered. The parameter identification for micromorphic problems is also a great challenge for us.

## Acknowledgment

This paper is based on investigations supported by the Deutsche Forschungsgemeinschaft (DFG) under grant MA 1979/17-1. Furthermore, the authors are grateful to several suggestions of the reviewers.

## A Primal and adjoint consistency analysis for linear elastic micromorphic continua

According to the general framework suggested by Hartmann [28], we perform, in the following, a primal and an adjoint consistency analysis for linear elastic micromorphic continua.

**General framework for linear problems.** Let

$$\begin{cases} \mathcal{L}u = \mathbf{f}, & \text{in } \mathcal{B} \\ \mathcal{B}u = \mathbf{g}, & \text{on } \partial\mathcal{B} \end{cases} \quad (\text{A.1})$$

be a linear differential problem with a linear differential operator  $\mathcal{L}$  on the domain  $\mathcal{B}$  and a linear differential operator  $\mathcal{B}$  on the boundary  $\partial\mathcal{B}$ . One might be interested in a target function as

$$Q(\mathbf{u}) = \int_{\mathcal{B}} \mathbf{q}_{\mathcal{B}} \cdot \mathbf{u} dv + \int_{\partial\mathcal{B}} \mathbf{q}_{\partial\mathcal{B}} \cdot \mathcal{C}u da, \quad (\text{A.2})$$

where  $\mathcal{C}$  is a boundary differential operator on  $\partial\mathcal{B}$ . The target function (A.2) is *compatible* with (A.1), provided that

$$(\mathcal{L}u, \mathbf{z})_{\mathcal{B}} + (\mathcal{B}u, \mathcal{C}^* \mathbf{z})_{\partial\mathcal{B}} = (\mathbf{u}, \mathcal{L}^* \mathbf{z})_{\mathcal{B}} + (\mathcal{C}u, \mathcal{B}^* \mathbf{z})_{\partial\mathcal{B}} \quad (\text{A.3})$$

holds, where  $\mathcal{L}^*$ ,  $\mathcal{B}^*$  and  $\mathcal{C}^*$  are the adjoint operators to  $\mathcal{L}$ ,  $\mathcal{B}$  and  $\mathcal{C}$ , respectively. Additionally,  $(\bullet, \bullet)_{\mathcal{B}}$  and  $(\bullet, \bullet)_{\partial\mathcal{B}}$  denote the  $L^2$  scalar products over the domain  $\mathcal{B}$  and over the boundary  $\partial\mathcal{B}$ , respectively. Assuming that Eq. (A.3) holds, the adjoint problem associated to (A.1) and (A.2) is then given by

$$\begin{cases} \mathcal{L}^*z = \mathbf{q}_{\mathcal{B}}, & \text{in } \mathcal{B} \\ \mathcal{B}^*z = \mathbf{q}_{\partial\mathcal{B}}, & \text{on } \partial\mathcal{B}, \end{cases} \quad (\text{A.4})$$

which ensures that

$$Q(\mathbf{u}) = (\mathbf{u}, \mathbf{q}_{\mathcal{B}})_{\mathcal{B}} + (\mathcal{C}\mathbf{u}, \mathbf{q}_{\partial\mathcal{B}})_{\partial\mathcal{B}} = (\mathbf{f}, \mathbf{z})_{\mathcal{B}} + (\mathbf{g}, \mathcal{C}^*z)_{\partial\mathcal{B}}, \quad (\text{A.5})$$

see e.g. [22]. Introducing an approximate space  $\mathcal{V}_h \subset \mathcal{V}$  by means of the finite element method, where  $\mathcal{V}$  is an appropriate Sobolev space, one can establish a discretized variational format of (A.1) as

$$B(\mathbf{u}_h, \mathbf{v}) = F(\mathbf{v}), \quad \forall \mathbf{v} \in \mathcal{V}_h, \quad (\text{A.6})$$

with a bilinear form  $B$  and a linear form  $F$ . The discretization (A.6) for the primal problem is said to be *consistent*, if the exact solution  $\mathbf{u} \in \mathcal{V}$  to (A.1) satisfies

$$B(\mathbf{u}, \mathbf{v}) = F(\mathbf{v}), \quad \forall \mathbf{v} \in \mathcal{V}. \quad (\text{A.7})$$

Similarly, the discretization (A.6) is said to be *adjoint consistent*, if the exact solution  $\mathbf{z} \in \mathcal{V}$  to the adjoint problem (A.4) satisfies

$$B(\mathbf{w}, \mathbf{z}) = Q(\mathbf{w}), \quad \forall \mathbf{w} \in \mathcal{V}. \quad (\text{A.8})$$

**Linear elastic micromorphic continua.** To specify the general differential problem (A.1), we recall the strong form (10) together with the boundary conditions in (11) as

$$\begin{cases} -(\boldsymbol{\sigma} + \bar{\mathbf{s}}) \cdot \nabla = \mathbf{0}, & \text{in } \mathcal{B} \\ -\bar{\mathbf{S}} \cdot \nabla - \bar{\mathbf{s}} = \mathbf{0}, & \text{in } \mathcal{B} \\ \mathbf{u} = \mathbf{u}^{pre}, & \text{on } \partial\mathcal{B}^u \\ \bar{\mathbf{H}} = \bar{\mathbf{H}}^{pre}, & \text{on } \partial\mathcal{B}^{\bar{\mathbf{H}}} \\ (\boldsymbol{\sigma} + \bar{\mathbf{s}}) \cdot \mathbf{N} = \mathbf{t}, & \text{on } \partial\mathcal{B}^t \\ \bar{\mathbf{S}} \cdot \mathbf{N} = \mathbf{0}, & \text{on } \partial\mathcal{B}^{\bar{\mathbf{Q}}}, \end{cases} \quad (\text{A.9})$$

which, in combination with the constitutive relations (16) and the kinematic relations (6), (7) and (9) as well as Eq. (23), becomes

$$\begin{cases} -(\mathbb{C}\nabla\mathbf{u} + \mathbb{A}\nabla\mathbf{u} + \mathbb{B}\bar{\mathbf{H}}) \cdot \nabla = \mathbf{0}, & \text{in } \mathcal{B} \\ -(\mathbb{D}\nabla\bar{\mathbf{H}}) \cdot \nabla - \mathbb{A}\nabla\mathbf{u} - \mathbb{B}\bar{\mathbf{H}} = \mathbf{0}, & \text{in } \mathcal{B} \\ \mathbf{u} = \mathbf{u}^{pre}, & \text{on } \partial\mathcal{B}^u \\ \bar{\mathbf{H}} = \bar{\mathbf{H}}^{pre}, & \text{on } \partial\mathcal{B}^{\bar{\mathbf{H}}} \\ (\mathbb{C}\nabla\mathbf{u} + \mathbb{A}\nabla\mathbf{u} + \mathbb{B}\bar{\mathbf{H}}) \cdot \mathbf{N} = \mathbf{t}, & \text{on } \partial\mathcal{B}^t \\ \mathbb{D}\nabla\bar{\mathbf{H}} \cdot \mathbf{N} = \mathbf{0}, & \text{on } \partial\mathcal{B}^{\bar{\mathbf{Q}}}. \end{cases} \quad (\text{A.10})$$

In accordance with the notion of generalized solution introduced in (24), we may identify the primal operators as

$$\begin{aligned}
\widehat{\mathcal{L}}\widehat{\mathbf{u}} &= - \begin{bmatrix} \nabla^{(2)} \mathbb{C} \cdot \nabla + \nabla^{(2)} \mathbb{A} \cdot \nabla & \nabla^{(2)} \mathbb{B} \\ \mathbb{A} \cdot \nabla & \nabla^{(3)} \mathbb{D} \cdot \nabla + \mathbb{B} \end{bmatrix} \cdot \begin{bmatrix} \mathbf{u} \\ \overline{\mathbf{H}} \end{bmatrix}, \quad \text{in } \mathcal{B} \\
\widehat{\mathcal{B}}\widehat{\mathbf{u}} &= \begin{bmatrix} \mathbf{u} \\ \overline{\mathbf{H}} \end{bmatrix}, \quad \text{on } \partial\mathcal{B}^u \cup \partial\mathcal{B}^{\overline{\mathbf{H}}} \\
\widehat{\mathcal{C}}\widehat{\mathbf{u}} &= \begin{bmatrix} (\mathbb{C}\nabla\mathbf{u} + \mathbb{A}\nabla\mathbf{u} + \mathbb{B}\overline{\mathbf{H}}) \cdot \mathbf{N} \\ \mathbb{D}\nabla\overline{\mathbf{H}} \cdot \mathbf{N} \end{bmatrix}, \quad \text{on } \partial\mathcal{B}^u \cup \partial\mathcal{B}^{\overline{\mathbf{H}}} \\
\widehat{\mathcal{B}}\widehat{\mathbf{u}} &= \begin{bmatrix} (\mathbb{C}\nabla\mathbf{u} + \mathbb{A}\nabla\mathbf{u} + \mathbb{B}\overline{\mathbf{H}}) \cdot \mathbf{N} \\ \mathbb{D}\nabla\overline{\mathbf{H}} \cdot \mathbf{N} \end{bmatrix}, \quad \text{on } \partial\mathcal{B}^t \cup \partial\mathcal{B}^{\overline{\mathbf{Q}}} \\
\widehat{\mathcal{C}}\widehat{\mathbf{u}} &= \begin{bmatrix} \mathbf{u} \\ \overline{\mathbf{H}} \end{bmatrix}, \quad \text{on } \partial\mathcal{B}^t \cup \partial\mathcal{B}^{\overline{\mathbf{Q}}},
\end{aligned} \tag{A.11}$$

whereby the differential equation (A.1) becomes

$$\begin{cases} \widehat{\mathcal{L}}\widehat{\mathbf{u}} = \mathbf{0}, & \text{in } \mathcal{B} \\ \widehat{\mathcal{B}}\widehat{\mathbf{u}} = \widehat{\mathbf{u}}^{pre}, & \text{on } \partial\mathcal{B}^u \cup \partial\mathcal{B}^{\overline{\mathbf{H}}} \\ \widehat{\mathcal{B}}\widehat{\mathbf{u}} = \widehat{\mathbf{t}}, & \text{on } \partial\mathcal{B}^t \cup \partial\mathcal{B}^{\overline{\mathbf{Q}}}, \end{cases} \tag{A.12}$$

where  $\widehat{\mathbf{u}}^{pre} = [\mathbf{u}^{pre} \overline{\mathbf{H}}^{pre}]^T$  and  $\widehat{\mathbf{t}}$  is defined in Eq. (24). Subsequently, we may specify the general definition of a linear quantity of interest (A.2) as

$$\begin{aligned}
Q(\widehat{\mathbf{u}}) &= \int_{\mathcal{B}} \mathbf{q}_B \cdot \mathbf{u} dV + \int_{\partial\mathcal{B}^u} \mathbf{q}_u \cdot ((\mathbb{C}\nabla\mathbf{u} + \mathbb{A}\nabla\mathbf{u} + \mathbb{B}\overline{\mathbf{H}}) \cdot \mathbf{N}) dA \\
&+ \int_{\partial\mathcal{B}^t} \mathbf{q}_t \cdot \mathbf{u} dA + \int_{\mathcal{B}} \overline{\mathbf{q}}_B : \overline{\mathbf{H}} dV \\
&+ \int_{\partial\mathcal{B}^{\overline{\mathbf{H}}}} \overline{\mathbf{q}}_{\overline{\mathbf{H}}} : (\mathbb{D}\nabla\overline{\mathbf{H}} \cdot \mathbf{N}) dA + \int_{\partial\mathcal{B}^{\overline{\mathbf{Q}}}} \overline{\mathbf{q}}_{\overline{\mathbf{Q}}} : \overline{\mathbf{H}} dA.
\end{aligned} \tag{A.13}$$

With the dual solution  $\widehat{\mathbf{z}} := [\mathbf{z} \overline{\mathbf{z}}]^T$ , the compatibility condition (A.3) becomes

$$\begin{aligned}
&(-(\mathbb{C}\nabla\mathbf{u} + \mathbb{A}\nabla\mathbf{u} + \mathbb{B}\overline{\mathbf{H}}) \cdot \nabla, \mathbf{z})_{\mathcal{B}} + (-(\mathbb{D}\nabla\overline{\mathbf{H}}) \cdot \nabla - \mathbb{A}\nabla\mathbf{u} - \mathbb{B}\overline{\mathbf{H}}, \overline{\mathbf{z}})_{\mathcal{B}} \\
&+ (\mathbf{u}, -(\mathbb{C}\nabla\mathbf{z} + \mathbb{A}\nabla\mathbf{z} + \mathbb{B}\overline{\mathbf{z}}) \cdot \mathbf{N})_{\partial\mathcal{B}^u} + (\overline{\mathbf{H}}, -\mathbb{D}\nabla\overline{\mathbf{z}} \cdot \mathbf{N})_{\partial\mathcal{B}^{\overline{\mathbf{H}}}} \\
&+ ((\mathbb{C}\nabla\mathbf{u} + \mathbb{A}\nabla\mathbf{u} + \mathbb{B}\overline{\mathbf{H}}) \cdot \mathbf{N}, \mathbf{z})_{\partial\mathcal{B}^t} + (\mathbb{D}\nabla\overline{\mathbf{H}} \cdot \mathbf{N}, \overline{\mathbf{z}})_{\partial\mathcal{B}^{\overline{\mathbf{Q}}}} \\
&= (\mathbf{u}, -(\mathbb{C}\nabla\mathbf{z} + \mathbb{A}\nabla\mathbf{z} + \mathbb{B}\overline{\mathbf{z}}) \cdot \nabla)_{\mathcal{B}} + (\overline{\mathbf{H}}, -(\mathbb{D}\nabla\overline{\mathbf{z}}) \cdot \nabla - \mathbb{A}\nabla\mathbf{z} - \mathbb{B}\overline{\mathbf{z}})_{\mathcal{B}} \\
&+ (-(\mathbb{C}\nabla\mathbf{u} + \mathbb{A}\nabla\mathbf{u} + \mathbb{B}\overline{\mathbf{H}}) \cdot \mathbf{N}, \mathbf{z})_{\partial\mathcal{B}^u} + (-\mathbb{D}\nabla\overline{\mathbf{H}} \cdot \mathbf{N}, \overline{\mathbf{z}})_{\partial\mathcal{B}^{\overline{\mathbf{H}}}} \\
&+ (\mathbf{u}, (\mathbb{C}\nabla\mathbf{z} + \mathbb{A}\nabla\mathbf{z} + \mathbb{B}\overline{\mathbf{z}}) \cdot \mathbf{N})_{\partial\mathcal{B}^t} + (\overline{\mathbf{H}}, \mathbb{D}\nabla\overline{\mathbf{z}} \cdot \mathbf{N})_{\partial\mathcal{B}^{\overline{\mathbf{Q}}}},
\end{aligned} \tag{A.14}$$

where we identify the adjoint operators as

$$\begin{aligned}
\widehat{\mathcal{L}}^* \widehat{\mathbf{z}} &= - \begin{bmatrix} \nabla \cdot \overset{(2)}{\mathbb{C}} \cdot \nabla + \nabla \cdot \overset{(2)}{\mathbb{A}} \cdot \nabla & \nabla \cdot \overset{(2)}{\mathbb{B}} \\ \mathbb{A} \cdot \nabla & \nabla \cdot \overset{(3)}{\mathbb{D}} \cdot \nabla + \mathbb{B} \end{bmatrix} \cdot \begin{bmatrix} \mathbf{z} \\ \bar{\mathbf{z}} \end{bmatrix}, & \text{in } \mathcal{B} \\
\widehat{\mathcal{B}}^* \widehat{\mathbf{z}} &= - \begin{bmatrix} \mathbf{z} \\ \bar{\mathbf{z}} \end{bmatrix}, & \text{on } \partial\mathcal{B}^u \cup \partial\mathcal{B}^{\bar{H}} \\
\widehat{\mathcal{C}}^* \widehat{\mathbf{z}} &= - \begin{bmatrix} (\mathbb{C}\nabla\mathbf{z} + \mathbb{A}\nabla\mathbf{z} + \mathbb{B}\bar{\mathbf{z}}) \cdot \mathbf{N} \\ \mathbb{D}\nabla\bar{\mathbf{z}} \cdot \mathbf{N} \end{bmatrix}, & \text{on } \partial\mathcal{B}^u \cup \partial\mathcal{B}^{\bar{H}} \\
\widehat{\mathcal{B}}^* \widehat{\mathbf{z}} &= \begin{bmatrix} (\mathbb{C}\nabla\mathbf{z} + \mathbb{A}\nabla\mathbf{z} + \mathbb{B}\bar{\mathbf{z}}) \cdot \mathbf{N} \\ \mathbb{D}\nabla\bar{\mathbf{z}} \cdot \mathbf{N} \end{bmatrix}, & \text{on } \partial\mathcal{B}^t \cup \partial\mathcal{B}^{\bar{Q}} \\
\widehat{\mathcal{C}}^* \widehat{\mathbf{z}} &= \begin{bmatrix} \mathbf{z} \\ \bar{\mathbf{z}} \end{bmatrix}, & \text{on } \partial\mathcal{B}^t \cup \partial\mathcal{B}^{\bar{Q}}.
\end{aligned} \tag{A.15}$$

Accordingly, the adjoint problem of type (A.4) takes the form

$$\left\{ \begin{array}{ll}
-(\mathbb{C}\nabla\mathbf{z} + \mathbb{A}\nabla\mathbf{z} + \mathbb{B}\bar{\mathbf{z}}) \cdot \nabla &= \mathbf{q}_{\mathcal{B}}, & \text{in } \mathcal{B} \\
-(\mathbb{D}\nabla\bar{\mathbf{z}}) \cdot \nabla - \mathbb{A}\nabla\mathbf{z} - \mathbb{B}\bar{\mathbf{z}} &= \bar{\mathbf{q}}_{\mathcal{B}}, & \text{in } \mathcal{B} \\
\mathbf{z} &= \mathbf{q}_u, & \text{on } \partial\mathcal{B}^u \\
\bar{\mathbf{z}} &= \bar{\mathbf{q}}_{\bar{H}}, & \text{on } \partial\mathcal{B}^{\bar{H}} \\
(\mathbb{C}\nabla\mathbf{z} + \mathbb{A}\nabla\mathbf{z} + \mathbb{B}\bar{\mathbf{z}}) \cdot \mathbf{N} &= \mathbf{q}_t, & \text{on } \partial\mathcal{B}^t \\
\mathbb{D}\nabla\bar{\mathbf{z}} \cdot \mathbf{N} &= \bar{\mathbf{q}}_{\bar{Q}}, & \text{on } \partial\mathcal{B}^{\bar{Q}}.
\end{array} \right. \tag{A.16}$$

As usual in the Galerkin finite element method [53, 52, 30], the discretized weak form of the primal problem (A.9) is established as

$$\begin{aligned}
B(\widehat{\mathbf{u}}_h, \delta\widehat{\mathbf{u}}_h) &:= \int_{\mathcal{B}} \{ \nabla\delta\mathbf{u}_h : (\mathbb{C}\nabla\mathbf{u}_h) + \nabla\delta\mathbf{u}_h : (\mathbb{A}\nabla\mathbf{u}_h + \mathbb{B}\bar{\mathbf{H}}_h) \\
&\quad + \nabla\delta\bar{\mathbf{H}}_h : (\mathbb{D}\nabla\bar{\mathbf{H}}_h) - \delta\bar{\mathbf{H}}_h : (\mathbb{A}\nabla\mathbf{u}_h + \mathbb{B}\bar{\mathbf{H}}_h) \} dV \\
&= \int_{\partial\mathcal{B}^t} \delta\mathbf{u}_h \cdot \mathbf{t} dA =: F(\delta\widehat{\mathbf{u}}_h), \quad \forall \delta\widehat{\mathbf{u}}_h \in \mathcal{V}_h,
\end{aligned} \tag{A.17}$$

which is denoted as an abstract form in (27) and with integration by parts becomes

$$\begin{aligned}
B(\widehat{\mathbf{u}}_h, \delta\widehat{\mathbf{u}}_h) &:= - \int_{\mathcal{B}} \delta\mathbf{u}_h \cdot \{(\mathbb{C}\nabla\mathbf{u}_h + \mathbb{A}\nabla\mathbf{u}_h + \mathbb{B}\overline{\mathbf{H}}_h) \cdot \nabla\} dV \\
&- \int_{\mathcal{B}} \delta\overline{\mathbf{H}}_h : \{(\mathbb{D}\nabla\overline{\mathbf{H}}_h) \cdot \nabla + \mathbb{A}\nabla\mathbf{u}_h + \mathbb{B}\overline{\mathbf{H}}_h\} dV \\
&+ \int_{\partial\mathcal{B}^t} \delta\mathbf{u}_h \cdot \{(\mathbb{C}\nabla\mathbf{u}_h + \mathbb{A}\nabla\mathbf{u}_h + \mathbb{B}\overline{\mathbf{H}}_h) \cdot \mathbf{N}\} dA \\
&+ \int_{\partial\mathcal{B}^{\overline{Q}}} \delta\overline{\mathbf{H}}_h : \{\mathbb{D}\nabla\overline{\mathbf{H}}_h \cdot \mathbf{N}\} dA \\
&+ \sum_{e=1}^{N_{el}} \int_{\partial\mathcal{B}^e \not\subseteq \partial\mathcal{B}} \delta\mathbf{u}_h \cdot \{(\mathbb{C}\nabla\mathbf{u}_h + \mathbb{A}\nabla\mathbf{u}_h + \mathbb{B}\overline{\mathbf{H}}_h) \cdot \mathbf{N}\} dA \\
&+ \sum_{e=1}^{N_{el}} \int_{\partial\mathcal{B}^e \not\subseteq \partial\mathcal{B}} \delta\overline{\mathbf{H}}_h : \{\mathbb{D}\nabla\overline{\mathbf{H}}_h \cdot \mathbf{N}\} dA \\
&= \int_{\partial\mathcal{B}^t} \delta\mathbf{u}_h \cdot \mathbf{t} dA =: F(\delta\widehat{\mathbf{u}}_h), \quad \forall \delta\widehat{\mathbf{u}}_h \in \mathcal{V}_h.
\end{aligned} \tag{A.18}$$

Here,  $\partial\mathcal{B}^e$  and  $N_{el}$  denote element boundaries and number of elements, respectively. For the interior element boundaries  $\partial\mathcal{B}^e \not\subseteq \partial\mathcal{B}$ , the last two terms in Eq. (A.18) exist due to the jumps of stresses between two neighboring elements sharing one common interior element boundary. Then, Eq. (A.18) can be rewritten in a discretized primal residual form as

$$\begin{aligned}
\varrho(\widehat{\mathbf{u}}_h; \delta\widehat{\mathbf{u}}_h) &= F(\delta\widehat{\mathbf{u}}_h) - B(\widehat{\mathbf{u}}_h; \delta\widehat{\mathbf{u}}_h) \\
&= \int_{\mathcal{B}} \delta\mathbf{u}_h \cdot \underbrace{\{(\mathbb{C}\nabla\mathbf{u}_h + \mathbb{A}\nabla\mathbf{u}_h + \mathbb{B}\overline{\mathbf{H}}_h) \cdot \nabla\}}_{:=R_{\mathcal{B}}(\mathbf{u}_h, \overline{\mathbf{H}}_h)} dV \\
&+ \int_{\mathcal{B}} \delta\overline{\mathbf{H}}_h : \underbrace{\{(\mathbb{D}\nabla\overline{\mathbf{H}}_h) \cdot \nabla + \mathbb{A}\nabla\mathbf{u}_h + \mathbb{B}\overline{\mathbf{H}}_h\}}_{:=\overline{R}_{\mathcal{B}}(\mathbf{u}_h, \overline{\mathbf{H}}_h)} dV \\
&+ \int_{\partial\mathcal{B}^t} \delta\mathbf{u}_h \cdot \underbrace{\{\mathbf{t} - (\mathbb{C}\nabla\mathbf{u}_h + \mathbb{A}\nabla\mathbf{u}_h + \mathbb{B}\overline{\mathbf{H}}_h) \cdot \mathbf{N}\}}_{:=R_t(\mathbf{u}_h, \overline{\mathbf{H}}_h)} dA \\
&- \int_{\partial\mathcal{B}^{\overline{Q}}} \delta\overline{\mathbf{H}}_h : \underbrace{\{\mathbb{D}\nabla\overline{\mathbf{H}}_h \cdot \mathbf{N}\}}_{:=\overline{R}_{\overline{Q}}(\overline{\mathbf{H}}_h)} dA \\
&- \sum_{e=1}^{N_{el}} \int_{\partial\mathcal{B}^e \not\subseteq \partial\mathcal{B}} \delta\mathbf{u}_h \cdot \{(\mathbb{C}\nabla\mathbf{u}_h + \mathbb{A}\nabla\mathbf{u}_h + \mathbb{B}\overline{\mathbf{H}}_h) \cdot \mathbf{N}\} dA \\
&- \sum_{e=1}^{N_{el}} \int_{\partial\mathcal{B}^e \not\subseteq \partial\mathcal{B}} \delta\overline{\mathbf{H}}_h : \{\mathbb{D}\nabla\overline{\mathbf{H}}_h \cdot \mathbf{N}\} dA = 0.
\end{aligned} \tag{A.19}$$

Obviously, according to the strong form (A.10), if the FE solution  $\widehat{\mathbf{u}}_h$  is replaced by the exact one  $\widehat{\mathbf{u}}$ , the four residuals defined in (A.19) vanish, i.e.  $R_{\mathcal{B}}(\mathbf{u}, \overline{\mathbf{H}}) = \mathbf{0}$ ,  $\overline{R}_{\mathcal{B}}(\mathbf{u}, \overline{\mathbf{H}}) = \mathbf{0}$ ,  $R_t(\mathbf{u}, \overline{\mathbf{H}}) = \mathbf{0}$  and  $\overline{R}_{\overline{Q}}(\overline{\mathbf{H}}) = \mathbf{0}$ . Additionally, the last two terms

vanish due to a smooth stress distribution (i.e. no interior stress jumps in an exact solution). Hence, the FE discretization (A.17) is consistent. Similarly, for an adjoint consistency analysis, we proceed with the discretized weak form of the dual problem (40)

$$\begin{aligned}
B(\widehat{\mathbf{z}}_h, \delta \widehat{\mathbf{u}}_h) &:= - \int_{\mathcal{B}} \delta \mathbf{u}_h \cdot \{(\mathbb{C}\nabla \mathbf{z}_h + \mathbb{A}\nabla \mathbf{z}_h + \mathbb{B}\bar{\mathbf{z}}_h) \cdot \nabla\} dV \\
&\quad - \int_{\mathcal{B}} \delta \bar{\mathbf{H}}_h : \{(\mathbb{D}\nabla \bar{\mathbf{z}}_h) \cdot \nabla + \mathbb{A}\nabla \mathbf{z}_h + \mathbb{B}\bar{\mathbf{H}}_h\} dV \\
&\quad + \int_{\partial \mathcal{B}^t} \delta \mathbf{u}_h \cdot \{(\mathbb{C}\nabla \mathbf{z}_h + \mathbb{A}\nabla \mathbf{z}_h + \mathbb{B}\bar{\mathbf{z}}_h) \cdot \mathbf{N}\} dA \\
&\quad + \int_{\partial \mathcal{B}^{\bar{Q}}} \delta \bar{\mathbf{H}}_h : \{\mathbb{D}\nabla \bar{\mathbf{z}}_h \cdot \mathbf{N}\} dA \\
&\quad + \sum_{e=1}^{N_{el}} \int_{\partial \mathcal{B}^e \not\subseteq \partial \mathcal{B}} \delta \mathbf{u}_h \cdot \{(\mathbb{C}\nabla \mathbf{z}_h + \mathbb{A}\nabla \mathbf{z}_h + \mathbb{B}\bar{\mathbf{z}}_h) \cdot \mathbf{N}\} dA \\
&\quad + \sum_{e=1}^{N_{el}} \int_{\partial \mathcal{B}^e \not\subseteq \partial \mathcal{B}} \delta \bar{\mathbf{H}}_h : \{\mathbb{D}\nabla \bar{\mathbf{z}}_h \cdot \mathbf{N}\} dA \tag{A.20} \\
&= \int_{\mathcal{B}} \delta \mathbf{u}_h \cdot \mathbf{q}_{\mathcal{B}} dV + \int_{\mathcal{B}} \delta \bar{\mathbf{H}}_h : \bar{\mathbf{q}}_{\mathcal{B}} dV \\
&\quad + \int_{\partial \mathcal{B}^u} ((\mathbb{C}\nabla \delta \mathbf{u}_h + \mathbb{A}\nabla \delta \mathbf{u}_h + \mathbb{B}\delta \bar{\mathbf{H}}_h) \cdot \mathbf{N}) \cdot \mathbf{q}_u dA \\
&\quad + \int_{\partial \mathcal{B}^t} \delta \mathbf{u}_h \cdot \mathbf{q}_t dA \\
&\quad + \int_{\partial \mathcal{B}^{\bar{H}}} (\mathbb{D}\nabla \delta \bar{\mathbf{H}}_h \cdot \mathbf{N}) : \bar{\mathbf{q}}_{\bar{H}} dA + \int_{\partial \mathcal{B}^{\bar{Q}}} \delta \bar{\mathbf{H}}_h : \bar{\mathbf{q}}_{\bar{Q}} dA \\
&=: Q(\delta \widehat{\mathbf{u}}_h), \quad \forall \delta \widehat{\mathbf{u}}_h \in \mathcal{V}_h.
\end{aligned}$$

Note that Eq. (A.20) is obtained from (A.18), where we replace the loading term  $F$  by the quantity of interest  $Q$  defined in (A.13) and replace their arguments corre-

spondingly. Now, we rewrite Eq. (A.20) in a discretized dual residual form as

$$\begin{aligned}
\varrho^*(\widehat{\mathbf{z}}_h; \delta\widehat{\mathbf{u}}_h) &= Q(\delta\widehat{\mathbf{u}}_h) - B(\widehat{\mathbf{z}}_h; \delta\widehat{\mathbf{u}}_h) \\
&= \int_{\mathcal{B}} \delta\mathbf{u}_h \cdot \underbrace{\{(\mathbb{C}\nabla\mathbf{z}_h + \mathbb{A}\nabla\mathbf{z}_h + \mathbb{B}\bar{\mathbf{z}}_h) \cdot \nabla + \mathbf{q}_{\mathcal{B}}\}}_{:=R_{\mathcal{B}}^*(\mathbf{z}_h, \bar{\mathbf{z}}_h)} dV \\
&\quad + \int_{\mathcal{B}} \delta\bar{\mathbf{H}}_h : \underbrace{\{(\mathbb{D}\nabla\bar{\mathbf{z}}_h) \cdot \nabla + \mathbb{A}\nabla\mathbf{z}_h + \mathbb{B}\bar{\mathbf{z}}_h + \bar{\mathbf{q}}_{\mathcal{B}}\}}_{:=\bar{R}_{\mathcal{B}}^*(\mathbf{z}_h, \bar{\mathbf{z}}_h)} dV \\
&\quad + \int_{\partial\mathcal{B}^t} \delta\mathbf{u}_h \cdot \underbrace{\{\mathbf{q}_t - (\mathbb{C}\nabla\mathbf{z}_h + \mathbb{A}\nabla\mathbf{z}_h + \mathbb{B}\bar{\mathbf{z}}_h) \cdot \mathbf{N}\}}_{:=R_t^*(\mathbf{z}_h, \bar{\mathbf{z}}_h)} dA \\
&\quad + \int_{\partial\mathcal{B}^{\bar{Q}}} \delta\bar{\mathbf{H}}_h : \underbrace{\{\bar{\mathbf{q}}_{\bar{Q}} - \mathbb{D}\nabla\bar{\mathbf{z}}_h \cdot \mathbf{N}\}}_{:=\bar{R}_{\bar{Q}}^*(\bar{\mathbf{z}}_h)} dA \\
&\quad + \int_{\partial\mathcal{B}^u} ((\mathbb{C}\nabla\delta\mathbf{u}_h + \mathbb{A}\nabla\delta\mathbf{u}_h + \mathbb{B}\delta\bar{\mathbf{H}}_h) \cdot \mathbf{N}) \cdot \mathbf{q}_u dA \\
&\quad + \int_{\partial\mathcal{B}^{\bar{H}}} (\mathbb{D}\nabla\delta\bar{\mathbf{H}}_h \cdot \mathbf{N}) : \bar{\mathbf{q}}_{\bar{H}} dA \\
&\quad - \sum_{e=1}^{N_{el}} \int_{\partial\mathcal{B}^e \not\subseteq \partial\mathcal{B}} \delta\mathbf{u}_h \cdot \{(\mathbb{C}\nabla\mathbf{z}_h + \mathbb{A}\nabla\mathbf{z}_h + \mathbb{B}\bar{\mathbf{z}}_h) \cdot \mathbf{N}\} dA \\
&\quad - \sum_{e=1}^{N_{el}} \int_{\partial\mathcal{B}^e \not\subseteq \partial\mathcal{B}} \delta\bar{\mathbf{H}}_h : \{\mathbb{D}\nabla\bar{\mathbf{z}}_h \cdot \mathbf{N}\} dA = 0.
\end{aligned} \tag{A.21}$$

Obviously, according to the strong form (A.16), if the FE solution  $\widehat{\mathbf{z}}_h$  is replaced by the exact one  $\widehat{\mathbf{z}}$ , the four residuals defined in (A.21) vanish, i.e.  $R_{\mathcal{B}}^*(\mathbf{z}, \bar{\mathbf{z}}) = \mathbf{0}$ ,  $\bar{R}_{\mathcal{B}}^*(\mathbf{z}, \bar{\mathbf{z}}) = \mathbf{0}$ ,  $R_t^*(\mathbf{z}, \bar{\mathbf{z}}) = \mathbf{0}$  and  $\bar{R}_{\bar{Q}}^*(\bar{\mathbf{z}}) = \mathbf{0}$ . Additionally, the last two jump terms vanish. As a result, the FE discretization (A.20) is adjoint consistent only if

$$\int_{\partial\mathcal{B}^u} ((\mathbb{C}\nabla\delta\mathbf{u}_h + \mathbb{A}\nabla\delta\mathbf{u}_h + \mathbb{B}\delta\bar{\mathbf{H}}_h) \cdot \mathbf{N}) \cdot \mathbf{q}_u dA + \int_{\partial\mathcal{B}^{\bar{H}}} (\mathbb{D}\nabla\delta\bar{\mathbf{H}}_h \cdot \mathbf{N}) : \bar{\mathbf{q}}_{\bar{H}} dA = 0. \tag{A.22}$$

If we consider a simplified target function of the type

$$Q(\widehat{\mathbf{u}}) = \int_{\mathcal{B}} \mathbf{q}_{\mathcal{B}} \cdot \mathbf{u} dV + \int_{\mathcal{B}} \bar{\mathbf{q}}_{\mathcal{B}} : \bar{\mathbf{H}} dV \tag{A.23}$$

as a special case where  $\mathbf{q}_u = \mathbf{q}_t = \mathbf{0}$  and  $\bar{\mathbf{q}}_{\bar{H}} = \bar{\mathbf{q}}_{\bar{Q}} = \mathbf{0}$ , the strong form of the adjoint problem (A.16) becomes

$$\left\{ \begin{array}{ll}
-(\mathbb{C}\nabla\mathbf{z} + \mathbb{A}\nabla\mathbf{z} + \mathbb{B}\bar{\mathbf{z}}) \cdot \nabla &= \mathbf{q}_{\mathcal{B}}, \quad \text{in } \mathcal{B} \\
-(\mathbb{D}\nabla\bar{\mathbf{z}}) \cdot \nabla - \mathbb{A}\nabla\mathbf{z} - \mathbb{B}\bar{\mathbf{z}} &= \bar{\mathbf{q}}_{\mathcal{B}}, \quad \text{in } \mathcal{B} \\
\mathbf{z} &= \mathbf{0}, \quad \text{on } \partial\mathcal{B}^u \\
\bar{\mathbf{z}} &= \mathbf{0}, \quad \text{on } \partial\mathcal{B}^{\bar{H}} \\
(\mathbb{C}\nabla\mathbf{z} + \mathbb{A}\nabla\mathbf{z} + \mathbb{B}\bar{\mathbf{z}}) \cdot \mathbf{N} &= \mathbf{0}, \quad \text{on } \partial\mathcal{B}^t \\
\mathbb{D}\nabla\bar{\mathbf{z}} \cdot \mathbf{N} &= \mathbf{0}, \quad \text{on } \partial\mathcal{B}^{\bar{Q}}.
\end{array} \right. \tag{A.24}$$

This ensures the adjoint consistency by satisfying (A.22).

## References

- [1] Ainsworth M, Oden J (2000) A posteriori error estimation in finite analysis. Pure and applied mathematics, John Wiley & Sons, New York
- [2] Ammar K, Appolaire B, Cailletaud G, Feyel F, Forest S (2009) Finite element formulation of a phase field model based on the concept of generalized stresses. *Computational materials science* 45(3):800–805
- [3] Arnold DN, Brezzi F, Cockburn B, Marini LD (2002) Unified analysis of discontinuous galerkin methods for elliptic problems. *SIAM journal on numerical analysis* 39(5):1749–1779
- [4] Babuska I, Whiteman J, Strouboulis T (2011) *Finite Elements: An Introduction to the Methods and Error Estimation*. Oxford University Press, New York
- [5] Becker R, Rannacher R (1996) A Feed-back approach to error control in finite element methods: basic analysis and examples. *East-West Journal of Numerical Mathematics* 4(4):237–264
- [6] Begley MR, Hutchinson JW (1998) The mechanics of size-dependent indentation. *J Mech Phys Solids* 46(10):2049–2068, DOI 10.1016/S0022-5096(98)00018-0
- [7] Cirak F, Ramm E (1998) A posteriori error estimation and adaptivity for linear elasticity using the reciprocal theorem. *Comput Methods Appl Mech Engrg* 156:351–362
- [8] Dillard T, Forest S, Jenny P (2006) Micromorphic continuum modelling of the deformation and fracture behaviour of nickel foams. *European Journal of Mechanics A/Solids* 25:526–549
- [9] Ehlers W, Scholz B (2007) An inverse algorithm for the identification and the sensitivity analysis of the parameters governing micropolar elasto-plastic granular material. *Arch Appl Mech* 77(12):911–931, DOI 10.1007/s00419-007-0162-9
- [10] Ehlers W, Volk W (1998) On theoretical and numerical methods in the theory of porous media based on polar and non-polar elasto-plastic solid materials. *Int J Solids Struct* 35(34-35):4597–4617, DOI 10.1016/S0020-7683(98)00086-9
- [11] Eriksson K, Estep D, Hansbo P, Johnson C (1995) *Introduction to Adaptive Methods for Differential Equations*. *Acta Numerica* 4:150–158
- [12] Eringen AC (1964) Mechanics of micromorphic materials. In: Görtler H (ed) *Applied Mechanics*, Springer, Berlin, Heidelberg, pp 131–138
- [13] Eringen AC (1965) Theory of micropolar continua. In: *Proceedings of the Ninth Midwestern Mechanics Conference*, University of Wisconsin, Wiley, p 23
- [14] Fish J (2013) *Practical multiscaleing*. John Wiley & Sons, The Atrium

- [15] Forest S (2009) Micromorphic approach for gradient elasticity, viscoplasticity, and damage. *Journal of Engineering Mechanics* 135(3):117–131, DOI 10.1061/(ASCE)0733-9399(2009)135:3(117)
- [16] Forest S, Aifantis EC (2010) Some links between recent gradient thermo-elastoplasticity theories and the thermomechanics of generalized continua. *Int J Solids Struct* 47(25-26):3367–3376, DOI 10.1016/j.ijsolstr.2010.07.009
- [17] Forest S, L E (2004) Localization phenomena and regularization methods. In: *Local Approach to Fracture*, Les Presses de l'Ecole des Mines, pp 311–371
- [18] Forest S, Sievert R (2006) Nonlinear microstrain theories. *Int J Solids Struct* (43):7224–7245
- [19] Forest S, Ammar K, Appolaire B (2011) In: Bernd Markert, (ed) *Advances in Extended and Multifield Theories for Continua*, Lecture Notes in Applied and Computational Mechanics, Springer Berlin Heidelberg, pp 69–88
- [20] Fried E, Gurtin ME (1993) Continuum theory of thermally induced phase transitions based on an order parameter. *Physica D: Nonlinear Phenomena* 68(3):326–343
- [21] Fried E, Gurtin ME (1994) Dynamic solid-solid transitions with phase characterized by an order parameter. *Physica D: Nonlinear Phenomena* 72(4):287–308
- [22] Giles MB, Pierce NA (1997) Adjoint equations in cfd: duality, boundary conditions and solution behaviour. *AIAA paper* 97:1850
- [23] Grammenoudis P, Tsakmakis C (2009) Micromorphic continuum. Part I: Strain and stress tensors and their associated rates. *Int J Nonlinear Mech* 44(9):943–956, DOI 10.1016/j.ijnonlinmec.2009.05.005
- [24] Grammenoudis P, Tsakmakis C, Hofer D (2009) Micromorphic continuum. Part II: Finite deformation plasticity coupled with damage. *Int J Nonlinear Mech* 44(9):957–974, DOI 10.1016/j.ijnonlinmec.2009.05.004
- [25] Grammenoudis P, Tsakmakis C, Hofer D (2010) Micromorphic continuum. Part III: Small deformation plasticity coupled with damage. *Int J Nonlinear Mech* 45(2):140–148, DOI 10.1016/j.ijnonlinmec.2009.10.003
- [26] Gurtin ME (1996) Generalized Ginzburg-Landau and Cahn-Hilliard equations based on a microforce balance. *Physica D: Nonlinear Phenomena* 92(3):178–192
- [27] Harriman K, Gavaghan D, Suli E (2004) The importance of adjoint consistency in the approximation of linear functionals using the discontinuous galerkin finite element method
- [28] Hartmann R (2007) Adjoint consistency analysis of discontinuous galerkin discretizations. *SIAM Journal on Numerical Analysis* 45(6):2671–2696

- [29] Hirschberger CB, Steinmann P (2009) Classification of concepts in thermodynamically consistent generalized plasticity. *Journal of Engineering Mechanics* 135(3):156–170, DOI 10.1061/(ASCE)0733-9399(2009)135:3(156)
- [30] Hughes TJ (2012) *The finite element method: linear static and dynamic finite element analysis*. Courier Corporation New York
- [31] Jirásek M, Rolshoven S (2009) Localization properties of strain-softening gradient plasticity models. Part I: Strain-gradient theories. *Int J Solids Struct* 46(11-12):2225–2238, DOI 10.1016/j.ijsolstr.2008.12.016
- [32] Ju X, Mahnken R (2016) An NTFA-based homogenization framework considering softening effects. *Mechanics of Materials* 96:106–125
- [33] Ju X, Mahnken R (2016) Model adaptivity on effective elastic properties coupled with adaptive FEM. *Computer methods in Applied Mechanics and Engineering* -:-, submitted
- [34] Ladevèze P, Pelle J (2005) *Mastering calculations in linear and non linear mechanics*. Mechanical Engineering Series, Springer, DOI 10.1007/b138705
- [35] Larsson P F Hansbo, Runesson K (2002) Strategies for computing goal-oriented a posteriori error measures in non-linear elasticity. *Int J Numer Mech Engng* 55:879–894
- [36] Leismann T, Mahnken R (2015) Comparison of hyperelastic micromorphic, micropolar and microstrain continua. *Int J Nonlinear Mech* 77:115–127, DOI 10.1016/j.ijnonlinmec.2015.08.004
- [37] Ma Q, Clarke DR (1995) Size dependent hardness of silver single crystals. *Journal of Materials Research* 10(4):853–863, DOI 10.1557/JMR.1995.0853
- [38] Mahnken R, Cheng C, Düsung M, Ehlenbröker U, Leismann T (2016) The concept of generalized stresses for computational manufacturing and beyond. *GAMM-Mitt* 39(2):229–265, DOI I 10.1002/gamm.201610013
- [39] Neff P, Jeong J, Fischle A (2010) Stable identification of linear isotropic Cosserat parameters: bounded stiffness in bending and torsion implies conformal invariance of curvature. *Acta Mechanica* 211(3):237–249, DOI 10.1007/s00707-009-0230-z
- [40] Paraschivoiu M, Peraire J, Patera A (1997) A posteriori finite element bounds for linear-functional outputs of elliptic partial differential equations. *Comput Methods Appl Mech Engrg* 150(1):289–312, DOI 10.1016/S0045-7825(97)00086-8
- [41] Peerlings RHJ, Geers MGD, de Borst R, Brekelmans WAM (2001) A critical comparison of nonlocal and gradient-enhanced softening continua. *Int J Solids Struct* 38(44-45):7723–7746, DOI 10.1016/S0020-7683(01)00087-7

- [42] Poole WJ, Ashby MF, Fleck NA (1996) Micro-hardness of annealed and work-hardened copper polycrystals. *Scripta Materialia* 34(4):559–564, DOI 10.1016/1359-6462(95)00524-2
- [43] Prudhomme S, Oden J (1999) On goal-oriented error estimation for elliptic problems: application to the control of pointwise errors. *Comput Methods Appl Mech Engrg* 176(1–4):313–331, DOI 10.1016/S0045-7825(98)00343-0
- [44] Qu J, Cherkaoui M (2006) *Fundamentals of Micromechanics of Solids*. Wiley, Hoboken, New Jersey
- [45] Rüter M (2003) *Error-controlled Adaptive Finite Element Methods in Large Strain Hyperelasticity and Fracture Mechanics*. PhD thesis, University of Hannover, Hannover
- [46] Stein E (ed) (2003) *Error-controlled Adaptive Finite Elements in Solid Mechanics*. Wiley, Chichester
- [47] Steinmann P (1994) A micropolar theory of finite deformation and finite rotation multiplicative elastoplasticity. *Int J Solids Struct* 31(8):1063–1084, DOI 10.1016/0020-7683(94)90164-3
- [48] Stelmashenko NA, Walls MG, Brown LM, Milman YUV (1993) Microindentations on W and Mo oriented single crystals: An STM study. *Acta Metallurgica et Materialia* 41(10):2855–2865, DOI 10.1016/0956-7151(93)90100-7
- [49] Verfürth R (1996) *A Review of A Posteriori Error Estimation and Adaptive Mesh-Refinement Techniques*. Wiley-Teubner, Stuttgart
- [50] Widany KU, Mahnken R (2012) Adaptivity for parameter identification of incompressible hyperelastic materials using stabilized tetrahedral elements. *Comput Methods Appl Mech Engrg* 245-246:117–131, DOI 10.1016/j.cma.2012.06.017
- [51] Zienkiewicz O, Zhu J (1992) Superconvergent patch recovery and a posteriori error estimates. Part 1: the recovery technique. *Int J Num Meth Eng* 33(7):1331–1364
- [52] Zienkiewicz OC, Taylor RL (2005) *The finite element method for solid and structural mechanics*. Butterworth-heinemann London
- [53] Zienkiewicz OC, Taylor RL, Zienkiewicz OC, Taylor RL (1977) *The finite element method, vol 3*. McGraw-hill London

---

## **Paper E**

Xiaozhe Ju and Rolf Mahnken

*Goal-oriented h-type adaptive finite elements for micromorphic elastoplasticity*  
Computer Methods in Applied Mechanics and Engineering 351 (2019), 297-329

---



# Goal-oriented h-type adaptive finite elements for micromorphic elastoplasticity

Xiaozhe Ju and Rolf Mahnken

Chair of Engineering Mechanics, University of Paderborn,  
Warburger Str. 100, 33098 Paderborn, Germany

## Abstract

Generalized continuum theories become necessary for many scenarios like strain localization phenomena or size effects. In this work, we consider a class of higher order continua, namely micromorphic continua, where the kinematics is enhanced by means of a microstructure undergoing an affine micro deformation. The increasing number of the degrees of freedom in such a theory clearly motivates an application of adaptive methods. For linear elastic micromorphic problems, we have shown the consistency of the resulted dual problem, ensuring an optimal convergence order, in [39]. In this work, we extend the framework of goal-oriented adaptivity to time-dependent problems, i.e. plasticity problems, where a backwards-in-time dual problem is crucial to account for the error accumulation over time caused by both error generation and error transport. Our focus is limited to an adaptive control of spatial discretization errors of the finite element method (FEM), while the temporal discretization errors are not considered for simplicity. Based on duality techniques, we derive exact error representations. For practice, four computable error estimators are proposed, where two different ways to obtain enhanced solutions are considered, and where additionally an approximate forwards-in-time dual problem neglecting error transport is introduced. By means of certain localization techniques, these estimators are used to drive an adaptive mesh refinement algorithm. Their effectiveness is shown by several numerical examples based on a prototype model.

**Keywords:** finite element method, micromorphic continua, elasto-plasticity, a posteriori error estimate, dual problems, goal-oriented adaptivity

## 1 Introduction

Size effects are well reported in the literature, see e.g. [65, 46, 58, 8] for metals and ceramics w.r.t. indentation hardness, [55, 3] for mechanical behavior of metallic foams and [21] for hole size effects of metallic and polymeric foams. The classical Cauchy-Boltzmann continuum theory is, on the one hand, not able to account for

such effects due to the lack of an internal length. On the other hand, an illposedness (mesh dependence) arises in the case of numerical simulation of softening behavior, see e.g. [51, 34, 11]. For a remedy, many different theories have been developed under the term of generalized continuum mechanics, including gradient theories [57, 37, 19], higher order theories as well as nonlocal theories, see e.g. [51, 70].

In this work, we focus on a class of higher order continuum theories, where additional degrees of freedom are introduced to each (macro) material point. Directors attached to each material point may evolve in different ways. Cosserat directors can only rotate, see e.g. [17, 64, 13, 12, 53] for a micropolar theory. On the contrary, microstrain theories account for the micro deformation part without rotation, see e.g. [25]. The so-called micromorphic theories were originally introduced as a general case by Eringen in [16], who endowed the microstructure with full degrees of freedom. As well known, the microstretch theory in [18] is a further special case of the micromorphic continua. Plasticity in micromorphic continua has been the subject of various publications in recent years, see e.g. [23, 22, 35, 29, 30, 31, 45]. The papers [22, 30, 31, 4] are also concerned with damage. A detailed comparison of micromorphic, micropolar and microstrain continua is given in [44]. As shown in [50], these theories can be seen as special cases within the framework of generalized stresses [27, 28, 32, 26, 2].

The finite element method (FEM) was invented by first publications [10, 67] for elasticity problems and has become a widely used tool for solving many different kinds of problems, see e.g. [73, 72, 36]. In order to obtain reliable results, the discretization errors of the FEM have to be properly controlled. Meeting both a user-defined accuracy level and a relatively high computational efficiency, adaptive FEM based on error estimators has been a well-established research field for several decades. While many error estimators were developed to control the discretization error in global norms since the seminal work [5], the so-called goal-oriented error estimate, aiming at a user-defined quantity of interest, was established by [15] and further developed by [7]. For the general framework of a posteriori error estimate, we refer to [15, 69, 1, 41, 6, 63]. Adaptive mesh refinement is then guided by error indicators which are localizations of the global error to elements. It is then advantageous to refine the mesh with the goal of minimizing the error in this quantity of interest. Relevant contributions to this topic can be found in [7, 56, 9, 59]. For time-dependent problems, a backwards-in-time dual problem is necessary to consider error accumulation over time, see e.g. [43, 62, 71]. Phase-field problems are considered e.g. in [48]. It is also worth mentioning that model adaptivity addressing modeling errors by a similar philosophy as the adaptive FEM is another well-established research field, see e.g. [54, 68, 66, 40]. In our previous work [39], goal-oriented error estimate has been applied to micromorphic continua for linear elasticity problems, where a primal and an adjoint consistency analysis have been performed, respectively. The present paper intends to extend the framework to micromorphic plasticity problems including the following aspects:

- Due to the time-dependent character of these problems, both a spatial and a temporal discretization are required for an FE solution. For simplicity, we will only deal with the spatial discretization errors of the FEM, whereas temporal discretization errors are not considered.

- It is common to introduce certain internal (state) variables to account for the time-dependency. These are usually governed by certain partial differential equations to be solved via a time integration, for which a temporal discretization (time-stepping) scheme has to be applied in practice. As a result, the spatial discretization errors accumulate over time. As pointed out in [42], there are two different sources for *error accumulation*:
  1. *Error generation*: discretization errors are newly generated on each single time step of user's interest.
  2. *Error transport*: discretization errors generated on the current time step are transported into the next time step. This effect was not considered in [42].

To account for both sources of error accumulation, we will derive a backwards-in-time dual (auxiliary) problem.

- Additionally, we propose an approximate forwards-in-time dual problem by neglecting error transport, which is quite attractive for a numerical implementation.
- Based on these two dual problems, four error estimators will be presented and studied, where the *patch recovery* technique for enhanced solutions proposed in [39, 40] is also considered.

This paper is structured as follows: In Section 2, the micromorphic continuum theory is revisited, including kinematic relations, balance laws in strong and weak form. Interpreting the considered framework as differential-algebraic equations, we adopt a general matrix form of local evolution equations and establish a corresponding weak form accounting for time integration. Subsequently, we provide a space-time FE formulation for a numerical solution of the primal (actual physical) problem. At the end of this section, we specify a prototype model. Section 3 is concerned with goal-oriented adaptivity, for which a dual problem is deduced from the Lagrange method. Correspondingly, a space-time FE formulation is given, clearly showing a backwards-in-time feature of the dual problem. By a further approximation, a forwards-in-time dual problem is additionally obtained. Based on duality techniques, exact error representations for spatial discretization errors are derived. For a practical implementation, we discuss four different possibilities towards a computable error estimate. In order to study the effectiveness of the proposed error estimators, three numerical examples are performed in Section 4. Finally, a conclusion and an outlook on further research are given in Section 5.

Notation: The scalar products of two vectors  $\mathbf{a}$  and  $\mathbf{b}$ , two second-order tensors  $\mathbf{A}$  and  $\mathbf{B}$  and two third-order tensors  $\mathbf{Q}$  and  $\mathbf{R}$  are

$$\mathbf{a} \cdot \mathbf{b} = a_i b_i, \quad \mathbf{A} : \mathbf{B} = A_{ij} B_{ij}, \quad \mathbf{Q} \cdot \mathbf{R} = Q_{ijk} R_{ijk}, \quad (1)$$

respectively, using the Einstein summation convention for repeated indices. The gradient operator  $\nabla$  is introduced as

$$\nabla \mathbf{c} := \mathbf{c} \otimes \nabla = c_{i,j} \mathbf{e}_i \otimes \mathbf{e}_j, \quad \text{with } c_{i,j} = \frac{\partial c_i}{\partial X_j}, \quad (2)$$

where  $\mathbf{e}_i$ ,  $i = 1, 2, 3$  is a Cartesian orthonormal basis and  $X_i$  are coordinates of the reference placement  $\mathbf{X}$ . By  $\otimes$  we denote the dyadic product. The divergence operator  $\text{Div}(\bullet)$  is defined as

$$\text{Div}(\boldsymbol{\sigma}) := \boldsymbol{\sigma} \cdot \nabla = \sigma_{ij,j} \mathbf{e}_i, \quad \text{with } \sigma_{ij,j} = \frac{\partial \sigma_{ij}}{\partial X_j}. \quad (3)$$

Gâteaux differentiation of a linear form  $F$  and a semilinear form  $B$  w.r.t. the argument  $\mathbf{u}$  is denoted as

$$D_{\mathbf{u}}F(\mathbf{u}; \mathbf{v}) = \lim_{\theta \rightarrow 0} \frac{1}{\theta} [F(\mathbf{u} + \theta \mathbf{v}) - F(\mathbf{u})], \quad (4a)$$

$$D_{\mathbf{u}}B(\mathbf{u}; \mathbf{w}, \mathbf{v}) = \lim_{\theta \rightarrow 0} \frac{1}{\theta} [B(\mathbf{u} + \theta \mathbf{v}; \mathbf{w}) - B(\mathbf{u}; \mathbf{w})], \quad (4b)$$

respectively. Moreover, the semilinear form  $B$  is nonlinear w.r.t. the arguments in front of the semicolon but linear w.r.t. the ones behind.

## 2 Elastoplasticity in micromorphic continuum

### 2.1 Kinematics

As illustrated in Fig. 1, a classical framework of micromorphic continuum is considered for quasi-static problems in solid mechanics. The macro deformation gradient is defined as

$$\mathbf{F}(\mathbf{X}, t) = \nabla \boldsymbol{\varphi}(\mathbf{X}, t), \quad (5)$$

with the time  $t$  and the operator  $\boldsymbol{\varphi}$  mapping the initial coordinates  $\mathbf{X}$  to the current coordinates  $\mathbf{x} = \boldsymbol{\varphi}(\mathbf{X})$ . The macro displacement is given by  $\mathbf{u} = \mathbf{x} - \mathbf{X}$ . For simplicity, small strains

$$\boldsymbol{\varepsilon} := \nabla^{\text{sym}} \mathbf{u} = \frac{1}{2}(\mathbf{H} + \mathbf{H}^T) \quad (6)$$

are assumed, where

$$\mathbf{H} = \nabla \mathbf{u} = \mathbf{F} - \mathbf{1} \quad (7)$$

is the displacement gradient, and where  $\mathbf{1}$  represents the second-order identity tensor. The underlying microstructure is assumed to undergo an affine micro deformation gradient  $\overline{\mathbf{F}}$ , which is related to the micro displacement gradient  $\overline{\mathbf{H}}$  by  $\overline{\mathbf{H}} = \overline{\mathbf{F}} - \mathbf{1}$ . Hence, an introduction of a specific microstructure, unlike homogenization schemes [60, 20, 38], is not required. Within a small strain framework [52, 11, 24], we define two additional strain measures: the second-order relative displacement gradient

$$\overline{\mathbf{e}}(\mathbf{X}, t) = \mathbf{H}(\mathbf{X}, t) - \overline{\mathbf{H}}(\mathbf{X}, t) \quad (8)$$

and the gradient of the micro displacement gradient being a third-order tensor

$$\overline{\mathbf{G}}(\mathbf{X}, t) = \nabla \overline{\mathbf{H}}(\mathbf{X}, t), \quad (9)$$

respectively, depending on the macro coordinates  $\mathbf{X}$  rather than micro ones.

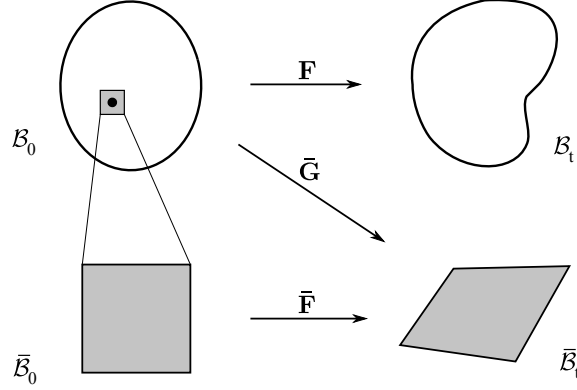


Figure 1: Kinematics of a micromorphic continuum

## 2.2 Balance laws and weak formulations

According to [11, 24] within a small strain framework, the following coupled balance laws for momentum and moment of momentum must be satisfied:

$$\text{Div}(\boldsymbol{\sigma} + \bar{\mathbf{s}}) = \mathbf{0}, \quad (10a)$$

$$\text{Div}(\bar{\mathbf{S}}) + \bar{\mathbf{s}} = \mathbf{0}, \quad \text{in } \mathcal{B} \times I. \quad (10b)$$

Here  $\boldsymbol{\sigma}$  is the (symmetric) Cauchy stress tensor,  $\bar{\mathbf{s}}$  the generally nonsymmetric relative stress tensor and  $\bar{\mathbf{S}}$  the third-order hyperstress tensor. Their thermodynamic counterparts, i.e. the corresponding strain tensors, are the small strain tensor  $\boldsymbol{\varepsilon}$  in Eq. (6), the relative strain tensor  $\bar{\boldsymbol{\varepsilon}}$  in Eq. (8) and the third-order tensor  $\bar{\mathbf{G}}$  in Eq. (9), respectively. Moreover,  $I = [0, T]$  represents the time interval under consideration. Note that body forces, couples and double forces are not considered here. The following boundary conditions, acting on  $\mathcal{B} = \mathcal{B}_0 = \mathcal{B}_t$  for small strains, apply:

$$\mathbf{u} = \mathbf{u}^{pre}(\mathbf{X}, t), \quad \text{on } \partial\mathcal{B}^u \times I, \quad (11a)$$

$$\bar{\mathbf{H}} = \bar{\mathbf{H}}^{pre}(\mathbf{X}, t), \quad \text{on } \partial\mathcal{B}^{\bar{\mathbf{H}}} \times I, \quad (11b)$$

$$(\boldsymbol{\sigma} + \bar{\mathbf{s}}) \cdot \mathbf{N} = \mathbf{t}(\mathbf{X}, t), \quad \text{on } \partial\mathcal{B}^t \times I, \quad (11c)$$

$$\bar{\mathbf{S}} \cdot \mathbf{N} = \bar{\mathbf{T}}(\mathbf{X}, t), \quad \text{on } \partial\mathcal{B}^{\bar{\mathbf{T}}} \times I. \quad (11d)$$

Here  $\mathbf{N}$  is the outward normal vector on the boundary  $\partial\mathcal{B}$  and  $\mathbf{t}$  the macro traction on the Neumann boundary  $\partial\mathcal{B}^t$ . The micro traction on the boundary  $\partial\mathcal{B}^{\bar{\mathbf{T}}}$  in Eq. (11d) is denoted as  $\bar{\mathbf{T}}$ . Additionally, the relations  $\partial\mathcal{B}^u \cup \partial\mathcal{B}^t = \partial\mathcal{B}$ ,  $\partial\mathcal{B}^u \cap \partial\mathcal{B}^t = \emptyset$ ,  $\partial\mathcal{B}^{\bar{\mathbf{H}}} \cup \partial\mathcal{B}^{\bar{\mathbf{T}}} = \partial\mathcal{B}$  and  $\partial\mathcal{B}^{\bar{\mathbf{H}}} \cap \partial\mathcal{B}^{\bar{\mathbf{T}}} = \emptyset$  hold. Furthermore, the initial conditions for the degrees of freedom read

$$\mathbf{u} = \mathbf{u}^0(\mathbf{X}) \quad \text{in } \mathcal{B} \times \{0\}, \quad (12a)$$

$$\bar{\mathbf{H}} = \bar{\mathbf{H}}^0(\mathbf{X}) \quad \text{in } \mathcal{B} \times \{0\}. \quad (12b)$$

Upon introducing test functions  $\delta \mathbf{u}$  and  $\delta \overline{\mathbf{H}}$ , the final expressions for the weak forms of the balance laws (10) are established as

$$\int_{\mathcal{B}} (\boldsymbol{\varepsilon}[\delta \mathbf{u}] : \boldsymbol{\sigma}[\mathbf{u}] + \mathbf{H}[\delta \mathbf{u}] : \overline{\mathbf{s}}[\mathbf{u}, \overline{\mathbf{H}}]) dV - \int_{\partial \mathcal{B}^t} \delta \mathbf{u} \cdot \mathbf{t} dA = 0, \quad \forall \delta \mathbf{u} \in \mathcal{V}_u, \quad (13a)$$

$$\int_{\mathcal{B}} (\overline{\mathbf{G}}[\delta \overline{\mathbf{H}}] : \overline{\mathbf{S}}[\overline{\mathbf{H}}] - \delta \overline{\mathbf{H}} : \overline{\mathbf{s}}[\mathbf{u}, \overline{\mathbf{H}}]) dV - \int_{\partial \mathcal{B}^{\overline{Q}}} \delta \overline{\mathbf{H}} : \overline{\mathbf{T}} dA = 0, \quad \forall \delta \overline{\mathbf{H}} \in \mathcal{V}_{\overline{\mathbf{H}}}, \quad (13b)$$

respectively, at each time point  $t \in I$ , where  $\mathcal{V}_u$  and  $\mathcal{V}_{\overline{\mathbf{H}}}$  are defined as

$$\mathcal{V}_u := \{ \delta \mathbf{u} = \delta u_i \mathbf{e}_i \mid \delta u_i \in H^1(\mathcal{B}), \delta \mathbf{u} = \mathbf{0} \text{ on } \partial \mathcal{B}^u \}, \quad (14)$$

$$\mathcal{V}_{\overline{\mathbf{H}}} := \{ \delta \overline{\mathbf{H}} = \delta \overline{H}_{ij} \mathbf{e}_i \otimes \mathbf{e}_j \mid \delta \overline{H}_{ij} \in H^1(\mathcal{B}), \delta \overline{\mathbf{H}} = \mathbf{0} \text{ on } \partial \mathcal{B}^{\overline{\mathbf{H}}} \}, \quad (15)$$

respectively. Here,  $H^1(\mathcal{B})$  denotes Sobolev spaces in a standard sense, see e.g. [1] for further mathematical details. A simple combination of the coupled weak forms (13) renders a compact representation

$$\begin{aligned} & \underbrace{\int_{\mathcal{B}} (\boldsymbol{\varepsilon}[\delta \mathbf{u}] : \boldsymbol{\sigma}[\mathbf{u}] + \overline{\mathbf{e}}[\delta \mathbf{u}, \delta \overline{\mathbf{H}}] : \overline{\mathbf{s}}[\mathbf{u}, \overline{\mathbf{H}}] + \overline{\mathbf{G}}[\delta \overline{\mathbf{H}}] : \overline{\mathbf{S}}[\overline{\mathbf{H}}]) dV}_{:=B(\mathbf{u}, \overline{\mathbf{H}}; \delta \mathbf{u}, \delta \overline{\mathbf{H}})} \\ &= \underbrace{\int_{\partial \mathcal{B}^t} \mathbf{t} \cdot \delta \mathbf{u} dA + \int_{\partial \mathcal{B}^{\overline{Q}}} \delta \overline{\mathbf{H}} : \overline{\mathbf{T}} dA}_{:=F(\delta \mathbf{u}, \delta \overline{\mathbf{H}})} \quad \forall \delta \mathbf{u} \in \mathcal{V}_u, \delta \overline{\mathbf{H}} \in \mathcal{V}_{\overline{\mathbf{H}}}, \end{aligned} \quad (16)$$

whose left hand side clearly shows three work conjugate pairs. Finally, upon introducing the notion of the generalized solution  $\widehat{\mathbf{u}}$  and its variation  $\delta \widehat{\mathbf{u}}$  as

$$\widehat{\mathbf{u}} := \begin{bmatrix} \mathbf{u} \\ \overline{\mathbf{H}} \end{bmatrix}, \quad (17a)$$

$$\delta \widehat{\mathbf{u}} := \begin{bmatrix} \delta \mathbf{u} \\ \delta \overline{\mathbf{H}} \end{bmatrix}, \quad (17b)$$

and taking the time integration and the initial conditions (12) as well as Eq. (16) into account, we obtain a compact residual form as

$$\varrho_u(\widehat{\mathbf{u}}, \mathbf{q}; \delta \widehat{\mathbf{u}}) = \int_I \{ F(\delta \widehat{\mathbf{u}}) - B(\widehat{\mathbf{u}}, \mathbf{q}; \delta \widehat{\mathbf{u}}) \} dt + (\widehat{\mathbf{u}}_0 - \widehat{\mathbf{u}}^0, \delta \widehat{\mathbf{u}}_0) = 0, \quad (18)$$

for all  $\delta \widehat{\mathbf{u}} \in \mathcal{V} := \mathcal{V}_u \times \mathcal{V}_{\overline{\mathbf{H}}}$ , with  $\widehat{\mathbf{u}}^0 := [\mathbf{u}^0 \ \overline{\mathbf{H}}^0]^T$ . Here,  $\widehat{\mathbf{u}}_0$  represents  $\widehat{\mathbf{u}}$  at the initial time  $t = 0$ , and the subscript 0 will be used throughout this paper for same purposes.  $B$  is a semilinear form, which, due to the plasticity under consideration, depends on certain internal variables  $\mathbf{q}$  introduced in the subsequent section.

**Remark 1.** The transformation of the weak form (16) into a time-integrated version (18) is introduced for ease of deriving a dual problem for a goal-oriented error estimate in Section 3. In a standard sense, (16), after the discretizations to be introduced in Section 2.4, forms the global (element) level of a two-level FE implementation to be solved via certain linearization scheme (here Newton method) at each time point, where the time-integrated version (18) is not explicitly used.

**Remark 2.** The test function spaces defined in (14) and (15) ensure some regularities, e.g. the Lebesgue integrability of the first derivatives and the boundary conditions etc. Similar definitions hold for solution spaces taking into account the corresponding boundary conditions (11a) and (11b), i.e.

$$\begin{aligned}\mathcal{V}_u^s &:= \{ \mathbf{u} = u_i \mathbf{e}_i \mid u_i \in H^1(\mathcal{B}), \mathbf{u} = \mathbf{u}^{pre} \text{ on } \partial\mathcal{B}^u \}, \\ \mathcal{V}_{\overline{\mathbf{H}}}^s &:= \{ \overline{\mathbf{H}} = \overline{H}_{ij} \mathbf{e}_i \otimes \mathbf{e}_j \mid \overline{H}_{ij} \in H^1(\mathcal{B}), \overline{\mathbf{H}} = \overline{\mathbf{H}}^{pre} \text{ on } \partial\mathcal{B}^{\overline{\mathbf{H}}} \}.\end{aligned}$$

**Remark 3.** As the test function spaces  $\mathcal{V}_u$  and  $\mathcal{V}_{\overline{\mathbf{H}}}$  respectively defined in (14) and (15) are only related to the spatial domain, its combination  $\mathcal{V}$  also remains spatial in Eq. (18). As a result,  $\delta\widehat{\mathbf{u}}$  and  $\mathcal{V}$  have a corresponding time-dependency in Eq. (18), i.e.  $\delta\widehat{\mathbf{u}}(t) \in \mathcal{V}(t) = \mathcal{V}_u(t) \times \mathcal{V}_{\overline{\mathbf{H}}}(t)$ . For brevity,  $(t)$  denoting this time-dependency is omitted.

## 2.3 A general form of local evolution equations and the time integration in a weak sense

For generality, we introduce a matrix representation of the evolution equations as

$$\underline{\mathbf{A}}\dot{\mathbf{q}} - \mathbf{r}(\widehat{\mathbf{u}}, \mathbf{q}) = \mathbf{0}, \quad (19)$$

where the vector  $\mathbf{q}$  contains internal variables, see also [14]. Furthermore,  $\underline{\mathbf{A}}$  is a quadratic matrix, while  $\mathbf{r}$  is another vector completing the evolution equations. Also note that we allow  $\mathbf{q}$ ,  $\underline{\mathbf{A}}$  and  $\mathbf{r}$  to have tensorial components for brevity. Eq. (19) is completed by an initial condition

$$\mathbf{q} = \mathbf{q}^0(\mathbf{X}) \quad \text{on } \mathcal{B} \times \{0\}, \quad (20)$$

resulting into an initial value problem. Upon introducing a test function  $\delta\mathbf{q} \in \mathcal{V}^q$ , taking both the volume and the time integration, and including the initial condition (20), we obtain a weak residual form of Eq. (19) as

$$\varrho_q(\widehat{\mathbf{u}}, \mathbf{q}; \delta\mathbf{q}) = \int_I \int_{\mathcal{B}} \{ \delta\mathbf{q} \cdot (\underline{\mathbf{A}}\dot{\mathbf{q}} - \mathbf{r}(\widehat{\mathbf{u}}, \mathbf{q})) \} dV dt + (\underline{\mathbf{A}}\mathbf{q}_0 - \underline{\mathbf{A}}\mathbf{q}^0, \delta\mathbf{q}_0) = 0, \quad (21)$$

becoming

$$\varrho_q(\widehat{\mathbf{u}}, \mathbf{q}; \delta\mathbf{q}) = (\underline{\mathbf{A}}\dot{\mathbf{q}}, \delta\mathbf{q})_I - \int_I R(\widehat{\mathbf{u}}, \mathbf{q}; \delta\mathbf{q}) dt + (\underline{\mathbf{A}}\mathbf{q}_0 - \underline{\mathbf{A}}\mathbf{q}^0, \delta\mathbf{q}_0) = 0, \quad (22)$$

by means of the following definitions

$$(\bullet, \bullet)_I := \int_I \int_{\mathcal{B}} (\bullet, \bullet) dV dt, \quad (23a)$$

$$(\bullet, \bullet) := \int_{\mathcal{B}} (\bullet, \bullet) dV, \quad (23b)$$

$$R(\widehat{\mathbf{u}}, \mathbf{q}; \delta\mathbf{q}) := \int_{\mathcal{B}} \delta\mathbf{q} \cdot \mathbf{r}(\widehat{\mathbf{u}}, \mathbf{q}) dV. \quad (23c)$$

Note that a definition of the test function space  $\mathcal{V}^q$  will be given in Section 2.5, where  $\mathbf{q}$  will be specified for a prototype model.

**Remark 4.** The evolution equation (19) completed by additional constitutive equations (27) introduced in Section 2.5, along with the discretizations introduced in Section 2.4, forms the local (material) level of a standard two-level FE implementation. Its solution does not necessarily rely on any variational form like (21). The sole purpose of the variational form (21) is the derivation of a goal-oriented error estimate and the related dual problem as will be shown in Section 3, see also [43] for a slightly different context.

## 2.4 Space-time finite elements for the primal problem

For a practical solution of the initial value problem (18) and (22) with the FEM, we firstly adopt a temporal discretization of dG(0) type denoted by a subscript  $k$ :

$$\varrho_u(\widehat{\mathbf{u}}_k, \mathbf{q}_k; \delta\widehat{\mathbf{u}}_k) = \sum_{n=1}^N \int_{I_n} \{F(\delta\widehat{\mathbf{u}}_k) - B(\widehat{\mathbf{u}}_k, \mathbf{q}_k; \delta\widehat{\mathbf{u}}_k)\} dt + (\widehat{\mathbf{u}}_{k,0} - \widehat{\mathbf{u}}^0, \delta\widehat{\mathbf{u}}_{k,0}) = 0, \quad (24a)$$

$$\begin{aligned} \varrho_q(\widehat{\mathbf{u}}_k, \mathbf{q}_k; \delta\mathbf{q}_k) &= \sum_{n=0}^{N-1} (\underline{A}[\mathbf{q}_k]_n, \delta\mathbf{q}_{k,n}^+) - \sum_{n=1}^N \int_{I_n} R(\widehat{\mathbf{u}}_k, \mathbf{q}_k; \delta\mathbf{q}_k) dt \\ &+ (\underline{A}\mathbf{q}_{k,0}^- - \underline{A}\mathbf{q}^0, \delta\mathbf{q}_{k,0}^-) = 0, \end{aligned} \quad (24b)$$

for all  $\delta\widehat{\mathbf{u}}_k \in \mathcal{V}_k$  and  $\delta\mathbf{q}_k \in \mathcal{V}_k^q$ , where we define

$$\mathbf{q}_{k,n}^+ := \lim_{t \downarrow t_n} \mathbf{q}_k(t), \quad (25a)$$

$$\mathbf{q}_{k,n}^- := \lim_{t \uparrow t_n} \mathbf{q}_k(t), \quad (25b)$$

$$[\mathbf{q}_k]_n := \mathbf{q}_{k,n}^+ - \mathbf{q}_{k,n}^-, \quad (25c)$$

respectively, and where the total time interval  $I$  is subdivided into  $N$  subintervals  $I_n := (t_{n-1}, t_n]$ ,  $\Delta t_n = t_n - t_{n-1}$ . By means of a further standard spatial discretization denoted by a subscript  $h$ , the above equations (24a) and (24b) become

$$\begin{aligned} \varrho_u(\widehat{\mathbf{u}}_{kh}, \mathbf{q}_{kh}; \delta\widehat{\mathbf{u}}_{kh}) &= \sum_{n=1}^N \int_{I_n} \{F(\delta\widehat{\mathbf{u}}_{kh}) - B(\widehat{\mathbf{u}}_{kh}, \mathbf{q}_{kh}; \delta\widehat{\mathbf{u}}_{kh})\} dt \\ &+ (\widehat{\mathbf{u}}_{kh,0} - \widehat{\mathbf{u}}^0, \delta\widehat{\mathbf{u}}_{kh,0}) = 0, \end{aligned} \quad (26a)$$

$$\begin{aligned} \varrho_q(\widehat{\mathbf{u}}_{kh}, \mathbf{q}_{kh}; \delta\mathbf{q}_{kh}) &= \sum_{n=0}^{N-1} (\underline{A}[\mathbf{q}_{kh}]_n, \delta\mathbf{q}_{kh,n}^+) - \sum_{n=1}^N \int_{I_n} R(\widehat{\mathbf{u}}_{kh}, \mathbf{q}_{kh}; \delta\mathbf{q}_{kh}) dt \\ &+ (\underline{A}\mathbf{q}_{kh,0}^- - \underline{A}\mathbf{q}^0, \delta\mathbf{q}_{kh,0}^-) = 0, \end{aligned} \quad (26b)$$

for all  $\delta\widehat{\mathbf{u}}_{kh} \in \mathcal{V}_{kh}$  and  $\delta\mathbf{q}_{kh} \in \mathcal{V}_{kh}^q$ , respectively.

**Remark 5.** The notion of dG(0) is referred to as discontinuous Galerkin method of zero-order, where piecewise constant functions are used in the temporal discretization, see also [62, 71]. In this work, the time integrals are evaluated equivalently to

the backward Euler integration scheme. It is an implicit integration scheme commonly applied in computational mechanics, especially when a stable final state is expected. Of course, other schemes like Runge-Kutta could also be applied, however, will not be considered in this work.

## 2.5 A prototype model

As shown in [34, 33], there are several possibilities in the literature for generalized plasticity. For simplicity, we choose in this work a prototype model, which falls into the category of MP-ETI (incompatible micromorphic plasticity based on total micro strains). This external-micro-variable approach incorporates the micromorphic continuum framework including balances of macro and micro momentum, while the plasticity framework is retained solely at the macro level. Despite of this simplification, [11] shows that such kind of approach is able to reproduce size effects and to offer a sufficient regularization power in case of softening.

The constitutive relations of the prototype model read

$$\boldsymbol{\sigma} = \mathbf{C}\boldsymbol{\varepsilon}^e = \boldsymbol{\sigma}^{vol} + \boldsymbol{\sigma}^{dev}, \quad (27a)$$

$$\bar{\mathbf{s}} = \lambda_s \text{tr}(\bar{\mathbf{e}})\mathbf{1} + 2\mu_s \bar{\mathbf{e}}^s + 2\mu_{cs} \bar{\mathbf{e}}^a, \quad (27b)$$

$$\bar{\mathbf{S}} = l^2(\lambda_m \mathbf{1} \otimes \nabla \text{tr}(\bar{\mathbf{H}}) + 2\mu_m \bar{\mathbf{G}}). \quad (27c)$$

Here  $\boldsymbol{\sigma}^{vol}$  and  $\boldsymbol{\sigma}^{dev}$  represent the volumetric and the deviatoric part of the macro stress tensor  $\boldsymbol{\sigma}$ , respectively. The elastic macro strain tensor  $\boldsymbol{\varepsilon}^e$  is given by  $\boldsymbol{\varepsilon}^e = \boldsymbol{\varepsilon} - \boldsymbol{\varepsilon}^p$ , where  $\boldsymbol{\varepsilon}$  and  $\boldsymbol{\varepsilon}^p$  are the total and the plastic strain tensor. The micro relations (27b) and (27c) are assumed to be linear, see also [11], where  $\bar{\mathbf{e}}^s$  and  $\bar{\mathbf{e}}^a$  are the symmetric and the skew-symmetric part of  $\bar{\mathbf{e}}$  in Eq. (8), respectively. For the macro part, we adopt the classical von Mises plasticity with isotropic hardening specified as

$$\mathbf{q} := \begin{bmatrix} \boldsymbol{\varepsilon}^p \\ \lambda \\ q \end{bmatrix}, \quad (28a)$$

$$\underline{\mathbf{A}} := \begin{bmatrix} \mathbf{1} & 0 & 0 \\ 0 & 0 & 0 \\ 0 & 0 & 1 \end{bmatrix}, \quad (28b)$$

$$\mathbf{r} := \begin{cases} \begin{bmatrix} \dot{\lambda} \mathbf{n} \\ \phi := \|\boldsymbol{\sigma}^{dev}\| - \sqrt{\frac{2}{3}}Y(q) \\ \sqrt{\frac{2}{3}}\dot{\lambda} \end{bmatrix}, & \text{plastic } (\phi = 0, \dot{\lambda} > 0) \\ \begin{bmatrix} \mathbf{0} \\ \dot{\lambda} \\ 0 \end{bmatrix}, & \text{elastic } (\phi < 0, \dot{\lambda} = 0) \end{cases} \quad (28c)$$

in the matrix representation (19), see also [71]. In Eq. (28a),  $q$  represents the equivalent plastic strain, while  $\lambda$  is a plastic multiplier satisfying the Karush-Kuhn-Tucker complementary conditions

$$\dot{\lambda}\phi = 0, \quad \phi \leq 0, \quad \dot{\lambda} \geq 0, \quad (29)$$

where  $\phi$  is the yield function defined in Eq. (28c). In Eq. (28c), we also define

$$\mathbf{n} = \frac{\boldsymbol{\sigma}^{dev}}{\|\boldsymbol{\sigma}^{dev}\|}, \quad (30a)$$

$$Y = Y_0 + R_i, \quad (30b)$$

where the isotropic hardening law reads

$$R_i(q) = Hq + c(1 - \exp(-bq)) \quad (31)$$

for our calculations. Consequently, the material parameters of this prototype model are summarized as

$$\boldsymbol{\kappa} = [K \ G \ \lambda_s \ \mu_s \ \mu_{cs} \ \lambda_m \ \mu_m \ l \ Y_0 \ H \ b \ c], \quad (32)$$

where  $K$  and  $G$  are the bulk and the shear modulus, respectively, describing isotropic elasticity.

**Remark 6.** For the prototype model, we define the test function space  $\mathcal{V}^q$  for Eq. (21) as  $\mathcal{V}^q := \mathcal{V}_1^q \times \mathcal{V}_2^q \times \mathcal{V}_3^q$ , where  $\mathcal{V}_1^q := \{\delta\boldsymbol{\varepsilon}^p = \delta\varepsilon_{ij}^p \mathbf{e}_i \otimes \mathbf{e}_j \mid \delta\varepsilon_{ij}^p \in H^1(\mathcal{B}) \cap L^2(\mathcal{B})\}$ ,  $\mathcal{V}_2^q := \{\delta\lambda \mid \delta\lambda \in L^2(\mathcal{B})\}$ , and  $\mathcal{V}_3^q := \{\delta q \mid \delta q \in H^1(\mathcal{B}) \cap L^2(\mathcal{B})\}$ , see also [43].

**Remark 7.** Compared to more complex models based on nonlinear elastoplastic micro relations, the above prototype model is much simpler to implement, on the one hand. On the other hand, it introduces comparably less material parameters, and therefore is quite attractive for parameter identification.

**Remark 8.** One may also notice that the Karush-Kuhn-Tucker conditions (29) are automatically ensured by the definition (28c). An alternative approach for plasticity would be a regularization of a viscoplastic model and then consider the limit situation, see e.g. [43].

**Remark 9.** This work is limited to isotropic hardening for simplicity. More complex effects could also be covered by the general matrix form (19). For instance, kinematic hardening considering the Bauschinger effect can be accounted for by additional internal variables, i.e. a back stress tensor, see e.g. [47].

## 3 Goal-oriented adaptivity

### 3.1 The Lagrange method and the dual problem

In the following, we assume that our ultimate interest of solving the primal problem given in the equations (18) and (22) is a so-called quantity of interest

$$Q(\hat{\mathbf{u}}, \mathbf{q}) := \int_I Q_1(\hat{\mathbf{u}}, \mathbf{q}) dt + Q_2(\hat{\mathbf{u}}_T, \mathbf{q}_T). \quad (33)$$

Note that  $Q$  could be any differentiable function of user's interest. We think that the definition (33) containing, both a time integral part w.r.t.  $Q_1$  and another part  $Q_2$  at the final time  $T$ , should cover most practical cases. Next, we introduce a Lagrangian as

$$\mathcal{L}(\hat{\mathbf{u}}, \mathbf{q}, \hat{\mathbf{z}}, \mathbf{y}) = Q(\hat{\mathbf{u}}, \mathbf{q}) + \varrho_u(\hat{\mathbf{u}}, \mathbf{q}; \hat{\mathbf{z}}) + \varrho_q(\hat{\mathbf{u}}, \mathbf{q}; \mathbf{y}). \quad (34)$$

Obviously, the stationary problems of (34) w.r.t. the dual variables  $\hat{\mathbf{z}}$  and  $\mathbf{y}$  coincide with the primal problems (18) and (22), respectively. The stationary problems of (34) w.r.t. the primal variables  $\hat{\mathbf{u}}$  and  $\mathbf{q}$  render the following dual equations:

$$\varrho_z(\hat{\mathbf{u}}, \mathbf{q}, \hat{\mathbf{z}}, \mathbf{y}; \delta\hat{\mathbf{u}}) := D_{\hat{\mathbf{u}}}\mathcal{L}(\hat{\mathbf{u}}, \mathbf{q}, \hat{\mathbf{z}}, \mathbf{y}; \delta\hat{\mathbf{u}}) \quad (35a)$$

$$= - \int_I \{D_{\hat{\mathbf{u}}}B(\hat{\mathbf{u}}, \mathbf{q}; \hat{\mathbf{z}}, \delta\hat{\mathbf{u}}) + D_{\hat{\mathbf{u}}}R(\hat{\mathbf{u}}, \mathbf{q}; \mathbf{y}, \delta\hat{\mathbf{u}})\} dt \\ + D_{\hat{\mathbf{u}}}Q(\hat{\mathbf{u}}, \mathbf{q}; \delta\hat{\mathbf{u}}) = 0,$$

$$\varrho_y(\hat{\mathbf{u}}, \mathbf{q}, \hat{\mathbf{z}}, \mathbf{y}; \delta\mathbf{q}) := D_{\mathbf{q}}\mathcal{L}(\hat{\mathbf{u}}, \mathbf{q}, \hat{\mathbf{z}}, \mathbf{y}; \delta\mathbf{q}) \quad (35b)$$

$$= - \int_I \{D_{\mathbf{q}}B(\hat{\mathbf{u}}, \mathbf{q}; \hat{\mathbf{z}}, \delta\mathbf{q}) + D_{\mathbf{q}}R(\hat{\mathbf{u}}, \mathbf{q}; \mathbf{y}, \delta\mathbf{q})\} dt \\ + D_{\mathbf{q}}(\underline{A}\dot{\mathbf{q}}, \mathbf{y})_I + D_{\mathbf{q}}Q(\hat{\mathbf{u}}, \mathbf{q}; \delta\mathbf{q}) = 0,$$

respectively.

**Remark 10.** As the above dual equations (35a) and (35b) merely consist of tangent forms, the dual problem is linear. Alternatively, the dual problem could be introduced as a secant form, see e.g. [61, 48, 49].

### 3.2 A backwards-in-time version of the dual problem

In analogy to the discretization of the primal problem in Section 2.4, a temporally discretized version of the dual equations (35a) and (35b) of a dG(0) type reads

$$\begin{aligned} \varrho_z(\widehat{\mathbf{u}}_k, \mathbf{q}_k, \widehat{\mathbf{z}}_k, \mathbf{y}_k; \delta\widehat{\mathbf{u}}_k) = \\ - \sum_{n=1}^N \int_{I_n} \{D_{\widehat{\mathbf{u}}} B(\widehat{\mathbf{u}}_k, \mathbf{q}_k; \widehat{\mathbf{z}}_k, \delta\widehat{\mathbf{u}}_k) + D_{\widehat{\mathbf{u}}} R(\widehat{\mathbf{u}}_k, \mathbf{q}_k; \mathbf{y}_k, \delta\widehat{\mathbf{u}}_k)\} dt \end{aligned} \quad (36a)$$

$$+ \sum_{n=1}^N \int_{I_n} D_{\widehat{\mathbf{u}}} Q_1(\widehat{\mathbf{u}}_k, \mathbf{q}_k; \delta\widehat{\mathbf{u}}_k) dt + D_{\widehat{\mathbf{u}}} Q_2(\widehat{\mathbf{u}}_{k,N}^-, \mathbf{q}_{k,N}^-; \delta\widehat{\mathbf{u}}_{k,N}^-) = 0,$$

$$\begin{aligned} \varrho_y(\widehat{\mathbf{u}}_k, \mathbf{q}_k, \widehat{\mathbf{z}}_k, \mathbf{y}_k; \delta\mathbf{q}_k) = \\ - \sum_{n=1}^N \int_{I_n} \{D_{\mathbf{q}} B(\widehat{\mathbf{u}}_k, \mathbf{q}_k; \widehat{\mathbf{z}}_k, \delta\mathbf{q}_k) + D_{\mathbf{q}} R(\widehat{\mathbf{u}}_k, \mathbf{q}_k; \mathbf{y}_k, \delta\mathbf{q}_k)\} dt \end{aligned} \quad (36b)$$

$$+ (\delta\mathbf{q}_{k,N}^-, \underline{A}^T \mathbf{y}_{k,N}^-) - \sum_{n=0}^{N-1} (\delta\mathbf{q}_{k,n}^+, \underline{A}^T [\mathbf{y}_k]_n)$$

$$- \sum_{n=0}^{N-1} (\delta\mathbf{q}_{k,n}^+, \underline{A}^T [\mathbf{y}_k]_{n+1})$$

$$+ \sum_{n=1}^N \int_{I_n} D_{\mathbf{q}} Q_1(\widehat{\mathbf{u}}_k, \mathbf{q}_k; \delta\mathbf{q}_k) dt + D_{\mathbf{q}} Q_2(\widehat{\mathbf{u}}_{k,N}^-, \mathbf{q}_{k,N}^-; \delta\mathbf{q}_{k,N}^-) = 0,$$

respectively, where we take the definition (33) into account. Now, we split the equations (36a) and (36b) into single time steps as

1. For  $n = N$ :

$$- \{D_{\widehat{\mathbf{u}}_N} B(\widehat{\mathbf{u}}_N, \mathbf{q}_N; \widehat{\mathbf{z}}_N, \delta\widehat{\mathbf{u}}_N) + D_{\widehat{\mathbf{u}}_N} R(\widehat{\mathbf{u}}_N, \mathbf{q}_N; \mathbf{y}_N, \delta\widehat{\mathbf{u}}_N)\} \Delta t_N \quad (37a)$$

$$+ D_{\widehat{\mathbf{u}}_N} Q_1(\widehat{\mathbf{u}}_N, \mathbf{q}_N; \delta\widehat{\mathbf{u}}_N) \Delta t_N + D_{\widehat{\mathbf{u}}_N} Q_2(\widehat{\mathbf{u}}_N, \mathbf{q}_N; \delta\widehat{\mathbf{u}}_N) = 0,$$

$$- \{D_{\mathbf{q}_N} B(\widehat{\mathbf{u}}_N, \mathbf{q}_N; \widehat{\mathbf{z}}_N, \delta\mathbf{q}_N) + D_{\mathbf{q}_N} R(\widehat{\mathbf{u}}_N, \mathbf{q}_N; \mathbf{y}_N, \delta\mathbf{q}_N)\} \Delta t_N \quad (37b)$$

$$+ (\delta\mathbf{q}_N, \underline{A}^T \mathbf{y}_N) + D_{\mathbf{q}_N} Q_1(\widehat{\mathbf{u}}_N, \mathbf{q}_N; \delta\mathbf{q}_N) \Delta t_N + D_{\mathbf{q}_N} Q_2(\widehat{\mathbf{u}}_N, \mathbf{q}_N; \delta\mathbf{q}_N) = 0,$$

2. For  $n = N - 1, \dots, 1$ :

$$- \{D_{\widehat{\mathbf{u}}_n} B(\widehat{\mathbf{u}}_n, \mathbf{q}_n; \widehat{\mathbf{z}}_n, \delta\widehat{\mathbf{u}}_n) + D_{\widehat{\mathbf{u}}_n} R(\widehat{\mathbf{u}}_n, \mathbf{q}_n; \mathbf{y}_n, \delta\widehat{\mathbf{u}}_n)\} \Delta t_n \quad (38a)$$

$$+ D_{\widehat{\mathbf{u}}_n} Q_1(\widehat{\mathbf{u}}_n, \mathbf{q}_n; \delta\widehat{\mathbf{u}}_n) \Delta t_n = 0,$$

$$- \{D_{\mathbf{q}_n} B(\widehat{\mathbf{u}}_n, \mathbf{q}_n; \widehat{\mathbf{z}}_n, \delta\mathbf{q}_n) + D_{\mathbf{q}_n} R(\widehat{\mathbf{u}}_n, \mathbf{q}_n; \mathbf{y}_n, \delta\mathbf{q}_n)\} \Delta t_n \quad (38b)$$

$$+ (\delta\mathbf{q}_n, \underline{A}^T [\mathbf{y}]_n)$$

$$- D_{\mathbf{q}_n} R(\widehat{\mathbf{u}}_{n+1}, \mathbf{q}_{n+1}; \mathbf{y}_{n+1}, \delta\mathbf{q}_n) \Delta t_{n+1} + (\delta\mathbf{q}_n, \underline{A}^T [\mathbf{y}]_{n+1})$$

$$+ D_{\mathbf{q}_n} Q_1(\widehat{\mathbf{u}}_n, \mathbf{q}_n; \delta\mathbf{q}_n) \Delta t_n = 0,$$

3. For  $n = 0$ :

$$\widehat{\mathbf{z}}_0 = \mathbf{0}, \quad (39a)$$

$$(\delta\mathbf{q}_0, \underline{A}^T [\mathbf{y}]_0) - D_{\mathbf{q}_0} R(\widehat{\mathbf{u}}_1, \mathbf{q}_1; \mathbf{y}_1, \delta\mathbf{q}_0) \Delta t_1 + (\delta\mathbf{q}_0, \underline{A}^T [\mathbf{y}]_1) = 0. \quad (39b)$$

For our convenience, we have omitted the subscript  $k$  in the above equations. Most importantly, the equations (37)–(39) clearly indicate a backwards-in-time problem, due to the terms related to the  $n+1$ st time step in Eq. (38b), see also [62, 71]. Then, with an additional spatial discretization denoted by  $h$ , we obtain a fully discretized version of (35a) and (35b) as

$$\begin{aligned} \varrho_z(\widehat{\mathbf{u}}_{kh}, \mathbf{q}_{kh}, \widehat{\mathbf{z}}_{kh}, \mathbf{y}_{kh}; \delta\widehat{\mathbf{u}}_{kh}) = & \\ - \sum_{n=1}^N \int_{I_n} \{D_{\widehat{\mathbf{u}}}B(\widehat{\mathbf{u}}_{kh}, \mathbf{q}_{kh}; \widehat{\mathbf{z}}_{kh}, \delta\widehat{\mathbf{u}}_{kh}) + D_{\widehat{\mathbf{u}}}R(\widehat{\mathbf{u}}_{kh}, \mathbf{q}_{kh}; \mathbf{y}_{kh}, \delta\widehat{\mathbf{u}}_{kh})\} dt & \\ + \sum_{n=1}^N \int_{I_n} D_{\widehat{\mathbf{u}}}Q_1(\widehat{\mathbf{u}}_{kh}, \mathbf{q}_{kh}; \delta\widehat{\mathbf{u}}_{kh}) dt & \quad (40a) \\ + D_{\widehat{\mathbf{u}}}Q_2(\widehat{\mathbf{u}}_{kh,N}^-, \mathbf{q}_{kh,N}^-; \delta\widehat{\mathbf{u}}_{kh,N}^-) = 0, & \end{aligned}$$

$$\begin{aligned} \varrho_y(\widehat{\mathbf{u}}_{kh}, \mathbf{q}_{kh}, \widehat{\mathbf{z}}_{kh}, \mathbf{y}_{kh}; \delta\mathbf{q}_{kh}) = & \\ - \sum_{n=1}^N \int_{I_n} \{D_{\mathbf{q}}B(\widehat{\mathbf{u}}_{kh}, \mathbf{q}_{kh}; \widehat{\mathbf{z}}_{kh}, \delta\mathbf{q}_{kh}) + D_{\mathbf{q}}R(\widehat{\mathbf{u}}_{kh}, \mathbf{q}_{kh}; \mathbf{y}_{kh}, \delta\mathbf{q}_{kh})\} dt & \\ + (\delta\mathbf{q}_{kh,N}^-, \underline{A}^T \mathbf{y}_{kh,N}^-) - \sum_{n=0}^{N-1} (\delta\mathbf{q}_{kh,n}^+, \underline{A}^T [\mathbf{y}_{kh}]_n) & \quad (40b) \\ - \sum_{n=0}^{N-1} (\delta\mathbf{q}_{kh,n}^+, \underline{A}^T [\mathbf{y}_{kh}]_{n+1}) + \sum_{n=1}^N \int_{I_n} D_{\mathbf{q}}Q_1(\widehat{\mathbf{u}}_{kh}, \mathbf{q}_{kh}; \delta\mathbf{q}_{kh}) dt & \\ + D_{\mathbf{q}}Q_2(\widehat{\mathbf{u}}_{kh,N}^-, \mathbf{q}_{kh,N}^-; \delta\mathbf{q}_{kh,N}^-) = 0. & \end{aligned}$$

**Remark 11.** From a computational point of view, the fully discretized version of the dual problem (40) shares a common structure with its primal counterpart (26). Firstly, the computation of Eq. (40a) for the nodal values of  $\widehat{\mathbf{z}}_{kh}$  is quite similar to a one-step Newton method applied for the primal equation (26a), but with a transposed tangential stiffness matrix and a different loading term. Secondly, by means of Eq. (40b), the evolution of the dual variable  $\mathbf{y}_{kh}$  is calculated at each integration point. In this manner, the classical FE framework with nodal and internal (state) variables is also preserved for the dual problem, see e.g. [71] for further details.

**Remark 12.** As already highlighted in Section 1, error accumulation consists of error generation and error transport. As error transport does not occur on the final state  $n = N$ , the equations (37a) and (37b) merely account for error generation. For the intermediate steps  $n = N - 1, \dots, 1$  where error generation and error transport simultaneously occur, the equations (38a) and (38b) are slightly different from the equations (37a) and (37b) for an additional consideration of error transport. Hence, the additional terms related to the  $n+1$ st time step in Eq. (38b) can be identified as those for error transport, and we shall call them *transport terms*. Similarly, the transport terms in Eq. (39b) for  $n = 0$  are those related to  $n = 1$ .

**Remark 13.** The backwards-in-time feature of the dual problem stems from the accumulative nature of the internal variables  $\mathbf{q}$ , thus resulting into the dependence of the current step  $n$  on the future step  $n + 1$  in Eq. (38b) for the intermediate time steps. It enables us to take into account error accumulation over time (error generation and error transport), however, requires additional memory to store the primal solutions  $\hat{\mathbf{u}}_{kh}$  and  $\mathbf{q}_{kh}$  computed over all time steps, see [62, 71] for more details. Hence, from a computational point of view, a forwards-in-time dual problem would be very attractive.

### 3.3 A forwards-in-time version of the dual problem

A forwards-in-time version of the dual problem may be obtained by omitting the transport terms in the equations (38b) and (39b), and reads

- For  $n = 0$ :

$$\hat{\mathbf{z}}_0^* = \mathbf{0}, \quad (41a)$$

$$\mathbf{y}_0^* = \mathbf{0}, \quad (41b)$$

- For  $n = 1, \dots, N - 1$ :

$$- \{D_{\hat{\mathbf{u}}_n} B(\hat{\mathbf{u}}_n, \mathbf{q}_n; \hat{\mathbf{z}}_n^*, \delta \hat{\mathbf{u}}_n) + D_{\hat{\mathbf{u}}_n} R(\hat{\mathbf{u}}_n, \mathbf{q}_n; \mathbf{y}_n^*, \delta \hat{\mathbf{u}}_n)\} \Delta t_n \quad (42a)$$

$$+ D_{\hat{\mathbf{u}}_n} Q_1(\hat{\mathbf{u}}_n, \mathbf{q}_n; \delta \hat{\mathbf{u}}_n) \Delta t_n = 0,$$

$$- \{D_{\mathbf{q}_n} B(\hat{\mathbf{u}}_n, \mathbf{q}_n; \hat{\mathbf{z}}_n^*, \delta \mathbf{q}_n) + D_{\mathbf{q}_n} R(\hat{\mathbf{u}}_n, \mathbf{q}_n; \mathbf{y}_n^*, \delta \mathbf{q}_n)\} \Delta t_n \quad (42b)$$

$$+ (\delta \mathbf{q}_n, \underline{A}^T [\mathbf{y}^*]_n) + D_{\mathbf{q}_n} Q_1(\hat{\mathbf{u}}_n, \mathbf{q}_n; \delta \mathbf{q}_n) \Delta t_n = 0.$$

- For  $n = N$ :

$$- \{D_{\hat{\mathbf{u}}_N} B(\hat{\mathbf{u}}_N, \mathbf{q}_N; \hat{\mathbf{z}}_N^*, \delta \hat{\mathbf{u}}_N) + D_{\hat{\mathbf{u}}_N} R(\hat{\mathbf{u}}_N, \mathbf{q}_N; \mathbf{y}_N^*, \delta \hat{\mathbf{u}}_N)\} \Delta t_N \quad (43a)$$

$$+ D_{\hat{\mathbf{u}}_N} Q_1(\hat{\mathbf{u}}_N, \mathbf{q}_N; \delta \hat{\mathbf{u}}_N) \Delta t_N + D_{\hat{\mathbf{u}}_N} Q_2(\hat{\mathbf{u}}_N, \mathbf{q}_N; \delta \hat{\mathbf{u}}_N) = 0,$$

$$- \{D_{\mathbf{q}_N} B(\hat{\mathbf{u}}_N, \mathbf{q}_N; \hat{\mathbf{z}}_N^*, \delta \mathbf{q}_N) + D_{\mathbf{q}_N} R(\hat{\mathbf{u}}_N, \mathbf{q}_N; \mathbf{y}_N^*, \delta \mathbf{q}_N)\} \Delta t_N \quad (43b)$$

$$+ (\delta \mathbf{q}_N, \underline{A}^T \mathbf{y}_N^*) + D_{\mathbf{q}_N} Q_1(\hat{\mathbf{u}}_N, \mathbf{q}_N; \delta \mathbf{q}_N) \Delta t_N + D_{\mathbf{q}_N} Q_2(\hat{\mathbf{u}}_N, \mathbf{q}_N; \delta \mathbf{q}_N) = 0.$$

As the forwards-in-time dual problem (41)–(43) is essentially an approximation of the backwards-in-time dual problem (37)–(39) by neglecting the effect of error transport, we have introduced a superscript  $*$  for the dual variables  $\hat{\mathbf{z}}$  and  $\mathbf{y}$  to indicate the forwards-in-time solution.

**Remark 14.** It should be pointed out that the way towards a forwards-in-time dual problem is not unique. The omission of the transport terms in the equations (38b) and (39b) as done above seems to be a most simple way. Alternatively, for a more effective method, the transport terms could be somehow approximated. However, this will not be considered in this work.

### 3.4 Exact error representations based on duality techniques

In this work, we focus on the spatial discretization error, while the temporal discretization error caused by the time-stepping scheme in the primal problem (24) is not considered. For our convenience, the subscript  $k$  denoting such a time-stepping scheme is omitted hereafter. We aim at the discretization error of the quantity of interest  $Q$  as

$$E(\widehat{\mathbf{u}}, \mathbf{q}, \widehat{\mathbf{u}}_h, \mathbf{q}_h) = Q(\widehat{\mathbf{u}}, \mathbf{q}) - Q(\widehat{\mathbf{u}}_h, \mathbf{q}_h). \quad (44)$$

For a linear quantity of interest  $Q$ , it follows  $E(\widehat{\mathbf{u}}, \mathbf{q}, \widehat{\mathbf{u}}_h, \mathbf{q}_h) = Q(\widehat{\mathbf{e}}_u, \widehat{\mathbf{e}}_q)$ , with the spatial discretization errors  $\widehat{\mathbf{e}}_u := \widehat{\mathbf{u}} - \widehat{\mathbf{u}}_h$  and  $\widehat{\mathbf{e}}_q := \mathbf{q} - \mathbf{q}_h$ . Due to the equations (18), (22), (26a) and (26b), the following identities hold:

$$Q(\widehat{\mathbf{u}}, \mathbf{q}) = \mathcal{L}(\widehat{\mathbf{u}}, \mathbf{q}, \widehat{\mathbf{z}}, \mathbf{y}), \quad (45a)$$

$$Q(\widehat{\mathbf{u}}_h, \mathbf{q}_h) = \mathcal{L}(\widehat{\mathbf{u}}_h, \mathbf{q}_h, \widehat{\mathbf{z}}_h, \mathbf{y}_h). \quad (45b)$$

By means of the abbreviations

$$\widehat{\boldsymbol{\xi}} := [\widehat{\mathbf{u}}, \mathbf{q}, \widehat{\mathbf{z}}, \mathbf{y}], \quad (46a)$$

$$\widehat{\boldsymbol{\xi}}_h := [\widehat{\mathbf{u}}_h, \mathbf{q}_h, \widehat{\mathbf{z}}_h, \mathbf{y}_h], \quad (46b)$$

we obtain an exact error representation in a secant form

$$\begin{aligned} E(\widehat{\mathbf{u}}, \mathbf{q}, \widehat{\mathbf{u}}_h, \mathbf{q}_h) &= Q(\widehat{\mathbf{u}}, \mathbf{q}) - Q(\widehat{\mathbf{u}}_h, \mathbf{q}_h) = \mathcal{L}(\widehat{\boldsymbol{\xi}}) - \mathcal{L}(\widehat{\boldsymbol{\xi}}_h) \\ &= \int_0^1 D_{\widehat{\boldsymbol{\xi}}} \mathcal{L}(\widehat{\boldsymbol{\xi}}_h + s\widehat{\mathbf{e}}_\xi; \widehat{\mathbf{e}}_\xi) ds, \end{aligned} \quad (47)$$

with  $0 \leq s \leq 1$  and  $\widehat{\mathbf{e}}_\xi := \widehat{\boldsymbol{\xi}} - \widehat{\boldsymbol{\xi}}_h$ , and where

$$D_{\widehat{\boldsymbol{\xi}}} \mathcal{L}(\widehat{\boldsymbol{\xi}}; \delta \widehat{\boldsymbol{\xi}}) = \varrho_u(\widehat{\mathbf{u}}, \mathbf{q}; \delta \widehat{\mathbf{z}}) + \varrho_q(\widehat{\mathbf{u}}, \mathbf{q}; \delta \mathbf{y}) + \varrho_z(\widehat{\mathbf{u}}, \mathbf{q}, \widehat{\mathbf{z}}, \mathbf{y}; \delta \widehat{\mathbf{u}}) + \varrho_y(\widehat{\mathbf{u}}, \mathbf{q}, \widehat{\mathbf{z}}, \mathbf{y}; \delta \mathbf{q}). \quad (48)$$

As shown in [62], an alternative representation of (47) takes the form

$$E(\widehat{\mathbf{u}}, \mathbf{q}, \widehat{\mathbf{u}}_h, \mathbf{q}_h) = \mathcal{L}(\widehat{\boldsymbol{\xi}}) - \mathcal{L}(\widehat{\boldsymbol{\xi}}_h) = \frac{1}{2} D_{\widehat{\boldsymbol{\xi}}} \mathcal{L}(\widehat{\boldsymbol{\xi}}_h; \widehat{\mathbf{e}}_\xi) + \mathcal{R}, \quad (49)$$

with the remainder term

$$\mathcal{R} = \int_0^1 D_{\widehat{\boldsymbol{\xi}}} D_{\widehat{\boldsymbol{\xi}}} D_{\widehat{\boldsymbol{\xi}}} \mathcal{L}(\widehat{\boldsymbol{\xi}}_h + s\widehat{\mathbf{e}}_\xi; \widehat{\mathbf{e}}_\xi, \widehat{\mathbf{e}}_\xi, \widehat{\mathbf{e}}_\xi) \cdot s \cdot (s-1) ds. \quad (50)$$

With (48) and the Galerkin orthogonality, the error representation (49) becomes

$$\begin{aligned} E(\widehat{\mathbf{u}}, \mathbf{q}, \widehat{\mathbf{u}}_h, \mathbf{q}_h) &= \frac{1}{2} (\varrho_u(\widehat{\mathbf{u}}_h, \mathbf{q}_h; \widehat{\mathbf{z}}) + \varrho_q(\widehat{\mathbf{u}}_h, \mathbf{q}_h; \mathbf{y})) \\ &\quad + \varrho_z(\widehat{\mathbf{u}}_h, \mathbf{q}_h, \widehat{\mathbf{z}}_h, \mathbf{y}_h; \widehat{\mathbf{u}}) + \varrho_y(\widehat{\mathbf{u}}_h, \mathbf{q}_h, \widehat{\mathbf{z}}_h, \mathbf{y}_h; \mathbf{q}) + \mathcal{R}. \end{aligned} \quad (51)$$

Since the residual  $\varrho_q$  of Eq. (26b) suggests a set of nonlinear equations to be solved at each integration point in an uncoupled manner, we obtain

$$\varrho_q(\widehat{\mathbf{u}}_h, \mathbf{q}_h; \mathbf{y}) = 0. \quad (52)$$

Similarly, the residual  $\varrho_y$  in Eq. (40b) governs the local evolution of the dual variable  $\mathbf{y}_h$  in a locally nonoverlapping manner, such that

$$\varrho_y(\widehat{\mathbf{u}}_h, \mathbf{q}_h, \widehat{\mathbf{z}}_h, \mathbf{y}_h; \mathbf{q}) = 0. \quad (53)$$

Finally, combining the above equations (51), (52) and (53), we have

$$E(\widehat{\mathbf{u}}, \mathbf{q}, \widehat{\mathbf{u}}_h, \mathbf{q}_h) = \frac{1}{2}(\varrho_u(\widehat{\mathbf{u}}_h, \mathbf{q}_h; \widehat{\mathbf{z}}) + \varrho_z(\widehat{\mathbf{u}}_h, \mathbf{q}_h, \widehat{\mathbf{z}}_h, \mathbf{y}_h; \widehat{\mathbf{u}})) + \mathcal{R}. \quad (54)$$

### 3.5 Several computable error estimators

With the exact error representation (54) at hand, we discuss, in the following, several different possibilities towards a computable error estimate.

- **Error estimator 1** (full computation, backwards-in-time): Obviously, the exact error representation (54) is practically not accessible, since it involves the exact solution  $\widehat{\boldsymbol{\xi}}$  in Eq. (46a), which is generally intractable. Hence, we replace  $\widehat{\boldsymbol{\xi}}$  by an *enhanced* solution  $\widehat{\boldsymbol{\xi}}_{h^+}$  on an enhanced FE space of a higher polynomial order, i.e.

$$\widehat{\boldsymbol{\xi}} \approx \widehat{\boldsymbol{\xi}}_{h^+}. \quad (55)$$

For instance, a linear FE space can be enhanced by a quadratic FE space. A straightforward way called *full computation* to obtain the enhanced solution  $\widehat{\boldsymbol{\xi}}_{h^+}$  is to compute it directly on the enhanced FE space. Although the dual problem is linear, one has to deal with the nonlinear primal problem on an enhanced FE space. As a result, a full computation is rather expensive. By neglecting the remainder term  $\mathcal{R}$  in (54), we obtain the error estimate  $\widetilde{E}^1$  as

$$\begin{aligned} E(\widehat{\mathbf{u}}, \mathbf{q}, \widehat{\mathbf{u}}_h, \mathbf{q}_h) &\approx \widetilde{E}^1(\widehat{\boldsymbol{\xi}}_{h^+}, \widehat{\boldsymbol{\xi}}_h) \\ &:= \frac{1}{2}(\varrho_u(\widehat{\mathbf{u}}_h, \mathbf{q}_h; \widehat{\mathbf{z}}_{h^+}) + \varrho_z(\widehat{\mathbf{u}}_h, \mathbf{q}_h, \widehat{\mathbf{z}}_h, \mathbf{y}_h; \widehat{\mathbf{u}}_{h^+})). \end{aligned} \quad (56)$$

- **Error estimator 2** (patch recovery, backwards-in-time): Slightly different to error estimator  $\widetilde{E}^1$ , we introduce a further approximation

$$\widehat{\boldsymbol{\xi}} \approx \widehat{\boldsymbol{\xi}}_{h^+} \approx \widehat{\boldsymbol{\xi}}_{h^+}(\widehat{\boldsymbol{\xi}}_h), \quad (57)$$

where the enhanced solution  $\widehat{\boldsymbol{\xi}}_{h^+}$  is approximated as  $\widehat{\boldsymbol{\xi}}_{h^+}$ , i.e. a smoothed version of the working solution  $\widehat{\boldsymbol{\xi}}_h$  in Eq. (46b) on the enhanced FE space, see [39, 40] for a patch recovery technique denoted by an additional subscript  $r$ . As shown in [39], the main idea of the recovery technique is to extrapolate the working solution  $\widehat{\boldsymbol{\xi}}_h$  to an enhanced FE space in such a way that the issue of Galerkin orthogonality with a direct use of  $\widehat{\boldsymbol{\xi}}_h$  can be avoided. As a merit,

this approach does not require any nonlinear calculations and is thus quite efficient. Correspondingly, we have

$$\begin{aligned} E(\widehat{\mathbf{u}}, \mathbf{q}, \widehat{\mathbf{u}}_h, \mathbf{q}_h) &\approx \tilde{E}^2(\widehat{\boldsymbol{\xi}}_{h_r^+}, \widehat{\boldsymbol{\xi}}_h) \\ &:= \frac{1}{2}(\varrho_u(\widehat{\mathbf{u}}_h, \mathbf{q}_h; \widehat{\mathbf{z}}_{h_r^+}) + \varrho_z(\widehat{\mathbf{u}}_h, \mathbf{q}_h, \widehat{\mathbf{z}}_h, \mathbf{y}_h; \widehat{\mathbf{u}}_{h_r^+})). \end{aligned} \quad (58)$$

- **Error estimator 3** (full computation, forwards-in-time): Slightly different to error estimator  $\tilde{E}^1$ , we replace the backwards-in-time dual problem (37)–(39) by the forwards-in-time version (41)–(43). As a result, we have

$$\begin{aligned} E(\widehat{\mathbf{u}}, \mathbf{q}, \widehat{\mathbf{u}}_h, \mathbf{q}_h) &\approx \tilde{E}^3(\widehat{\boldsymbol{\xi}}_{h^+}^*, \widehat{\boldsymbol{\xi}}_h^*) \\ &:= \frac{1}{2}(\varrho_u(\widehat{\mathbf{u}}_h, \mathbf{q}_h; \widehat{\mathbf{z}}_{h^+}^*) + \varrho_z(\widehat{\mathbf{u}}_h, \mathbf{q}_h, \widehat{\mathbf{z}}_h^*, \mathbf{y}_h^*; \widehat{\mathbf{u}}_{h^+}^*)), \end{aligned} \quad (59)$$

where we use the superscript  $*$  introduced in the equations (41)–(43) to indicate the (approximate) forwards-in-time dual problem. For the enhanced solution  $\widehat{\boldsymbol{\xi}}_{h^+}^*$ , full computation is used as described for error estimator  $\tilde{E}^1$ .

- **Error estimator 4** (patch recovery, forwards-in-time): Slightly different to error estimator  $\tilde{E}^2$ , we replace the backwards-in-time dual problem (37)–(39) by the forwards-in-time version (41)–(43). Consequently, we obtain

$$\begin{aligned} E(\widehat{\mathbf{u}}, \mathbf{q}, \widehat{\mathbf{u}}_h, \mathbf{q}_h) &\approx \tilde{E}^4(\widehat{\boldsymbol{\xi}}_{h_r^+}^*, \widehat{\boldsymbol{\xi}}_h^*) \\ &:= \frac{1}{2}(\varrho_u(\widehat{\mathbf{u}}_h, \mathbf{q}_h; \widehat{\mathbf{z}}_{h_r^+}^*) + \varrho_z(\widehat{\mathbf{u}}_h, \mathbf{q}_h, \widehat{\mathbf{z}}_h^*, \mathbf{y}_h^*; \widehat{\mathbf{u}}_{h_r^+}^*)), \end{aligned} \quad (60)$$

where we use the superscript  $*$  introduced in the equations (41)–(43) to indicate the (approximate) forwards-in-time dual problem. As for error estimator  $\tilde{E}^2$  in Eq. (57), the subscript  $r$  in the enhanced solution  $\widehat{\boldsymbol{\xi}}_{h_r^+}^*$  indicates the use of patch recovery [39, 40].

**Remark 15.** Since the evaluation of the higher order remainder term  $\mathcal{R}$  in (50) is rather demanding, for simplicity it is omitted in the above estimators. As a result, the above estimators are actually a linearization of the secant representation (47) by a trapezoidal rule, see also [62, 71].

**Remark 16.** Since the derivation of the forwards-in-time dual problem (41)–(43) is based on a rather rough approximation, i.e. neglecting the effect of error transport, the estimators  $\tilde{E}^3$  and  $\tilde{E}^4$  are not expected to be able to make a good prediction of the exact error. However, they are a comparably cheaper choice to drive an adaptive mesh refinement algorithm. Most importantly, they eliminate the need of storage of the primal solutions over all time steps for the computation of the dual problem. Their effectiveness for an adaptive algorithm will be reported in Section 4.

**Remark 17.** At first glance, it seems that all error estimators presented above do not depend on the enhanced primal internal variables  $\mathbf{q}_{h^+}$  and their dual counterparts  $\mathbf{y}_{h^+}$ . However, this is not the case for  $\tilde{E}^1$  and  $\tilde{E}^3$ , since  $\mathbf{q}_{h^+}$  and  $\mathbf{y}_{h^+}$  do have an impact on the computation of  $\hat{\mathbf{u}}_{h^+}$  and  $\hat{\mathbf{z}}_{h^+}$  due to the coupling of the primal equations (26a) and (26b) and the coupling of the dual equations (40a) and (40b) by definition. Given the fact that the recovery technique delivers a smoothed version of the working solution on an enhanced FE space, the estimators  $\tilde{E}^2$  and  $\tilde{E}^4$  do not depend on  $\mathbf{q}_{h^+}$  and  $\mathbf{y}_{h^+}$ .

**Remark 18.** As an alternative approach, the work [49] presents error estimators in terms of tangent forms rather than residuals.

### 3.6 Adaptive algorithm

In order to adaptively control the discretization error, we adopt Algorithm 1.

Initialization: set the initial mesh  $\mathcal{V}_{h^0}^0$  and adaptive refinement step  $j = 0$ ;  
 Define a stopping criterion  $\tilde{E} \leq TOL$  for the adaptive refinement loop, where  $TOL$  is a user-defined threshold value related to the desired accuracy;

**while**  $\tilde{E} > TOL$  **do**

Solve the primal problem given by the coupled equations (26a) and (26b) on the current mesh;

Solve the coupled dual equations (40a) and (40b) via the FEM on the current mesh;

Approximate the exact solutions using certain recovery technique on an enhanced FE space, see [39, 40];

Compute the error estimator chosen from  $i = 1, \dots, 4$  for (56), (58), (59) and (60) (global and local) via

$$\tilde{E}^i(\hat{\boldsymbol{\xi}}_{h^+}, \hat{\boldsymbol{\xi}}_h) = \sum_{e=1}^{N_{el}} \eta_e^i, \quad (61)$$

where  $\eta_e^i$  denotes the element contributions of the error estimator  $\tilde{E}^i$  and  $N_{el}$  the number of elements;

Adaptive refinement: a fixed quota, here  $\alpha = 5\%$ , of the elements with the largest  $|\eta_e^i|$  is spatially refined, and update the adaptive refinement step  $j \rightarrow j + 1$ .

**end**

**Algorithm 1:** Adaptive algorithm

**Remark 19.** In this work, the global error estimators  $\tilde{E}^i$  are only localized into their element contributions  $\eta_e^i$  as indicated in Eq. (61), see e.g. [71] for further technical details in a similar context. Consequently, this leads to a fixed mesh at all time steps during one adaptive refinement step. Alternatively, those element contributions  $\eta_e^i$  could be further localized into individual time steps, such that dynamic meshes apply for different time steps, see e.g. [62, 48]. As a drawback, this

alternative approach requires an additional transfer of all variables  $\widehat{\xi}_h$  in Eq. (46b) between nonmatching meshes.

## 4 Numerical examples

In this section, a perforated sheet is investigated as an elastoplastic micromorphic continuum. As shown in Fig. 2a, we consider a quarter model of the sheet, which is stretched by a displacement  $u^{pre} = 0.05$  mm in 1-direction. The indices 1 and 2 represent the horizontal and the vertical direction, respectively. Despite of the time independence of the plasticity under consideration, we introduce a pseudo time axis  $I = [0, 50s]$ . We restrict ourselves to a two-dimensional case using the notations given in Appendix. A plane strain state is assumed, where the third strain component  $\varepsilon_{33}$  implying the strain in the thickness direction is always zero. The material parameters related to the prototype model in Section 2.5 are summarized in Tab. 1. The adaptive FEM starts with the initial mesh  $\mathcal{V}_{h0}$  shown in Fig. 2b, consisting of linear triangular elements. All four error estimators (56), (58), (59) and (60) will be used to drive the adaptive algorithm in Section 3.6, thus leading to four different adaptive procedures. For an effectiveness study of those adaptive procedures, a further comparison with uniform refinements will be done.

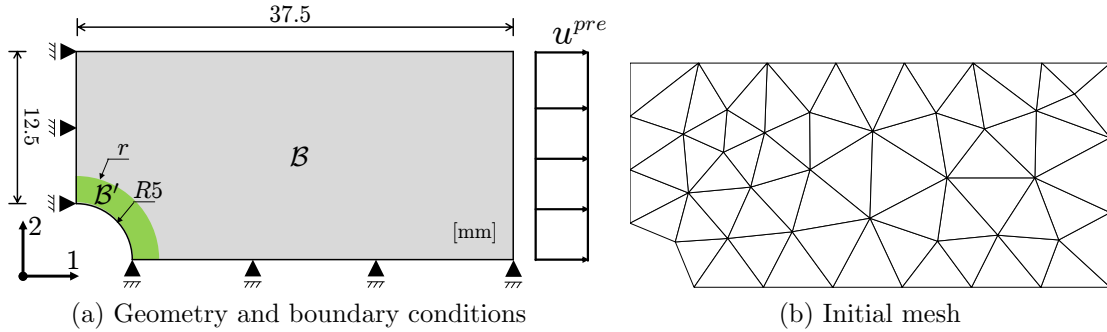


Figure 2: Perforated sheet in micromorphic elastoplasticity

$K$	$G$	$\lambda_s$	$\mu_s$	$\mu_{cs}$	$l$
[MPa]	[MPa]	[MPa]	[MPa]	[MPa]	[mm]
175000	80769	175000	80769	80769	0.1
$\lambda_m$	$\mu_m$	$Y_0$	$H$	$b$	$c$
[MPa]	[MPa]	[MPa]	[MPa]	[-]	[MPa]
175000	80769	312	1551	240	36

Table 1: Summary of material parameters

In the following, we will present three numerical examples of engineering interest,

considering three different types for the quantity of interest  $Q$

$$1. \text{ global:} \quad Q := \int_I \int_{\mathcal{B}} \sigma_{ij} dV dt, \quad (62a)$$

$$2. \text{ local:} \quad Q := \int_I \int_{\mathcal{B}'} \sigma_{ij} dV dt = \int_I \int_{\mathcal{B}} \phi(\mathbf{x}) \sigma_{ij} dV dt, \quad (62b)$$

$$3. \text{ local:} \quad Q := \int_{\mathcal{B}'} \sigma_{ij,T} dV, \quad (62c)$$

respectively, with a regularization function

$$\phi(\mathbf{X}) = \begin{cases} 1, & \text{if } \mathbf{X} \in \mathcal{B}', \\ 0, & \text{otherwise.} \end{cases} \quad (63)$$

Here  $\sigma_{ij}$  represents a certain coefficient of the stress tensor  $\boldsymbol{\sigma}$ . Further,  $\mathcal{B}'$  is a local domain out of the whole domain  $\mathcal{B}$ , i.e. the green area marked in Fig. 2a, with  $r = 8$  mm, while the subscript  $T = 50$ s in Eq. (62c) represents the dependence on the final time. Clearly, all quantities of interest (62a)–(62c) are concerned with stresses, which are of engineering interest. Moreover, (62a) represents a global quantity of interest, while its two different local versions (62b) and (62c) demonstrate the power of the goal-oriented adaptivity in a more convincing manner. Additionally, the switch between global and local quantities of interest is beneficial for a profound understanding of the proposed error estimators as will be shown below.

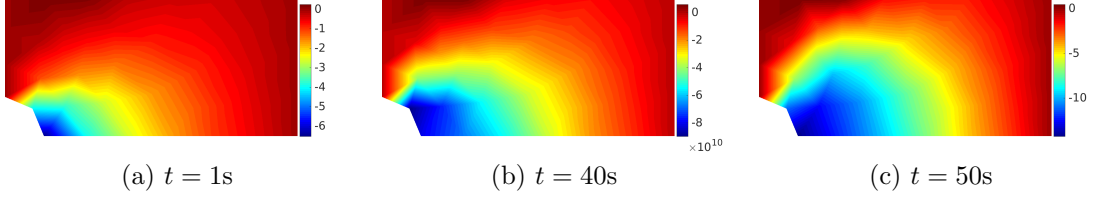
#### 4.1 Example 1: Global quantity of interest

This example deals with the global quantity of interest defined in Eq. (62a), with the choice  $i = j = 1$ . As Eq. (62a) considers the whole time interval  $I$ , both error generation and error transport take place. The computations are performed by a dG(0) time discretization with  $N = 50$  equidistant time steps, as described in the sections 2.4 and 3.2. As already stated in Section 3.4, neglecting the temporal discretization error, we focus merely on the spatial discretization error.

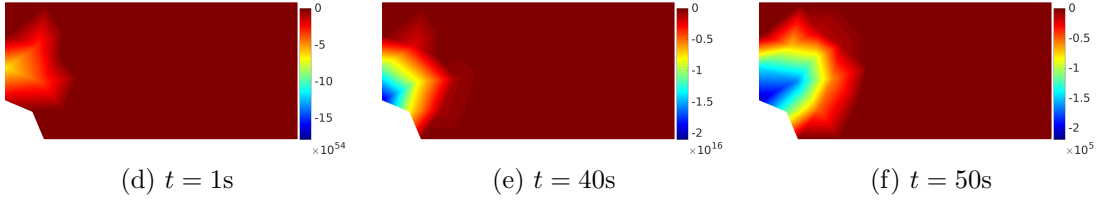
Following the notations (A.2) and (A.4) and adding a subscript  $h$  for FE solutions, the dual displacement  $\hat{z}_{h,1}$  and the dual equivalent plastic strain  $y_{h,6}$  performed on the initial mesh in Fig. 2b are shown in Figs. 3a–3c and 3d–3f for several different time steps, respectively. They are obtained from the backwards-in-time dual problem (37)–(39). Most importantly, the dual equivalent plastic strain  $y_{h,6}$  evolves backwards in time from Fig. 3f to Fig. 3e, where a large accumulation can be observed. The dual displacements  $\hat{z}_{h,1}$  in Figs. 3a–3c also differ from each other. For comparison, the counterparts  $\hat{z}_{h,1}^*$  and  $y_{h,6}^*$  obtained from the forwards-in-time dual problem (41)–(43) are shown in Figs. 3g–3i and 3j–3l for several different time steps, respectively. One may clearly observe that the results in Figs 3i and 3l for the last time step ( $t = 50$ s) coincide with those in Figs. 3c and 3f, respectively. This is because no transport effect has to be considered by the backwards-in-time dual problem for the last time step  $n = N$ , as revealed in the equations (37a) and (37b). In contrast to  $y_{h,6}$ ,  $y_{h,6}^*$  does not account for error transport (also for other time steps  $n \neq N$ ) and decreases to zero for  $t = 1$  s in Fig. 3j. Due to the same

reason, the distribution of  $\widehat{z}_{h,1}^*$  in Fig. 3h largely differs from that of  $\widehat{z}_{h,1}$  in Fig. 3b for  $t = 40$ s. Interestingly, due to the purely elastic stage where no transport effect takes place,  $\widehat{z}_{h,1}^*$  in Fig. 3g coincides with  $\widehat{z}_{h,1}$  in Fig. 3a for  $t = 1$ s.

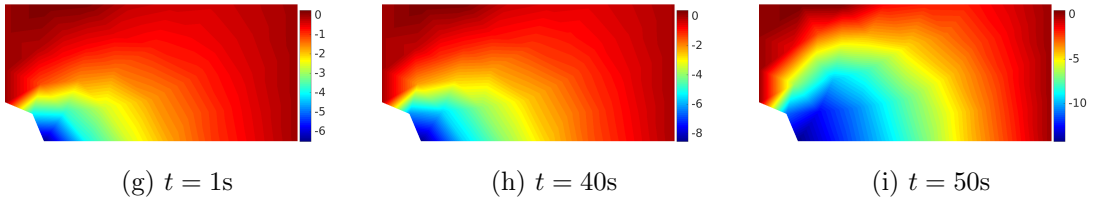
Dual displacement  $\widehat{z}_{h,1}$  on the initial mesh (backwards in time)



Dual equivalent plastic strain  $y_{h,6}$  on the initial mesh (backwards in time)



Approximate dual displacement  $\widehat{z}_{h,1}^*$  on the initial mesh (forwards in time)



Approximate dual equivalent plastic strain  $y_{h,6}^*$  on the initial mesh (forwards in time)

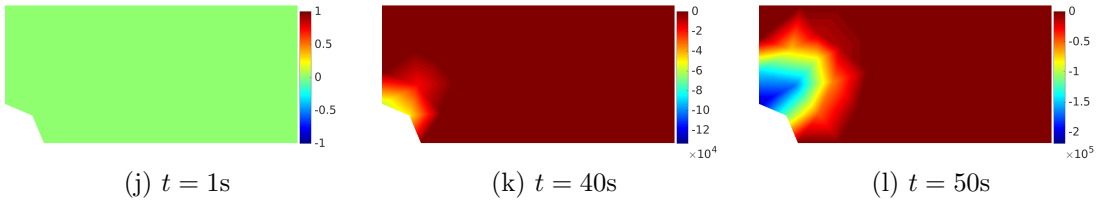
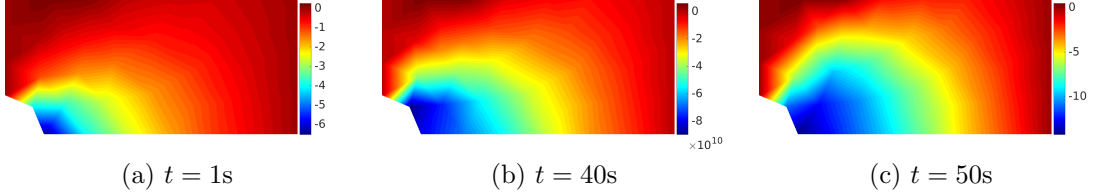


Figure 3: Example 1: Comparison between the backwards-in-time and the approximate forwards-in-time dual problem

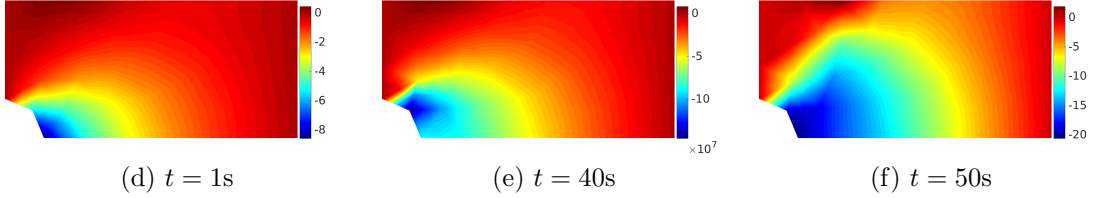
In Fig. 4, three different versions of the backwards-in-time solution  $\widehat{z}_1$  are compared with each other for three different time steps of the initial adaptive step: 1. the working solution  $\widehat{z}_{h,1}$  in Eq. (46b) computed on the current (linear) mesh, 2. the enhanced solution  $\widehat{z}_{h^+,1}$  obtained by full computation (55) on a corresponding quadratic mesh and 3. the enhanced solution  $\widehat{z}_{h_r^+,1}$  obtained by patch recovery (57) on a corresponding quadratic mesh. The distributions of  $\widehat{z}_{h,1}$  in Figs. 4a–4c are the same as in Figs. 3a–3c. The enhanced solution  $\widehat{z}_{h^+,1}$  in Figs. 4d–4f somewhat

differs from the working one  $\widehat{z}_{h,1}$  in Figs. 4a–4c. By comparing Figs. 4g–4i with Figs. 4a–4c, we may see that, based on the same quadratic mesh as for  $\widehat{z}_{h^+,1}$ , patch recovery delivers a smoothed version of  $\widehat{z}_{h,1}$ , i.e.  $\widehat{z}_{h^r^+,1}$ .

Dual displacement  $\widehat{z}_{h,1}$  on the initial (linear) mesh



Dual displacement  $\widehat{z}_{h^+,1}$  on the enhanced (quadratic) initial mesh by full computation



Dual displacement  $\widehat{z}_{h^r^+,1}$  on the enhanced (quadratic) initial mesh by patch recovery

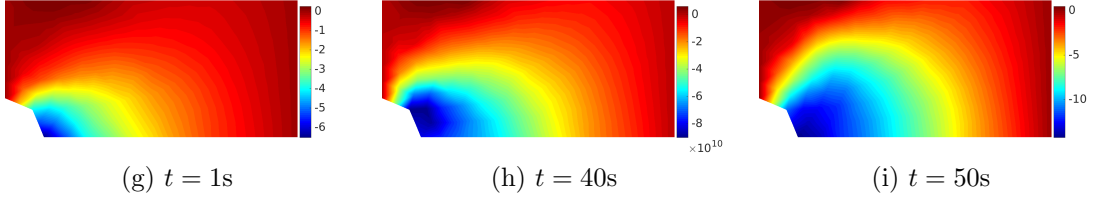


Figure 4: Example 1: Comparison between three different dual solutions

Fig. 5 shows the adaptively refined meshes driven by the four error estimators (56), (58), (59) and (60). Clearly, different error estimators  $\tilde{E}^i$  lead to (more or less) different refinement patterns. Moreover, the two estimators  $\tilde{E}^2$  and  $\tilde{E}^4$  based on patch recovery (57) commonly lead to a shear-band like pattern at the end of the refinements, see Figs. 5f and 5l, which is not the case for  $\tilde{E}^1$  and  $\tilde{E}^3$ . At this point, it is still difficult to judge which pattern is more effective for the adaptive refinements, since it heavily depends on what quantity of interest  $Q$  is chosen. Hence, for an effectiveness study, a comparison w.r.t. error reduction will be shown below. Furthermore, it is interesting to see the local error distributions of  $|\eta_e^i|$  in Eq. (61), which result into the locally refined meshes in Fig. 5. These are depicted in Fig. 6 for localization of different error estimators  $\tilde{E}^i$ , respectively. We observe that all four local indicators  $|\eta_e^i|$  are balanced and strongly reduced in the course of adaptive refinements. By a comparison between Figs. 6a–6c and Figs. 6d–6f or a comparison between Figs. 6g–6i and Figs. 6j–6l, we see that patch recovery (57) tends to deliver a higher value of  $|\eta_e^i|$  than full computation (55). By a comparison between Figs. 6a–6c and Figs. 6g–6i or a comparison between Figs. 6d–6f and Figs.

6j–6l, the forwards-in-time dual problem (41)–(43) appears to deliver a much lower value for  $|\eta_e^i|$  than the backwards-in-time dual problem (37)–(39).

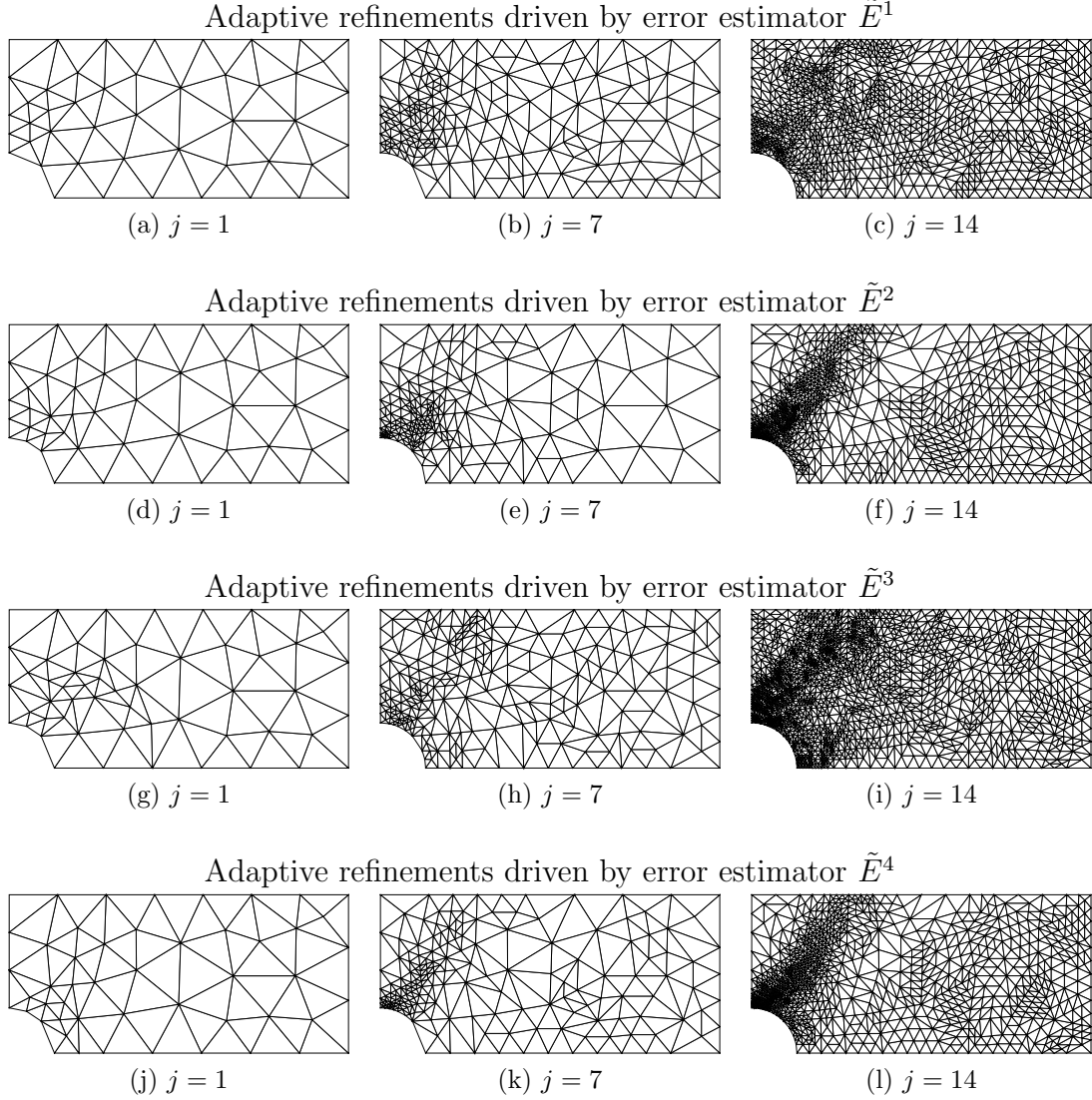


Figure 5: Example 1: Adaptively refined meshes

For an effectiveness study, we introduce an accurate estimate of the exact global error  $E^{i,j}$  in Eq. (44), called the *actual error*  $\hat{E}^{i,j}$ , as

$$E^{i,j} = Q - Q_h^{i,j} \approx Q_{ref} - Q_h^{i,j} =: \hat{E}^{i,j}, \quad i = 1, \dots, 4, \quad j = 0, 1, \dots, N_s. \quad (64)$$

Here  $Q_h^{i,j}$  represents the quantity of interest computed on the current ( $j$ -th) mesh, where the superscript  $i$  corresponds to error estimators  $\tilde{E}^i$  and  $N_s$  denotes the number of adaptive refinement steps. Furthermore,  $Q_{ref}$  represents a reference solution, which is independent of  $i$  and  $j$ . It is obtained by using a mesh that is refined uniformly once from the last adaptive mesh (here by  $\tilde{E}^1$  shown in Fig. 5c). Additionally, we introduce a normalized actual error

$$\hat{E}_{norm}^{i,j} := \left| \frac{\hat{E}^{i,j}}{Q_{ref}} \right|, \quad (65)$$

and a normalized error estimator

$$\tilde{E}_{norm}^{i,j} := \left| \frac{\tilde{E}^{i,j}}{Q_{ref}} \right|, \quad (66)$$

respectively. Fig. 7 gives a comparison between four different adaptive procedures based on different error estimators (56), (58), (59) and (60) and a uniform refinement procedure. As the uniform refinement procedure renders a new sequence of refined meshes, the equations (64) and (65) become in this case

$$E^{uni,j'} = Q - Q_h^{uni,j'} \approx Q_{ref} - Q_h^{uni,j'} =: \hat{E}^{uni,j'}, \quad (67)$$

$$\hat{E}_{norm}^{uni,j'} := \left| \frac{\hat{E}^{uni,j'}}{Q_{ref}} \right|, \quad (68)$$

respectively, where the superscript  $j' = 0, 1, \dots, N_s^u$  denotes uniform refinement steps with an initial step  $j' = 0$ . For our convenience, the superscripts  $j$  and  $j'$  for refinement steps will be omitted hereafter. Fig. 7a shows  $Q$  for these procedures versus the number of DoFs. In Fig. 7b, the normalized actual errors  $\hat{E}_{norm}^i$  and  $\tilde{E}_{norm}^i$  are plotted. All four adaptive procedures perform very well in view of an error reduction, and converge always much faster than uniform refinements. Although  $\tilde{E}^3$  and  $\tilde{E}^4$  are not expected to give a good prediction in Remark 16, the adaptive procedure based on  $\tilde{E}^4$  performs as well as those based on  $\tilde{E}^1$  and  $\tilde{E}^2$ , while the adaptive procedure based on  $\tilde{E}^3$  shows a clear advantage.

Furthermore, in Fig. 8, we study the prediction qualities of different estimators  $\tilde{E}^i$  by a comparison with corresponding actual errors  $\hat{E}^i$ . For comparability, both normalized quantities  $\tilde{E}_{norm}^i$  in Eq. (65) and  $\hat{E}_{norm}^i$  in Eq. (66) are depicted, where error estimators based on a backwards-in-time and a forwards-in-time dual problem are separated for clarity. From Fig. 8a we can see that both  $\tilde{E}^1$  and  $\tilde{E}^2$  overestimate the values of the actual errors  $\hat{E}^1$  and  $\hat{E}^2$ , respectively, however, are able to reproduce the decreasing trends of the actual errors. With increasing adaptive refinements,  $\tilde{E}^1$  and  $\tilde{E}^2$  both become more accurate. This is reasonable, because the enhanced solutions are also getting closer to the exact ones with increasing adaptive refinements. Moreover,  $\tilde{E}^1$  performs better than  $\tilde{E}^2$  as expected, because more accurate enhanced solutions (by full computation) are used for  $\tilde{E}^1$ . In addition, 92.9% of estimates made by  $\tilde{E}^1$  (13 out of 14 adaptive steps) correctly predict the sign of the actual error  $\hat{E}^1$ , while the correctness ratio of  $\tilde{E}^2$  is 100%. From Fig. 8b we observe that both  $\tilde{E}^3$  and  $\tilde{E}^4$  render values of the order of the actual errors  $\hat{E}^3$  and  $\hat{E}^4$ , respectively, however, fail to reproduce the decreasing trends of the actual errors. Additionally, only 14.3% of estimates made by  $\tilde{E}^3$  (2 out of 14 adaptive steps) correctly predict the sign of the actual error  $\hat{E}^3$ , while the correctness ratio of  $\tilde{E}^4$  is 100%. In summary, for a reliable prediction of the actual error, the backwards-in-time dual problem (37)–(39) is required.

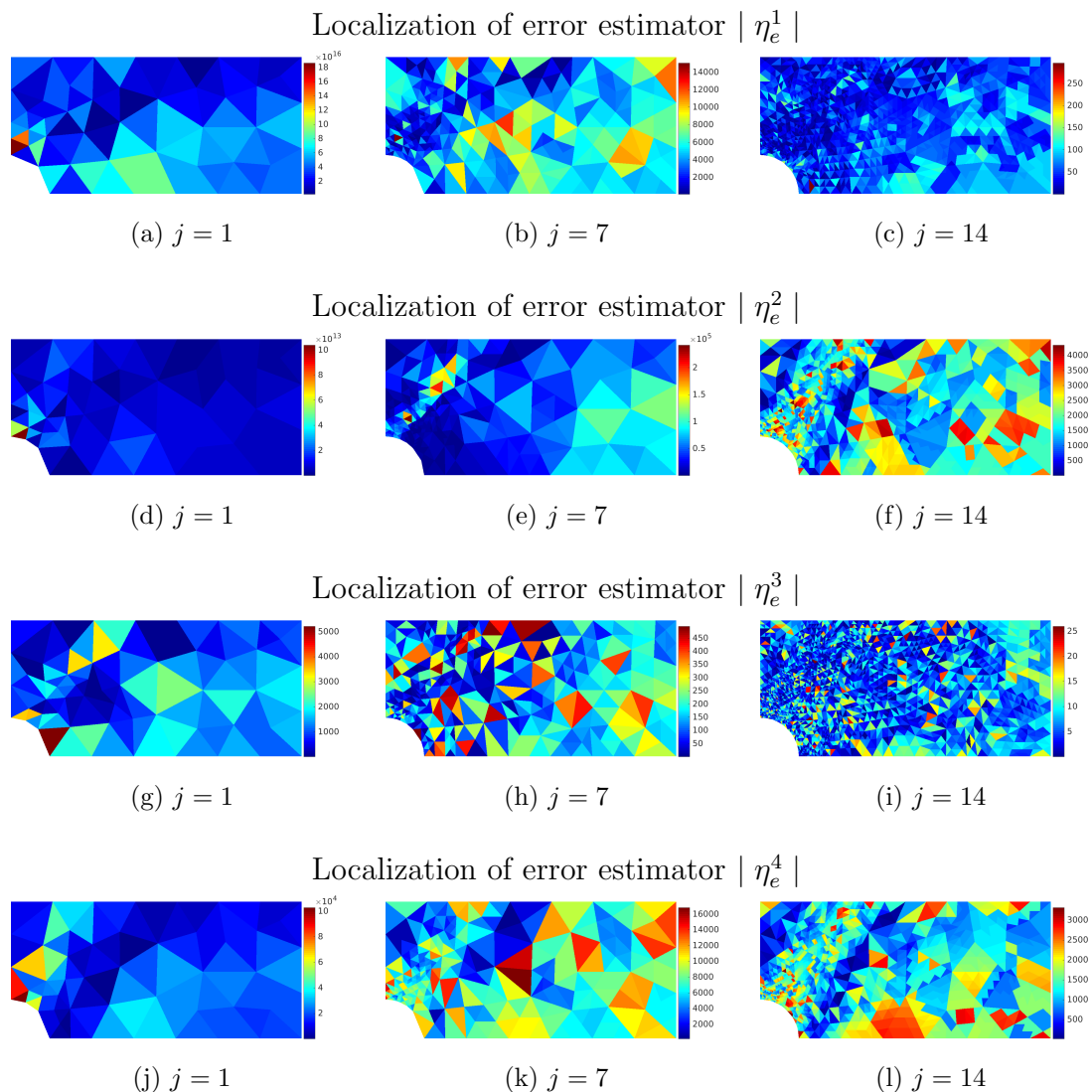
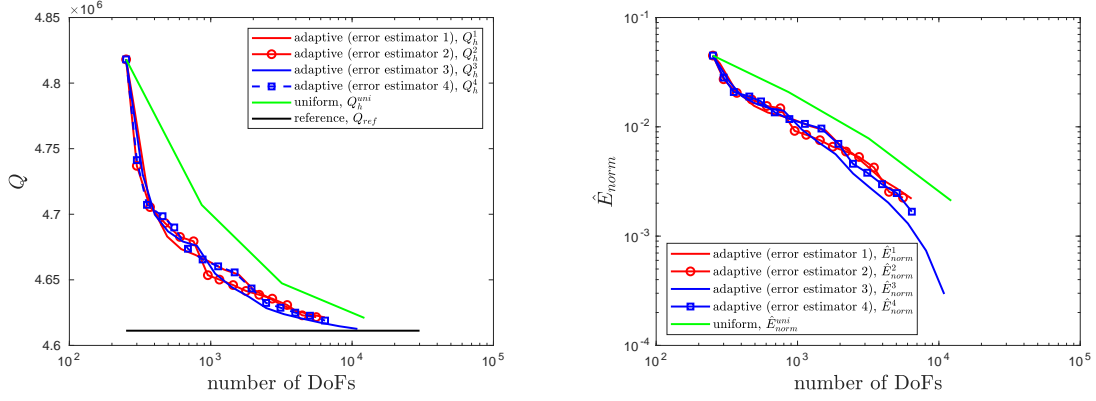


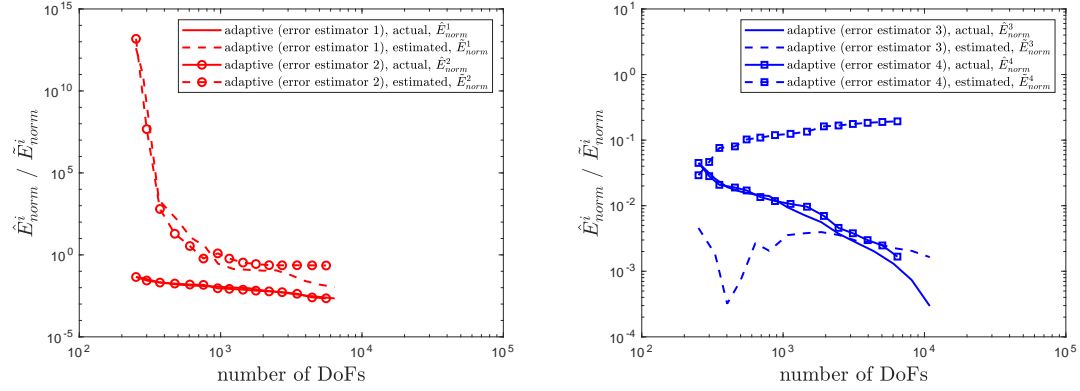
Figure 6: Example 1: Local error indicators  $|\eta_e^i|$

Finally, we study the accumulative characters of the four error estimators (56), (58), (59) and (60). As they contain residuals with time integrals, they are practically evaluated by a sum over time steps as indicated in the equations (18) and (35a). Fig. 9 shows how this is done in a forwards-in-time manner for different error estimators  $\tilde{E}^i$  for the final adaptive step  $N_s = 14$ , where the sign is also considered. For  $\tilde{E}^1$ , the accumulation effect becomes more obvious for the later time steps where the dissipation effect (plasticity) takes place, whereas the accumulation effect of  $\tilde{E}^3$  is much weaker than for  $\tilde{E}^1$ . This is quite reasonable, because the backwards-in-time error estimator  $\tilde{E}^1$  accounts for the additional effect of error transport, which largely contributes to the total error accumulation. As may be observed from  $\tilde{E}^2$  and  $\tilde{E}^4$ , patch recovery (57) leads to much larger values than full computation (55).



(a) Quantities of interest  $Q_h^i$ ,  $Q_h^{uni}$  and  $Q_{ref}$       (b) Normalized actual errors  $\hat{E}_{norm}^i$  and  $\hat{E}_{norm}^{uni}$

Figure 7: Example 1: Comparison between different refinement procedures



(a) Backwards-in-time error estimators  $\tilde{E}^1$  and  $\tilde{E}^2$       (b) Forwards-in-time error estimators  $\tilde{E}^3$  and  $\tilde{E}^4$

Figure 8: Example 1: Comparison between the estimated error  $\tilde{E}^i$  and the actual error  $\hat{E}^i$  for different adaptive refinements

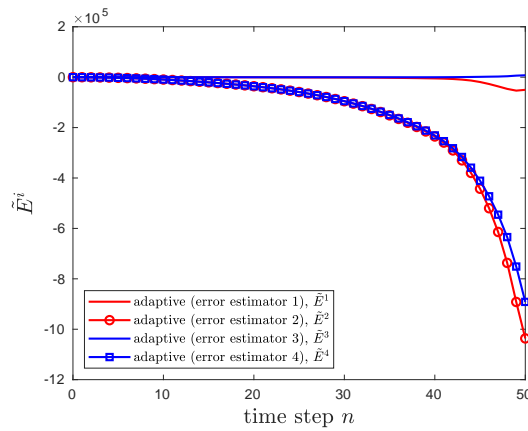


Figure 9: Example 1: Error accumulation over time for different error estimators  $\tilde{E}^i$  on the final adaptive step  $N_s = 14$

## 4.2 Example 2: Spatially local quantity of interest

This example deals with the local quantity of interest defined in Eq. (62b), with the choice  $i = j = 1$ . As Eq. (62b) considers the whole time interval  $I$ , both error generation and error transport take place. The computations are performed by a dG(0) time discretization with  $N = 50$  equidistant time steps, as described in the sections 2.4 and 3.2. As already stated in Section 3.4, neglecting the temporal discretization error, we focus merely on the spatial discretization error. This example differs from Example 1 in Section 4.1 only by the fact that the quantity of interest (62b) involves the volume integral in a local sense on  $\mathcal{B}'$ , resulting into totally different dual solutions as shown in Fig. 10. Compared to Figs. 3a–3f, both the dual displacement  $\widehat{z}_{h,1}$  and the dual equivalent plastic strain  $y_{h,6}$  for the backwards-in-time dual problem (37)–(39) on the initial mesh in Fig. 2b evolve in a different way as shown in Figs. 10a–10f. As the quantity of interest  $Q$  is now switched to a local domain  $\mathcal{B}'$ , the active area of  $y_{h,6}$  also becomes somewhat smaller in Figs. 10d–10f. Furthermore, the counterparts  $\widehat{z}_{h,1}^*$  and  $y_{h,6}^*$  obtained from the forwards-in-time dual problem (41)–(43) are shown in Figs. 10g–10i and Figs. 10j–10l for several different time steps, respectively. When compared with Figs. 3a–3f for the backwards-in-time dual problem (37)–(39), similar effects already discussed in Example 1 can be seen. Most importantly, the evolution of  $y_{h,6}^*$  shown in Figs. 10j–10l clearly illustrates that the forwards-in-time dual problem (41)–(43) does not account for error transport. Indeed, when viewed backwards in time,  $y_{h,6}^*$  decreases to zero in Fig. 10j for  $t = 1$ s.

As done for Example 1, all four error estimators (56), (58), (59) and (60) are individually used to drive the adaptive algorithm in Section 3.6. Fig. 11 shows four different sequences of adaptively refined meshes driven by these error estimators. Obviously, different error estimators  $\widetilde{E}^i$  lead to different refinement patterns. However, they do show a common feature that the refinements are mainly located in the local domain  $\mathcal{B}'$ , such that the shape of  $\mathcal{B}'$  becomes recognizable at the end of the refinements, especially for the error estimators  $\widetilde{E}^1$  and  $\widetilde{E}^3$  based on full computation (55). Unlike the results of Example 1 (e.g. Figs 5f and 5l), a shear-band like pattern is not observed in Fig. 11. This confirms again that the refinement pattern heavily depends on the choice of the quantity of interest  $Q$ . In Fig. 12, the corresponding local error distributions of  $|\eta_e^i|$  in Eq. (61) are depicted for localization of different error estimators  $\widetilde{E}^i$ , respectively. We observe that all four local indicators  $|\eta_e^i|$  are balanced and strongly reduced in the course of adaptive refinements. When we do a similar comparison between the results in Fig. 12 as for Example 1, the following statements of Example 1 are also supported here: 1. patch recovery (57) tends to deliver a higher value of  $|\eta_e^i|$  than full computation (55) and 2. the forwards-in-time dual problem (41)–(43) appears to deliver a much lower value of  $|\eta_e^i|$  than the backwards-in-time dual problem (37)–(39).

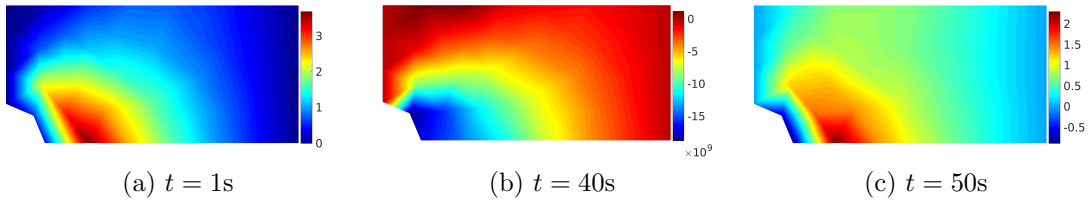
For an effectiveness study, a comparison between four different adaptive procedures based on different error estimators (56), (58), (59) and (60) and a uniform refinement procedure is given in Fig. 13. Fig. 13a shows  $Q$  for these procedures versus the number of DoFs, while Fig. 13b depicts the normalized actual errors  $\widehat{E}_{norm}^i$  in Eq. (65) and  $\widehat{E}_{norm}^{uni}$  in Eq. (68). While all four adaptive procedures perform a much faster convergence rate than the uniform refinement procedure, their progress is not as smooth as that of Example 1 in Fig. 7b. This is due to the fact

that the local domain  $\mathcal{B}'$  is not exactly reproduced by the FE discretizations and the reproduction quality changes in the course of the adaptive refinements.

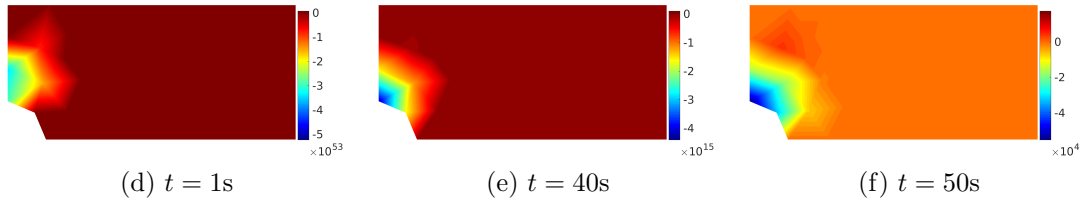
Furthermore, in Fig. 14, we study the prediction qualities of different estimators  $\tilde{E}^i$  by a comparison with corresponding actual errors  $\hat{E}^i$ . For comparability, both normalized quantities  $\tilde{E}_{norm}^i$  in Eq. (65) and  $\tilde{E}_{norm}^i$  in Eq. (66) are depicted, where error estimators based on a backwards-in-time and a forwards-in-time dual problem are separated for clarity. From Fig. 14a we see that both  $\tilde{E}^1$  and  $\tilde{E}^2$  overestimate the values of the actual errors  $\hat{E}^1$  and  $\hat{E}^2$ , respectively, however, are able to reproduce the decreasing trends of the actual errors. With increasing adaptive refinements,  $\tilde{E}^1$  and  $\tilde{E}^2$  both become more accurate. Moreover,  $\tilde{E}^1$  performs better than  $\tilde{E}^2$ . In addition, 92.9% of estimates made by  $\tilde{E}^1$  (13 out of 14 adaptive steps) correctly predict the sign of the actual error  $\hat{E}^1$ , while the correctness ratio of  $\tilde{E}^2$  remains the same (92.9%). From Fig. 14b we observe that both  $\tilde{E}^3$  and  $\tilde{E}^4$  render values of the order of the actual errors  $\hat{E}^3$  and  $\hat{E}^4$ , respectively, however, fail to reproduce the decreasing trends of the actual errors. Additionally, only 35.7% of estimates made by  $\tilde{E}^3$  (5 out of 14 adaptive steps) correctly predict the sign of the actual error  $\hat{E}^3$ , while the correctness ratio of  $\tilde{E}^4$  is 100%. It is thus evident that the backwards-in-time dual problem (37)–(39) provides a more reliable estimate of actual errors than the forwards-in-time dual problem (41)–(43).

Finally, we study the accumulative characters of the four error estimators (56), (58), (59) and (60). As done for Example 1, Fig. 15 shows the accumulation of different error estimators  $\tilde{E}^i$  over time in a forwards-in-time manner for the final adaptive step  $N_s = 14$ . For  $\tilde{E}^1$ , the accumulation effect becomes more obvious for the later time steps where the dissipation effect (plasticity) takes place, whereas the accumulation effect of  $\tilde{E}^3$  is much weaker than that of  $\tilde{E}^1$ . This is quite reasonable, because the backwards-in-time error estimator  $\tilde{E}^1$  accounts for the additional effect of error transport, which largely contributes to the total error accumulation. As may be observed from  $\tilde{E}^2$  and  $\tilde{E}^4$ , patch recovery (57) leads to much larger values than full computation (55). These are actually the same observations as obtained for Example 1. As the quantity of interest  $Q$  involves the local domain  $\mathcal{B}'$  rather than the whole domain  $\mathcal{B}$ , the absolute values of  $\tilde{E}^i$  are comparably small.

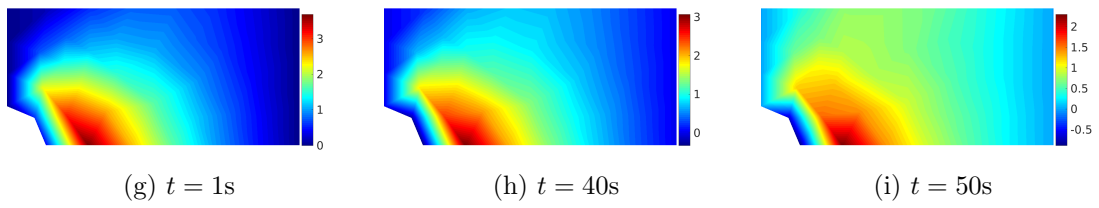
Dual displacement  $\widehat{z}_{h,1}$  on the initial mesh (backwards in time)



Dual equivalent plastic strain  $y_{h,6}$  on the initial mesh (backwards in time)



Approximate dual displacement  $\widehat{z}_{h,1}^*$  on the initial mesh (forwards in time)



Approximate dual equivalent plastic strain  $y_{h,6}^*$  on the initial mesh (forwards in time)

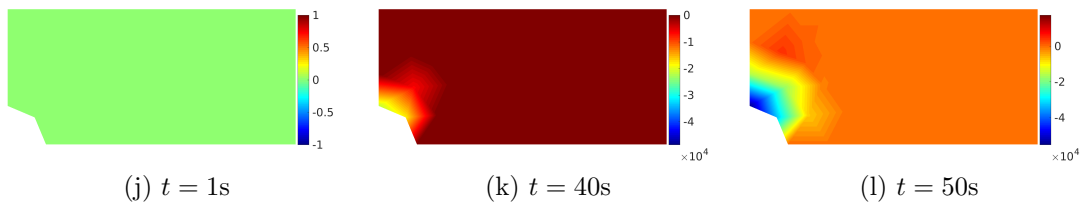


Figure 10: Example 2: Comparison between the backwards-in-time and the approximate forwards-in-time dual problem

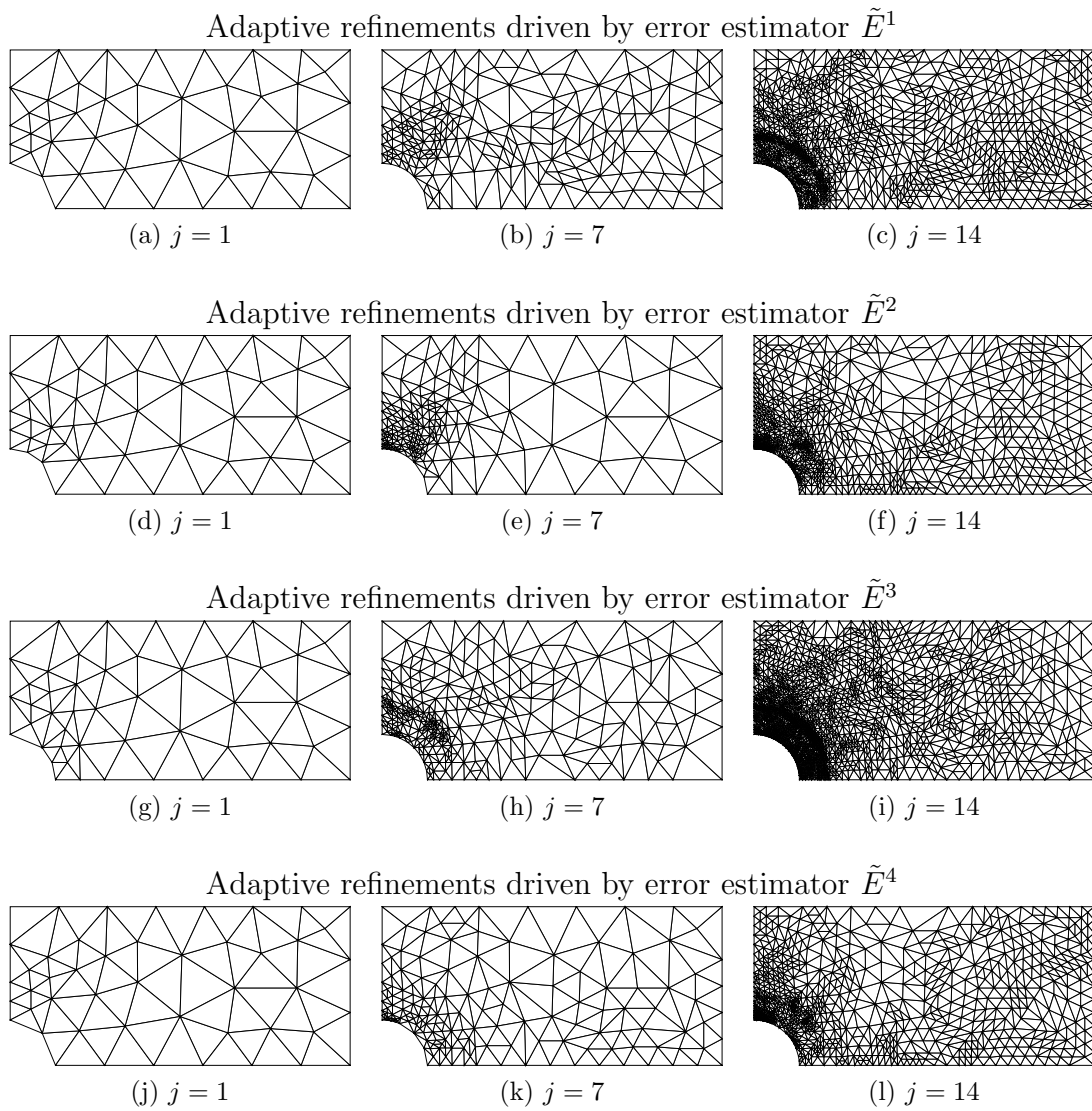


Figure 11: Example 2: Adaptively refined meshes

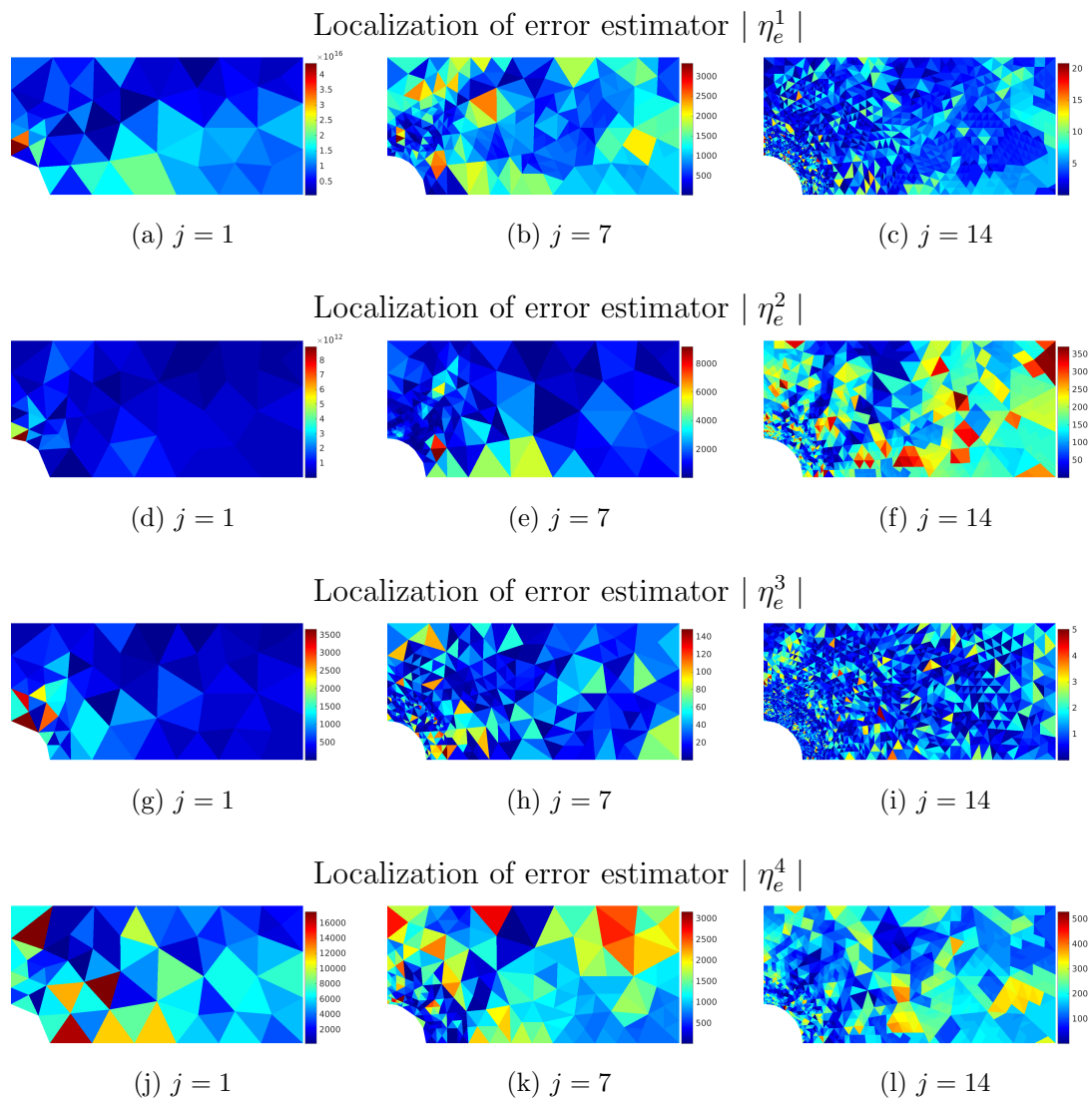


Figure 12: Example 2: Local error indicators  $|\eta_e^i|$

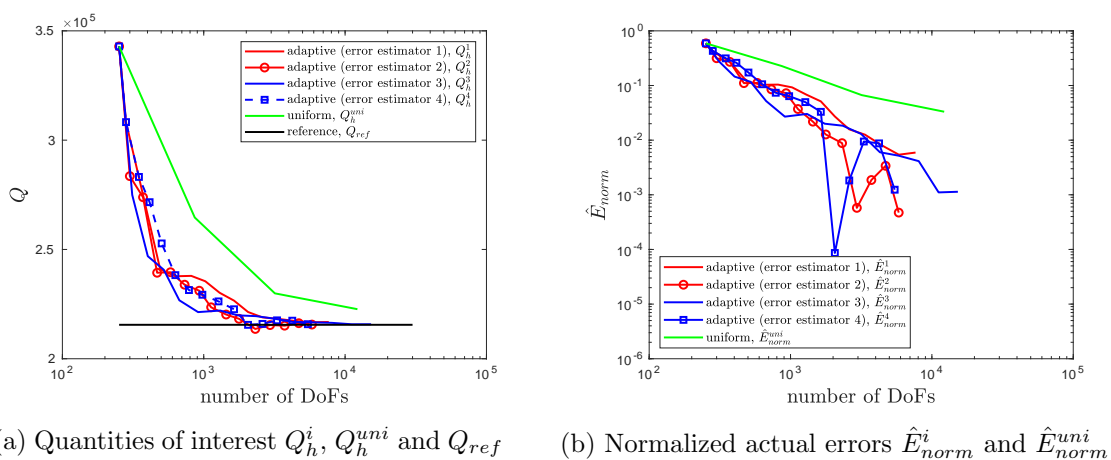
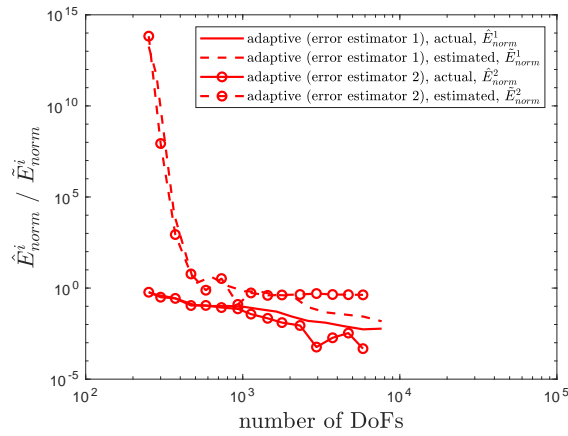
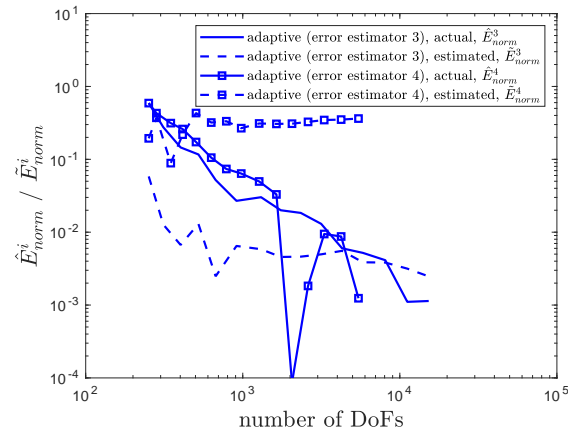


Figure 13: Example 2: Comparison between different refinement procedures



(a) Backwards-in-time error estimators  $\tilde{E}^1$  and  $\tilde{E}^2$



(b) Forwards-in-time error estimators  $\tilde{E}^3$  and  $\tilde{E}^4$

Figure 14: Example 2: Comparison between the estimated error  $\tilde{E}^i$  and the actual error  $\hat{E}^i$  for different adaptive refinements

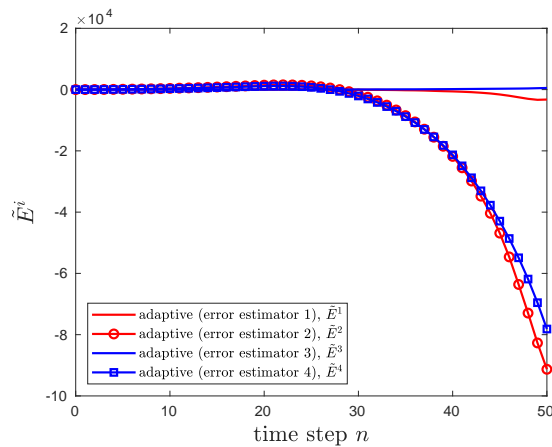


Figure 15: Example 2: Error accumulation over time for different error estimators  $\tilde{E}^i$  on the final adaptive step  $N_s = 14$

### 4.3 Example 3: Spatially and temporally local quantity of interest

This example deals with the local quantity of interest defined in Eq. (62c), with the choice  $i = j = 1$ , where the only difference from Example 2 in Section 4.2 is the switch from a time interval to the final time. This enables us to study (nearly) pure error transport, because error generation only occurs at the final time. The computations are performed by a dG(0) time discretization with  $N = 50$  equidistant time steps, as described in the sections 2.4 and 3.2. As already stated in Section 3.4, neglecting the temporal discretization error, we focus merely on the spatial discretization error. As done for the previous examples 1 and 2, different dual solutions computed on the initial mesh are shown in Fig. 16. Compared to Figs. 10a–10f, both the dual displacement  $\widehat{z}_{h,1}$  and the dual equivalent plastic strain  $y_{h,6}$  for the backwards-in-time dual problem (37)–(39) evolve in a different manner as shown in Figs. 16a–16f. The zero-field of  $\widehat{z}_{h,1}$  at  $t = 1$ s is resulted from the fact that  $Q$  in Eq. (62c) does not involve that time point and the transport terms vanish due to the purely elastic stage. The same results as shown in Figs. 10c and 10f are obtained here in Figs. 16c and 16f for  $t = 50$ s, respectively, since both quantities of interest (62b) and (62c) consider the final state. The further evolution of  $y_{h,6}$  in Figs. 16d and 16e slightly differs from that of Example 2 in Figs. 10d and 10e, because, unlike Example 2, the  $Q$ -related term in the backwards-in-time dual problem (37)–(39) vanishes for time steps  $n < N$  for this example. Furthermore, the counterparts  $\widehat{z}_{h,1}^*$  and  $y_{h,6}^*$  obtained from the forwards-in-time dual problem (41)–(43) are also shown in Figs. 16g–16i and Figs. 16j–16l for several different time steps, respectively. Most strikingly,  $\widehat{z}_{h,1}^*$  and  $y_{h,6}^*$  both become zero for  $t = 1$ s and  $t = 40$ s, since  $Q$  in Eq. (62.3) does not involve those time points and the transport terms are neglected in the forwards-in-time dual problem (41)–(43).

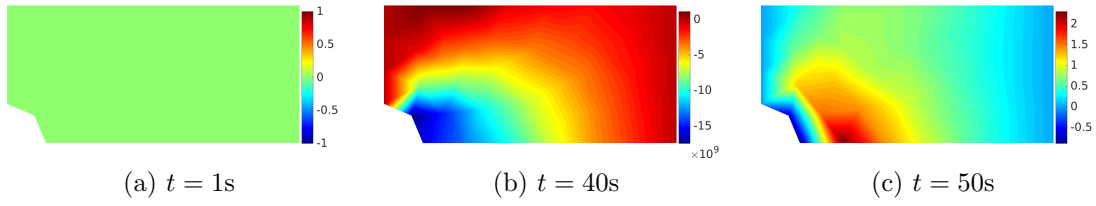
As done for the previous examples 1 and 2, all four error estimators (56), (58), (59) and (60) are individually used to drive the adaptive algorithm in Section 3.6. Fig. 17 shows four different sequences of adaptively refined meshes driven by these error estimators. Not surprisingly, different error estimators  $\widetilde{E}^i$  lead to different refinement patterns. Here, the error estimators  $\widetilde{E}^1$  and  $\widetilde{E}^3$  show a common feature that the refinements are mainly located in the local domain  $\mathcal{B}'$ , such that the shape of  $\mathcal{B}'$  becomes recognizable at the end of the refinements. Similarly to the results of Example 1 in Figs 5f and 5l, a shear-band like pattern is formed by  $\widetilde{E}^2$  and  $\widetilde{E}^4$  as clearly depicted in Figs. 17f and 17l. This confirms again that the refinement pattern heavily depends on the choice of the quantity of interest  $Q$ . In Fig. 18, the corresponding local error distributions of  $|\eta_e^i|$  in Eq. (61) are depicted for localization of different error estimators  $\widetilde{E}^i$ , respectively. We observe that all four local indicators  $|\eta_e^i|$  are balanced and strongly reduced in the course of adaptive refinements. When we do a similar comparison between the results in Fig. 12 as for Example 1, the following statements of Example 1 are supported again: 1. patch recovery (57) tends to deliver a higher value of  $|\eta_e^i|$  than full computation (55) (except for Figs. 18a and 18d) and 2. the forwards-in-time dual problem (41)–(43) appears to deliver a much lower value of  $|\eta_e^i|$  than the backwards-in-time dual problem (37)–(39).

For an effectiveness study, a comparison between four different adaptive procedures based on four different error estimators (56), (58), (59) and (60) and a uniform refinement procedure is given in Fig. 19. Fig. 19a shows  $Q$  for different procedures versus the number of DoFs, while Fig. 19b depicts the normalized actual errors  $\hat{E}_{norm}^i$  in Eq. (65) and  $\hat{E}_{norm}^{uni}$  in Eq. (68). The effectiveness of all four adaptive procedures is clearly observed, despite of its nonsmooth course due to the same reasons stated in Section 4.2. Additionally, the error estimators  $\tilde{E}^3$  and  $\tilde{E}^4$  perform surprisingly well, although they are based on an approximate dual problem, i.e. the forwards-in-time dual problem (41)–(43).

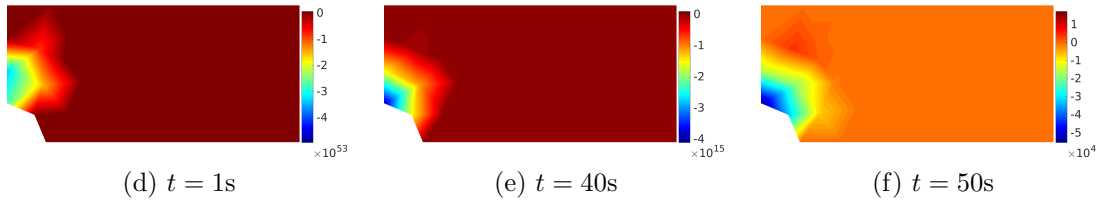
Furthermore, in Fig. 20, we study the prediction qualities of different estimators  $\tilde{E}^i$  by a comparison with corresponding actual errors  $\hat{E}^i$ . For comparability, both normalized quantities  $\hat{E}_{norm}^i$  in Eq. (65) and  $\tilde{E}_{norm}^i$  in Eq. (66) are depicted, where error estimators based on a backwards-in-time and a forwards-in-time dual problem are separated for clarity. From Fig. 20a we see that both  $\tilde{E}^1$  and  $\tilde{E}^2$  overestimate the values of the actual errors  $\hat{E}^1$  and  $\hat{E}^2$ , respectively, however, are able to reproduce the decreasing trends of the actual errors. With increasing adaptive refinements,  $\tilde{E}^1$  and  $\tilde{E}^2$  both become more accurate. Moreover,  $\tilde{E}^1$  performs better than  $\tilde{E}^2$ . In addition, 92.9% of estimates made by  $\tilde{E}^1$  (13 out of 14 adaptive steps) correctly predict the sign of the actual error  $\hat{E}^1$ , while the correctness ratio of  $\tilde{E}^2$  remains the same (92.9%). From Fig. 20b we observe that both  $\tilde{E}^3$  and  $\tilde{E}^4$  render values of the order of the actual errors  $\hat{E}^3$  and  $\hat{E}^4$ , respectively, however, fail to reproduce the decreasing trends of the actual errors. Additionally, only 14.3% of estimates made by  $\tilde{E}^3$  (2 out of 14 adaptive steps) correctly predict the sign of the actual error  $\hat{E}^3$ , while the correctness ratio of  $\tilde{E}^4$  is 100%. As shown by the previous examples 1 and 2, it is evident that the backwards-in-time dual problem (37)–(39) provides a more reliable estimate of actual errors than the forwards-in-time dual problem (41)–(43).

Finally, we study the accumulative characters of the four error estimators (56), (58), (59) and (60). Fig. 21 shows the accumulation of different error estimators  $\tilde{E}^i$  over time in a forwards-in-time manner for the final adaptive step  $N_s = 14$ . The results in Fig. 21 support the same statements made for the previous examples 1 and 2. Most interestingly, there is no accumulation at all before the final time step  $n = N$  for  $\tilde{E}^3$  and  $\tilde{E}^4$  based on the forwards-in-time dual problem (41)–(43), since error transport is not accounted for. In contrast to that, the error accumulation begins much earlier for  $\tilde{E}^1$  and  $\tilde{E}^2$  based on the backwards-in-time dual problem (37)–(39), while error transport due to plasticity occurs.

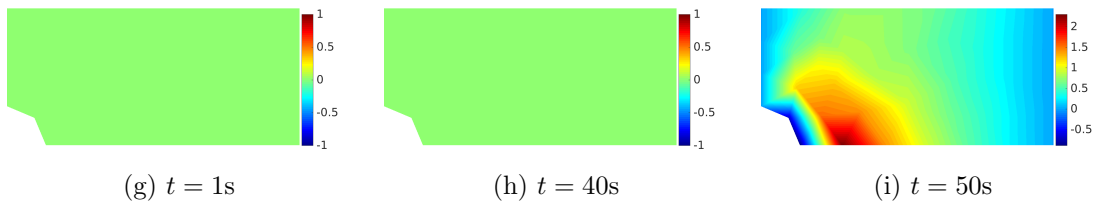
Dual displacement  $\widehat{z}_{h,1}$  on the initial mesh (backwards in time)



Dual equivalent plastic strain  $y_{h,6}$  on the initial mesh (backwards in time)



Approximate dual displacement  $\widehat{z}_{h,1}^*$  on the initial mesh (forwards in time)



Approximate dual equivalent plastic strain  $y_{h,6}^*$  on the initial mesh (forwards in time)

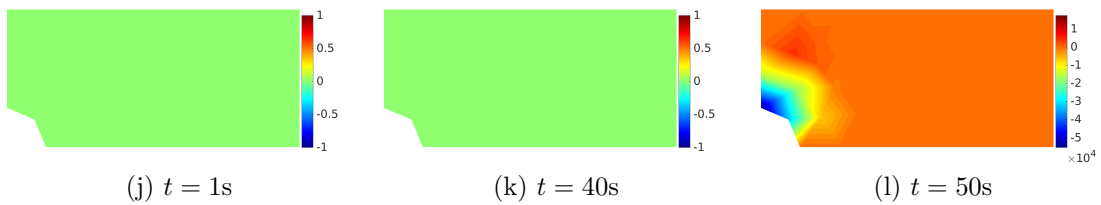
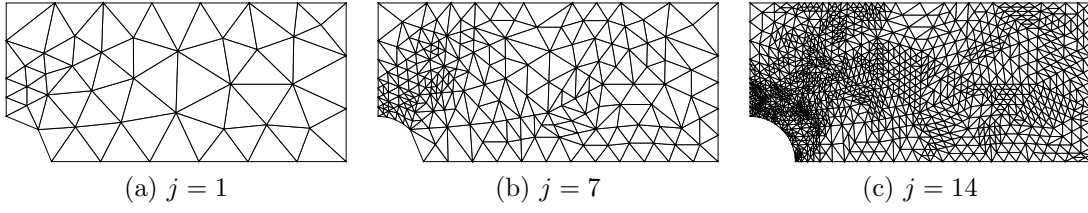
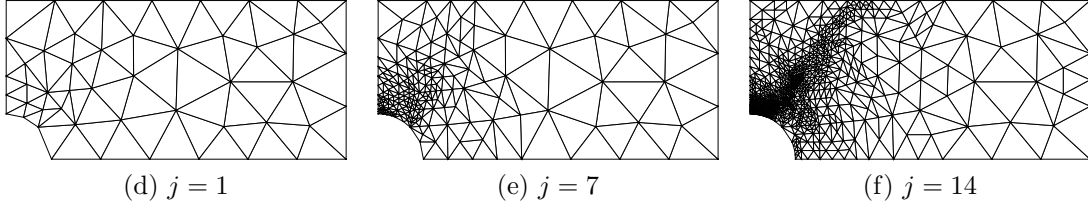


Figure 16: Example 3: Comparison between the backwards-in-time and the approximate forwards-in-time dual problem

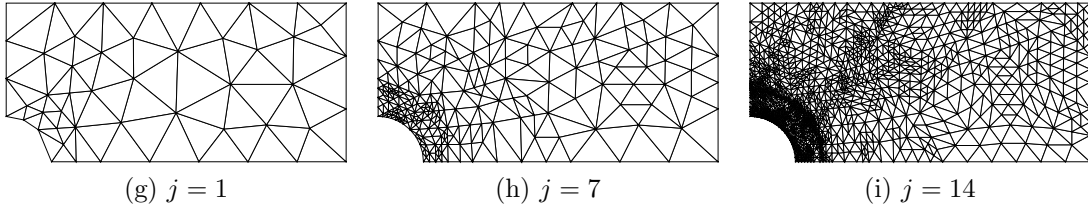
Adaptive refinements driven by error estimator  $\tilde{E}^1$



Adaptive refinements driven by error estimator  $\tilde{E}^2$



Adaptive refinements driven by error estimator  $\tilde{E}^3$



Adaptive refinements driven by error estimator  $\tilde{E}^4$

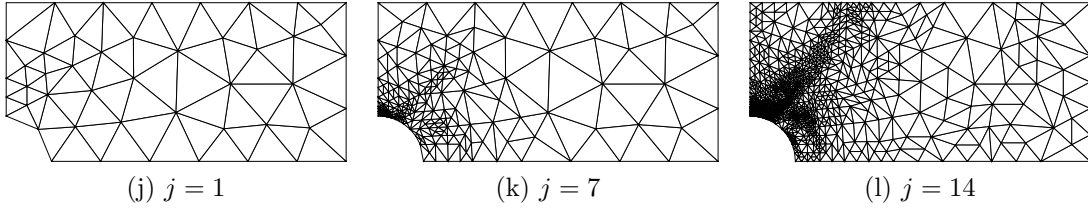


Figure 17: Example 3: Adaptively refined meshes

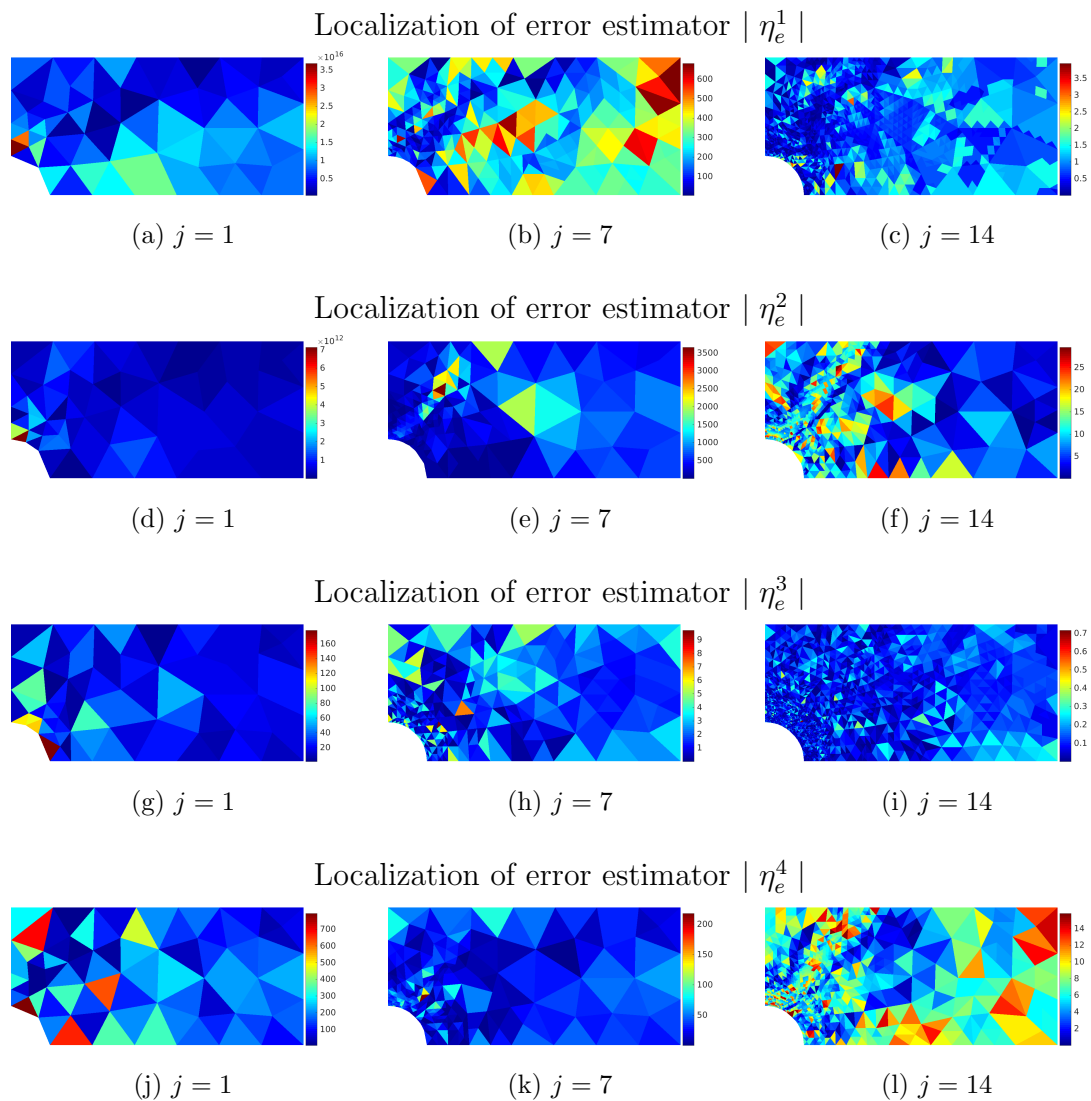


Figure 18: Example 3: Local error indicators  $|\eta_e^i|$

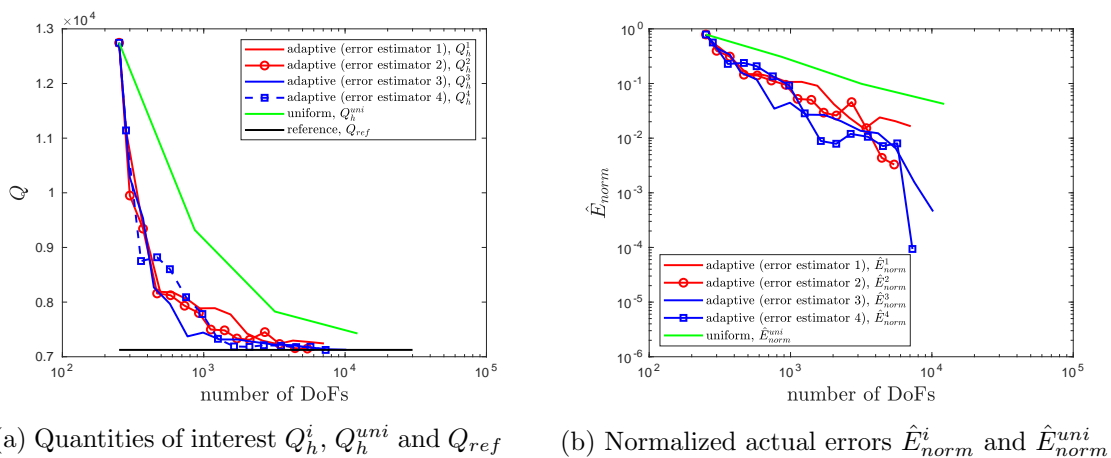
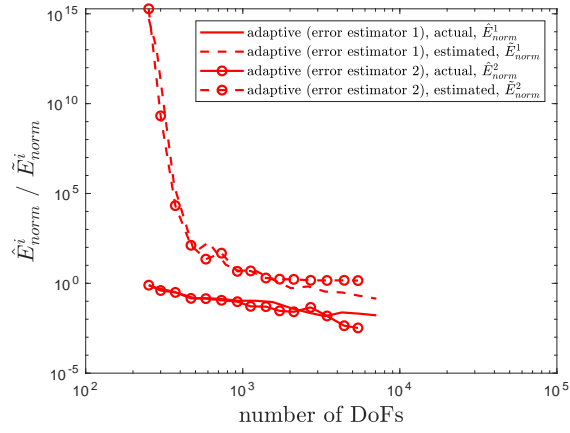
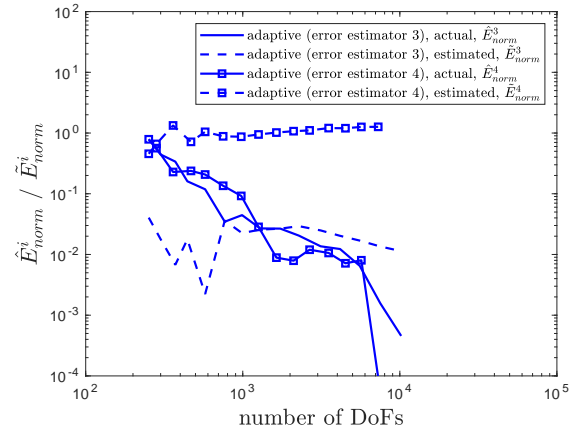


Figure 19: Example 3: Comparison between different refinement procedures



(a) Backwards-in-time error estimators  $\tilde{E}^1$  and  $\tilde{E}^2$



(b) Forwards-in-time error estimators  $\tilde{E}^3$  and  $\tilde{E}^4$

Figure 20: Example 3: Comparison between the estimated error  $\tilde{E}^i$  and the actual error  $\hat{E}^i$  for different adaptive refinements

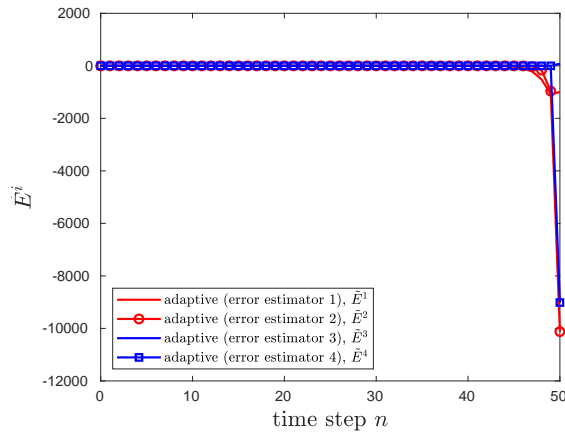


Figure 21: Example 3: Error accumulation over time for different error estimators  $\tilde{E}^i$  on the final adaptive step  $N_s = 14$

## 5 Conclusion and outlook

In this work, we have considered a class of micromorphic plasticity problems as a double multifield formulation, interpreting the whole framework as differential-algebraic equations. The first multifield formulation stems from the nature of micromorphic continua, where we introduce the notion of generalized solution for an abstract setting. The second multifield formulation accounts for local evolution of internal variables, where we adopted a general matrix representation. On this basis, weak forms in a time integration sense have been established for both formulations, respectively. The proposed formulation is less standard in the literature, as it does not alter the practical FE implementation in fact. However, it has been shown to be beneficial to derive a dual problem required for a goal-oriented error estimate. In order to account for the time-dependent character of the underlying problem, a backwards-in-time dual problem has been obtained from the Lagrange method. By means of duality techniques, exact error representations have been derived. Finally, we have proposed four computable error estimators based on a linearization of an exact secant error representation and studied them by several numerical examples w.r.t. a prototype model. These are summarized as follows:

- **Error estimator  $\tilde{E}^1$**  (full computation, backwards-in-time) is a most expensive version based on a backwards-in-time dual problem accounting for both error generation and error transport, where the enhanced solutions are obtained by full computation requiring nonlinear computations on an enhanced FE space. Numerical examples show that this estimator is reliable to drive an adaptive algorithm, while it is also able to mimic the trends of the actual error.
- **Error estimator  $\tilde{E}^2$**  (patch recovery, backwards-in-time) is a computationally cheaper variant of error estimator  $\tilde{E}^1$ , where the full computation is replaced by the patch recovery technique [39, 40] for enhanced solutions. The patch recovery technique avoids the need of nonlinear calculations, and therefore is computationally efficient. Numerical examples show that this estimator is effective to drive an adaptive algorithm, while it is also able to reproduce the trends of the actual error. However, the quantity of the prediction is slightly worse than that of error estimator  $\tilde{E}^1$ .
- **Error estimator  $\tilde{E}^3$**  (full computation, forwards-in-time) is also a variant of error estimator  $\tilde{E}^1$ , where the backwards-in-time dual problem is approximated as a forwards-in-time one by neglecting error transport. As a merit, this reduces much storage requirement for the computation of the dual problem. However, the forwards-in-time dual problem is not designed to account for error transport. Numerical examples show that this estimator performs quite well to drive an adaptive algorithm, whereas its prediction of the actual error is less reliable than error estimators  $\tilde{E}^1$  and  $\tilde{E}^2$ .
- **Error estimator  $\tilde{E}^4$**  (patch recovery, forwards-in-time) is a variant of error estimator  $\tilde{E}^3$ , where the full computation is replaced by the patch recovery technique [39, 40] for enhanced solutions. Obviously, it is the cheapest choice.

Numerical examples show that this estimator performs quite well to drive an adaptive algorithm, whereas its prediction of the actual error is less reliable than error estimators  $\tilde{E}^1$  and  $\tilde{E}^2$ .

As an important advantage, these error estimators are quite simple to implement, since the dual problem preserves a similar structure as the primal one such that many terms and structures of the primal problem can be reused, see also [71].

For an accuracy improvement of the error estimate, a further study on a secant formulation of dual problems is worth mentioning, see e.g. [48] for a time-dependent phase-field problem. Since the way towards a forwards-in-time dual problem is not unique, more effective methods should be developed in future. As this work is merely concerned with the spatial discretization errors, the coupling to time step adaptivity towards a full error analysis would be of our interest as well. Future works will also be directed to the field of parameter identification.

## Acknowledgment

This paper is based on investigations supported by the Deutsche Forschungsgemeinschaft (DFG) under grants MA 1979/17-1 and MA 1979/30-1.

## Appendix. Some notations for a two-dimensional implementation

In the following, we declare some notations used in Section 4. In a two-dimensional case, the primal solution  $\hat{\mathbf{u}}$  in Eq. (17a) practically reduces to a  $(6 \times 1)$ -vector as

$$\hat{\mathbf{u}} = [u_1 \ u_2 \ \bar{H}_{11} \ \bar{H}_{22} \ \bar{H}_{12} \ \bar{H}_{21}]^T. \quad (\text{A.1})$$

By a one-to-one correspondence to Eq. (A.1), we define a  $(6 \times 1)$ -vector as

$$\hat{\mathbf{z}} = [\hat{z}_1 \ \hat{z}_2 \ \hat{z}_3 \ \hat{z}_4 \ \hat{z}_5 \ \hat{z}_6]^T, \quad (\text{A.2})$$

for the dual solution  $\hat{\mathbf{z}}$  in Eq. (35). Consequently, we shall call  $\hat{z}_1$  and  $\hat{z}_2$  dual displacements, while  $\hat{z}_3$ ,  $\hat{z}_4$ ,  $\hat{z}_5$  and  $\hat{z}_6$  are called dual micro deformations. In a similar way, the practical counterparts for the primal internal variables  $\mathbf{q}$  in Eq. (28a) and the dual internal variables  $\mathbf{y}$  in Eq. (35) are defined as

$$\underline{\mathbf{q}} = [\varepsilon_{11}^p \ \varepsilon_{22}^p \ \varepsilon_{33}^p \ \varepsilon_{12}^p \ \lambda \ q]^T, \quad (\text{A.3})$$

$$\underline{\mathbf{y}} = [y_1 \ y_2 \ y_3 \ y_4 \ y_5 \ y_6]^T, \quad (\text{A.4})$$

respectively. As a result,  $y_1$ ,  $y_2$ ,  $y_3$  and  $y_4$  are dual plastic strains, while  $y_5$  and  $y_6$  are dual plastic multiplier and dual equivalent plastic strain, respectively.

## References

- [1] Ainsworth M, Oden J (2000) A posteriori error estimation in finite analysis. Pure and applied mathematics, John Wiley & Sons, New York
- [2] Ammar K, Appolaire B, Cailletaud G, Feyel F, Forest S (2009) Finite element formulation of a phase field model based on the concept of generalized stresses. *Computational materials science* 45(3):800–805
- [3] Andrews E, Gioux G, Onck P, Gibson L (2001) Size effects in ductile cellular solids. part ii: experimental results. *International Journal of Mechanical Sciences* 43(3):701–713
- [4] Aslan O, Cordero N, Gaubert A, Forest S (2011) Micromorphic approach to single crystal plasticity and damage. *International Journal of Engineering Science* 49(12):1311–1325
- [5] Babuška I, Rheinboldt WC (1978) A-posteriori error estimates for the finite element method. *International Journal for Numerical Methods in Engineering* 12(10):1597–1615
- [6] Babuska I, Whiteman J, Strouboulis T (2011) *Finite Elements: An Introduction to the Methods and Error Estimation*. Oxford University Press, New York
- [7] Becker R, Rannacher R (1996) A Feed-back approach to error control in finite element methods: basic analysis and examples. *East-West Journal of Numerical Mathematics* 4(4):237–264
- [8] Begley MR, Hutchinson JW (1998) The mechanics of size-dependent indentation. *J Mech Phys Solids* 46(10):2049–2068, DOI 10.1016/S0022-5096(98)00018-0
- [9] Cirak F, Ramm E (1998) A posteriori error estimation and adaptivity for linear elasticity using the reciprocal theorem. *Comput Methods Appl Mech Engrg* 156:351–362
- [10] Courant R (1943) Variational methods for the solution of problems of equilibrium and vibrations. *Bulletin of the American mathematical Society* 49(1):1–23
- [11] Dillard T, Forest S, Jenny P (2006) Micromorphic continuum modelling of the deformation and fracture behaviour of nickel foams. *European Journal of Mechanics A/Solids* 25:526–549
- [12] Ehlers W, Scholz B (2007) An inverse algorithm for the identification and the sensitivity analysis of the parameters governing micropolar elasto-plastic granular material. *Arch Appl Mech* 77(12):911–931, DOI 10.1007/s00419-007-0162-9
- [13] Ehlers W, Volk W (1998) On theoretical and numerical methods in the theory of porous media based on polar and non-polar elasto-plastic solid materials. *Int J Solids Struct* 35(34-35):4597–4617, DOI 10.1016/S0020-7683(98)00086-9

- [14] Ellsiepen P, Hartmann S (2001) Remarks on the interpretation of current non-linear finite element analyses as differential–algebraic equations. *International Journal for Numerical Methods in Engineering* 51(6):679–707
- [15] Eriksson K, Estep D, Hansbo P, Johnson C (1995) Introduction to Adaptive Methods for Differential Equations. *Acta Numerica* 4:150–158
- [16] Eringen AC (1964) Mechanics of micromorphic materials. In: Görtler H (ed) *Applied Mechanics*, Springer, Berlin, Heidelberg, pp 131–138
- [17] Eringen AC (1965) Theory of micropolar continua. In: *Proceedings of the Ninth Midwestern Mechanics Conference*, University of Wisconsin, Wiley, p 23
- [18] Eringen AC (1990) Theory of thermo-microstretch elastic solids. *International Journal of Engineering Science* 28(12):1291–1301
- [19] Faghihi D, Voyiadjis GZ (2014) A thermodynamic consistent model for coupled strain-gradient plasticity with temperature. *Journal of Engineering Materials and Technology* 136(1):011,002
- [20] Fish J (2013) *Practical multiscaling*. John Wiley & Sons, The Atrium
- [21] Fleck N, Olurin O, Chen C, Ashby M (2001) The effect of hole size upon the strength of metallic and polymeric foams. *Journal of the Mechanics and Physics of Solids* 49(9):2015–2030
- [22] Forest S (2009) Micromorphic approach for gradient elasticity, viscoplasticity, and damage. *Journal of Engineering Mechanics* 135(3):117–131, DOI 10.1061/(ASCE)0733-9399(2009)135:3(117)
- [23] Forest S, Aifantis EC (2010) Some links between recent gradient thermo-elastoplasticity theories and the thermomechanics of generalized continua. *Int J Solids Struct* 47(25-26):3367–3376, DOI 10.1016/j.ijsolstr.2010.07.009
- [24] Forest S, L E (2004) Localization phenomena and regularization methods. In: *Local Approach to Fracture*, Les Presses de l’Ecole des Mines, pp 311–371
- [25] Forest S, Sievert R (2006) Nonlinear microstrain theories. *Int J Solids Struct* (43):7224–7245
- [26] Forest S, Ammar K, Appolaire B (2011) In: Bernd Markert, (ed) *Advances in Extended and Multifield Theories for Continua*, Lecture Notes in Applied and Computational Mechanics, Springer Berlin Heidelberg, pp 69–88
- [27] Fried E, Gurtin ME (1993) Continuum theory of thermally induced phase transitions based on an order parameter. *Physica D: Nonlinear Phenomena* 68(3):326–343
- [28] Fried E, Gurtin ME (1994) Dynamic solid-solid transitions with phase characterized by an order parameter. *Physica D: Nonlinear Phenomena* 72(4):287–308

- [29] Grammenoudis P, Tsakmakis C (2009) Micromorphic continuum. Part I: Strain and stress tensors and their associated rates. *Int J Nonlinear Mech* 44(9):943–956, DOI 10.1016/j.ijnonlinmec.2009.05.005
- [30] Grammenoudis P, Tsakmakis C, Hofer D (2009) Micromorphic continuum. Part II: Finite deformation plasticity coupled with damage. *Int J Nonlinear Mech* 44(9):957–974, DOI 10.1016/j.ijnonlinmec.2009.05.004
- [31] Grammenoudis P, Tsakmakis C, Hofer D (2010) Micromorphic continuum. Part III: Small deformation plasticity coupled with damage. *Int J Nonlinear Mech* 45(2):140–148, DOI 10.1016/j.ijnonlinmec.2009.10.003
- [32] Gurtin ME (1996) Generalized Ginzburg-Landau and Cahn-Hilliard equations based on a microforce balance. *Physica D: Nonlinear Phenomena* 92(3):178–192
- [33] Hirschberger C, Steinmann P (2009) Classification of concepts in thermodynamically consistent generalized plasticity. *Journal of engineering mechanics* 135(3):156–170
- [34] Hirschberger CB (2008) A treatise on micromorphic continua. Theory, Homogenization, Computation. PhD thesis, University of Kaiserslautern, Kaiserslautern
- [35] Hirschberger CB, Steinmann P (2009) Classification of concepts in thermodynamically consistent generalized plasticity. *Journal of Engineering Mechanics* 135(3):156–170, DOI 10.1061/(ASCE)0733-9399(2009)135:3(156)
- [36] Hughes TJ (2012) *The finite element method: linear static and dynamic finite element analysis*. Courier Corporation New York
- [37] Jirásek M, Rolshoven S (2009) Localization properties of strain-softening gradient plasticity models. Part I: Strain-gradient theories. *Int J Solids Struct* 46(11-12):2225–2238, DOI 10.1016/j.ijsolstr.2008.12.016
- [38] Ju X, Mahnken R (2016) An NTFA-based homogenization framework considering softening effects. *Mechanics of Materials* 96:106–125
- [39] Ju X, Mahnken R (2017) Goal-oriented adaptivity for linear elastic micromorphic continua based on primal and adjoint consistency analysis. *International Journal for Numerical Methods in Engineering* 112:1017–1039
- [40] Ju X, Mahnken R (2017) Model adaptivity on effective elastic properties coupled with adaptive FEM. *Computer methods in Applied Mechanics and Engineering* 322:208–237
- [41] Ladevèze P, Pelle J (2005) *Mastering calculations in linear and non linear mechanics*. Mechanical Engineering Series, Springer, DOI 10.1007/b138705
- [42] Larsson F, Runesson K (2004) Modeling and discretization errors in hyperelasto-(visco-) plasticity with a view to hierarchical modeling. *Computer methods in applied mechanics and engineering* 193(48-51):5283–5300

- [43] Larsson F, Runesson K, Hansbo P (2003) Time finite elements and error computation for (visco) plasticity with hardening or softening. *International journal for numerical methods in engineering* 56(14):2213–2232
- [44] Leismann T, Mahnken R (2015) Comparison of hyperelastic micromorphic, micropolar and microstrain continua. *Int J Nonlinear Mech* 77:115–127, DOI 10.1016/j.ijnonlinmec.2015.08.004
- [45] Ling C, Forest S, Besson J, Tanguy B, Latourte F (2018) A reduced micromorphic single crystal plasticity model at finite deformations. application to strain localization and void growth in ductile metals. *International Journal of Solids and Structures* 134:43–69
- [46] Ma Q, Clarke DR (1995) Size dependent hardness of silver single crystals. *Journal of Materials Research* 10(4):853–863, DOI 10.1557/JMR.1995.0853
- [47] Mahnken R (1999) Improved implementation of an algorithm for non-linear isotropic/kinematic hardening in elastoplasticity. *Communications in numerical methods in engineering* 15(10):745–754
- [48] Mahnken R (2013) Goal-oriented adaptive refinement for phase field modeling with finite elements. *International Journal for Numerical Methods in Engineering* 94(4):418–440
- [49] Mahnken R (2017) Identification of material parameters for constitutive equations. In *Encyclopedia of Computational Mechanics Second Edition* (eds E Stein, R Borst and T J Hughes) DOI 10.1002/9781119176817.ecm2043
- [50] Mahnken R, Cheng C, Düsung M, Ehlenbröcker U, Leismann T (2016) The concept of generalized stresses for computational manufacturing and beyond. *GAMM-Mitt* 39(2):229–265, DOI I 10.1002/gamm.201610013
- [51] Maugin GA, Metrikine AV (2010) Mechanics of generalized continua. *Advances in mechanics and mathematics* 21
- [52] Mindlin RD (1964) Micro-structure in linear elasticity. *Archive for Rational Mechanics and Analysis* 16(1):51–78
- [53] Neff P, Jeong J, Fischle A (2010) Stable identification of linear isotropic Cosserat parameters: bounded stiffness in bending and torsion implies conformal invariance of curvature. *Acta Mechanica* 211(3):237–249, DOI 10.1007/s00707-009-0230-z
- [54] Oden JT, Vemaganti KS (2000) Estimation of local modeling error and goal-oriented adaptive modeling of heterogeneous materials: I. error estimates and adaptive algorithms. *Journal of Computational Physics* 164(1):22–47
- [55] Onck P, Andrews E, Gibson L (2001) Size effects in ductile cellular solids. part i: modeling. *International Journal of Mechanical Sciences* 43(3):681–699

- [56] Paraschivoiu M, Peraire J, Patera A (1997) A posteriori finite element bounds for linear-functional outputs of elliptic partial differential equations. *Comput Methods Appl Mech Engrg* 150(1):289–312, DOI 10.1016/S0045-7825(97)00086-8
- [57] Peerlings RHJ, Geers MGD, de Borst R, Brekelmans WAM (2001) A critical comparison of nonlocal and gradient-enhanced softening continua. *Int J Solids Struct* 38(44-45):7723–7746, DOI 10.1016/S0020-7683(01)00087-7
- [58] Poole WJ, Ashby MF, Fleck NA (1996) Micro-hardness of annealed and work-hardened copper polycrystals. *Scripta Materialia* 34(4):559–564, DOI 10.1016/1359-6462(95)00524-2
- [59] Prudhomme S, Oden J (1999) On goal-oriented error estimation for elliptic problems: application to the control of pointwise errors. *Comput Methods Appl Mech Engrg* 176(1–4):313–331, DOI 10.1016/S0045-7825(98)00343-0
- [60] Qu J, Cherkaoui M (2006) *Fundamentals of Micromechanics of Solids*. Wiley, Hoboken, New Jersey
- [61] Rüter M (2003) *Error-controlled Adaptive Finite Element Methods in Large Strain Hyperelasticity and Fracture Mechanics*. PhD thesis, University of Hannover, Hannover
- [62] Schmich M, Vexler B (2008) Adaptivity with dynamic meshes for space-time finite element discretizations of parabolic equations. *SIAM Journal on Scientific Computing* 30(1):369–393
- [63] Stein E (ed) (2003) *Error-controlled Adaptive Finite Elements in Solid Mechanics*. Wiley, Chichester
- [64] Steinmann P (1994) A micropolar theory of finite deformation and finite rotation multiplicative elastoplasticity. *Int J Solids Struct* 31(8):1063–1084, DOI 10.1016/0020-7683(94)90164-3
- [65] Stelmashenko NA, Walls MG, Brown LM, Milman YUV (1993) Microindentations on W and Mo oriented single crystals: An STM study. *Acta Metallurgica et Materialia* 41(10):2855–2865, DOI 10.1016/0956-7151(93)90100-7
- [66] Tinsley Oden J, Prudhomme S, Romkes A, Bauman PT (2006) Multiscale modeling of physical phenomena: Adaptive control of models. *SIAM Journal on Scientific Computing* 28(6):2359–2389
- [67] Turner MJ, Clough RW, Martin HC, Topp LJ (1956) Stiffness and deflection analysis of complex structures. *journal of the Aeronautical Sciences* 23:805–823
- [68] Vemaganti KS, Oden JT (2001) Estimation of local modeling error and goal-oriented adaptive modeling of heterogeneous materials: Part ii: a computational environment for adaptive modeling of heterogeneous elastic solids. *Computer Methods in Applied Mechanics and Engineering* 190(46-47):6089–6124

- [69] Verfürth R (1996) A Review of A Posteriori Error Estimation and Adaptive Mesh-Refinement Techniques. Wiley-Teubner, Stuttgart
- [70] Voyiadjis GZ, Faghihi D (2014) Overview of enhanced continuum theories for thermal and mechanical responses of the microsystems in the fast-transient process. *Journal of Engineering Materials and Technology* 136(4):041,003
- [71] Widany KU, Mahnken R (2016) Dual-based adaptive fem for inelastic problems with standard fe implementations. *International Journal for Numerical Methods in Engineering* 107(2):127–154
- [72] Zienkiewicz OC, Taylor RL (2005) *The finite element method for solid and structural mechanics*. Butterworth-heinemann London
- [73] Zienkiewicz OC, Taylor RL, Zienkiewicz OC, Taylor RL (1977) *The finite element method*, vol 3. McGraw-hill London

## 4 Summary

This thesis consists of the following two main parts, which commonly contribute to the mechanics of heterogeneous materials.

1. The papers A, B and C dealt with first order homogenization problems assuming a scale separation. Their topics covered all the four classes of homogenization methods introduced in Section 1.3.
  - The general coupled adaptive strategy developed in Paper A for linear elastic heterogeneous materials inherits the common idea from the literature, where model adaptivity and adaptive FEM are applied in a coupled manner for balancing model and discretization error on the macroscale. For an error control with respect to a user-defined quantity of interest, the general concept of goal-oriented adaptivity has been adopted. Specific error estimators based on duality techniques have been derived for both model and discretization errors, where an important role is played by enhanced solutions, which replace the unknown exact solutions. To compute the enhanced solutions in an efficient way, a novel patch recovery technique has additionally been developed and compared to other existing techniques. The most important and challenging part was to formulate hierarchical models for model adaptivity, whose hierarchical structures are not as apparent as those of the finite elements. As a result, an investigation of different homogenization methods has been done. In Paper A, a variational homogenization method for higher order bounds of effective properties was used to provide a model hierarchy in a theoretically consistent manner. Indeed, a clear hierarchical model structure is obtained by a truncation of the underlying Neumann series. In Paper B, our attention is distracted to mean-field and computational (full-field) homogenization methods, which are combined to establish a model hierarchy. Several mean-field methods have been examined, such that two hierarchical models are established using a priori knowledge for an initial stage of the model hierarchy. It is expected that, for a relatively large region of the structure, the two models within the frame of mean-field methods suffice for both purposes of modeling and error estimate. For regions of largest importance to the quantity of interest determined by an error estimate, a computational (full-field) method is adopted, where a unit cell problem is solved via the FEM under an appropriate micro boundary condition. The use of the FEM enables an additional consideration of the unit cell size, where hierarchical unit cells are established. For a further accuracy improvement, the unit cell size is hierarchically enlarged. For the materials under study, a periodic boundary condition was chosen prior to the adaptive procedure for a fast convergence rate. In summary, the papers A and B presented

two different adaptive approaches including three important classes of homogenization methods, i.e. mean-field, computational and variational methods, for model adaptivity in linear elasticity, where a model reduction is not necessary. The effectiveness of the proposed adaptive procedures has been shown by several numerical examples.

- Paper C considered a physically nonlinear homogenization problem including softening effects, for which a model order reduction method shows a clear advantage. The NTFA was chosen due to its closed-form evolution equations for the reduced variables, which guarantee a computational efficiency. However, these evolution equations have to be tailored for the micro problem under study, and therefore require an extension for softening effects. It was found that the NTFA becomes less accurate than that reported in the literature [99, 123, 101, 45, 81] for plasticity problems (pure hardening without softening). This seems to be a common issue for model reduction of a damage analysis, see e.g. [34] in a slightly different context. Since the NTFA, in its original form, possesses an even model structure, we referred to it as the even NTFA. For an accuracy improvement, two new methods have additionally been developed. In the uneven NTFA, additional correction parameters are introduced, thus resulting into an uneven model structure. The numerical example in [67] shows a satisfactory correction even by using one single correction parameter set for a structural analysis. One could also think of a partitioning scheme to introduce different parameter sets for different loading cases, if required. In the adaptive NTFA, the concept of adaptive modeling is adopted, where an effective empirical indicator is used to determine the need for a replacement by the FE<sup>2</sup> method for an accuracy improvement.
2. The papers D and E handled micromorphic continua, which are of crucial importance to model size effects and localization phenomena. They are complementary to the first order homogenization schemes considered in the papers A, B and C. For simplicity, conventional micromorphic continua have been considered on a phenomenological basis in contrast to higher order homogenization schemes.
- Paper D dealt with linear micromorphic continua, where a primal and an adjoint consistency analysis have been performed to theoretically ensure an optimal convergence order. By introducing the notion of generalized solution, the abstract setting preserves a classical format, which was shown to be very convenient for deriving a goal-oriented error estimate. This error estimate, along with certain localization techniques, has been successfully used to drive an adaptive mesh refinement algorithm, where a novel patch recovery technique was used to efficiently approximate the exact solutions.
  - Paper E extended the topic of Paper D to micromorphic elastoplasticity. A double multifield formulation of such problem has been proposed, where weak forms in a time integration sense were established for both the equilibrium and the evolution equations. This formulation has been shown to be beneficial for deriving a goal-oriented error estimate. One difficulty

arises due to the time-dependent feature of the primal problem, such that discretization errors accumulate over time. For a complete consideration of error accumulation, one has to deal with both error generation and error transport. To this end, a backwards-in-time dual problem has been derived from a Lagrange method. We have additionally shown that a simplified forwards-in-time dual problem can be easily obtained by neglecting error transport. Compared to the backwards-in-time version, this forwards-in-time version significantly reduces the memory requirement for a numerical implementation. Based on both dual problems, four error estimators have been proposed and studied with respect to the effectiveness for driving an adaptive mesh refinement algorithm, where the patch recovery technique developed in the papers A and D was additionally considered. As a merit, the patch recovery eliminates the need for any nonlinear calculations and is thus quite efficient.

While the papers A, B, D and E aim at different targets in the mechanics of heterogeneous materials, the main novelty is the development of adaptive methods within the common framework of goal-oriented adaptivity. The novelties of Paper C are the extension of the NTFA to consider softening effects and the two related new methods. The proposed adaptive NTFA, in its current form, relies on an empirical basis.



## 5 Outlook

Although this thesis covers a wide spectrum of adaptive methods in the mechanics of heterogeneous materials, much more effort remains to be paid for future research as follows.

Concerning model adaptivity for homogenization of heterogeneous materials, Paper A adopts a singular approximation for evaluating higher order bounds of effective properties. For a higher level of accuracy, one should resort to certain numerical methods [105, 70]. While model adaptivity has been addressed for linear homogenization problems in the papers A and B, model adaptivity for nonlinear homogenization problems like plasticity problems appears to be a widely open area. Paper C was apparently such an attempt on an early stage. The proposed empirical indicator enables an on-the-fly model switch, however, does not give information about the model error. In future, the concept of goal-oriented adaptivity should be extended to such problems in order to make the multiscale simulation efficient and reliable. Indeed, reduced order homogenization schemes like the NTFA are very attractive in view of a numerical efficiency, however, their prediction quality strongly relies on the quality of the a priori chosen reduced basis functions. For a reliable simulation, the model error resulted from such schemes should be controlled. Apparently, this is a quite challenging task due to the nonlinearities and the time-dependent characteristics involved.

Moreover, although the adaptive methods in the papers A and B are designed for mechanical problems, they are transferable to other kinds of physical problems like heat transfer etc.

In the context of micromorphic continua, the application of goal-oriented adaptivity in the papers D and E for the direct problem showed first successes. Since Paper E was merely concerned with the spatial discretization error of micromorphic plasticity problems, the temporal discretization error resulted from a certain time-stepping scheme should be addressed in future for a full error analysis. Additionally, Paper E initialized a way towards a forwards-in-time dual problem, which is quite attractive for a numerical implementation. Since the way towards a forwards-in-time dual problem is not unique, more effective methods should be developed considering error transport to a certain extent. Furthermore, our recent work [69] shows that the parameter identification of such problems, often viewed as an inverse problem, is another challenging task for both numerical and experimental aspects. Recent international studies [64, 13] tend to seek for a link between micromorphic continua and homogenization methods, such that a clear physical interpretation can be attached to the morphic variables. This might facilitate the parameter identification of micromorphic models in future.

Furthermore, the small strain theories assumed throughout this thesis do not hinder the illustration of the underlying general concepts. An extension to finite strains

would be straightforward. From a computational point of view, the numerical results presented in the papers A–E were generated by specific codes developed in MATLAB [97] by the author. Two-dimensional problems were handled to investigate and illustrate the effectiveness of the developed methodologies for academic purposes. For a real-world structural analysis, these codes need to be extended to three-dimensional cases. It also makes sense to couple them to a commercial FE software like Abaqus via appropriate interfaces.

# Bibliography

- [1] A. Abdulle and Y. Bai. “Adaptive reduced basis finite element heterogeneous multiscale method”. *Computer Methods in Applied Mechanics and Engineering* 257 (2013), pp. 203–220.
- [2] M. Ainsworth and J. T. Oden. *A posteriori error estimation in finite analysis*. Pure and applied mathematics. John Wiley & Sons, New York, 2000. ISBN: 0-471-29411-X.
- [3] K. Ammar, B. Appolaire, G. Cailleaud, F. Feyel, and S. Forest. “Finite element formulation of a phase field model based on the concept of generalized stresses”. *Computational materials science* 45.3 (2009), pp. 800–805.
- [4] E. Andrews, G. Gioux, P. Onck, and L. Gibson. “Size effects in ductile cellular solids. Part II: experimental results”. *International Journal of Mechanical Sciences* 43.3 (2001), pp. 701–713.
- [5] I. Babuška and T. Strouboulis. “Can we trust the computational analysis of engineering problems?” In: *Mathematical Modeling and Numerical Simulation in Continuum Mechanics*. Springer, Berlin, Heidelberg, 2002, pp. 169–183.
- [6] I. Babuska, J. Whiteman, and T. Strouboulis. *Finite Elements: An Introduction to the Methods and Error Estimation*. Oxford University Press, New York, 2011. ISBN: 978-0-19-850670-6.
- [7] I. Babuška and W. C. Rheinboldt. “A-posteriori error estimates for the finite element method”. *International Journal for Numerical Methods in Engineering* 12.10 (1978), pp. 1597–1615.
- [8] W. Bangerth and R. Rannacher. *Adaptive finite element methods for differential equations*. Birkhäuser, Berlin, 2013.
- [9] R. Becker and R. Rannacher. “A Feed-back approach to error control in finite element methods: basic analysis and examples”. *East-West Journal of Numerical Mathematics* 4.4 (1996), pp. 237–264. ISSN: 09280200.
- [10] R. Becker and R. Rannacher. “An optimal control approach to a posteriori error estimation in finite element methods”. *Acta numerica* 10 (2001), pp. 1–102.
- [11] A. Bensoussan, J.-L. Lions, and G. Papanicolaou. *Asymptotic analysis for periodic structures*. Vol. 374. American Mathematical Soc., Providence, 2011.
- [12] M. Berveiller and A. Zaoui. “An extension of the self-consistent scheme to plastically-flowing polycrystals”. *J. Mech. Phys. Solids* 26 (1978), pp. 325–344.
- [13] R. Biswas and L. H. Poh. “A micromorphic computational homogenization framework for heterogeneous materials”. *Journal of the Mechanics and Physics of Solids* 102 (2017), pp. 187–208.

- [14] M. Braack and A. Ern. “A posteriori control of modeling errors and discretization errors”. *Multiscale Model. Simul.* 1.2 (2003), pp. 221–238.
- [15] P. P. Castañeda. “Linear Comparison Methods for Nonlinear Composites”. In: *Nonlinear Homogenization and its Applications to Composites, Polycrystals and Smart Materials*. Springer, New York, 2004, pp. 247–268.
- [16] F. Cirak and E. Ramm. “A posteriori error estimation and adaptivity for linear elasticity using the reciprocal theorem”. *Comput. Methods Appl. Mech. Engrg.* 156 (1998), pp. 351–362.
- [17] R. Courant. “Variational methods for the solution of problems of equilibrium and vibrations”. *Bulletin of the American mathematical Society* 49.1 (1943), pp. 1–23.
- [18] P. H. Dederichs and R. Zeller. “Variational treatment of the elastic constants of disordered materials”. *Zeitschrift für Physik* 259.2 (1973), pp. 103–116.
- [19] T. Dillard, S. Forest, and P. Ienny. “Micromorphic continuum modelling of the deformation and fracture behaviour of nickel foams”. *European Journal of Mechanics A/Solids* 25 (2006), pp. 526–549.
- [20] G. Dvorak, Y. Bahei-El-Din, and A. Wafa. “The modeling of inelastic composite material with the transformation field analysis”. *Modelling and simulation in materials science and engineering* 2 (1994), pp. 571–586.
- [21] G. Dvorak and Y. Benveniste. “On transformation strains and uniform fields in multiphase elastic media”. *Proceedings of the Royal Society of London* 437.A (1992), pp. 291–310.
- [22] W. Ehlers, E. Ramm, S. Diebels, and G. d’Addetta. “From particle ensembles to Cosserat continua: homogenization of contact forces towards stresses and couple stresses”. *International Journal of Solids and Structures* 40.24 (2003), pp. 6681–6702.
- [23] W. Ehlers and B. Scholz. “An inverse algorithm for the identification and the sensitivity analysis of the parameters governing micropolar elasto-plastic granular material”. *Arch Appl Mech* 77.12 (2007), pp. 911–931. DOI: 10.1007/s00419-007-0162-9.
- [24] W. Ehlers and W. Volk. “On theoretical and numerical methods in the theory of porous media based on polar and non-polar elasto-plastic solid materials”. *Int. J. Solids Struct.* 35.34-35 (1998), pp. 4597–4617. DOI: 10.1016/S0020-7683(98)00086-9.
- [25] K. Eriksson, D. Estep, P. Hansbo, and C. Johnson. “Introduction to Adaptive Methods for Differential Equations”. *Acta Numerica* 4 (1995), pp. 150–158.
- [26] A. C. Eringen. “Mechanics of micromorphic materials”. *Applied Mechanics. Proceedings of the Eleventh International Congress of Applied Mechanics Munich (Germany) 1964*. Ed. by H. Görtler. Springer, Berlin, Heidelberg, 1964, pp. 131–138.
- [27] A. C. Eringen. “Theory of micropolar continua”. *Proceedings of the Ninth Midwestern Mechanics Conference*. University of Wisconsin. Wiley, 1965, pp. 23–40.

- [28] A. C. Eringen. “Theory of thermo-microstretch elastic solids”. *International Journal of Engineering Science* 28.12 (1990), pp. 1291–1301.
- [29] A. C. Eringen and D. Edelen. “On nonlocal elasticity”. *International Journal of Engineering Science* 10.3 (1972), pp. 233–248.
- [30] J. D. Eshelby. “The determination of the elastic field of an ellipsoidal inclusion, and related problems”. *Proc. R. Soc. Lond. A* 241.1226 (1957), pp. 376–396.
- [31] F. Feyel and J.-L. Chaboche. “FE2 multiscale approach for modelling the elastoviscoplastic behaviour of long fibre SiC/Ti composite materials”. *Computer methods in applied mechanics and engineering* 183.3-4 (2000), pp. 309–330.
- [32] J. Fish. *Practical multiscaling*. John Wiley & Sons, The Atrium, 2013. ISBN: 1-118-41068-8.
- [33] J. Fish and R. Fan. “Mathematical homogenization of nonperiodic heterogeneous media subjected to large deformation transient loading”. *International Journal for numerical methods in engineering* 76.7 (2008), pp. 1044–1064.
- [34] J. Fish, V. Filonova, and Z. Yuan. “Hybrid impotent–incompatible eigenstrain based homogenization”. *International Journal for Numerical Methods in Engineering* 95.1 (2013), pp. 1–32.
- [35] N. Fleck, O. Olurin, C. Chen, and M. Ashby. “The effect of hole size upon the strength of metallic and polymeric foams”. *Journal of the Mechanics and Physics of Solids* 49.9 (2001), pp. 2015–2030.
- [36] S. Forest. “Micromorphic approach for gradient elasticity, viscoplasticity, and damage”. *Journal of Engineering Mechanics* 135.3 (2009), pp. 117–131. DOI: 10.1061/(ASCE)0733-9399(2009)135:3(117).
- [37] S. Forest and E. C. Aifantis. “Some links between recent gradient thermoelasto-plasticity theories and the thermomechanics of generalized continua”. *Int. J. Solids Struct.* 47.25-26 (2010), pp. 3367–3376. DOI: 10.1016/j.ijsolstr.2010.07.009.
- [38] S. Forest and E. L. “Localization phenomena and regularization methods”. *Local Approach to Fracture*. Les Presses de l’Ecole des Mines, 2004, pp. 311–371.
- [39] S. Forest and R. Sievert. “Nonlinear microstrain theories”. *Int. J. Solids Struct.* 43 (2006), pp. 7224–7245.
- [40] S. Forest. “Homogenization methods and mechanics of generalized continua-part 2”. *Theoretical and applied mechanics* 28-29 (2002), pp. 113–144.
- [41] S. Forest, K. Ammar, and B. Appolaire. In: *Advances in Extended and Multifield Theories for Continua*. Ed. by Bernd Markert, Lecture Notes in Applied and Computational Mechanics. Springer Berlin Heidelberg, 2011, pp. 69–88.
- [42] S. Forest and K. Sab. “Cosserat overall modeling of heterogeneous materials”. *Mechanics Research Communications* 25.4 (1998), pp. 449–454.

- [43] E. Fried and M. E. Gurtin. “Continuum theory of thermally induced phase transitions based on an order parameter”. *Physica D: Nonlinear Phenomena* 68.3 (1993), pp. 326–343.
- [44] E. Fried and M. E. Gurtin. “Dynamic solid-solid transitions with phase characterized by an order parameter”. *Physica D: Nonlinear Phenomena* 72.4 (1994), pp. 287–308.
- [45] F. Fritzen and T. Böhlke. “Three-dimensional finite element implementation of the nonuniform transformation field analysis”. *International Journal for Numerical Methods in Engineering* 84 (2010), pp. 803–829.
- [46] M. Geers, V. Kouznetsova, and W. Brekelmanns. “Multi-scale computational homogenization: Trends and Challenges”. *Journal of Computational and Applied Mathematics* 234 (2010), pp. 2175–2182.
- [47] S. Ghosh, K. Lee, and S. Moorthy. “Two scale analysis of heterogeneous elastic-plastic materials with asymptotic homogenization and Voronoi cell finite element model”. *Computer methods in applied mechanics and engineering* 132.1-2 (1996), pp. 63–116.
- [48] S. Ghosh, K. Lee, and P. Raghavan. “A multi-level computational model for multi-scale damage analysis in composite and porous materials”. *International Journal of Solids and Structures* 38.14 (2001), pp. 2335–2385.
- [49] C. González and J. LLorca. “Mechanical behavior of unidirectional fiber-reinforced polymers under transverse compression: microscopic mechanisms and modeling”. *Composites Science and Technology* 67.13 (2007), pp. 2795–2806.
- [50] P. Grammenoudis and C. Tsakmakis. “Micromorphic continuum. Part I: Strain and stress tensors and their associated rates”. *Int. J. Nonlinear Mech.* 44.9 (2009), pp. 943–956. DOI: 10.1016/j.ijnonlinmec.2009.05.005.
- [51] P. Grammenoudis, C. Tsakmakis, and D. Hofer. “Micromorphic continuum. Part II: Finite deformation plasticity coupled with damage”. *Int. J. Nonlinear Mech.* 44.9 (2009), pp. 957–974. DOI: 10.1016/j.ijnonlinmec.2009.05.004.
- [52] P. Grammenoudis, C. Tsakmakis, and D. Hofer. “Micromorphic continuum. Part III: Small deformation plasticity coupled with damage”. *Int. J. Nonlinear Mech.* 45.2 (2010), pp. 140–148. DOI: 10.1016/j.ijnonlinmec.2009.10.003.
- [53] M. Groeber, S. Ghosh, M. D. Uchic, and D. M. Dimiduk. “A framework for automated analysis and simulation of 3D polycrystalline microstructures.: Part 1: Statistical characterization”. *Acta Materialia* 56.6 (2008), pp. 1257–1273.
- [54] M. E. Gurtin. *An introduction to continuum mechanics*. Vol. 158. Academic press, New York, 1982.
- [55] M. E. Gurtin. “Generalized Ginzburg-Landau and Cahn-Hilliard equations based on a microforce balance”. *Physica D: Nonlinear Phenomena* 92.3 (1996), pp. 178–192.

- [56] L. Hagen, F. Hoffmann, N. Sievers, and W. Tillmann. “Results of Project A4 SFB/TR TRR30” (2012).
- [57] R. Hill. “Elastic properties of reinforced solids: some theoretical principles”. *Journal of the mechanics and physics of solids* 11 (1963), pp. 357–372.
- [58] R. Hill. “A self-consistent mechanics of composite materials”. *Journal of the Mechanics and Physics of Solids* 13.4 (1965), pp. 213–222.
- [59] C. B. Hirschberger and P. Steinmann. “Classification of concepts in thermodynamically consistent generalized plasticity”. *Journal of Engineering Mechanics* 135.3 (2009), pp. 156–170. DOI: 10.1061/(ASCE)0733-9399(2009)135:3(156).
- [60] C. B. Hirschberger. “A treatise on micromorphic continua. Theory, Homogenization, Computation”. PhD thesis. Kaiserslautern: University of Kaiserslautern, June 2008.
- [61] U. Hornung. *Homogenization and porous media*. Springer, New York, 1996. ISBN: 0-387-94786-8.
- [62] Y. Huang, K. Hu, X. Wei, and A. Chandra. “A generalized self-consistent mechanics method for composite materials with multiphase inclusions”. *Journal of the Mechanics and Physics of Solids* 42.3 (1994), pp. 491–504.
- [63] T. J. Hughes. *The finite element method: linear static and dynamic finite element analysis*. Courier Corporation New York, 2012.
- [64] G. Hütter. “Homogenization of a Cauchy continuum towards a micromorphic continuum”. *Journal of the Mechanics and Physics of Solids* 99 (2017), pp. 394–408.
- [65] V. V. Jikov, S. M. Kozlov, and O. A. Oleinik. *Homogenization of differential operators and integral functionals*. Springer Science & Business Media, Berlin, 2012.
- [66] M. Jirásek and S. Rolshoven. “Localization properties of strain-softening gradient plasticity models. Part I: Strain-gradient theories”. *Int. J. Solids Struct.* 46.11-12 (2009), pp. 2225–2238. DOI: 10.1016/j.ijsolstr.2008.12.016.
- [67] X. Ju and R. Mahnken. “Two accuracy improvements on nonuniform transformation field analysis for plasticity coupled to softening”. *PAMM* 16.1 (2016), pp. 527–528.
- [68] X. Ju and R. Mahnken. “Corrigendum to: goal-oriented adaptivity for linear elastic micromorphic continua based on primal and adjoint consistency analysis”. *International Journal for Numerical Methods in Engineering* (2018). DOI: 10.1002/nme.5996.
- [69] X. Ju and R. Mahnken. “Goal-oriented adaptivity for parameter identification in linear micromorphic elasticity”. *PAMM* (2018), e201800098. DOI: 10.1002/pamm.201800098.
- [70] M. Kabel and H. Andrä. “Fast numerical computation of precise bounds of effective elastic moduli”. *Report of the Fraunhofer ITWM* 224 (2013).

- [71] A. S. Khan and S. Huang. *Continuum theory of plasticity*. John Wiley & Sons, New York, 1995.
- [72] V. Kouznetsova, M. Geers, and W. Brekelmanns. “Multi-scale constitutive modelling of heterogeneous materials with a gradient-enhanced computational homogenization scheme”. *International Journal for Numerical Methods in Engineering* 54 (2002), pp. 1235–1260.
- [73] V. Kouznetsova, M. Geers, and W. Brekelmanns. “Multi-scale second-order computational homogenization of multi-phase materials: a nested finite element solution strategy”. *Comput. Methods Appl. Mech. Engrg.* 193.48-51 (2004), pp. 5525–5550.
- [74] E. Kröner. “Berechnung der elastischen Konstanten des Vielkristalls aus den Konstanten des Einkristalls”. *Z. Phys.* 151 (1958), pp. 504–518.
- [75] E. Kröner. “Bounds for effective elastic moduli of disordered materials”. *J. Mech. Phys. Solids* 25 (1977), pp. 137–155.
- [76] E. Kröner and B. Datta. “Nichtlokale elastostatik: Ableitung aus der gittertheorie”. *Zeitschrift für Physik* 196.3 (1966), pp. 203–211.
- [77] P. Ladevèze and J. Pelle. *Mastering calculations in linear and non linear mechanics*. Mechanical Engineering Series. Springer, New York, 2005. ISBN: 978-0-387-21294-4.
- [78] D. C. Lagoudas, A. C. Gavazzi, and H. Nigam. “Elastoplastic behavior of metal matrix composites based on incremental plasticity and the Mori–Tanaka averaging scheme”. *Comput. Mech.* 8 (1991), pp. 193–203.
- [79] N. Lahellec and P. Suquet. “On the effective behavior of nonlinear inelastic, composites: I. Incremental variational principles”. *Journal of the Mechanics and Physics of Solids* 55 (2007), pp. 1932–1963.
- [80] N. Lahellec and P. Suquet. “On the effective behavior of nonlinear inelastic, composites: II. A second-order procedure”. *Journal of the Mechanics and Physics of Solids* 55 (2007), pp. 1964–1992.
- [81] R. Largeton, J.-C. Michel, and P. Suquet. “Extension of the Nonuniform Transformation Field Analysis to linear viscoelastic composites in the presence of aging and swelling”. *Mechanics of Materials* (2014).
- [82] F. Larsson, P. Hansbo, and K. Runesson. “Strategies for computing goal-oriented a posteriori error measures in non-linear elasticity”. *Int. J. Numer. Mech. Engrng* 55 (2002), pp. 879–894.
- [83] F. Larsson and K. Runesson. “Modeling and discretization errors in hyperelasto-(visco-)plasticity with a view to hierarchical modeling”. *Comput. Methods Appl. Mech. Engrg.* 193 (2004), pp. 5283–5300.
- [84] F. Larsson and K. Runesson. “Adaptive computational meso-macro-scale modeling of elastic composites”. *Comput. Methods Appl. Mech. Engrg.* 195 (2006), pp. 324–338.
- [85] F. Larsson and K. Runesson. “RVE computation with error control and adaptivity: the power of duality”. *Comp. Meths.* 39 (2007), pp. 647–661.

- [86] F. Larsson and K. Runesson. “On two-scale adaptive FE analysis of micro-heterogeneous media with seamless scale-bridging”. *Computer Methods in Applied Mechanics and Engineering* 200 (2011), pp. 2662–2674.
- [87] F. Larsson, K. Runesson, and P. Hansbo. “Time finite elements and error computation for (visco) plasticity with hardening or softening”. *International journal for numerical methods in engineering* 56.14 (2003), pp. 2213–2232.
- [88] M. Leuschner and F. Fritzen. “Reduced order homogenization for viscoplastic composite materials including dissipative imperfect interfaces”. *Mechanics of Materials* 104 (2017), pp. 121–138.
- [89] R. Mahnken. “Identification of material parameter for constitutive equations”. In: *Encyclopedia of Computational Mechanics Second Edition*. Ed. by E. Stein, R. deBorst, and J. Hughes. John Wiley & Sons, Ltd., 2017. DOI: 10.1002/9781119176817.ecm2043.
- [90] R. Mahnken, C. Cheng, M. Düsung, U. Ehlenbröker, and T. Leismann. “The concept of generalized stresses for computational manufacturing and beyond”. *GAMM-Mitt.* 39.2 (2016), pp. 229–265. DOI: I10.1002/gamm.201610013.
- [91] R. Mahnken. “Theoretische und numerische Aspekte zur Parameteridentifikation und Modellierung bei metallischen Werkstoffen”. PhD thesis. Inst. für Baumechanik und Numerische Mechanik, University of Hannover, 1998.
- [92] R. Mahnken and C. Dammann. “A three-scale framework for fibre-reinforced-polymer curing Part I: Microscopic modeling and mesoscopic effective properties”. *International Journal of Solids and Structures* 100 (2016), pp. 341–355.
- [93] R. Mahnken and C. Dammann. “A three-scale framework for fibre-reinforced-polymer curing part II: Mesoscopic modeling and macroscopic effective properties”. *International Journal of Solids and Structures* 100 (2016), pp. 356–375.
- [94] R. Mahnken and E. Stein. “The identification of parameters for visco-plastic models via finite-element methods and gradient methods”. *Modelling and simulation in materials science and engineering* 2.3A (1994), p. 597.
- [95] R. Mahnken and E. Stein. “A unified approach for parameter identification of inelastic material models in the frame of the finite element method”. *Computer methods in applied mechanics and engineering* 136.3 (1996), pp. 225–258.
- [96] M. Maier. “Duality-based adaptivity of model and discretization in multiscale finite-element methods”. PhD thesis. Ruprecht Karl University of Heidelberg, 2015.
- [97] MATLAB. *version 9.4.0.813654 (R2018a)*. Natick, Massachusetts: The MathWorks Inc., 2018.
- [98] G. A. Maugin and A. V. Metrikine. *Mechanics of generalized continua*. Springer, New York, 2010.
- [99] J. Michel and P. Suquet. “Nonuniform transformation field analysis”. *International Journal for Solids and Structures* 40 (2003), pp. 6937–6955.

- [100] J. Michel and P. Suquet. “Computational analysis of nonlinear composite structures using the nonuniform transformation field analysis”. *Computer Methods in Applied Mechanics and Engineering* 193 (2004), pp. 5477–5502.
- [101] J.-C. Michel and P. Suquet. “Nonuniform transformation field analysis: a reduced model for multiscale nonlinear problems in solid mechanics”. In: *Multiscale Modelling in Solid Mechanics - Computational Approaches*. 2009. Chap. 4, pp. 159–206.
- [102] J.-C. Michel, H. Moulinec, and P. Suquet. “Effective properties of composite materials with periodic microstructure: a computational approach”. *Computer methods in applied mechanics and engineering* 172.1-4 (1999), pp. 109–143.
- [103] C. Miehe, J. Schröder, and J. Schotte. “Computational homogenization analysis in finite plasticity simulation of texture development in polycrystalline materials”. *Computer methods in applied mechanics and engineering* 171.3-4 (1999), pp. 387–418.
- [104] T. Mori and K. Tanaka. “Average stress in matrix and average elastic energy of materials with misfitting inclusions”. *Acta metallurgica* 21.5 (1973), pp. 571–574.
- [105] H. Moulinec and P. Suquet. “A numerical method for computing the overall response of nonlinear composites with complex microstructure”. *Computer methods in applied mechanics and engineering* 157.1-2 (1998), pp. 69–94.
- [106] V. Müller, M. Kabel, H. Andrä, and T. Böhlke. “Homogenization of linear elastic properties of short-fiber reinforced composites—A comparison of mean field and voxel-based methods”. *International Journal of Solids and Structures* 67 (2015), pp. 56–70.
- [107] P. Neff, J. Jeong, and A. Fischle. “Stable identification of linear isotropic Cosserat parameters: bounded stiffness in bending and torsion implies conformal invariance of curvature”. *Acta Mechanica* 211.3 (2010), pp. 237–249. DOI: 10.1007/s00707-009-0230-z.
- [108] J. T. Oden and S. Prudhomme. “Estimation of Modeling Error in Computational Mechanics”. *Journal of Computational Physics* 182 (2002), pp. 496–515.
- [109] J. T. Oden, S. Prudhomme, D. Hammerand, and M. Kuczma. “Modeling error and adaptivity in nonlinear continuum mechanics”. *Comput. Methods Appl. Mech. Eng.* 190 (2001), pp. 6663–6684.
- [110] J. T. Oden, S. Prudhomme, A. Romkes, and P. Bauman. “Multiscale modelling of physical phenomena: adaptive control of models”. *SAIM J. SCI. Comput.* 28 (2006), pp. 2359–2389.
- [111] J. T. Oden and K. S. Vemaganti. “Estimation of local modeling error and goal-oriented adaptive modeling of heterogeneous materials; Part I: Error Estimates and Adaptive Algorithms”. *Journal of Computational Physics* 164 (2000), pp. 22–47.

- [112] J. Oden. “A posteriori estimation of modeling and approximation error in computational science and engineering: new tools for verification and validation of computer simulations”. *Fifth World Congress on Computational Mechanics*. 2002.
- [113] P. Onck, E. Andrews, and L. Gibson. “Size effects in ductile cellular solids. Part I: modeling”. *International Journal of Mechanical Sciences* 43.3 (2001), pp. 681–699.
- [114] M. Paraschivoiu, J. Peraire, and A. Patera. “A posteriori finite element bounds for linear-functional outputs of elliptic partial differential equations”. *Comput. Methods Appl. Mech. Engrg.* 150.1 (1997), pp. 289–312. DOI: 10.1016/S0045-7825(97)00086-8.
- [115] R. H. J. Peerlings, M. G. D. Geers, R. de Borst, and W. A. M. Brekelmans. “A critical comparison of nonlocal and gradient-enhanced softening continua”. *Int. J. Solids Struct.* 38.44-45 (2001), pp. 7723–7746. DOI: 10.1016/S0020-7683(01)00087-7.
- [116] P. Ponte-Castañeda. “A finite-strain constitutive theory for electro-active polymer composites via homogenization”. *International Journal of Non-Linear Mechanics* 47(2) (2012), pp. 293–306.
- [117] S. Prudhomme and J. T. Oden. “On goal-oriented error estimation for elliptic problems: application to the control of pointwise errors”. *Comput. Methods Appl. Mech. Engrg.* 176.1-4 (1999), pp. 313–331. DOI: 10.1016/S0045-7825(98)00343-0.
- [118] J. Qu and M. Cherkaoui. *Fundamentals of Micromechanics of Solids*. Wiley, Hoboken, New Jersey, 2006. ISBN: 978-0-471-46451-8.
- [119] A. Reuss. “Berechnung der fließgrenze von mischkristallen auf grund der plastizitätsbedingung für einkristalle.” *ZAMM-Journal of Applied Mathematics and Mechanics/Zeitschrift für Angewandte Mathematik und Mechanik* 9.1 (1929), pp. 49–58.
- [120] T. Richter and T. Wick. “Variational localizations of the dual weighted residual estimator”. *Journal of Computational and Applied Mathematics* 279 (2015), pp. 192–208.
- [121] F. Rieger and T. Böhlke. “Microstructure based prediction and homogenization of the strain hardening behavior of dual-phase steel”. *Archive of Applied Mechanics* 85.9-10 (2015), pp. 1439–1458.
- [122] P. J. Roache. *Verification and validation in computational science and engineering*. Hermosa Publishers, Albuquerque, 1998.
- [123] S. Roussette, J. Michel, and P. Suquet. “Nonuniform transformation field analysis of elastic-viscoplastic composites”. *Composite Science and Technology* 69 (2009), pp. 22–27.
- [124] M. Rüter. “Error-controlled Adaptive Finite Element Methods in Large Strain Hyperelasticity and Fracture Mechanics”. PhD thesis. Hannover: University of Hannover, May 2003. ISBN: 3-935732-08-2.

- [125] E. Sanchez-Palencia. “General introduction to asymptotic methods”. In: *Homogenization techniques for composite media*. Springer, Berlin, 1987, pp. 121–136.
- [126] M. Schmich and B. Vexler. “Adaptivity with dynamic meshes for space-time finite element discretizations of parabolic equations”. *SIAM J. Sci. Comput.* 30.1 (2008), pp. 369–393.
- [127] J. C. Simo and T. J. R. Hughes. *Computational inelasticity*. Vol. 7. Springer Science & Business Media, New York, 2006.
- [128] E. Stein, ed. *Error-controlled Adaptive Finite Elements in Solid Mechanics*. Chichester: Wiley, Chichester, 2003. ISBN: 0-471-49650-2.
- [129] E. Stein, S. Ohnibus, and M. Rüter. “Hierarchical model-and discretization-error estimation of elasto-plastic structures”. In: *Mechanics for a New Millennium*. Kluwer Academic Publishers, Netherlands, 2001, pp. 373–388.
- [130] E. Stein and M. Olavi Rüter. “Finite element methods for elasticity with error-controlled discretization and model adaptivity”. *Encyclopedia of Computational Mechanics Second Edition (eds E. Stein, R. Borst and T. J. Hughes)* (2018), pp. 1–96.
- [131] P. Steinmann. “A micropolar theory of finite deformation and finite rotation multiplicative elastoplasticity”. *Int. J. Solids Struct.* 31.8 (1994), pp. 1063–1084. DOI: 10.1016/0020-7683(94)90164-3.
- [132] N. Takano, Y. Ohnishi, M. Zako, and K. Nishiyabu. “The formulation of homogenization method applied to large deformation problem for composite materials”. *International Journal of Solids and Structures* 37.44 (2000), pp. 6517–6535.
- [133] M. J. Turner, R. W. Clough, H. C. Martin, and L. J. Topp. “Stiffness and deflection analysis of complex structures”. *Journal of the Aeronautical Sciences* 23 (1956), pp. 805–823.
- [134] K. S. Vemaganti and J. T. Oden. “Estimation of local modeling error and goal-oriented adaptive modeling of heterogeneous materials; Part II: a computational environment for adaptive modeling of heterogeneous elastic solids”. *Comput. Methods Appl. Mech. Engrg.* 190 (2001), pp. 6089–6124.
- [135] R. Verfürth. *A Review of A Posteriori Error Estimation and Adaptive Mesh-Refinement Techniques*. Wiley-Teubner, Stuttgart, 1996. ISBN: 0-471-96795-5.
- [136] W. Voigt. “Ueber die Beziehung zwischen den beiden Elasticitätsconstanten isotroper Körper”. *Annalen der physik* 274.12 (1889), pp. 573–587.
- [137] K.-U. Widany and R. Mahnken. “Adaptivity for parameter identification of incompressible hyperelastic materials using stabilized tetrahedral elements”. *Comput. Methods Appl. Mech. Engrg.* 245-246 (2012), pp. 117–131.
- [138] K.-U. Widany and R. Mahnken. “Dual-based adaptive FEM for inelastic problems with standard FE implementations”. *International Journal for Numerical Methods in Engineering* 107.2 (2016), pp. 127–154.

- [139] T. Wiederkehr, B. Klusemann, D. Gies, H. Müller, and B. Svendsen. “An image morphing method for 3D reconstruction and FE-analysis of pore networks in thermal spray coatings”. *Computational Materials Science* 47.4 (2010), pp. 881–889.
- [140] P. Wriggers. *Nonlinear finite element methods*. Springer, Berlin, 2008.
- [141] J. Yvonnet and Q.-C. He. “The reduced model multiscale method (R3M) for the non-linear homogenization of hyperelastic media at finite strains”. *Journal of Computational Physics* 223 (2007), pp. 341–368.
- [142] Q.-S. Zheng and D.-X. Du. “An explicit and universally applicable estimate for the effective properties of multiphase composites which accounts for inclusion distribution”. *Journal of the Mechanics and Physics of Solids* 49.11 (2001), pp. 2765–2788.
- [143] H. T. Zhu, H. Zbib, and E. Aifantis. “Strain gradients and continuum modeling of size effect in metal matrix composites”. *Acta Mechanica* 121.1-4 (1997), pp. 165–176.
- [144] O. Zienkiewicz and J. Zhu. “Superconvergent patch recovery and a posteriori error estimates. Part 1: the recovery technique”. *Int. J. Num. Meth. Eng.* 33.7 (1992), pp. 1331–1364.
- [145] O. C. Zienkiewicz and R. L. Taylor. *The finite element method for solid and structural mechanics*. Butterworth-heinemann London, 2005.
- [146] O. C. Zienkiewicz, R. L. Taylor, O. C. Zienkiewicz, and R. L. Taylor. *The finite element method*. Vol. 3. McGraw-hill London, 1977.
- [147] T. I. Zohdi, J. T. Oden, and G. J. Rodin. “Hierarchical modeling of heterogeneous bodies”. *Comput. Methods Appl. Mech. Eng.* 138 (1996), pp. 273–298.
- [148] T. I. Zohdi and P. Wriggers. “Introduction to computational micromechanics”. *Springer, Berlin* (2008).



## Schriftenreihe des Lehrstuhls für Technische Mechanik

Bisher in dieser Reihe erschienen:

1. Gockel, Franz-Barthold: Projektierung einer Arbeitsplattform zur Schädigungsanalyse und Validierung von Simulationsmodellen unter Thermoschockbedingungen; P-2008-1; Dissertation 2008; ISBN 978-3-8322-7465-8
2. Hentrich, Manuel: Geklebte Strukturen unter Crashbeanspruchung; P-2010-2; Dissertation 2010; ISBN 978-3-8322-8964-5
3. Wilmanns, Stefan: Phänomenologische und mikroskopische Modellierung von Form- gedächtnislegierungen; P-2010-3; Dissertation 2010; ISBN 978-3-8322-9485-4
4. Caylak, Ismail: Stabilized Mixed Triangular and Tetrahedral Finite Elements with Volume and Area Bubble Functions; P-2011-4; Dissertation 2011; ISBN 978-3-8440- 0084-9
5. Shaban, Ahmed: Experiments and Modelling of Elasto-Viscoplasticity for Thermoplastics with Asymmetric Effects; P-2010-5; Dissertation 2010; ISBN 978-3-8440-0351-2
6. Sauerland, Kim-Henning: Phenomenological Process Simulation and Multiscale Tool Simulation directed to a Hybrid Forming Process; P-2013-6; Dissertation 2013; ISBN 978-3-8440-1918-6
7. Schneidt, Andreas: Mehrphasige phänomenologische sowie mehrskalige mikroskopische Modellierung von Phasenumwandlungen in einem Hybridumformprozess; P-2017-1; Dissertation 2017; ISBN 978-3-8440-5671-6
8. Düsing, Martin: Simulation of bainitic transformation with the phase field method; P-2018-1; Dissertation 2018; ISBN 978-3-8440-6293-9
9. Widany, Kai-Uwe: Adaptive Finite Element Methods for Direct and Inverse Problems in Nonlinear Solid Mechanics; P-2019-1; Dissertation 2019; ISBN 978-3-8440-6414-8
10. Cheng, Chun: A multi-mechanism model for cutting simulations combining asymmetric effects and gradient phase transformations; P-2019-2; Dissertation 2019; ISBN 978-3-8440-6504-6